Equivalent Dynamic Models of Active Distribution Networks with Grid Following and Grid Forming Converters

Von der Fakultät für Energie-, Verfahrens- und Biotechnik
der Universität Stuttgart zur Erlangung der Würde eines
Doktors der Ingenieurwissenschaften (Dr.-Ing.)
genehmigte Abhandlung

vorgelegt von
Jakob Ungerland
aus Rosenheim

Hauptberichter:	Prof. Dr.-Ing. Hendrik Lens
Mitberichter:	Prof. Dr.-Ing. Christof Wittwer

Tag der mündlichen Prüfung: 27.07.2023

Institut für Feuerungs- und Kraftwerkstechnik der Universität Stuttgart
2023

Summary

The increase in converter based generation, e.g., photovoltaic or battery storage systems, challenges the way of handling power systems. It jeopardizes not only system stability due to the lack of rotating masses stabilizing the grid, an ability inherently provided by synchronous machines. Moreover, due to the evolution of load-dominated to active distribution networks, the importance of accurate modeling of these networks in the context of system stability analysis is increased.

So-called grid forming converters meet the former challenge. This control aims at substituting the stabilizing capabilities of synchronous machines by emulating inertia. The latter challenge calls for ideally detailed models of active distribution networks. However, embedding detailed distribution network models in a dynamic transmission system model is impracticable due to model complexity. Complexity-reduced equivalent dynamic models solve this obstacle.

Putting these two points together, i.e., considering grid forming converters in equivalent dynamic distribution network models, displays a research gap not addressed in previous work. Hence, this work provides a validated methodology to create equivalent dynamic active distribution networks including grid forming converters with the application in comprehensive stability studies of future power systems. The proposed approach for deriving the equivalent dynamic model is a gray-box parameter identification method based on the clustering of the components in the corresponding detailed network. Voltage sensitivities are deployed to represent the grid's strength at the grid forming converter's connection point. The approach utilizes knowledge about the detailed network model and, hence, dynamic simulation or measurement data are not required for parameter identification. This renders a fast equivalent dynamic model derivation possible.

The proposed method is validated in dynamic simulations of four scenarios. The detailed active distribution networks of the scenarios, which are aggregated applying the proposed method, vary in the number of grid forming converters and network topologies. The approach is compared to an existing gray-box approach capable of creating equivalent models

for networks dominated by conventional grid following converters for benchmarking purposes. Simulation results for different events of the detailed and equivalent models are compared. The equivalent model aggregated with the proposed approach reproduces the detailed network's dynamic behavior adequately, while the existing approach fails to meet validation criteria. Moreover, the derived equivalent model reduces the detailed network model significantly in terms of nodes and simulation time.

This work also proposes a simplified adaptation of the derived equivalent dynamic model to new operating points. The adapted model is valid for a considerable range of load and generation scenarios. This renders stability studies based on a variety of different operating point scenarios possible since it avoids a new derivation of the equivalent model.

Kurzfassung

Die Zunahme an umrichterbasierter Erzeugung, wie beispielsweise Photovoltaikanlagen oder Batteriespeichersysteme, verändert den bisherigen Umgang mit Energiesystemen. Sie gefährdet nicht nur die Systemstabilität aufgrund fehlender rotierender Masse, die das Netz stabilisieren, was eine inhärente Fähigkeit von Synchronmaschinen ist. Aufgrund der Entwicklung von lastdominierten zu aktiven Verteilungsnetzen wird auch die Bedeutung einer genauen Modellierung dieser Netze im Rahmen von Stabilitätsanalysen größer.

Die erste Herausforderung wird durch so genannte netzbildende Umrichter bewältigt. Diese Regelung ersetzt die stabilisierenden Fähigkeiten von Synchronmaschinen durch eine Nachbildung ihrer Trägheit. Für die letztgenannte Herausforderung sind idealerweise detaillierte Modelle aktiver Verteilungsnetze erforderlich. Die Einbettung detaillierter Verteilungsnetzmodelle in ein dynamisches Übertragungsnetzmodell ist jedoch aufgrund der Modellkomplexität nicht praktikabel. Komplexitätsreduzierte äquivalente dynamische Modelle lösen diese Herausforderung.

Die Verknüpfung dieser beiden Punkte, also die Berücksichtigung netzbildender Umrichter in äquivalenten dynamischen Verteilungsnetzmodellen, offenbart eine Forschungslücke, die in früheren Arbeiten nicht behandelt wurde. Daher liefert diese Arbeit eine validierte Methodik zur Erstellung äquivalenter dynamischer aktiver Verteilungsnetze mit Berücksichtigung netzbildender Umrichter für die Anwendung in umfassenden Stabilitätsstudien zukünftiger Energiesysteme. Der vorgeschlagene Ansatz zur Erzeugung eines äquivalenten dynamischen Modells ist eine gray-box Parameteridentifikationsmethodik basierend auf einer Clusterung der Komponenten im entsprechenden detaillierten Netzmodell. Spannungssensitivitäten werden verwendet, um die Stärke des Netzes am Anschlusspunkt des netzbildenden Umrichters abzubilden. Der Ansatz nutzt das Wissen über das detaillierte Netzmodell, so dass für die Parameteridentifikation keine dynamischen Simulations- oder Messdaten erforderlich sind. Dies ermöglicht eine schnelle Erstellung des äquivalenten dynamischen Modells.

Die vorgeschlagene Methodik wird in dynamischen Simulationen von vier Szenarien validiert. Die detaillierten aktiven Verteilungsnetze der Szenarien, die mit der vorgeschlagenen Methode aggregiert werden, unterscheiden sich in der Anzahl der netzbildenden Umrichter und der Netztopologie. Zu Vergleichszwecken wird der Ansatz mit einem bestehenden graybox Ansatz verglichen, der in der Lage ist, äquivalente Modelle für Netze zu erstellen, die von konventionellen netzfolgenden Umrichtern dominiert werden. Die Simulationsergebnisse für verschiedene Ereignisse des detaillierten und des äquivalenten Modells werden verglichen. Das mit dem vorgeschlagenen Ansatz aggregierte äquivalente Modell reproduziert das dynamische Verhalten des detaillierten Netzes angemessen, während der bestehende Ansatz die Validierungskriterien nicht erfüllt. Darüber hinaus reduziert das äquivalente Modell die Komplexität des detaillierten Netzmodells bezüglich Knotenanzahl und Simulationsdauer erheblich.

Eine vereinfachte Anpassung des erzeugten äquivalenten dynamischen Modells an neue Arbeitspunkte wird in dieser Arbeit ebenfalls vorgeschlagen. Das angepasste Modell ist für eine beträchtliche Bandbreite von Last- und Erzeugungsszenarien gültig. Dies ermöglicht Stabilitätsstudien anhand einer Vielzahl unterschiedlicher Arbeitspunktszenarien, da eine aufwendige Erstellung des äquivalenten Modells vermieden wird.

Abbreviations

ADN	Active Distribution Network
aFRR	automatic Frequency Restoration Reserve
CBG	Converter Based Generation
EDAM	Equivalent Dynamic Active Distribution Network Model
EHV	Extra High Voltage
FCR	Frequency Containment Reserve
GFLC	Grid Following Converter
GFMC	Grid Forming Converter
HV	High Voltage
LV	Low Voltage
mFRR	manual Frequency Restoration Reserve
MV	Medium Voltage
OHL	Overhead Line
PCC	Point of Common Coupling
PLL	Phase-Locked Loop
PSO	Particle Swarm Optimization
PV	Photovoltaic
PWM	Pulse-Width Modulation
RMS	Root Mean Square
SCR	Short Circuit Ratio
STCA	Sensitivity-Technology-Control-Clustered Approach
TCA	Technology-Control-Clustered Approach

Contents

Chapter 1

Introduction

1.1 Background

Power systems face significant changes since distributed renewable energy sources supplant conventional power plants based on synchronous machines. This trend is intensified especially in Europe, with the committed goal of achieving greenhouse-gas-neutrality by 2050 [Eur19]. Figure 1.1 shows the increase in installed power capacity of renewable energy sources and the fading out of conventional generation, e.g., nuclear power plants or coal-fired power plants, in Germany. This trend will continue [Bra+21] in order to reach the goal specified by the German government to reach greenhouse-gas-neutrality by 2045 [Ksg]. The importance and relevance of this trend can be seen already today. Figure 1.2 shows the daily share of renewable energy sources of the total net electricity generation in Germany for January and February of the year 2022. Here, it can be seen that the share reached almost 80 % on some of the days.

One challenge and topic of research projects like *MIGRATE* [Mig] or *VerbundnetzStabil* [Rog+21] is the stability of power systems whose generation is dominated by renewable energy sources. The focus is not only on the issue of fluctuating generation but more on the fading out of inertia provided by the rotating mass of synchronous machines. The rotating masses provide an instantaneous power in the event of disturbances and, hence, stabilize the system. For the interface between renewable power plants and the grid, in most cases a converter rather than a synchronous machine is utilized. However, converter based generation (CBG) lacks the inherent ability to provide inertia. Therefore, research work focuses on grid forming converter (GFMC) control capable of emulating inertia and stabilizing the grid [Mat+19; ZW11].

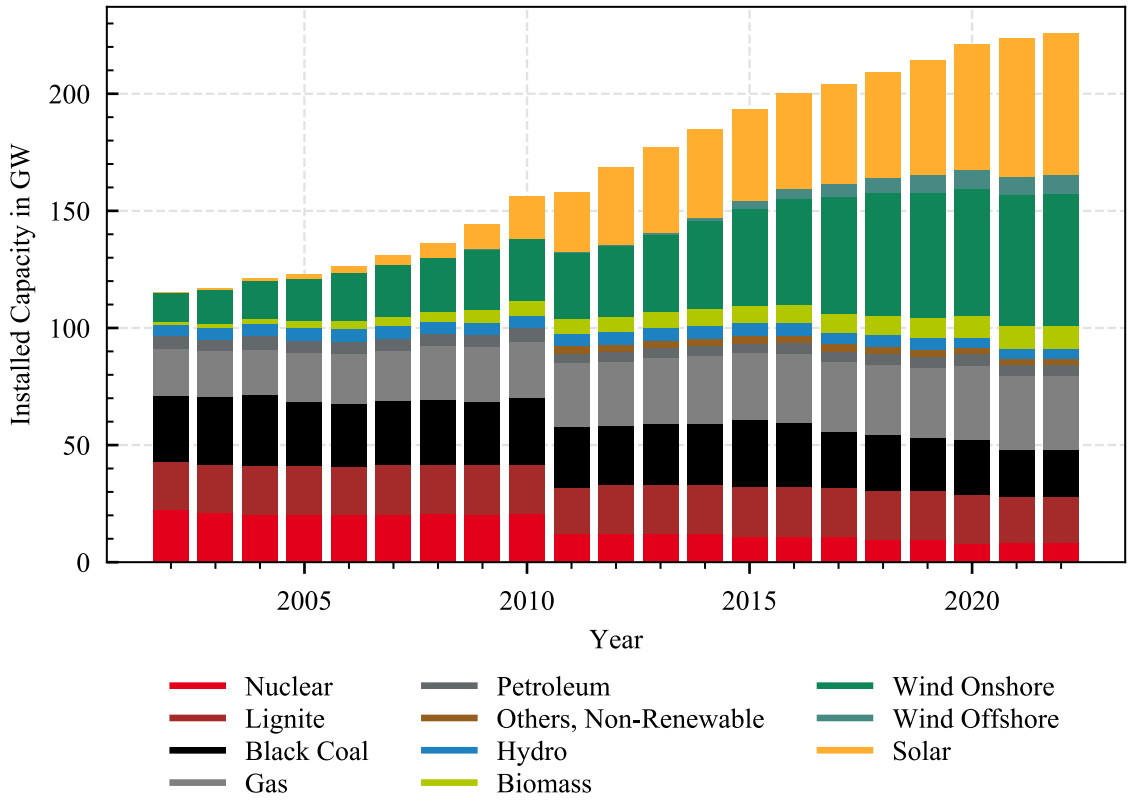

Figure 1.1: Net installed capacity of different electricity generation technologies in Germany [Bur]

The relevance of power system stability studies cannot be overstated. Significant disturbances of the year 2021 emphasize this importance. On the 24th of July, the Spanish and Portuguese grids were disconnected for more than half an hour from the interconnected network of Continental Europe [EEa]. In Rogowiec in Poland, a human error at a substation caused a loss of more than 3 GW of generation capacity on the 17th of May. This led to a frequency drop to 49.84 Hz [EEb]. Also, on the 8th of January, the synchronous area of Continental Europe experienced a system split for about an hour [EEc]. The reason was a violation of the n-1 principle, which requires transmission grid operators to guarantee a stable system in case of an outage of one grid component.

These critical events are not directly related to high CBG penetration. Also, the quick return to stable grid operation after each of the events proves the emergency mechanisms functional. Nevertheless, lower inertia in the system due to a higher CBG penetration significantly deteriorates system stability. Therefore, stability studies of future grids are essential to pave the way to a stable future power system dominated by renewable energy sources.

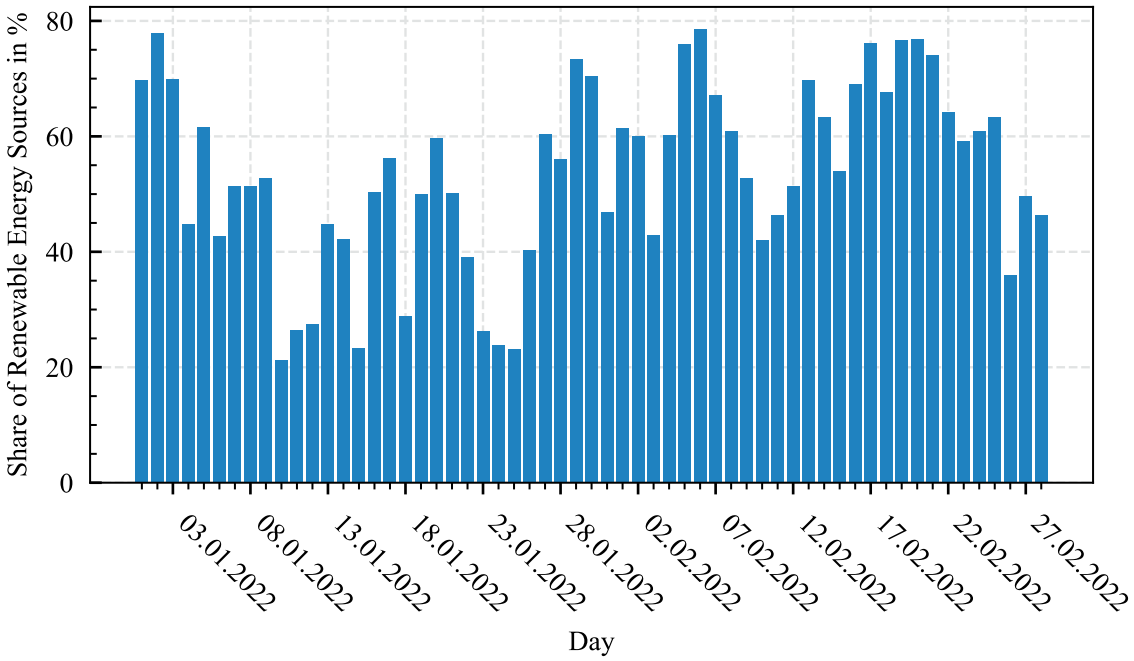

Figure 1.2: Daily renewable energy sources share of net electricity generation in Germany [Bur]

As opposed to conventional power plants being connected to the transmission grid, installations of distributed renewable energy sources are in the distribution grid, stressing the importance of the same. Studies investigating the stability of interconnected power systems focus on transmission systems. Nevertheless, with the increasing penetration of CBG, their dynamic response to events needs to be considered in stability studies. This necessitates a consideration of distribution network models including CBG in network models utilized for stability studies.

Distribution networks of conventional power systems behave relatively uniformly and can be adequately modeled by rather simple models, e.g., as equivalent loads. However, a more complex, ideally detailed, modeling is necessary as the penetration of generation in general and CBG in particular in distribution networks increases. Otherwise, the influence of these active elements within active distribution networks (ADN) on the transmission system cannot be captured adequately. To avoid detailed ADN models requiring high computational power, the concept of equivalent dynamic models was developed. An equivalent model reproduces the significant dynamic behavior of the detailed ADN in complexity-reduced models.

1.2 Challenges of High CBG Penetration for Power System Stability

The increasing penetration of renewable energy sources and, hence, of CBG challenges the stability of interconnected systems. Not only the fluctuating energy provision calls for smart operation of electricity grids to balance generation and demand, but also the fading out of synchronous machine based generation providing inertia jeopardizes system stability. For a better understanding of the term *power system stability*, the definition according to [Kun+04] is given as

> "(...) the ability of an electric power system, for a given initial operating condition, to regain a state of operating equilibrium after being subjected to a physical disturbance, with most system variables bounded so that practically the entire system remains intact." [Kun+04, p. 1388]

A further classification of power system stability can be found in Section C.1. With a focus on frequency stability, there are measures to balance generation and demand by providing active power in case of a sudden load increase or generation decrease. The temporal sequence of such a power provision according to [Eur17] is shown in Figure 1.3. The balancing services are Frequency Containment Reserve (FCR), automatic Frequency Restoration Reserve (aFRR), and manual Frequency Restoration Reserve (mFRR).

It can be seen that the different types of balancing services overlap in order to provide a time buffer for the next control reserve to be fully activated. The FCR activation depends directly on the grid frequency, and active power is provided within up to 30 seconds after a frequency deviation occurs. The instantaneous provision of active power by synchronous machines providing inertia stabilizes the grid until FCR is fully activated. This is essential since these few seconds can be sufficient to destabilize the power system if inertia is absent [Øru+15].

For a better understanding of the term *inertia*, the swing equation describing the combined moment of inertia of a generator and a turbine, J, in case of an imbalance between the mechanical torque T_m and electromagnetic torque T_e is given according to [Kun94, pp. 128ff.] as

$$J\frac{\partial \omega_\mathrm{m}}{\partial t} = T_\mathrm{m} - T_\mathrm{e}, \tag{1.1}$$

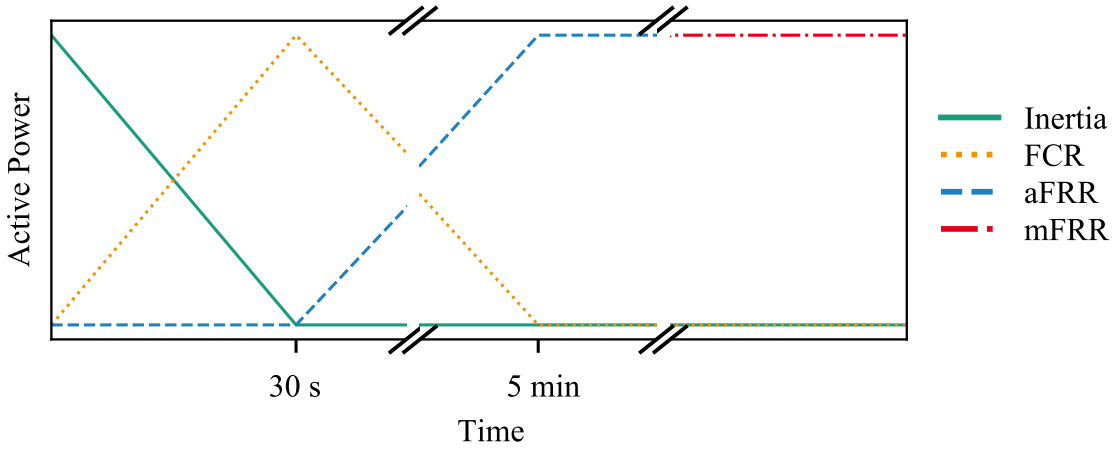

Figure 1.3: Simplified temporal sequence of active power provision as frequency balancing services according to [Eur17]

where ω_m is the the angular velocity of the rotor and t the time. Based on this equation, the term *inertia constant* H is introduced as the stored kinetic energy at rated angular velocity $\omega_{0\,\mathrm{m}}$ divided by the rated apparent power S_rat, that is,

$$H = \frac{1}{2}\frac{J\omega_{0\mathrm{m}}^2}{S_\mathrm{rat}}. \tag{1.2}$$

Merging equations (1.1) and (1.2) results in

$$2H\frac{\partial}{\partial t}\left(\frac{\omega_\mathrm{m}}{\omega_{0\,\mathrm{m}}}\right) = (T_\mathrm{m} - T_\mathrm{e})\frac{\omega_{0\,\mathrm{m}}}{S_\mathrm{rat}}. \tag{1.3}$$

Equation (1.3) illustrates that an imbalance between the mechanical and electromagnetic torque results in a rate of change of frequency dependent on the inertia constant H and, hence, on the stored kinetic energy in a turbine based generator.

An increase in CBG reduces the total inertia of a power system. This may lead to frequency stability issues due to the higher rate of change of frequency resulting from a low system inertia. Therefore, GFMC emulating inertia of synchronous machines are expected to become essential components of stable CBG dominated systems [Tam+17; Mil+18]. This increasing importance leads to the necessity of including a proper representation of the GFMC's dynamic behavior in equivalent dynamic models of ADN implemented in models for stability analysis of future power systems.

1.3 Objectives

To render comprehensive stability studies of interconnected systems dominated by CBG in the distribution network possible, equivalent dynamic ADN models (EDAM) are applied. Compared to a detailed modeling, EDAM reduce the computational effort for dynamic stability simulations remarkably. Their derivation methodologies must be capable of aggregating realistic ADN topologies with different CBG technologies, including GFMC. Hence, the main objective of this thesis can be summarized as follows:

> A validated methodology is developed to create EDAM of CBG dominated distribution networks including GFMC that can be applied in comprehensive stability studies of future power systems.

This main objective can be broken down into the following subordinate objectives:

1. Review and categorization of state-of-the-art methods for creating EDAM (Chapter 2).
   How do methods available in the literature differ from each other, and how can they be categorized? Which methodology is promising for CBG dominated networks, and are GFMC considered properly in such approaches? How simple is applying the methods, and which input data are required?

2. Identification of important factors influencing the dynamic behavior of GFMC (Chapter 2 and 3)
   How can GFMC be modeled? What factors influence the active and reactive power injection of a GFMC during and after a disturbance?

3. Development of an EDAM creation methodology that considers GFMC (Chapter 4).
   Can a state-of-the-art methodology be further developed to meet the main objective? How can the dynamic behavior of GFMC be represented in EDAM? What are the limitations of the developed methodology? What data are needed?

4. Validation of methodology on test networks and comparison of different EDAM complexity degrees (Chapter 5).
   What validation procedure is suitable for evaluating the EDAM accuracy? What network topologies and scenarios should be applied for an evaluation? How well do EDAM aggregated by the proposed approach perform in comparison to EDAM aggregated by state-of-the-art approaches? Is the aggregation of multiple GFMC to a significantly lower number of equivalent GFMC reasonable? What constraints need to be considered for a GFMC aggregation?

5. Evaluation of operating point dependency and simplified adaptation of an EDAM to new operating points (Chapter 5).
   How strongly does the EDAM depend on the operating point of the detailed network for which it was parameterized? Is a simplified re-parameterization of the EDAM possible for new operating points?

The EDAM evaluation conducted in this thesis focuses on dynamic simulations considering electromechanical transients (RMS simulations) performed in the software *DIgSILENT PowerFactory*. Electromagnetic transients, e.g., due to saturation of magnetizing inductance of transformers, are neglected since the EDAM application is for stability studies in large-scale power systems. For such investigations, RMS models are dominant in industry practice [Lam+17].

1.4 Outline

Chapter 2 – This chapter starts with an overview of methods for creating EDAM. The focus of this work is the aggregation of distribution networks. Hence, a differentiation is made between methods suitable for conventional and for active distribution networks. Especially clustering based gray-box parameter identification methods are found to be suitable for creating CBG dominated EDAM with the application in system stability studies. In the last part of this chapter, the challenges of considering GFMC in EDAM are identified, and a solution is proposed. (Objectives 1 and 2)
Chapter 3 – This chapter deals with the modeling of the components utilized in this work. Loads are modeled as constant impedances, and conventional grid following converters (GFLC) are modeled as photovoltaic (PV) systems with two different control strategies. The GFMC model is based on a droop concept and capable of current limitation. The model is equivalent to a PV system with a battery storage. (Objective 2)
Chapter 4 – Here, a methodology for creating EDAM including GFMC based on a consideration of voltage sensitivities is proposed. The general model derivation, the parameter identification process, and the generic EDAM topology are described in detail. Also, the challenge and limitation of aggregating multiple GFMC to one equivalent GFMC in the EDAM are explained. (Objective 3)
Chapter 5 – An evaluation of the proposed methodology is given in this chapter. The first section of this chapter introduces the different scenarios applied for the evaluation. Then, a suitable validation procedure to quantify the EDAM accuracy is introduced. Faults are

simulated in two different network topologies, an open ring and a closed ring topology. The biggest part of this chapter is the section with simulation and validation results of the scenarios. In the following section, the operating point dependency of the EDAM is investigated. Here, the detailed network's operating point is changed compared to the operating point the EDAM was parameterized to. Additionally, a simplified adaptation of the EDAM to new operating points of the detailed network is proposed. This avoids a complete new derivation of the EDAM for slight operating point changes, which is handy for stability studies with multiple scenarios. In the last part of this chapter, an evaluation of the EDAM complexity is conducted. Here, the EDAM's complexity is set in relation to its validity. (Objectives 4 and 5)

Chapter 6 – This work concludes with a final summary of the results and the main research contributions. An outlook for possible future work, which addresses the limitations of this work, is given as well.

1.5 List of Publications

Scientific Papers

The work that lead to this thesis partially has been presented in the following publications:

[Rog+21] S. Rogalla, A. Greulich, J. Lehner, H. Lens, P. Ernst, T. Schaupp, R. Singer, J. Ungerland, C. Schöll, R. Denninger & A. Salman. "Grid Forming Converters in Interconnected Systems - Final Results from the Joint Research Project VerbundnetzStabil". In: *20th Wind Integration Workshop*. September. 2021.

[Sal+21] A. Salman, P. N. Pham, P. Ernst & J. Ungerland. "Stabilitätsuntersuchungen von Netzbildenden Wechselrichtern in DIgSILENT PowerFactory". In: *PV Symposium*. 2021.

[UBL23] J. Ungerland, W. Biener & H. Lens. "Evaluation of Dynamic Equivalents of Active Distribution Networks with Grid Forming Converters in the Context of System Stability Studies". In: *27th International Conference on Electricity Distribution*. CIRED, 2023.

[UL23] J. Ungerland & H. Lens. "Evaluation of Equivalent Dynamic Active Distribution Network Models with Individual and Aggregated Consideration of Grid Forming Converters". In: *Energy Technology* 2300336 (2023).

[Ung+21] J. Ungerland, N. Poshiya, W. Biener & H. Lens. “Equivalent Active Distribution Networks Considering Grid Forming Converters”. In: *IEEE PES Innovative Smart Grid Technologies Europe (ISGT-Europe)*. 2021.

[Ung+22a] J. Ungerland, R. Bhadani, W. Biener & H. Lens. “Operating Point Dependency and Adaptation of Dynamic Active Distribution Network Equivalents”. In: *13th IEEE International Symposium on Power Electronics for Distributed Generation Systems (PEDG)*. 2022.

[Ung+22b] J. Ungerland, N. Poshiya, W. Biener & H. Lens. “A Voltage Sensitivity Based Equivalent for Active Distribution Networks Containing Grid Forming Converters”. In: *IEEE Transactions on Smart Grid* 14.4 (2022), pp. 2825 –2836.

[UP20] J. Ungerland & P. Pant. “Challenges of Modelling Equivalent Active Distribution Grids under Consideration of Grid Forming Inverters”. In: *Virtual 19th Wind Integration Workshop*. 2020.

[VRU20] M. F. Valois-Rodriguez & J. Ungerland. “Evaluation of Grid Reduction Techniques for Distribution Networks with a High Penetration of Inverter-based Generation”. In: *IEEE PES Innovative Smart Grid Technologies Europe (ISGT-Europe)*. 2020, pp. 824–828.

The following publication is not directly linked to the work presented in this thesis:

[Mar+21] S. Marchand, C. Monsalve, T. Reimann, W. Heckmann, J. Ungerland, H. Lauer, S. Ruhe & C. Krauß. “Microgrid Systems: Towards a Technical Performance Assessment Frame”. In: *Energies* 14.8 (2021).

Supervised Master Theses

[Bha22] R. Bhadani. *Operating Point Dependency and Adaptation of an Equivalent Dynamic Model Derived from an Active Distribution Network Including Grid Forming Converters*. 2022.

[Pan20] P. Pant. *Grid Reduction of Power Systems Dominated by Inverter-Based Generation in Consideration of Grid Forming Inverters*. 2020.

[Pos21] N. Poshiya. *Performance Evaluation of Modelling Methods for Developing Equivalent Active Distribution Grids*. 2021.

[VR19] M. F. Valois-Rodriguez. *Evaluation of Grid Reduction Techniques for Conducting Frequency Stability Analysis in Power Systems Dominated by Inverter-Based Generation*. 2019.

Project Reports

[Ern+22] P. Ernst, S. Rogalla, A. Salman, R. Singer, J. Ungerland, J. Lehner, T. Schaupp, A. Greulich, H. Oberascher, H. Lens & C. Schöll. *Forschungsprojekt VerbundnetzStabil: Stabiles Verbundsystemverhalten bei umrichterbasierter Erzeugung - Schlussbericht*. 2022.

Chapter 2

State-of-the-Art Methods for Modeling Equivalent Dynamic Active Distribution Networks

2.1 Introduction

In most cases, only a part of a network is the system of interest, i.e., events located here are simulated and its stability is evaluated. Detailed modeling of the network outside the system of interest, the so-called external system, is challenging due to high computational efforts and data availability. To avoid such detailed modeling, equivalent dynamic models were developed [War49; BC55; Dav66; Dim75]. Equivalent models aim at reproducing the significant dynamic behavior of the detailed model in a lower order model, i.e., a less complex mathematical representation compared to the detailed model.

Figure 2.1 illustrates the concept of the system of interest and external system. In this case, the system of interest is the IEEE 9 bus system [Iee]. Within this transmission system, the fault is located and the system's stability is analyzed. To capture the dynamic response of the active distribution networks, they are connected to the system of interest. Nevertheless, only the dynamic behavior at the boundary buses between the external system and system of interest is relevant for the stability analysis. Hence, an aggregated complexity-reduced modeling of the external system is reasonable.

It is important to mention that the system of interest and the external system can be on the same voltage level, i.e., both can be part of the transmission or distribution system. Nevertheless, this work focuses on creating equivalent dynamic models for stability analysis of systems dominated by CBG in the distribution network. Hence, in the following, distribu-

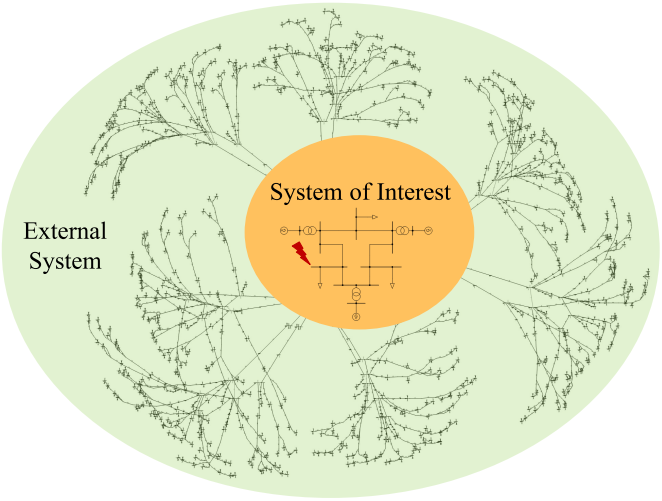

Figure 2.1: Schematic showing system of interest and external system

tion networks are the external system to be aggregated, while the transmission network is the system of interest.

Previous scientific work categorized the methods for developing equivalent dynamic models dependent on the application. Table 2.1 tries to give an overview of the most relevant literature and the corresponding method classifications. References [Zal12; Wu16; Ram99; RMM13] categorize between conventional approaches capable of creating equivalent dynamic models of a conventional synchronous machine dominated network and approaches for ADN, while [MBB11] differentiates between online and offline analysis. Reference [ÐS12] separates the applications between control theory and large-scale power system analysis. Reference [Ann+12] classifies the approaches in a high frequency, low frequency, and wideband equivalent. Finally, [SZ22] differentiates between the analysis of electromagnetic transients and of steady-state and electromechanical transients.

Motivated by [Zal12; Wu16; Ram99; RMM13] and in line with the defined objective of this work (Section 1.3), a classification of the methods is proposed as shown in Figure 2.2. Methods are distinguished between the ones that generate equivalent dynamic models of ADN with conventional generation only, i.e., synchronous generators, and of ADN with a relevant penetration of CBG.

Conventional networks comprise synchronous machine based generation, mostly connected to the transmission system, while the distribution networks are load dominated. As a result, conventional equivalent distribution network models usually do not consider generation at all or only implicitly by allowing for reverse flow but without distinguishing load and generation dynamics [ML21a]. Methods suitable for such networks as coherency based approaches or

modal analysis are described in Section 2.2. Furthermore, as soon as the penetration of CBG within distribution networks increases, new approaches are required to capture the dynamic behavior of these active elements within the ADN. These parameter identification approaches are described in Section 2.3.

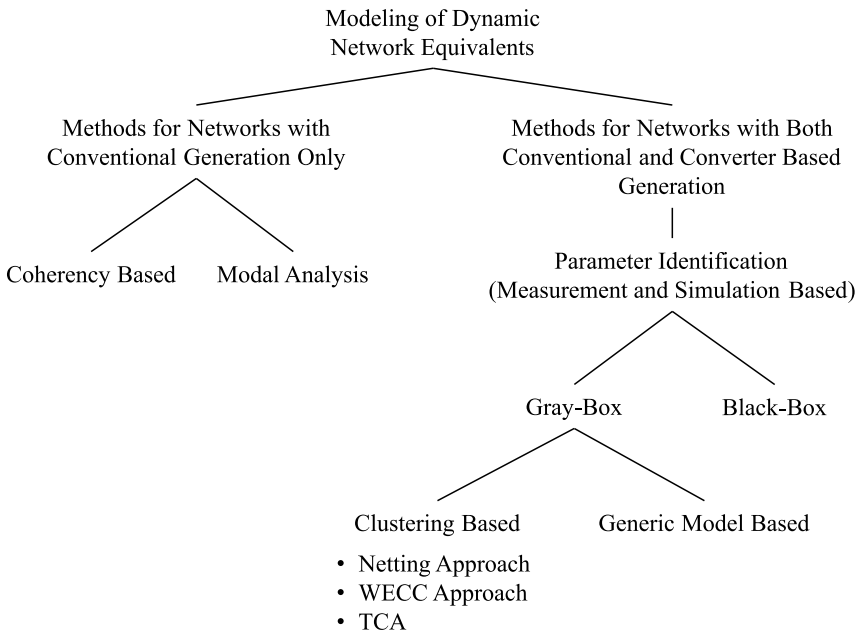

Figure 2.2: Proposed classification of methods for deriving equivalent dynamic models

Table 2.1: Literature review of equivalent dynamic model derivation classifications

Classification	**Description**	**Reference**
Conventional Approaches	• *Coherency Based Aggregation*: coherent generators are found and aggregated to equivalent generators • *Modal Analysis*: detailed system is linearized and focus is on dominant eigenvalues	[Zal12, pp. 60ff.]
Parameter Identification Approaches	Measurements or simulation results utilized for parameter identification algorithms • *Gray-Box (Model Based)*: equivalent model is derived utilizing parameter identification algorithms; subdivision in Artificial Model Based (equivalent model derived directly from parameter identification algorithms) and Physic Model Based (equivalent model based on physical modeling of power components) possible • *Black-Box (Model Free)*: application of Artificial Neural Networks to parameterize the equivalent model	[Wu16, pp. 11ff.] [Ram99] [RMM13]
Online Assessment	*Parameter Identification Approaches*: measurements utilized as input for algorithms	
Offline Analysis (Model Reduction)	• *Physical Reduction*: according to the study to be conducted network components are modeled in detail or not • *Topological Reduction*: nodes and generation units are aggregated and/or eliminated • *Modal Analysis*	[MBB11, pp. 557ff.]
Application in Control Theory	• *Linear Systems*: methods suitable are Singular Perturbations Analysis, Modal Analysis, Singular Value Decomposition, Moment Matching, combination of Singular Value Decomposition and Moment Matching • *Nonlinear Systems*: methods suitable are Proper Orthogonal Decomposition, Trajectory Piecewise Linear Method, balancing based methods, reduction by optimizing system matrices, projection from a linearized model	[ÐS12]
Application in Large-Scale Power Systems	• *Coherency Based Aggregation* • *Synchrony*: synchronic generators are found and aggregated to equivalent generators • *Singular Perturbations Analysis*: analysis of power system dynamics in separate time scales • *Modal Analysis* • *Parameter Identification Approaches*	
High Frequency Equivalent	• *Frequency-Dependent Network Equivalent*: vector fitting techniques utilized for parameterization of equivalent model • *(Modified) Two-Layer Network Equivalent*: separation of detailed network in low-order frequency-dependent transmission lines and low-order frequency-dependent network equivalent	[Ann+12]
Low Frequency Equivalent	• *Modal Analysis* • *Coherency Based Aggregation* • *Parameter Identification Approaches*	
Wideband Equivalent	Utilized for sub-synchronous oscillation analysis	
Electromagnetic Transients	Equivalent model derivation is subdivided into optimal structure search in time (Norton Equivalent, Modal Decomposition) and/or frequency domain and parameter identification utilizing optimization methods	[SZ22]
Steady-State and Electromechanical Transients	• *Modal Analysis* • *Coherency Based Aggregation* • *Coherence-Modal Methods*: combination of Modal Analysis and Coherency Based Aggregation	

2.2 Equivalent Dynamic Conventional Distribution Network Models

The most commonly used methods for creating equivalent dynamic models of conventional distribution networks are coherency and modal based approaches. Coherency based equivalent dynamic models are obtained by aggregating coherent generators. A similar rotor angle swing qualifies generators to be aggregated applying Zhukov's method [Zhu64]. Then, the method developed by Dimo [Dim75] reduces the whole network [MBB11]. As listed in [ĐS12], an aggregation of synchronic generators is proposed by [Ram+96]. Synchronic generators can be found by analyzing their rotor angle swings to the excitation of modes within a selected mode subset. Both methods depend on rotor angle swings, a characteristic that is lacking in CBG.

An example of coherent generators is given in Figure 2.3. Here, the rotor angle responses to a fault of three different synchronous machines are shown. Since the rotor angle swings of Synchronous Machine 1 and 2 are similar, these two machines are coherent and can be aggregated. However, Synchronous Machine 3 has a different rotor angle response and is not coherent with the other two machines.

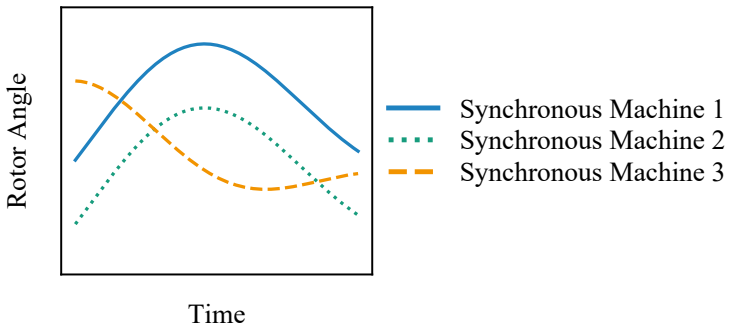

Figure 2.3: Rotor angle responses to a fault of three synchronous machines

Modal based aggregation approaches reduce the order of the detailed system by linearizing it and focusing on dominant eigenvalues. As such, only the small signal behavior can be replicated adequately [Dav66]. However, for stability analysis, the simulation of severe faults leading to nonlinear large-signal responses of CBG is essential [RMM13]. Examples of the derivation of equivalent dynamic models based on modal approaches are given in [UT71; Und+71; Pri+78; PR81; VPAS82; PAVS82].

2.3 Equivalent Dynamic Active Distribution Network Models

2.3.1 Introduction

For aggregating ADN, new approaches need to be utilized. The majority of promising methods for creating EDAM of CBG dominated systems are parameter identification approaches [VRU20], which utilize data as input for the parameter identification algorithm. Data can be gained either from real networks, e.g., measurement data derived from phasor measurement units, or from detailed simulation models. With the gained input data, parameters of either a gray-box or a black-box model based on an artificial neural network can be identified.

Black-box based EDAM are created by training an artificial neural network. Input training data can comprise time series of loads, CBG, and switching states. The parameters of the artificial neural network are optimized to match the input data to the corresponding output training data, i.e., power exchange at the boundary bus, as accurately as possible [Liu+20]. Black-box based EDAM can be found in [Liu+20; MV12; AES04].

Methods for creating gray-box model based EDAM can be further categorized into generic model based and clustering based approaches (Figure 2.2). The former utilize a generic model structure often comprising a ZIP load and an induction motor model [RJH06; Cho+06]. This model can be extended by a CBG or an exponential recovery model [KH94], possibly adapted to take generation into account [ML21a]. The model parameters, including the dynamic control parameters, are estimated by utilizing parameter identification algorithms based on comprehensive input data such as time series of voltage, frequency, active and reactive power [ZM13]. Examples of generic model based gray-box EDAM are published in [Cou22; Cha+21; ML21b; CDS19; Sha+19; Ful+20; Kon+19; Wu+18; Sam+15; ZM13; IMK07; FLB07].

Both black-box and generic model based gray-box methods don't rely on insight into the network to be aggregated. However, in case input data for parameter identification are gained from detailed simulation models, the computational effort for data generation is high. Also, data from real network measurements need to be processed and mostly don't comprise large disturbances. Further drawbacks are the dependency of the created model on the data set used for the parameterization and the high computational effort of parameterizing such an EDAM.

If complete insight into and knowledge about the network to be aggregated, i.e., the ADN, is available, this knowledge should be utilized for the EDAM creation. This is considered

in clustering based gray-box EDAM. Here, the basic process of creating a gray-box based EDAM derived from a known detailed network model can be categorized in the following steps:

1. Clustering of Components
2. Model Creation
3. Parameterization

The detailed network's components are clustered according to specific criteria in the first step. Based on these clusters, equivalent components per cluster are created and connected to a model structure. Parameters that cannot be derived directly from the detailed network are found in the last step utilizing parameter identification algorithms. Examples for clustering based methods for deriving EDAM are the Netting Approach [Kun94], the WECC Approach developed by the *Western Electricity Coordinating Council (WECC)* [WEC10], and an approach developed by [Böm16]. This work refers to the latter as the *Technology-Control-Clustered Approach (TCA)*.
This work aims to provide EDAM for stability analysis of a future system. To this end, the transmission system is the system of interest, while the distribution network is the external system to be aggregated. As opposed to modeling real networks, it can be sufficient for stability analysis to model representative expected ADN structures from which EDAM will be derived. Therefore, complete insight into and knowledge about the network to be aggregated, i.e., the ADN, can be assumed, and clustering based methods can be applied.
The adequate consideration of the dynamic behavior of GFMC in the EDAM is an important focus of this work. The work of [Cou22] introduces a generic model based gray-box method to derive an EDAM containing GFMC. Nevertheless, as a generic model based EDAM, the method comes with the mentioned drawbacks.

2.3.2 Netting and WECC Approach

An overview of international industry practice to derive clustering based gray-box EDAM in a simulation environment is given by [Joi18; Lam+17]. Netting the loads and generators to a single equivalent load is the most commonly used method (Netting Approach) [Kun94]. Here all loads and generators are aggregated to a single unit by summation of the active and reactive power demand, where generators are considered as negative loads (Figure 2.4). Also, the equivalent load is directly connected to the system of interest, i.e., the transmission

system, neglecting different voltage levels. A boundary bus is the common link between the transmission system and the equivalent model. It becomes clear that no dynamic behavior, especially of CBG, can be considered in such a simplified model.

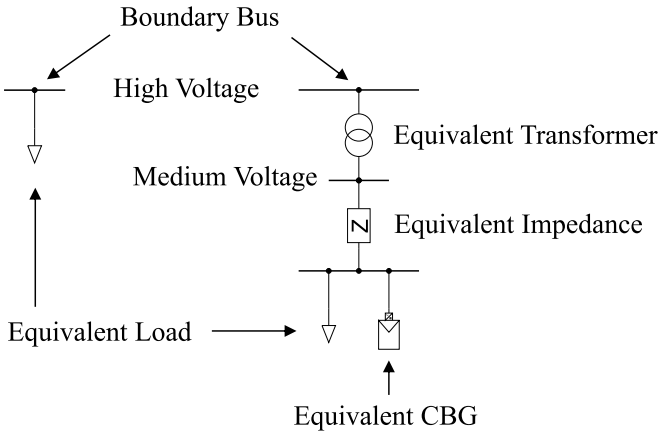

Figure 2.4: Schematic of equivalent models aggregated by Netting Approach (left) and WECC Approach (right)

A further, more detailed model can be derived with the WECC Approach [WEC10]. Here, the detailed network's components are clustered as groups of loads and generators. For each cluster, a corresponding equivalent component is created by summation of their active and reactive power demand and generation, respectively. Also, an equivalent transformer and equivalent impedance connect the MV level with the transmission system. For optimizing the equivalent impedance parameters, the objective is to minimize the deviation of the equivalent model's steady-state power flow at the boundary bus from the power flow observed at the boundary bus of the detailed network model. Figure 2.4 shows an exemplary equivalent model aggregated by the WECC approach. In this case, an equivalent PV system represents all the CBG in the corresponding detailed network.
Nevertheless, both the Netting and WECC Approach lack differentiation between generation technologies, control strategies, and voltage levels leading to insufficient simulation results for networks with high CBG penetration [VRU20].

2.3.3 Technology-Control-Clustered Approach

As elaborated in [Ung+22b], the mentioned drawback of both Netting and WECC Approach is addressed in [Böm16] with the introduction of the TCA. Based on knowledge about the network to be aggregated, i.e., technologies and control strategies of components as well

as static load flow data, the TCA application creates an EDAM capable of approximately reproducing the dynamic response of a CBG dominated ADN with acceptable accuracy.

TCA is a gray-box aggregation method that clusters the detailed network's components according to technology, control strategy, and voltage level [Böm16]. The components are aggregated as a single equivalent unit based on the respective cluster. Each voltage level has a single equivalent node to which the corresponding components are connected. Equivalent transformers and equivalent impedances connect the different voltage levels. Similarly to the WECC Approach, the equivalent impedance parameters are tuned to minimize the deviation of the EDAM's steady-state power flow at the boundary bus from the power flow observed at the boundary bus of the detailed network model.

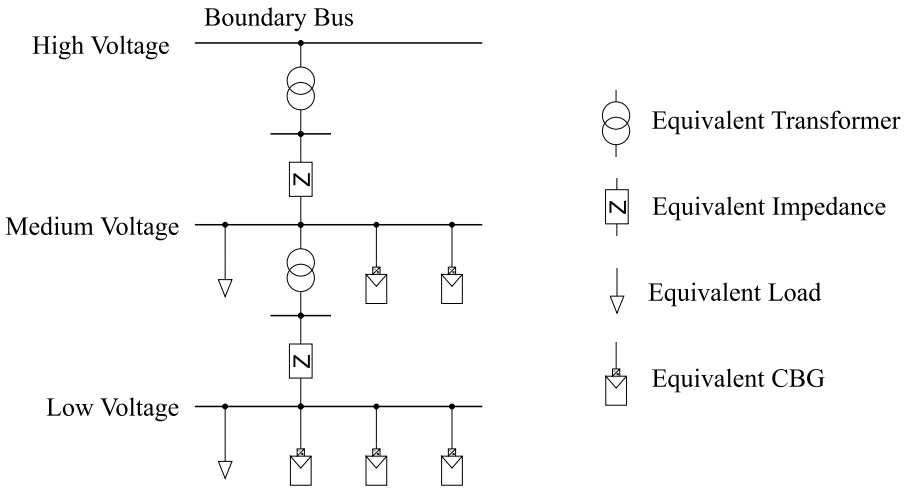

Figure 2.5: Schematic of an EDAM aggregated by TCA

Figure 2.5 shows an EDAM aggregated by TCA derived from an ADN comprising the medium and low voltage levels. Only PV systems represent the CBG, and two different GFLC control strategies, i.e., different behavior during events or faults, were implemented in the MV network. GFLC in the LV network comprise three different control strategies. This results in five generator clusters: MV GFLC with two control strategies and LV GFLC with three control strategies. All loads and generators of each cluster were aggregated to a single equivalent unit by summation of their active and reactive power demand and generation, respectively. It is important to mention that this example only considers PV systems as generation technology. As elaborated in [Böm16], other generation technologies such as wind turbines or combined heat and power components can be adequately represented in an individual cluster, i.e., individual equivalent component.

2.3.4 Comparison of Methods

The results of this method comparison can also be found in [Ung22].
In the following, the three presented clustering based gray-box methods are compared in three scenarios with different GFLC shares. GFMC are not considered in this evaluation since the performance of TCA based EDAM with GFMC is studied in detail in Section 5.4. For this comparison, a test network model is created consisting of a transmission and distribution system (Figure 2.6). The MV and LV networks are aggregated using Netting Approach, WECC Approach, and TCA. In all cases, the transmission system is modeled according to the IEEE 9 bus system [Iee]. Three detailed distribution networks are used to replace the original loads at the nodes 5, 6, and 8 in the transmission network as marked in Figure 2.6. The European MV and LV benchmark systems [Str+14] are used to represent the distribution networks. A total of nine MV benchmark systems in the European configuration are used. Seven of the MV loads are replaced by LV benchmark systems in the European configuration. A PV system was installed as a GFLC with the same rated power for each load in the MV and LV networks. Generation and load datasets of the distribution grids to be aggregated are summarized in Table 2.2 and Table 2.3.

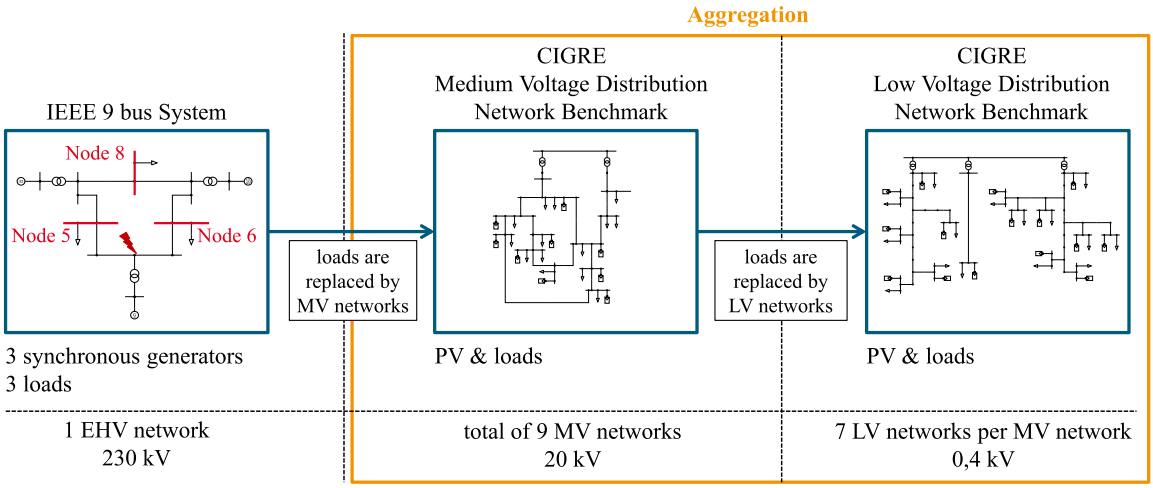

Figure 2.6: Overview of the test network

Three GFLC penetration scenarios are considered for this study. To this end, the installed capacity of the PV systems of Table 2.3 was reduced by the corresponding factor. In the first scenario, a GFLC penetration of about 25 % of the total generation (synchronous machines in the transmission system and GFLC in the distribution system) is implemented. In the second scenario, 51 % of the total generation is covered by GFLC, while in the third scenario, it is 77 %. To compare the three aggregation methods, a 230 ms short circuit is simulated

Table 2.2: Distribution of loads per voltage level

Voltage Level		**Distribution per EHV Node**			**Total Load**
		Node 5	Node 6	Node 8	
MV	P in MW	119.46	79.70	79.70	**278.86**
	Q in Mvar	27.99	18.66	18.66	**65.31**
LV	P in MW	14.42	9.61	9.61	**33.64**
	Q in Mvar	5.97	3.98	3.98	**13.93**
Total	P in MW	**133.88**	**89.31**	**89.31**	**312.50**
	Q in Mvar	**33.96**	**22.64**	**22.64**	**79.24**

Table 2.3: Distribution of PV systems per voltage level

EHV Node	**Voltage Level**	**Nominal PV Power** in MVA	**Share** in %
5	MV	122.94	38.01
	LV	15.67	4.85
6	MV	81.96	25.34
	LV	10.44	3.23
8	MV	81.96	25.34
	LV	10.44	3.23
Total		**323.41**	**100**

in the transmission network as shown in Figure 2.6. The active and reactive power flows at node 8 of all models (detailed model, EDAM aggregated by Netting Approach, EDAM aggregated by WECC Approach, and EDAM aggregated by TCA) are compared and shown in Figure 2.7.

In the 25 % scenario, the EDAM aggregated with the WECC Approach and the TCA represent the active and reactive power flow of the detailed network model very well. The EDAM aggregated by the Netting Approach shows slight deviation in the active power flow. Especially during the short circuit the reactive power drop of the detailed model cannot be captured by the EDAM aggregated by the Netting Approach.

Significant differences between the EDAM are evident for the 51 % GFLC penetration scenario. The EDAM aggregated by the Netting Approach and the WECC Approach are not

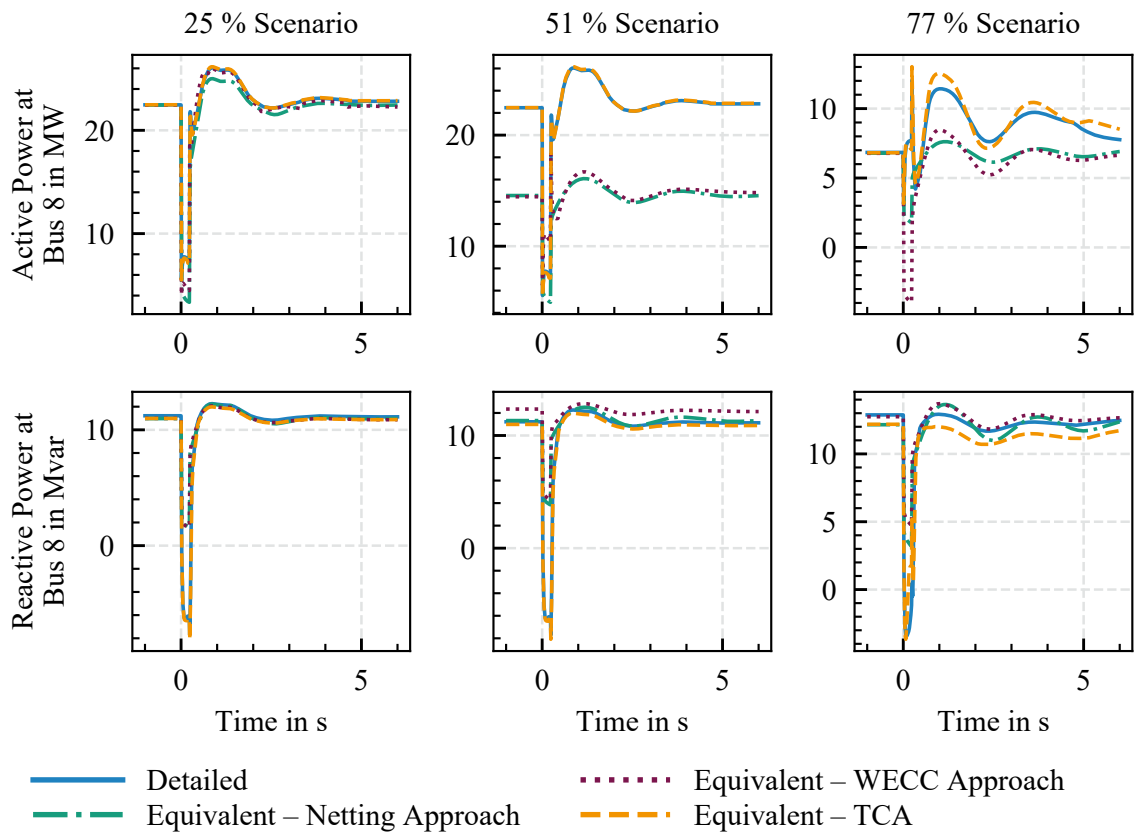

Figure 2.7: Active and reactive power flows at bus 8 from transmission to distribution system of detailed and equivalent network models for different CBG penetration levels; positive reactive power values: over-excited state; negative reactive power values: under-excited state

able to reproduce both active and reactive power flows of the detailed network model. Only the EDAM aggregated by the TCA adequately reproduces the behavior of the detailed network model.

The power responses of the third scenario with a GFLC penetration of 77 % also show that the EDAM aggregated by the Netting and WECC Approach represent the behavior of the detailed network model inadequately. As opposed to that, the EDAM aggregated by the TCA represents the detailed network's dynamic behavior better than the other EDAM. Nevertheless, deviations can be observed.

It can be concluded that the Netting Approach is suitable for aggregating networks with minor GFLC penetration (25 %). Nevertheless, in such a penetration scenario, the results of the EDAM aggregated by the WECC Approach and the TCA reproduce the detailed model more accurately. For higher penetration scenarios, the detailed network model is inadequately represented by the EDAM aggregated by both Netting Approach and WECC Approach. Only

the TCA can reproduce the dynamic behavior of the detailed network model quite well even for high GFLC penetrations (77 %). The TCA is evaluated for aggregating ADN comprising both GFLC and GFMC in Section 5.4.

2.4 Challenges of Considering Grid Forming Converters

2.4.1 Dynamic Behavior Dependencies of Grid Forming Converters

GFMC play a significant role in the stability of CBG dominated systems (Section 1.2). Therefore, a proper reproduction of the GFMC's dynamic behavior in EDAM is crucial. To this end, an understanding of the dependencies of dynamic responses of GFMC is evaluated in the following. To illustrate the basic behavior of a GFMC, the Thévenin equivalent [Bri90] consisting of a voltage source behind an impedance can be used (Figure 2.8). A voltage angle difference of ϑ is between the GFMC and the grid.

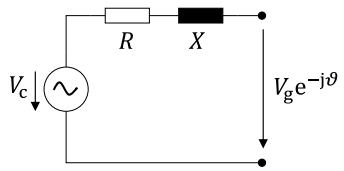

Figure 2.8: A voltage source connected to the grid via an impedance

As stated in Section 3.2.3, the active and reactive power flow between the GFMC as a voltage source with the voltage V_c and the grid voltage $V_g e^{-j\vartheta}$ separated by an impedance with negligible resistance is defined as

$$P = \frac{V_c \cdot V_g \cdot \sin(\vartheta)}{X}, \tag{2.1}$$

$$Q = \frac{V_c^2 - V_c \cdot V_g \cdot \cos(\vartheta)}{X}. \tag{2.2}$$

The dynamic power injection of the GFMC highly depends on the grid impedance and, hence, on the electrical distance to the higher voltage grid and the grid's strength at its Point of Common Coupling (PCC). Also, the grid's state, i.e., voltage magnitude and angle, influences the power injection. Therefore, these factors need to be considered in EDAM that represent the dynamic behavior of GFMC.

However, in the EDAM created with the TCA, all network components of one voltage level are connected to a single busbar. Therefore, this EDAM cannot capture the grid impedance at the GFMC's PCC in the detailed network. Hence, the dynamic behavior of the detailed ADN differs significantly from its TCA based EDAM as soon as GFMC are introduced [UP20]. This work utilizes voltage sensitivities at each PCC of the GFMC in the detailed network to represent the grid's strength and state at the corresponding GFMC's PCC in the EDAM.

2.4.2 Voltage Sensitivities

The content presented in this chapter has been published in [Ung+22b]. The voltage sensitivity of a node is defined as the change in voltage magnitude V or voltage angle ϑ due to a change in active P or reactive power Q at that specific node i, that is,

$$\frac{\partial V_i}{\partial P_i}, \frac{\partial V_i}{\partial Q_i}, \frac{\partial \vartheta_i}{\partial P_i}, \frac{\partial \vartheta_i}{\partial Q_i}. \tag{2.3}$$

The inverse of the Jacobian matrix, which is used in the Newton-Raphson power flow calculation method, can be interpreted as a sensitivity matrix, from which voltage sensitivities at each network node can be extracted. The calculation of the Jacobian matrix is briefly explained in the following paragraph.

Usually, the currents at nodes of a network are unknown. However, dependent on the nodal admittances $\underline{Y}$ and the voltages $\underline{V}$ of all nodes, the nonlinear equation to obtain the complex power $\underline{S}$ can be derived as

$$\underline{S}_i = P_i + \mathrm{j}Q_i = \underline{V}_i \sum_{j=1}^{n} \underline{Y}_{ij}^* \underline{V}_j^*; \;\; i \in 1,2,...,n. \tag{2.4}$$

By expressing the voltages in polar coordinates as

$$\underline{V}_i = V_i(\cos\vartheta_i + \mathrm{j}\sin\vartheta_i), \tag{2.5}$$

the active power P and reactive power Q balances at node i can be written as

$$P_i = V_i \sum_{j=1}^{n} V_j (G_{ij} \cos \vartheta_{ij} + B_{ij} \sin \vartheta_{ij}), \tag{2.6a}$$

$$Q_i = V_i \sum_{j=1}^{n} V_j (G_{ij} \sin \vartheta_{ij} - B_{ij} \cos \vartheta_{ij}), \tag{2.6b}$$

where $\underline{Y}_{ij} = G_{ij} + \mathrm{j}B_{ij}$ are the bus admittances of the network. $\vartheta_{ij} = \vartheta_i - \vartheta_j$ defines the voltage angle difference between node i and j. [Zhu09; OO11]

In order to derive voltage sensitivities, we linearize equations (2.6a) and (2.6b) by a first order Taylor series approximation. Assuming that node 1 is the slack node, the resulting set of linear equations can be written in matrix form as

$$\begin{bmatrix} \Delta P_2 \\ \vdots \\ \Delta P_n \\ \Delta Q_2 \\ \vdots \\ \Delta Q_n \end{bmatrix} = \begin{bmatrix} \frac{\partial P_2}{\partial \vartheta_2} & \cdots & \frac{\partial P_2}{\partial \vartheta_n} & \frac{\partial P_2}{\partial V_2} & \cdots & \frac{\partial P_2}{\partial V_n} \\ \vdots & \ddots & \vdots & \vdots & \ddots & \vdots \\ \frac{\partial P_n}{\partial \vartheta_2} & \cdots & \frac{\partial P_n}{\partial \vartheta_n} & \frac{\partial P_n}{\partial V_2} & \cdots & \frac{\partial P_n}{\partial V_n} \\ \frac{\partial Q_2}{\partial \vartheta_2} & \cdots & \frac{\partial Q_2}{\partial \vartheta_n} & \frac{\partial Q_2}{\partial V_2} & \cdots & \frac{\partial Q_2}{\partial V_n} \\ \vdots & \ddots & \vdots & \vdots & \ddots & \vdots \\ \frac{\partial Q_n}{\partial \vartheta_2} & \cdots & \frac{\partial Q_n}{\partial \vartheta_n} & \frac{\partial Q_n}{\partial V_2} & \cdots & \frac{\partial Q_n}{\partial V_n} \end{bmatrix} \begin{bmatrix} \Delta \vartheta_2 \\ \vdots \\ \Delta \vartheta_n \\ \Delta V_2 \\ \vdots \\ \Delta V_n \end{bmatrix}, \tag{2.7}$$

$$\Delta \boldsymbol{Z} = \boldsymbol{G} \cdot \Delta \boldsymbol{X}, \tag{2.8}$$

where $\Delta \boldsymbol{Z}$ is the vector of power deviations, $\Delta \boldsymbol{X}$ is the vector of small voltage deviations, and $\boldsymbol{G}$ is the Jacobian matrix, as a matrix of partial derivatives of independent variables. Solving these for $\Delta \boldsymbol{X}$ yields

$$\Delta \boldsymbol{X} = \boldsymbol{G}^{-1} \cdot \Delta \boldsymbol{Z} = \boldsymbol{F} \cdot \Delta \boldsymbol{Z}, \tag{2.9}$$

$$\boldsymbol{F} = \begin{bmatrix} \boldsymbol{H} & \boldsymbol{N} \\ \boldsymbol{J} & \boldsymbol{L} \end{bmatrix}. \tag{2.10}$$

The inverse Jacobian matrix $\boldsymbol{F}$ contains the basic information for the voltage sensitivity calculation [Sch12]. It is important to mention that the Jacobian matrix is updated at each iteration of the load flow calculation. The matrix used to extract sensitivities corresponds to the final iteration and, thus, to a converged stationary solution of the load flow problem.

For this work, we focus on the diagonal elements of the four submatrices $\boldsymbol{H}$, $\boldsymbol{N}$, $\boldsymbol{J}$, and $\boldsymbol{L}$ of (2.10). These elements refer to the response at one node to changes at the same node. As such, they describe how sensitive the node voltage is with respect to changes of active and reactive power injection changes. The voltage sensitivities $\frac{\partial V_i}{\partial P_i}$, $\frac{\partial V_i}{\partial Q_i}$, $\frac{\partial \vartheta_i}{\partial P_i}$, and $\frac{\partial \vartheta_i}{\partial Q_i}$ at node i represent the change in voltage with respect to a change in active or reactive power. For example, a voltage sensitivity $\frac{\partial \vartheta}{\partial P}$ of $0.5 \frac{1}{\mathrm{pu}}$ corresponds to a voltage angle change of 0.005

as a result to an active power change of 0.01 pu at the same node. The stronger the grid, the lesser the voltage is influenced by power changes. Hence, these diagonal elements are suitable parameters to investigate the grid's strength at a certain node.

For the rest of this work, the voltage sensitivities are written as a vector $\vec{s}_i$, that is,

$$\vec{s}_i = \begin{pmatrix} \frac{\partial V_i}{\partial P_i} \\ \frac{\partial V_i}{\partial Q_i} \\ \frac{\partial \vartheta_i}{\partial P_i} \\ \frac{\partial \vartheta_i}{\partial Q_i} \end{pmatrix}. \tag{2.11}$$

For an exemplary radial medium voltage network, in which the transformer to the high voltage network is placed in the center of the network, the voltage sensitivities $\frac{\partial \vartheta_i}{\partial P_i}$ are calculated and plotted as a heat map in Figure 2.9. It can be seen that voltage sensitivities are low around the transformer, and increase with the increasing distance to the network's center. Since the transformer connects this distribution network to a stronger transmission network (represented by a slack node), the grid is the strongest around the transformer. Hence, voltage sensitivities at nodes around the transformer are the lowest. No voltage controlled node is implemented in the shown network. Such would decrease the voltage sensitivity around its node.

These observations are coherent with the statement that voltage sensitivities are a suitable measure of the grid's strength. One could argue that parameterizing impedances according to the electrical distance between a node and the transmission system would yield the same result. However, while the calculation of the electrical distance is non-trivial, voltage sensitivities can easily be derived from the load flow calculation results. Moreover, if the grid's strength were represented by the electrical distance alone, the effect of voltage controlled nodes would be neglected.

The following example illustrates the influence of different voltage sensitivities $\vec{s}_i$ at the PCC of a GFLC and a GFMC on their respective dynamic behavior. Four test setups as shown in Figure 2.10 are used for this comparison. All models comprise an external grid represented by a voltage source, an impedance $Z_{\text{external\_Grid}}$ and an EHV/MV transformer. Connected to the lower voltage side of the transformer is either a GFLC, a GFLC with an impedance, a GFMC, or a GFMC with an impedance. The parameters of the external grid components are the same for all four setups. The nominal power values of the GFLC and GFMC are also identical. The GFLC and GFMC are connected to the lower voltage side of the transformer either with or without an impedance. The impedances of the scenarios *GFLC far* and *GFMC far* could not be parameterized to achieve the same voltage sensitivities at the PCC of the

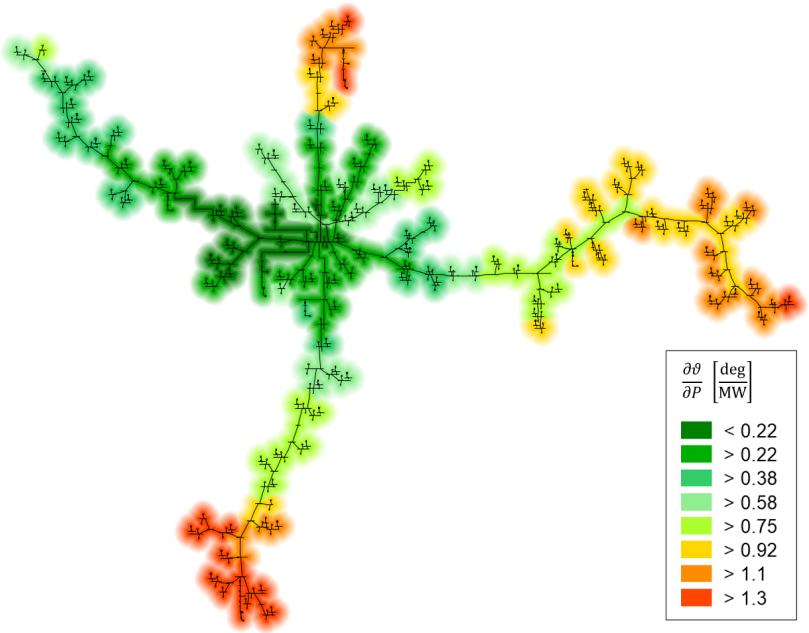

Figure 2.9: Heatmap of $\frac{\partial \vartheta_i}{\partial P_i}$ sensitivities in a radial example network [Ung+22b]

GFLC and GFMC, since GFMC as voltage sources have a stronger influence on the voltage sensitivities compared to GFLC. Hence, the impedances of the two scenarios *GFLC far* and *GFMC far* have the same parameters. The resulting voltage sensitivities at the PCC of each generator are listed in Table 2.4. The dynamic control model of the GFLC is the PVD1 model, which is explained in detail in Section 3.2.2. The GFMC is modeled with a droop based dynamic control according to [PSS20] and is described in detail in Section 3.2.3.

Table 2.4: Voltage sensitivities at the PCC of each generator in Figure 2.10

	$\frac{\partial \vartheta}{\partial P}$ in $\frac{\text{deg}}{\text{MW}}$	$\frac{\partial V}{\partial Q}$ in $\frac{\text{pu}}{\text{Mvar}}$	$\frac{\partial V}{\partial P}$ in $\frac{\text{pu}}{\text{MW}}$	$\frac{\partial \vartheta}{\partial Q}$ in $\frac{\text{deg}}{\text{Mvar}}$
GFLC close	0.0512	0.0009	0.0002	−0.0120
GFLC far	0.1987	0.0035	0.0054	−0.3028
GFMC close	0.0513	0.0009	0.0002	−0.0116
GFMC far	0.2585	0.0030	0.0047	−0.2642

A short circuit of 130 ms duration is simulated at the PCC of the voltage source of the external grid. Figure 2.11 shows the active and reactive power flows at the lower voltage side of the EHV/MV transformer of each test setup. It can be seen that the dynamic response of the two GFLC are almost the same. Hence, the additional impedance resulting in different voltage sensitivities at the GFLC's PCC does not influence the GFLC's dynamic response

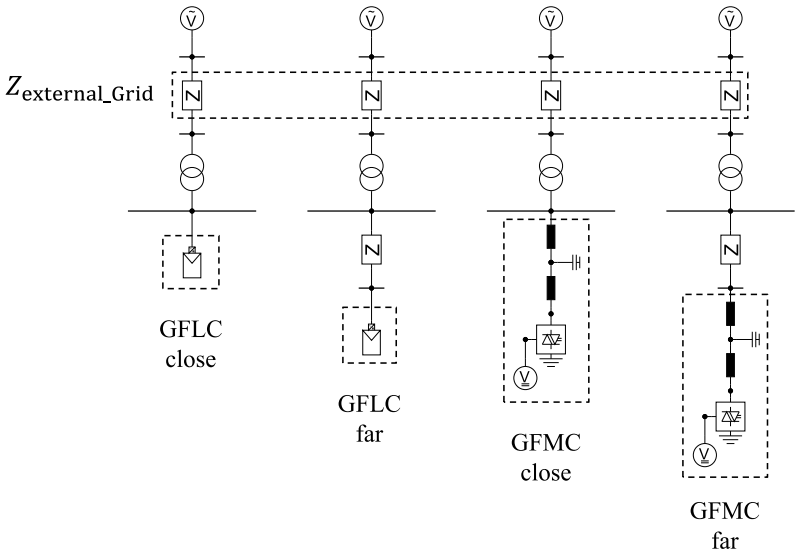

Figure 2.10: GFLC and GFMC connected to an external voltage source with different impedances

significantly. Opposed to that, the dynamic response of the two GFMC are very different. This shows the strong dependency of the dynamic GFMC response to the voltage sensitivities at their PCC.

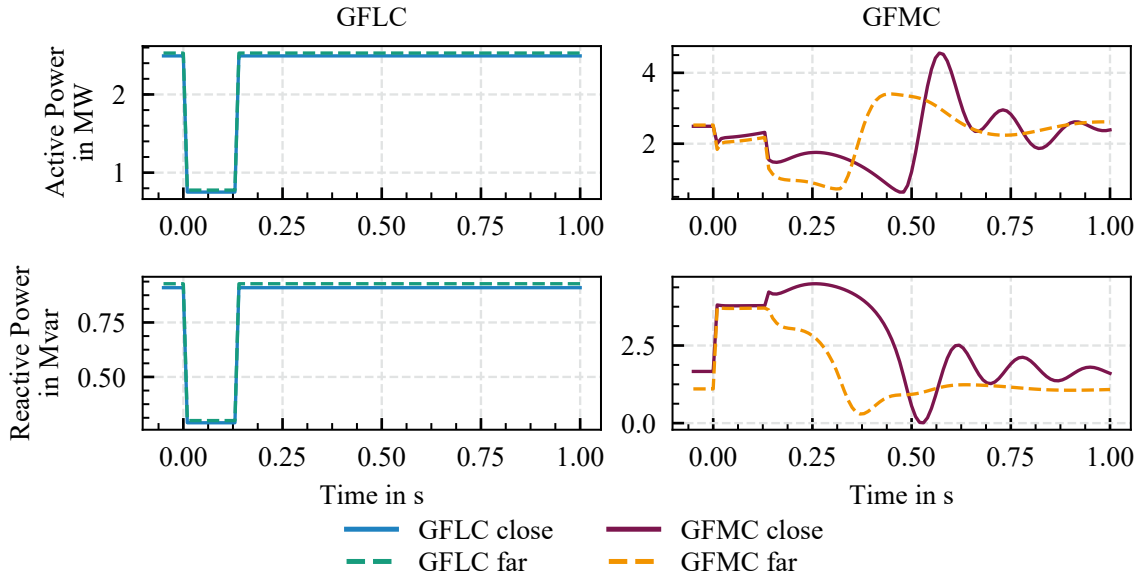

Figure 2.11: Active and reactive power flow at the lower voltage side of the transformer; positive reactive power values: over-excited state; negative reactive power values: under-excited state

2.5 Summary

This section provides an overview of methods for creating equivalent dynamic ADN models. Here, the TCA was identified as a promising parameter identification method for creating EDAM of CBG dominated networks. Nevertheless, the introduction of GFMC in power systems requires a modification of the TCA. The dynamic behavior of GFMC is highly dependent on the grid's strength at its PCC, and, hence, this factor must be reproduced in EDAM. This can be achieved by considering the voltage sensitivities $\vec{s}_i$ at the PCC of GFMC i in the detailed network at the PCC of the corresponding equivalent GFMC in the EDAM.

Chapter 3

Component Modeling

3.1 Load Model

Loads of power systems can be modeled with a static or dynamic behavior. The most commonly used static load model is the ZIP-model comprising a constant impedance (Z), constant current (I), and constant power (P) load. The relation of the consumed complex power $\underline{S}_\mathrm{L}$ and the voltage V_L at the load can be described as

$$\underline{S}_\mathrm{L} = P_\mathrm{L} + \mathrm{j}Q_\mathrm{L} = \underline{S}_0 \sum_{i=1}^{3} K_i \left(\frac{V_\mathrm{L}^{i-1}}{V_0} \right), \tag{3.1}$$

where S_0 and V_0 correspond to the pre-disturbance conditions and K_i are coefficients specifying the static behavior of the physical load [DN06]. The dependency of power and voltage is quadratic for the constant impedance load, linear for the constant current load, whereas the constant power load does not depend on voltage changes [Nav05]. The loads considered in this work are constant impedance load models only. Hence, the coefficients K_2 and K_3 of (3.1) are set to zero.

Nevertheless, the importance of dynamic load modeling for voltage stability studies is evident [Nav05]. Dynamic loads are often modeled as induction motors, whose parameters can be either identified by applying measurement based approaches or component based approaches [Lin+93; KH94]. The latter approach utilizes knowledge, e.g., derived from surveys, about the dynamic behavior of individual loads.

The studies conducted in [Böm16] consider static as well as dynamic load models, and the developed TCA was validated for both load model types. The proposed STCA is a further development of the TCA, and the representation of loads in the EDAM is adapted directly

from the TCA. Hence, this work stresses the adequate representation of GFMC in EDAM and simplifies the load modeling by solely considering constant impedance loads. In [Ung+22b], the STCA is evaluated with dynamic load models.

3.2 Converter Model

3.2.1 Introduction

ENTSO-E has introduced three classes of converter controls depending on their respective capabilities [ENT20]. *Class 1* and *class 2* refer to current controlled converters. *Class 1* converters comprise basic level functionalities focusing on converter survivability, while *class 2* includes more advanced control by adding grid supporting functionalities to the control structure. Both classes are defined as grid following converters (GFLC) in this work. Voltage controlled converters, also known as GFMC, capable of providing inertia are listed as *class 3*.

The most widely used converters, e.g., for application in PV generators, are GFLC and behave approximately like a current source. The desired active and reactive power is fed by changing the converter's output voltage depending on the voltage at the PCC on a very short timescale. Typically a Phase-Lock-Loop (PLL) and a current control loop are applied. An external voltage source is needed to provide the reference values for voltage and frequency [Du+21]. Hence, GFLC are not capable of working in a stand-alone mode.

A GFLC can behave like a constant current source (*class 1*) controlled by specific active and reactive power set points. Alternatively, it can be operated as a controlled current source capable of dynamic grid support, e.g., voltage dependent reactive power output or frequency dependent active power output [EE18]. Being more advanced, ENTSO-E attributes converters with such a control to the *class 2 Power Park Modules* [ENT20] and this work focuses on that concept for GFLC.

By acting as a voltage source, GFMC can emulate the inertia of the rotating mass of synchronous machines. Hence, GFMC stabilize power systems and can work in stand-alone mode without other voltage sources. Such a control represents the future needs of a system with high penetration of CBG, and the ENTSO-E refers to it as the *class 3 Power Park Modules* [ENT20].

For an application as a network's sole energy source, e.g., in islanded networks, GFMC can be operated as a constant voltage source with fixed frequency and voltage set points. On the other hand, parallel operation of multiple GFMC, e.g., in interconnected networks or

microgrids, demands a behavior as a controlled voltage source, whose output voltage can change with a slow dynamic response. The latter kind of GFMC control is implemented in this work. Unlike synchronous machines tolerating short-term overload, the GFMC's output current is strictly limited to protect the converter's power electronics.
Table 3.1 provides an overview of the different converter control strategies and their respective class according to [ENT20].

Table 3.1: Classification of converter control strategies according to [ENT20]

	Grid Following		**Grid Forming**	
	Class 1	**Class 2**	**Class 3**	
Source Type	Constant Current Source	Controlled Current Source	Constant Voltage Source	Controlled Voltage Source
Application	Power Injection	Power Injection and Dynamic Grid Support	Network's Sole Generator	Parallel Operation

3.2.2 Grid Following Converter

The focus of this work is the adequate representation of GFMC in EDAM. A detailed evaluation of considering different GFLC generation technologies and control strategies, e.g., wind turbines with double fed induction generators or full converter interface units, or combined heat and power, can be found in [Böm16]. The proposed STCA adopts the methodology of the TCA developed by [Böm16] in terms of GFLC representation. Hence, this work simplifies the GFLC modeling by considering only PV systems with two different control models, both developed by [WEC14]: *generic model for large-scale PV plants* and *generic model for distributed and small PV plants*. Both models focus on the PV system's response to disturbances and neglect solar irradiance transients. To this end, a constant available solar power is assumed.
The model for the large-scale PV plant comprises two control models and a protection model as shown in Figure 3.1. The electrical controls of the converter determine the desired values for active and reactive current based on reference values, the PCC voltage V_{PCC}, and power measurements P_{PCC} and Q_{PCC} at the PCC. Here, the user can define whether the active or reactive power current is prioritized. Finally, the converter interface with the grid sets the actual active and reactive power output based on their reference values and the voltage at the

PCC. Here, predefined limits, such as the maximum rate of change of reactive current, are considered. A protection model for critical voltage and frequency values sends a tripping signal to the PV plant based on voltage and frequency measurements at the PCC. A detailed description of the control models and their parameters can be found in [WEC14]. Parameters of the electrical control model, the converter interface model, the protection model, and voltage reference values as implemented in the large-scale PV model in this work are shown in Table A.5 to Table A.8 of Appendix A.

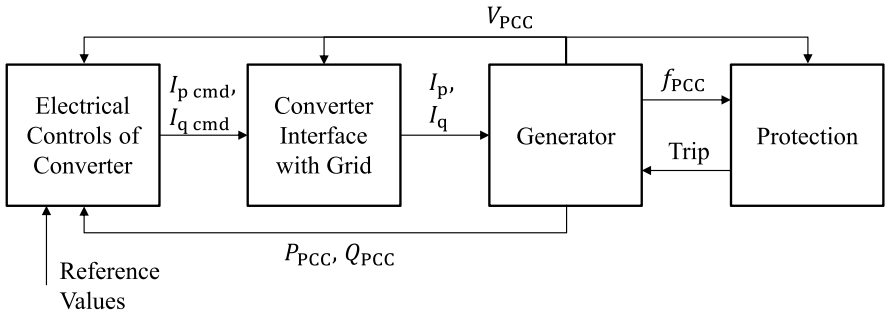

Figure 3.1: Simplified control structure of generic model for large-scale PV plants developed by [WEC14]

The generic model for distributed and small PV plants (PVD1 model) comprises one control model and is, therefore, a more simplified control model than the large-scale PV plant model (Figure 3.2). The model contains a protection model and controls active and reactive power output, where the user can prioritize either active or reactive current. The active power control can be operated with a constant active power set point or with a frequency dependent control. Similarly, the reactive power control can be set to a constant reactive power set point, or a voltage dependent reactive power output can be calculated. [WEC14]

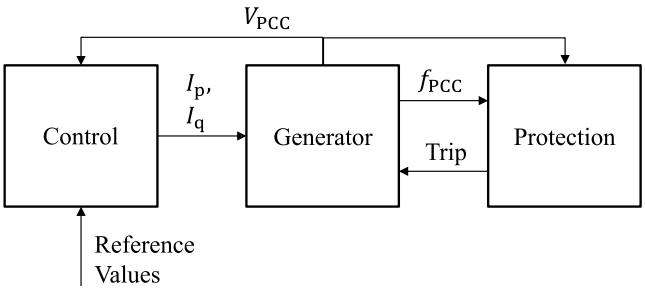

Figure 3.2: Simplified control structure of generic model for distributed PV plants developed by [WEC14]

The model also includes voltage and frequency dependent generation tripping. In Figure 3.3, the generation tripping dependent on predefined voltage threshold values is shown. Similarly, the generation tripping can be dependent on frequency threshold values. Additionally, the user can define a total or partial reconnection of the generation after a disturbance.

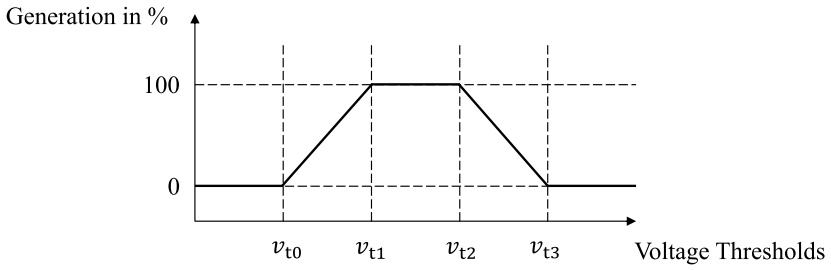

Figure 3.3: Voltage dependent generation tripping of generic model for distributed and small PV plants developed by [WEC14]

The parameters of this dynamic PVD1 control model as implemented in this work are shown in detail in Table A.9 of Appendix A.

3.2.3 Grid Forming Converter

The content in this chapter has partly been published in [UL23]. Current research focuses on GFMC development and modeling, and multiple approaches for GFMC control are possible. Droop control [Du+21; CDA93; Roc+12; PPG07], virtual synchronous machine [DV08; Wes+09; ZW11; BH07] or virtual oscillators [Joh+14] are some examples of possible realizations of GFMC controls. Moreover, a combination of modeling approaches have been developed, e.g., a droop based virtual synchronous machine [DS14]. It is important to mention that some control concepts are similar and partly equivalent. A comparison study of different control concepts can be found in [SL21].

In Figure 2.8, a GFMC simplified as a voltage source is connected to the grid via an impedance. Based on this simplified circuit, the power flow between the GFMC as a voltage source with the voltage V_c and the grid voltage $V_g e^{-j\vartheta}$, which are separated by the impedance $Z = R + jX$,

can be calculated as

$$\underline{S} = V_\mathrm{c} \cdot \left(\frac{V_\mathrm{c} - V_\mathrm{g} \mathrm{e}^{-\mathrm{j}\vartheta}}{R + \mathrm{j}X} \right)^* , \tag{3.2}$$

$$= V_\mathrm{c} \cdot \left(\frac{(V_\mathrm{c} - V_\mathrm{g} \mathrm{e}^{-\mathrm{j}\vartheta}) \cdot (R - \mathrm{j}X)}{R^2 + X^2} \right)^* . \tag{3.3}$$

Utilizing the relation

$$\mathrm{e}^{-\mathrm{j}\vartheta} = \cos(\vartheta) - \mathrm{j}\sin(\vartheta), \tag{3.4}$$

(3.3) can be rearranged to

$$\underline{S} = \frac{R \cdot V_\mathrm{c}^2 - R \cdot V_\mathrm{c} \cdot V_\mathrm{g} \cdot \cos(\vartheta) + X \cdot V_\mathrm{c} \cdot V_\mathrm{g} \cdot \sin(\vartheta)}{R^2 + X^2}$$

$$+ \mathrm{j} \left(\frac{X \cdot V_\mathrm{c}^2 - R \cdot V_\mathrm{c} \cdot V_\mathrm{g} \cdot \sin(\vartheta) - X \cdot V_\mathrm{c} \cdot V_\mathrm{g} \cdot \cos(\vartheta)}{R^2 + X^2} \right), \tag{3.5}$$

where the real and imaginary part corresponds to the active and reactive power, respectively. For inductive grids, the resistance can be neglected and (3.5) can be simplified to

$$\underline{S} = \frac{V_\mathrm{c} \cdot V_\mathrm{g} \cdot \sin(\vartheta)}{X} + \mathrm{j} \frac{V_\mathrm{c}^2 - V_\mathrm{c} \cdot V_\mathrm{g} \cdot \cos(\vartheta)}{X}, \tag{3.6}$$

$$P = \frac{V_\mathrm{c} \cdot V_\mathrm{g} \cdot \sin(\vartheta)}{X}, \tag{3.7}$$

$$Q = \frac{V_\mathrm{c}^2 - V_\mathrm{c} \cdot V_\mathrm{g} \cdot \cos(\vartheta)}{X}. \tag{3.8}$$

For small signal behavior, i.e., the phase angle difference ϑ is very small leading to $\sin\vartheta \approx \vartheta$ and $\cos\vartheta \approx 1$, (3.7) and (3.8) can be written as

$$\vartheta \approx \frac{X}{V_\mathrm{c} \cdot V_\mathrm{g}} \cdot P, \tag{3.9}$$

$$V_\mathrm{c} - V_\mathrm{g} \approx \frac{X}{V_\mathrm{c}} \cdot Q. \tag{3.10}$$

It can be seen that under the assumption of an inductive grid and a slight angle difference, the active power relates to the voltage angle. In contrast, reactive power relates to the voltage magnitude difference. This renders the implementation of a droop control concept possible, in which the active and reactive power control are implemented in separate control loops.
Since some networks do not fulfill the required condition of an inductive grid, additional measures are necessary to apply the concept of droop control. One of these methods is the implementation of a virtual impedance, which acts in series to the network impedance and thus influences it [RCRPP20].
As the requirements for a droop control implementation are established, the basic principle of this control for GFMC application is explained in the example of a droop based virtual synchronous machine. The aim is to emulate the behavior of a synchronous machine with particular emphasis on the instantaneous power provision due to the inertia of the rotating mass. This is realized via a conventional droop control in which a measurement delay is implemented [DS14].
The idea of droop control is the dynamic alignment of the active and reactive power supply depending on the frequency and voltage at the converter's PCC. In the following, due to the substantial similarity between the active and reactive power droop, only the active power droop will be described in detail. If the angular frequency ω is replaced by the voltage V and active power by reactive power, the reactive power droop can be derived. Mathematically, the active power droop can be represented as

$$\omega^* = \omega_\mathrm{g} - m_\mathrm{p}(p_\mathrm{m} - p_0) \Rightarrow p_\mathrm{m} = \frac{\omega_\mathrm{g} - \omega^*}{m_\mathrm{p}} + p_0, \tag{3.11}$$

$$\Theta(s) = \frac{1}{s} \cdot \Omega^*(s), \tag{3.12}$$

where

m_p: active power droop constant,
ω_g: angular frequency set point,
ω^*: angular frequency reference value,
Ω^*: angular frequency reference value in Laplace domain,
p_0: active power set point,
p_m: active power measurement,
θ: GFMC angle reference value,
Θ: GFMC angle reference value in Laplace domain.

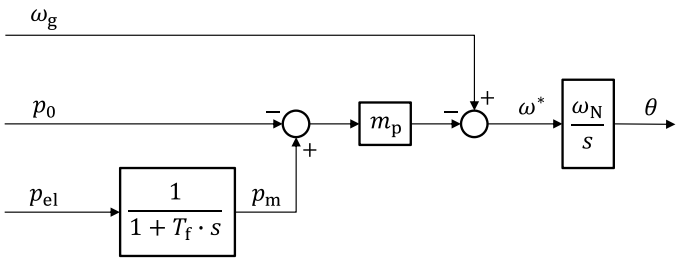

Figure 3.4: Active power droop control according to [DS14]

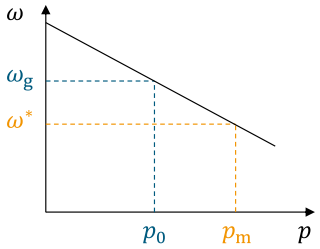

Figure 3.5: Active power droop curve according to [DS14]

The corresponding droop control system and the droop curve are shown in Figure 3.4 and Figure 3.5. By implementing the low-pass filter with the time constant T_f, the desired delayed response is integrated to realize the desired inertia. (3.11) can be written into the following equation, if p_{el} is taken as input and the low-pass filter in the Laplace domain is represented by the constant T_f, that is,

$$\frac{p_{el}}{1+T_f \cdot s} = \frac{\omega_g - \omega^*}{m_p} + p_0, \tag{3.13}$$

$$p_{el} = (1+T_f \cdot s)\left(\frac{\omega_g - \omega^*}{m_p} + p_0\right), \tag{3.14}$$

$$p_{el} = \frac{\omega_g - \omega^*}{m_p} + p_0 + \frac{T_f}{m_p} \cdot s \cdot \omega_g - \frac{T_f}{m_p} \cdot s \cdot \omega^* + T_f \cdot s \cdot p_0. \tag{3.15}$$

A virtual synchronous machine according to [DS14] is described in the Laplace domain as

$$T_a \cdot s \cdot \omega_{VSM} \approx p_0 - p_{el} - k_d(\omega_{VSM} - \omega_g), \tag{3.16}$$

where

T_a : mechanical time constant describing inertia,

k_d : damping coefficient,

ω_{VSM} : angular frequency of the virtual synchronous machine.

In order to be able to establish an equivalence between the described droop control (3.15) and a virtual synchronous machine (3.16), the following assumptions are necessary:

- Constant frequency set point ω_g
- Constant active power set point p_0

These assumptions cause the terms $s \cdot \omega_g$ and $s \cdot p_0$ in (3.15) to become zero, which allows the equation to be written as

$$\frac{T_f}{m_p} \cdot s \cdot \omega^* = p_0 - p_{el} - \frac{1}{m_p}(\omega^* - \omega_g). \tag{3.17}$$

Comparing (3.16) with (3.17), an equivalence as

$$T_a = \frac{T_f}{m_p} \tag{3.18}$$

$$k_d = \frac{1}{m_p} \tag{3.19}$$

can be established. With (3.18), the importance of the delay of the measured active power p_{el} for the modeling of the inertia of a synchronous machine becomes clear. If the time constant of the low-pass filter T_f is set to zero, the time constant of the rotor inertia T_a of the virtual synchronous machine also becomes zero. Also, the possibility of using a conventional droop control to model a virtual synchronous machine emulating inertia becomes evident.

In this work, an electromechanical model of a droop based GFMC according to [PSS20] is applied. On the left side of Figure 3.6 the GFMC components are shown. An ideal DC voltage source is connected to a two-level Pulse-Width Modulation (PWM) converter, which is modeled as a fundamental frequency model [DIg22b]. The PWM converter is then connected to the grid, i.e., the PCC, via an LCL component filtering harmonics [LBH05; Rez+14]. The filter parameterization depends on the nominal power values of the GFMC according to [Rez+14]. The detailed calculation of the parameters is shown in Section A.2.2.

The ideal DC voltage source allows for both increasing and decreasing active and reactive power injection. Hence, the GFMC model implemented in this work can be considered as a PV system connected to a battery storage system. The storage capacity is assumed to be unlimited for the scenarios considered in this work.

The converter and grid current i_c and i_g, respectively, as well as the voltage v at the capacitor are measured and utilized as inputs for the droop control and Park transformation. Based on set points for the voltage magnitude, angular frequency, active power, and reactive power, the droop control outputs are voltage angle θ and voltage magnitude v_s. The grid current in the dq-frame $i_{g\,dq}$ is utilized to calculate the voltage $v_{v\,dq}$ dependent on the virtual impedance $Z_v = R_v + j\omega L_v$ as

$$v_{v\,d} = R_v \cdot i_{g\,d} - \omega L_v \cdot i_{g\,q}, \tag{3.20}$$

$$v_{v\,q} = R_v \cdot i_{g\,q} + \omega L_v \cdot i_{g\,d}. \tag{3.21}$$

This calculated voltage $v_{v\,dq}$, the measured voltage v_{dq}, the measured converter current $i_{c\,dq}$, and the droop output voltage magnitude v_s are inputs to the cascaded voltage and current control. This inner control loop, as shown in Figure 3.6, is realized with a PI controller as explained in [PSS20]. The output is transformed to the $\alpha\beta$-frame and the resulting voltage $v^*_{\alpha\beta}$ is utilized by the PWM converter.

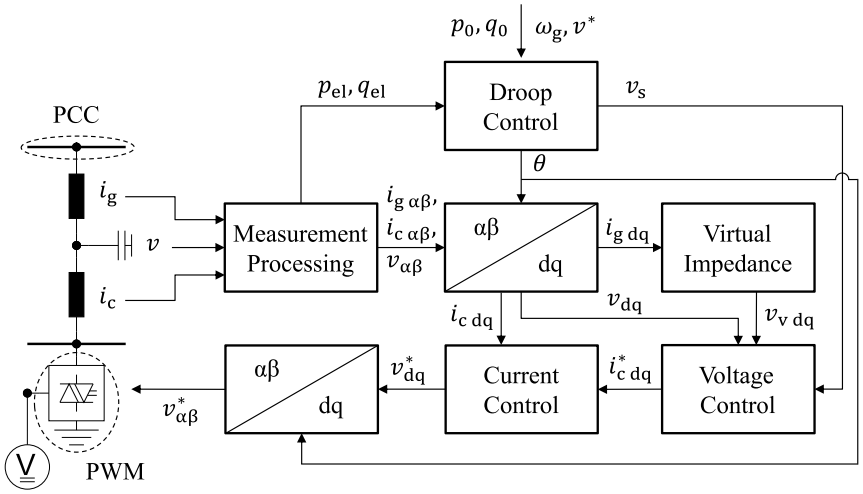

Figure 3.6: GFMC control according to [PSS20]

An important feature of GFMC is the limitation of the output current to protect the converter's power electronics. There are multiple approaches for limiting the current, and [GDS15] provides an evaluation of these. The GFMC model implemented in this work

utilizes the vector amplitude limitation concept to limit the output current $i^*_{\mathrm{c\,dq}}$ of the voltage control [PSS20]. The limited current $i^*_{\mathrm{c\,dq\,lim}}$ reduces both dq components of $i^*_{\mathrm{c\,dq}}$ simultaneously and is defined as

$$i^*_{\mathrm{c\,dq\,lim}} = \begin{cases} \frac{i^*_{\mathrm{c\,dq}}}{\sqrt{i^{*2}_{\mathrm{c\,d}} + i^{*2}_{\mathrm{c\,q}}}} i_{\max}, & \text{if } \sqrt{i^{*2}_{\mathrm{c\,d}} + i^{*2}_{\mathrm{c\,q}}} > i_{\max}, \\ i^*_{\mathrm{c\,dq}}, & \text{otherwise.} \end{cases} \tag{3.22}$$

A full list of all parameters of the GFMC dynamic control model as implemented in this work can be found in Table A.10 of Appendix A. In this work, only the described GFMC model according to [PSS20] is implemented in the detailed network models from which EDAM are derived. In [Ung+22b], EDAM with Synchronverter models and Virtual Synchronous Machine models as GFMC are created and analyzed.

3.3 Summary

This work focuses on an adequate GFMC representation in EDAM. The modeling of equivalent loads and GFLC is adopted from the TCA developed by [Böm16], where a detailed evaluation of considering different loads and GFLC technologies can be found. In order to stress the GFMC focus of this work, somewhat simplified models for load and GFLC are considered.

All loads implemented in this work are constant impedance loads. GFLC are represented by PV systems with two different dynamic control models developed by [WEC14]. The parameters of a control model, i.e., either the *generic model for large-scale PV plants* or the *generic model for distributed and small PV plants*, are the same for all PV systems equipped with this control. The GFMC model considered in this work can be compared to a PV system with battery storage. The dynamic control model is realized with a cascaded inner current and voltage control loop, including a current limitation. The outer control loop is modeled based on the droop concept. All GFMC models have the same control parameters and differ only in nominal power values and, hence, LCL filter parameters.

Chapter 4

Sensitivity-Technology-Control-Clustered Approach STCA

4.1 Introduction and Assumptions

The most promising method found in the literature to aggregate CBG dominated networks is the TCA developed by [Böm16] (Section 2.3.3). This approach can aggregate loads and GFLC of different technologies and control strategies. However, with the introduction of GFMC, the TCA based EDAM fails to capture the dynamic behavior of the corresponding detailed network adequately. So the proposed method focuses on the representation of GFMC in the EDAM.

The dynamic response of GFMC is highly dependent on its location within the network (Section 2.4.1). The electrical grid's strength at the GFMC's PCC is an essential factor in the GFMC's behavior. Also, the electrical distance to other GFMC influences the response of the GFMC. These factors need to be considered in the network equivalent to representing GFMC properly.

To this end, the GFMC are connected to the EDAM with equivalent impedances dependent on the network's topology, i.e., the location of GFMC in the detailed network. The voltage sensitivities $\vec{s_i}$ at the PCC of each GFMC i in a network are good measures to consider the electrical grid's strength and state at the GFMC's PCC (Section 2.4.2). Therefore, the equivalent impedances are tuned in order to match the voltage sensitivities at the PCC of each GFMC in the EDAM with the voltage sensitivities of the corresponding GFMC in the detailed network.

For an accurate reproduction of the network's characteristics at the PCC of the GFMC in the detailed network, each GFMC should be considered individually in the EDAM, i.e., the

number of GFMC in the detailed model should be the same as the number of equivalent GFMC in the EDAM. However, for a more significant reduction of the EDAM's complexity, aggregating multiple neighboring GFMC of the same network branch to one equivalent GFMC is an option. Aggregating non-neighboring GFMC to one equivalent GFMC can lead to a less valid EDAM, since the detailed network's topology cannot be considered anymore. The proposed method for deriving an EDAM from a CBG dominated network, including GFMC builds upon the following key findings, in which the third point derives from the second point:

1. Loads and GFLC can be aggregated in a way similar to TCA (Section 2.3.3).
2. The network's topology should be considered in terms of GFMC locations.
3. Voltage sensitivities at the PCC of each GFMC should be similar in detailed and equivalent network.
4. Multiple neighboring GFMC of one branch with similar voltage sensitivities can be aggregated to one equivalent GFMC, since the detailed network's topology can be considered in the EDAM creation.

Since the proposed method builds upon the TCA (Section 2.3.3) and considers voltage sensitivities, it is called Sensitivity-Technology-Control-Clustered Approach (STCA). The STCA based derivation of the EDAM's model structure and its parameterization is explained in Section 4.2. Furthermore, an introduction of the EDAM's generic topology is given in Section 4.3. If the number of GFMC in the detailed network differs from the desired number of equivalent GFMC, multiple GFMC can be aggregated to less equivalent GFMC. A possible method for this aggregation is proposed in Section 4.3.3.

4.2 EDAM Derivation Methodology

The EDAM derivation of a CBG dominated network including GFMC is based on the three steps described in Section 2.3 and shown in Figure 4.1:

1. Clustering of Components
2. Model Creation
3. Parameterization

The first part of this section introduces the general EDAM derivation process. The second part focuses on the optimal parameterization of the equivalent impedances, which is crucial for the accuracy of the derived EDAM.

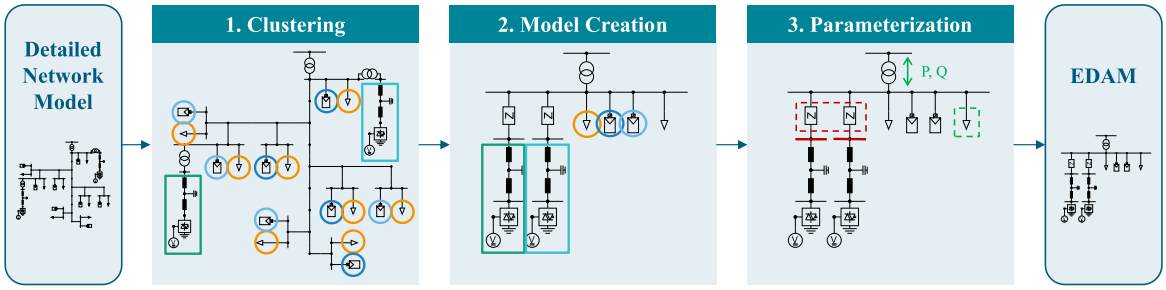

Figure 4.1: Simplified overview of EDAM Derivation Methodology

4.2.1 General Process

With insight into the detailed network model, the network structure, parameterization of generators as well as loads, load flow data, and voltage sensitivities at the nodes are known. From this input data, the EDAM can be derived as shown in Figure 4.2. This process is valid for one voltage level. However, other voltage levels can be added by repeating the process in a bottom-up way, starting with the lowest voltage level and ending with the highest voltage level of the system to be aggregated. An exemplary STCA based EDAM is shown in Figure 4.3.

Clustering of Components

In a first step, the loads of the detailed network are assigned to clusters similar to the clustering process in the TCA [Böm16]. For example, if the detailed network model comprises both induction motors and constant impedances as loads, there will be two load clusters for both load technologies. Then, the GFLC and GFMC are clustered according to generation technologies and control strategies. The GFLC of one cluster are aggregated to equivalent GFLC according to the respective clusters. The GFMC of one cluster are aggregated according to similar voltage sensitivities at their PCC to the desired number of equivalent GFMC in the EDAM. Ideally, the number of GFMC clusters, i.e., the number of equivalent GFMC, equals the number of GFMC in the detailed network. This allows proper consideration of the voltage sensitivities at the corresponding PCC and of the detailed network's topology. Nevertheless, an aggregation of GFMC is possible and described in detail in Section 4.3.3.

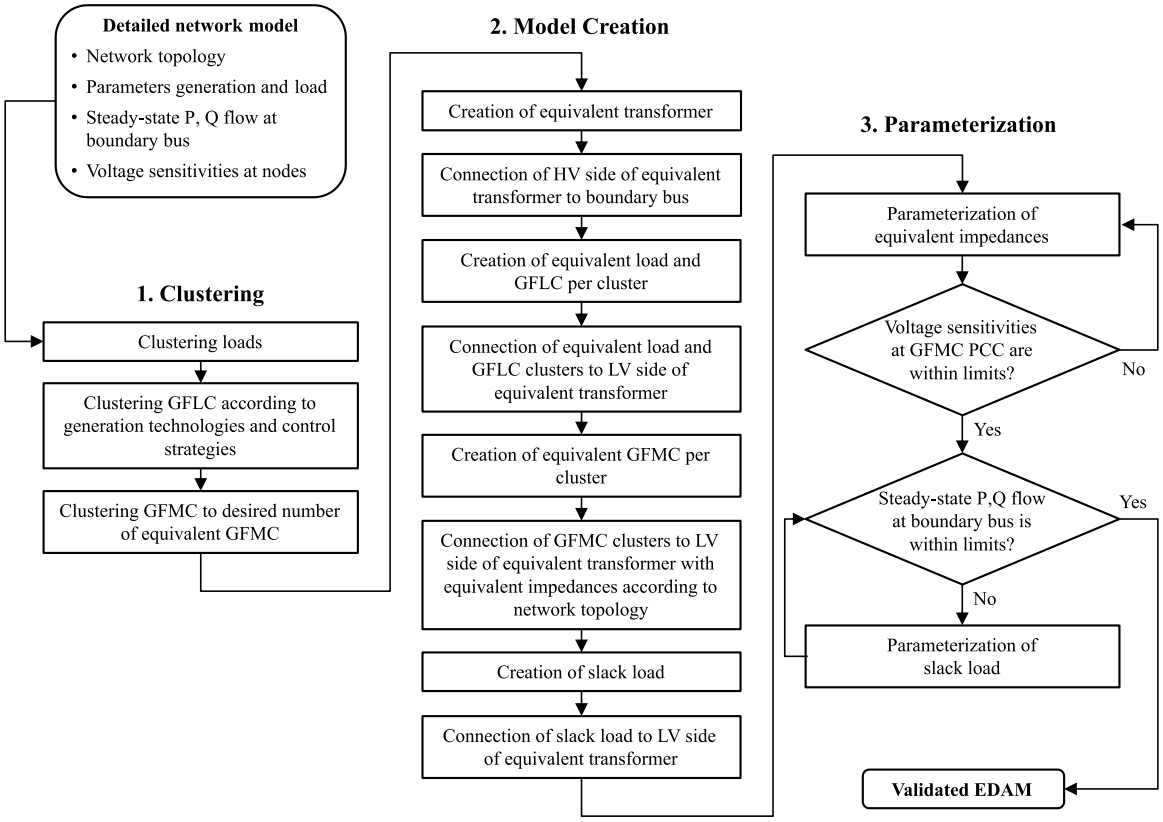

Figure 4.2: Overview of process to derive an STCA based EDAM of one voltage level

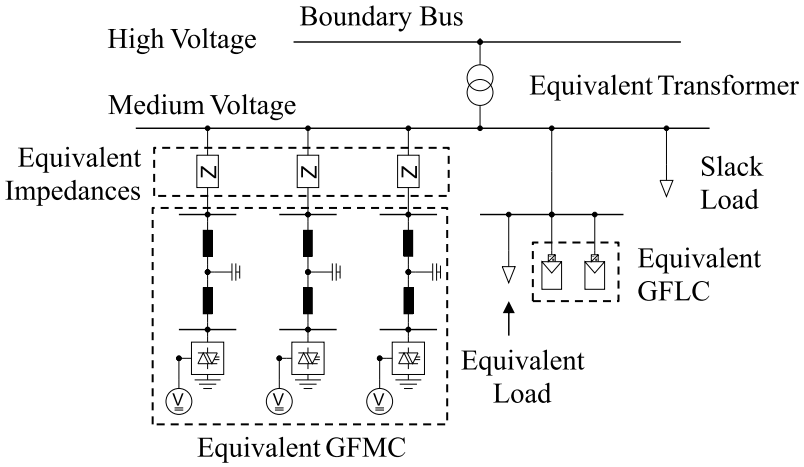

Figure 4.3: Schematic of an STCA based EDAM

As stated, a different control strategy results in a separate cluster and, hence, in an equivalent component. The goal of this work is the EDAM derivation of a representative synthetic future ADN opposed to an EDAM derivation of a real network. Hence, it is reasonable

that this work focuses on GFLC and GFMC with similar control strategies. In the scenarios in Section 5.4, two different GFLC control strategies are considered and the GFMC are modeled with the same control strategy.

Model Creation

After the clustering steps, the gray-box model is created, starting with the equivalent transformer. Its parameters are the same as the transformer between the detailed distribution network and the transmission system. If multiple transformers in parallel connect the ADN to the boundary bus, these transformers are considered individually with the respective parameters in the EDAM. The other equivalent components are created according to the clusters, with one equivalent component per cluster. The equivalent load's active and reactive power demand is given by the sum of the respective demand of each load in the detailed network. The sum of active and reactive power generation of the individual GFLC per cluster in the detailed network corresponds to the respective equivalent GFLC generation. The equivalent GFLC and GFMC's dynamic control parameters match the corresponding components' dynamic control parameters in the detailed network.

The equivalent GFMC are connected to the lower voltage side of the equivalent transformer according to the network topology with equivalent impedances. A detailed description of the GFMC connection with impedances is given in Section 4.3. The active and reactive power generation of the equivalent GFMC corresponds to the sum of the active and reactive power generation of the corresponding GFMC per cluster in the detailed network. Parameters of the equivalent GFMC's dynamic control should match the parameters of the corresponding GFMC's dynamic control in the detailed network.

A slack load is created to achieve a similar steady-state power flow at the boundary bus in the EDAM compared to the power flow observed at the boundary bus of the detailed network. This is different to the model structure of a TCA based EDAM[1]. Here, an equivalent impedance connects the PCC of the equivalent components to the lower voltage side of the equivalent transformer and is parameterized to match the steady-state power flows. However, it was found that a slack load parameterized accordingly can substitute the equivalent impedance of a TCA based EDAM. Also, in an STCA based EDAM, the equivalent impedances corresponding to equivalent GFMC are parameterized to match the voltage sensitivities $\vec{s}_i$, which is described in the parameterization step of the EDAM derivation process. A model structure similar to the TCA based EDAM with the equivalent impedance instead

[1] A schematic comparing the EDAM of both TCA and STCA is shown in Figure 5.6.

of the slack load complicates the parameterization process of the equivalent impedances connecting the equivalent GFMC significantly.

Parameterization

The result of the two steps *clustering* and *model creation* is a model structure with correct parameters of the equivalent load and generation components. The remaining unknown parameters of the equivalent impedances and of the slack load are found in the last step of the EDAM derivation. In an iterative procedure, the parameters of the equivalent impedances are set to achieve the same voltage sensitivities $\vec{s}_i$ at the PCC of each equivalent GFMC i compared to the PCC of the corresponding GFMC of one cluster in the detailed network. Section 4.2.2 describes in detail the parameter identification process of the equivalent impedances.
In a final step, the slack load is parameterized to have the same steady-state active and reactive power flow at the boundary bus in the EDAM compared to the one at the boundary bus of the detailed network. In some cases, the slack load can also be operated as a negative load.

4.2.2 Parameter Identification of Equivalent Impedances

The correct parameterization of the equivalent impedances in the EDAM plays a significant role for its validity. The heuristic approach of the parameter identification process is shown in Figure 4.4. The input data are the sensitivities $\vec{s}_i$ at the nodes i of the detailed network. Dependent on the resulting EDAM topology (Section 4.3) equivalent impedances correspond to specific nodes, mostly PCC of equivalent GFMC but also links between different branches or branch nodes connecting three or more branches. Correct parameters of these equivalent impedances need to be identified with the goal of similar voltage sensitivities at the corresponding node in the EDAM compared to the corresponding node or nodes in the detailed network. Here, each voltage sensitivity should be within an error margin ε. It was found that with $\varepsilon = \pm 5\,\%$, EDAM perform very well and model validation is passed (Section 5.7).
Figure 4.5 shows the deviation of all voltage sensitivities $\vec{s}_i$ at the PCC of each equivalent GFMC i in the EDAM compared to the PCC of the corresponding GFMC in the detailed network for five different scenarios[2]. The violin plots show the maximum and minimum deviation as well as the median. It can be seen that most voltage sensitivities in the EDAM match very well the corresponding voltage sensitivities of the detailed network.

[2] The five scenarios *DINGO6, DINGO8, SimBench10, DINGO20*, and *DINGO15* are introduced in Chapter 5

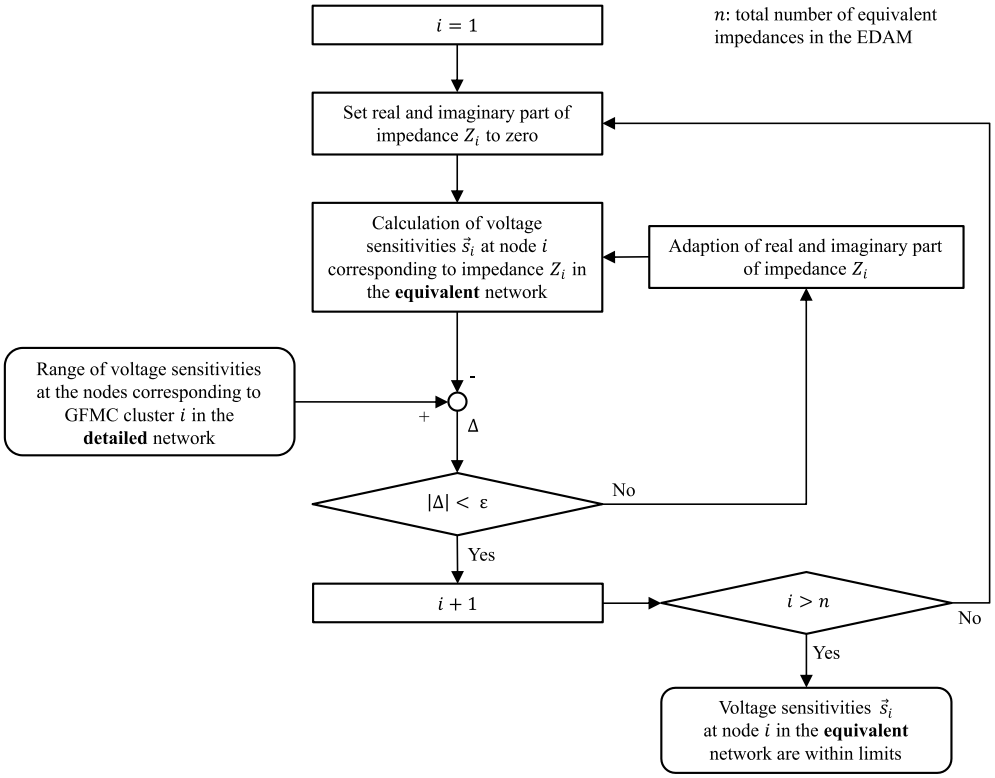

Figure 4.4: Overview of equivalent impedance parameterization

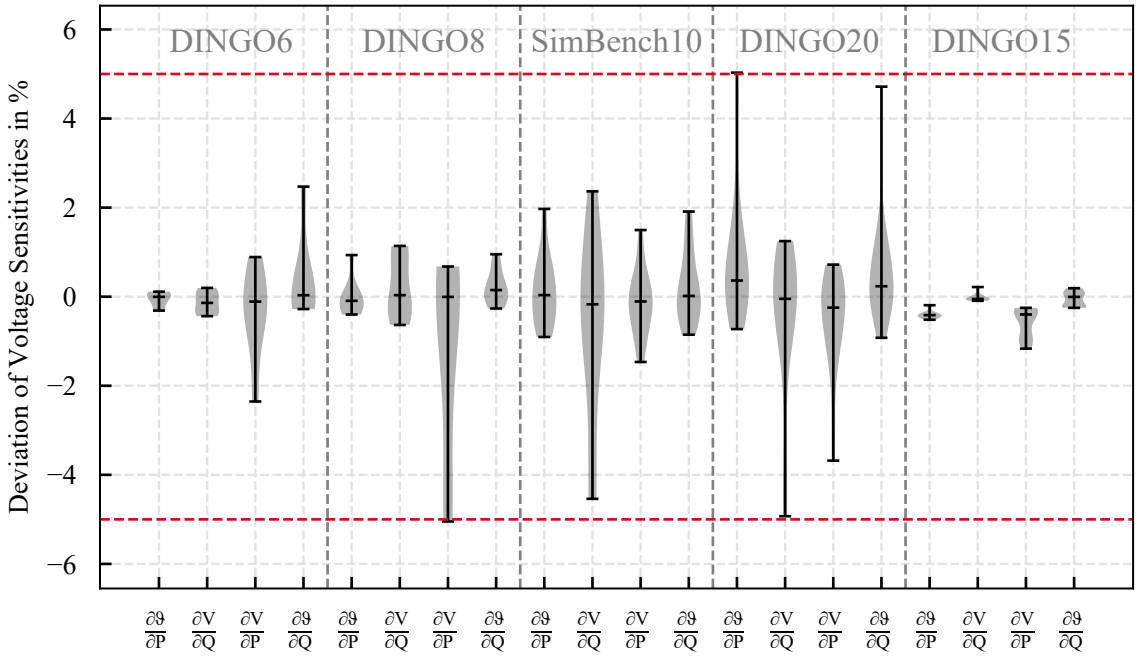

Figure 4.5: Deviation of voltage sensitivities in the EDAM compared to the corresponding voltage sensitivities in the detailed network for different scenarios

The unknown impedance parameters can also be found utilizing a particle swarm optimization (PSO) introduced by [KE95]. The basic principle of a PSO is described in the following. The new position x_i^{new} of a particle i of a set of particles, i.e., the swarm, within a search space is dependent on the current particle position x_i, the best point of the particle in the past b_i, and the global best point found by the swarm in the past b_g, that is,

$$x_i^{\text{new}} = x_i + v_i^{\text{new}}, \tag{4.1}$$

where

$$v_i^{\text{new}} = f(t)w_{i0}v_i + r_1 w_{i1}(b_i - x_i) + r_2 w_{i2}(b_\text{g} - x_i). \tag{4.2}$$

Here, v_i is called the velocity of the particle i, $f(t)$ is a function that decreases with the progress of the iterations, w_{ik} with $k = 0,1,2$ are fixed weights, and r_j with $j = 1,2$ are random numbers [MF02]. The first term of (4.2), that is, $f(t)w_{i0}v_i$, refers to the inertia of the particle. The second term $r_1 w_{i1}(b_i - x_i)$ is called memory, since it depends on the best point of the particle in the past. The last part of (4.2), that is, $r_2 w_{i2}(b_\text{g} - x_i)$, changes the velocity of the particle towards the global best point found by the swarm in the past and is called cooperation. One particle of the swarm includes the impedance parameters, i.e., real and imaginary part, of all equivalent impedances. Minimum and maximum allowed values for the particle need to be defined as well as the minimum and maximum allowed velocities.

The goal of the equivalent impedance parameterization is the minimization of the deviation between the voltage sensitivities of relevant nodes, i.e., PCC of GFMC and branch nodes connecting three or more branches (Section 4.3), in the detailed network model and the voltage sensitivities at the corresponding nodes in the EDAM. The voltage sensitivities of one node in the EDAM depend among others on the real and imaginary part, i.e., R and X, respectively, of the equivalent impedance connecting the node. Hence, the optimization problem can be written as

$$\underset{R \in \mathbb{R}^n, X \in \mathbb{R}^n}{\text{minimize}} \quad \sum_{i=1}^{n} \sum_{j=1}^{4} (y_{ji}^{\text{det}}(R,X) - y_{ji}^{\text{eq}}(R,X))^2 \tag{4.3a}$$

$$\text{subject to} \quad 0 \leq R_i \leq R_{\max} \quad \forall i = 1,2,\ldots,n, \tag{4.3b}$$

$$0 \leq X_i \leq X_{\max} \quad \forall i = 1,2,\ldots,n. \tag{4.3c}$$

The function $y(R,X)$ calculates the voltage sensitivities $\vec{s}_i$ for each relevant node i, that is,

$$\begin{pmatrix} y_{1i}(R,X) \\ y_{2i}(R,X) \\ y_{3i}(R,X) \\ y_{4i}(R,X) \end{pmatrix} := \begin{pmatrix} \frac{\partial V_i}{\partial P_i}(R,X) \\ \frac{\partial V_i}{\partial Q_i}(R,X) \\ \frac{\partial \vartheta_i}{\partial P_i}(R,X) \\ \frac{\partial \vartheta_i}{\partial Q_i}(R,X) \end{pmatrix}. \tag{4.4}$$

The voltage sensitivities of the detailed network are calculated with $y^{\text{det}}(R,X)$, whereas $y^{\text{eq}}(R,X)$ calculates the voltage sensitivities of the EDAM. The values for $R_{\max}$ and $X_{\max}$ are dependent on the used network and GFMC location within the network. For the scenarios calculated in this work, $R_{\max} = 0.5\,\text{m}\Omega$ and $X_{\max} = 0.4\,\text{m}\Omega$ proved to be sufficient.

Suppose each GFMC in the detailed network is considered individually in the EDAM. In that case, the dimensions of the resulting matrices of $y^{\text{det}}(R,X)$ and $y^{\text{eq}}(R,X)$ are the same, i.e., $\mathbb{R}^{4\times n}$ with n as the number of equivalent impedances. If GFMC in the detailed network model are aggregated to equivalent GFMC, n refers to the number of equivalent GFMC that are not derived by aggregating multiple GFMC in the detailed network, i.e., n GFMC in the detailed network are considered individually in the EDAM. The parameters for the equivalent impedances that connect the remaining aggregated equivalent GFMC are found by varying the impedance parameters such that the voltage sensitivities at the PCC of the aggregated equivalent GFMC are within the range of voltage sensitivities of each GFMC of the corresponding cluster in the detailed network (Section 4.3.3).

4.3 STCA Topology

In the *model creation* step of the EDAM derivation process introduced in Section 4.2.1, the GFMC clusters should be connected to the equivalent transformer with equivalent impedances. The EDAM topology should be similar to the detailed network's topology in terms of GFMC's PCC. The dependency of the GFMC's dynamic behavior on the network topology will be investigated in Section 4.3.1. Based on this, a generic STCA based EDAM topology will be introduced in Section 4.3.2. The clustering process to aggregate multiple GFMC to one equivalent GFMC are described in Section 4.3.3. This chapter ends with some examples of possible STCA based EDAM.

4.3.1 Multiple GFMC in One Network Branch

ADN may contain multiple GFMC in one branch connected in series. Figure 4.6 shows one branch with four GFMC of the DINGO network taken from the scenario *DINGO20* (Section 5.4.4). If the detailed network's topology were not considered in the EDAM, all equivalent GFMC would be connected to the lower voltage side of the transformer in parallel, similarly to the GFLC in the TCA. The equivalent GFMC corresponding to GFMC far away from the boundary bus in the detailed network would be connected to the EDAM with a higher equivalent impedance than the equivalent GFMC corresponding to GFMC close to the boundary bus in the detailed network. This is because the voltage sensitivities are higher the further away the nodes are from the boundary bus (Section 2.4.2).
In such a scenario, the two GFMC that can be seen at the bottom of Figure 4.6 would be both represented with equivalent GFMC whose equivalent impedances would be relatively high. Hence, the two GFMC in the EDAM would have a higher electrical distance between each other than in the detailed network. This would result in different dynamic behavior of the GFMC in the EDAM compared to the same GFMC in the detailed network.

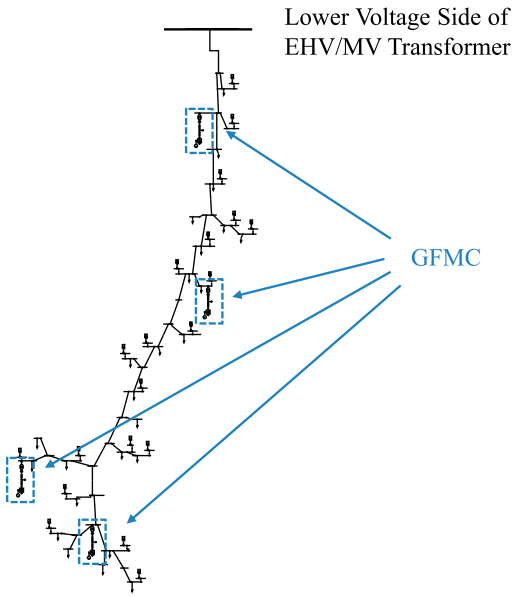

Figure 4.6: Four GFMC in one branch of the *DINGO20* network

The following simulation explains this obstacle in detail. Figure 4.7 shows the two models which are compared. Both models are connected to an external voltage source with the same impedance $Z_{\text{external\_Grid}}$ and the same transformer. The first model shown on the left connects *GFMC close* and *GFMC far* in series with the impedances $Z_{\text{GFMC\_close\_1}}$ and $Z_{\text{GFMC\_far\_1}}$. The second model shown on the right connects the same two GFMC in parallel with the

impedances $Z_{\text{GFMC\_close\_2}}$ and $Z_{\text{GFMC\_far\_2}}$, which are parameterized to achieve the same voltage sensitivities compared to the PCC of the GFMC in the left model.

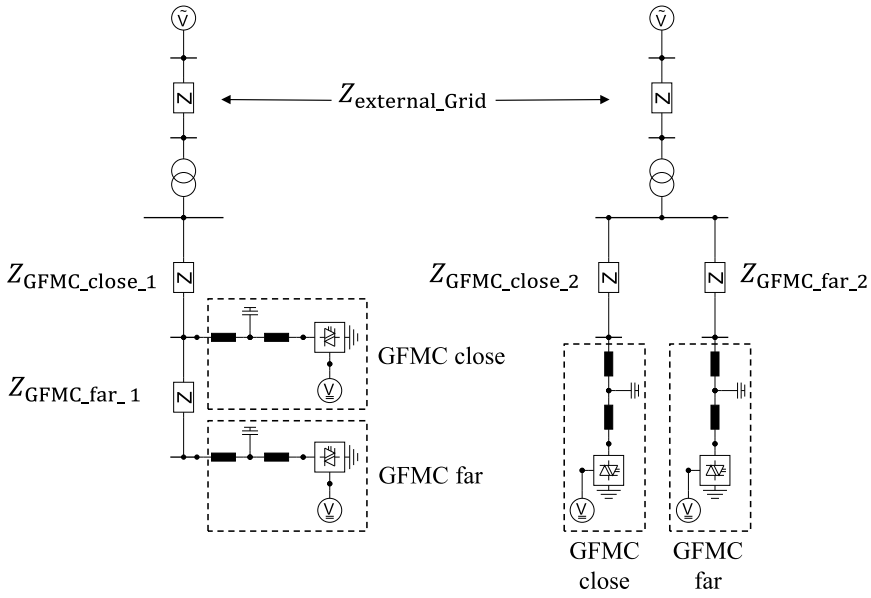

Figure 4.7: Two GFMC connected to an external voltage source in two different ways: series (left) and parallel (right)

The voltage source connected to the boundary bus induces at time 0 s a phase angle jump from 0° to 10°. The active and reactive power flow are compared between the two models at the lower voltage side of the transformer, i.e., where the GFMC are connected, as well as the active and reactive power generation of each GFMC in the respective model (Figure 4.8). Despite the same parameterization, it can be seen that *GFMC close* and *GFMC far* have a completely diverse behavior due to the different electrical distances between each other in the two models.

The necessity of considering the network's topology in terms of GFMC location in the EDAM can also be explained from a mathematical point of view. As explained in Section 2.4.2 and Section 4.2.2, only the diagonal elements of the four partial matrices $\boldsymbol{H}$, $\boldsymbol{N}$, $\boldsymbol{J}$, and $\boldsymbol{L}$ of equation (2.10) describing the voltage sensitivities are taken as input for parameterizing the equivalent impedances in the EDAM. This results in a neglect of the non-diagonal elements. However, connecting GFMC in the EDAM according to the network topology, the influence of neighboring GFMC on the voltage and voltage angle is considered. Hence, the non-diagonal elements of the partial matrices are not neglected anymore.

With this in mind, the importance of the detailed network's topology consideration regarding GFMC location in the STCA based EDAM becomes clear. Therefore, the aggregation of

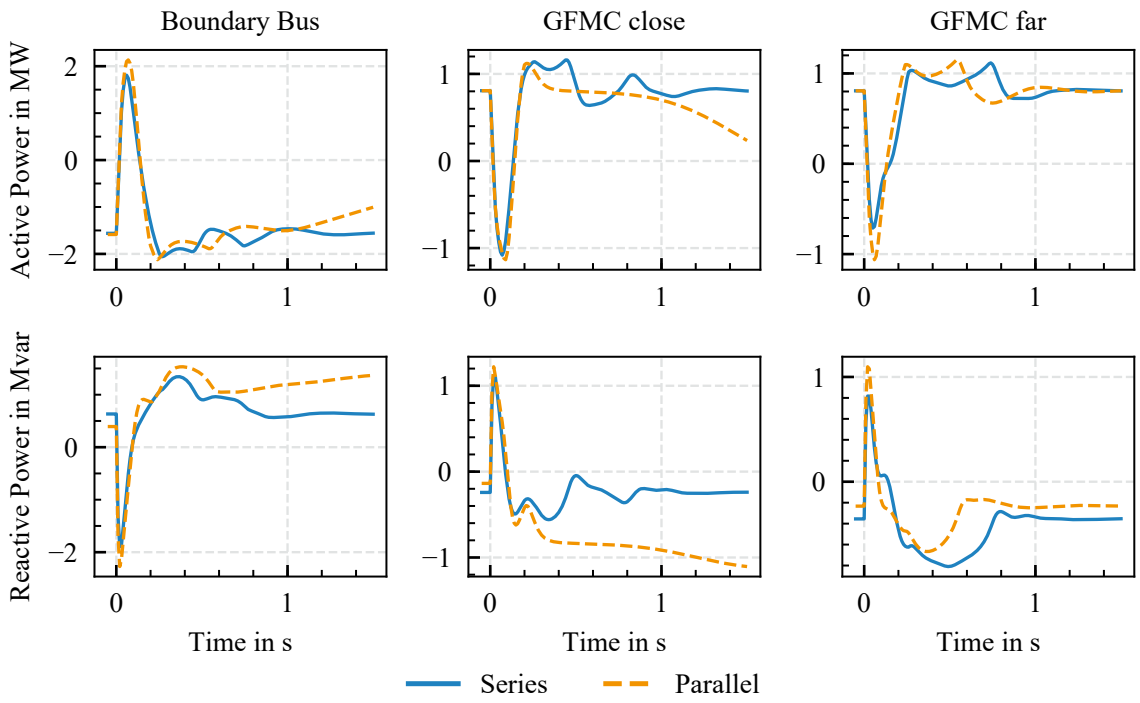

Figure 4.8: Active and reactive power flow at the lower voltage side of the transformer, i.e., where the GFMC are connected, as well as active and reactive power generation of *GFMC close* and *GFMC far*; positive reactive power values: over-excited state; negative reactive power values: under-excited state

multiple GFMC to one equivalent GFMC should be avoided since it neglects the GFMC locations within the detailed network. A generic EDAM topology allowing consideration of the GFMC location within the detailed network is described in the following section.

4.3.2 Generic STCA Based EDAM Topology

This section introduces a generic EDAM topology capable of representing all possible topologies of detailed networks, excluding the constraints described in Section 5.3.4. As elaborated in Section 4.1, GFLC and loads of the detailed network are considered in the EDAM according to the TCA. For the remaining GFMC, graph theory is applied to describe the connection of the equivalent GFMC dependent on the detailed network topology. Hence, the following generic topology refers to the connection of the equivalent GFMC with equivalent impedances.

The equivalent GFMC connection can be described as a graph $G = (\mathscr{N}, \mathscr{E})$ with vertices $N_i \in \mathscr{N}$ and edges $E_{ij} \in \mathscr{E}$ where $i, j \in \mathbb{N}$ and $i \neq j$. A vertex N_i can be either a GFMC

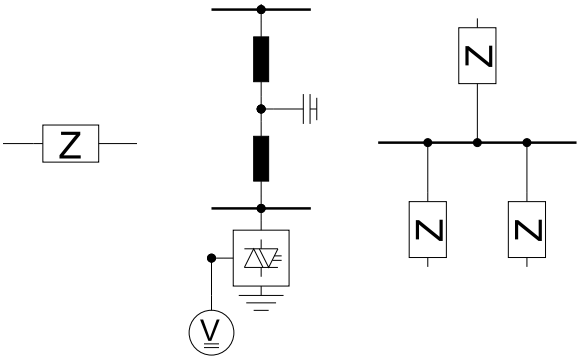

Figure 4.9: Impedance as edge (left), GFMC with its PCC node as vertex (middle), and a branch node as vertex with three edges (right)

with its PCC node and all its corresponding parameters (Section 3.2.3) or a branch node connecting three or more branches. An edge E_{ij} connecting the vertices N_i and N_j contains the parameters of an impedance $\underline{Z}_{ij}$. Otherwise, the edge does not exist, i.e., the edge equals zero, that is,

$$E_{ij} = \begin{cases} \underline{Z}_{ij}, & \text{if } E_{ij} \text{ connects vertices } N_i \text{ and } N_j, \\ 0, & \text{otherwise.} \end{cases} \tag{4.5}$$

The boundary bus has the same properties as a branch node connecting three or more branches and is set to be the vertex N_0, from which edges lead to n subgraphs referring to n branches in the detailed network. These subgraphs are trees, and they can be interconnected via an edge under the constraint that only one interconnecting edge per subgraph is allowed. This is in line with the network topology assumptions as given in Section 4.1. It is important to mention that this graph is similar but not equal to an actual rooted tree because of the interconnection of subgraphs.

The graph is built to represent the GFMC location in the detailed network as closely as possible. Two GFMC in the same branch are two vertices connected with an edge in series. Two GFMC in two different branches not connected will be in two different subgraphs only connected via the vertex N_0. The number of vertices equals the number of GFMC in the detailed network in addition to the number of branch nodes connecting three or more branches and the vertex N_0. The number of edges depends on the number of vertices and interconnections between two subgraphs.

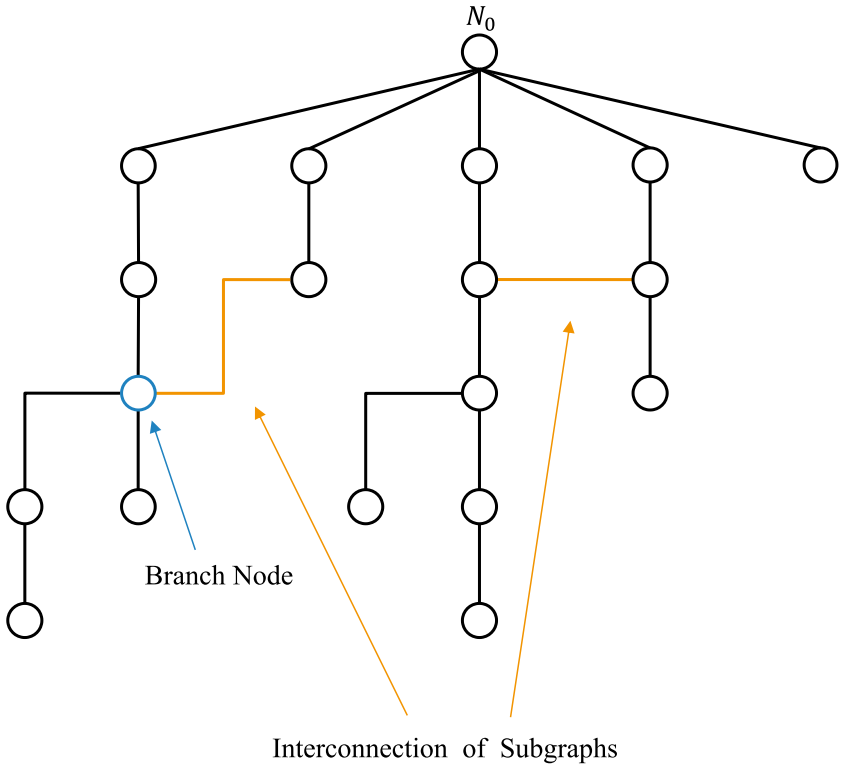

Figure 4.10: Example of EDAM topology graph

An example of an EDAM topology graph with five subgraphs and two interconnections of subgraphs is shown in Figure 4.10. The depth of the subgraph trees can vary dependent on the topology of the detailed network.
The same graph is also shown in Figure 4.11, where the vertices and edges are replaced by GFMC and impedances as introduced in Figure 4.9. This topology is an EDAM without equivalent load, equivalent GFLC, and slack load.

4.3.3 Clustering of Multiple GFMC

Ideally, every GFMC is considered individually in the STCA based EDAM. This allows the most accurate consideration of the detailed network's topology when connecting the equivalent GFMC in the EDAM. Dependent on the application, too many equivalent GFMC can be challenging to handle. Therefore, the desired number of GFMC clusters can differ from the number of GFMC in the detailed network. This section describes the clustering of multiple GFMC to one equivalent GFMC resulting in an EDAM with reduced complexity.
The main challenge when aggregating multiple GFMC to one equivalent GFMC is the appropriate consideration of the detailed network's topology in the EDAM. To render such a

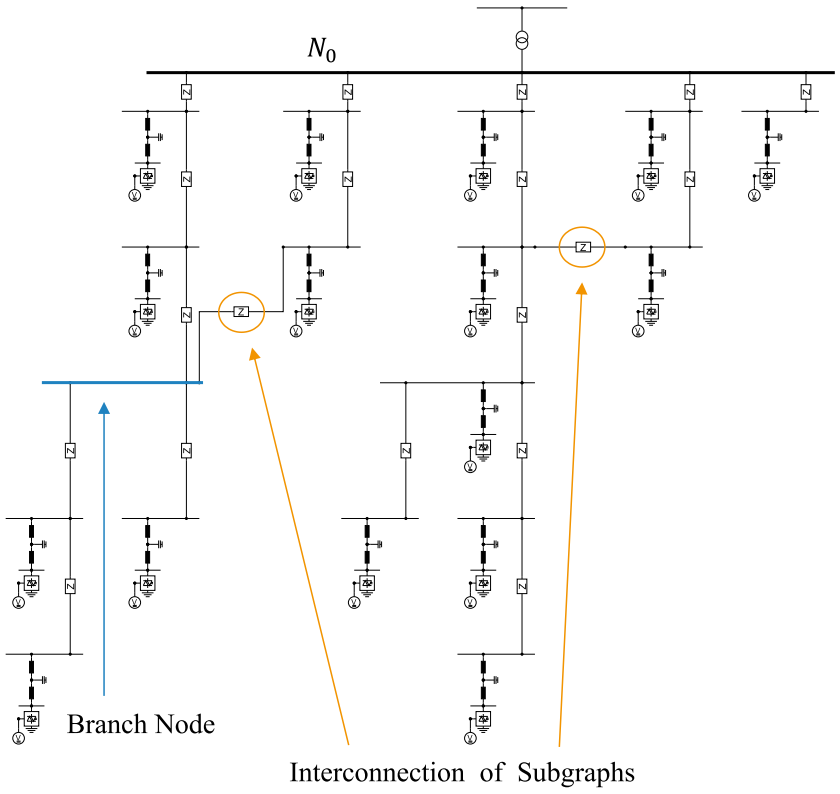

Figure 4.11: Example of EDAM topology including only GFMC

consideration possible the clustering of multiple GFMC should have the constraint of aggregating only neighboring GFMC of one network branch. To identify a cluster of GFMC that can be aggregated to one equivalent GFMC, voltage sensitivities $\vec{s}_i$ at the PCC of the GFMC are taken as input data for the k-means clustering algorithm [Mac67; Llo82]. The output of the algorithm are clusters of GFMC with similar voltage sensitivities.

The GFMC are then aggregated according to the clusters by summing up their nominal active and reactive power generation values. Each GFMC has a corresponding LCL output filter dependent on the nominal power values. The LCL filter parameters of the GFMC considered in this work are all tuned according to [Rez+14] (Section 3.2.3). Therefore, the LCL filter of the aggregated GFMC is also parameterized the same way.

After this aggregation, each equivalent GFMC of one cluster is connected to the lower voltage side of the equivalent transformer with an equivalent impedance according to the detailed network's topology. Its parameters are tuned to match the voltage sensitivities at the aggregated GFMC's PCC to the range of voltage sensitivities of each GFMC of the corresponding cluster.

Dependent on the number of GFMC in the detailed network model, the constraint of aggregating only neighboring GFMC of one network branch may reduce the EDAM complexity only slightly compared to an individual consideration of the GFMC in the EDAM. Opposed to that, a consideration of all GFMC in the detailed network for the k-means clustering algorithm and a corresponding aggregation reduces the EDAM complexity more significantly. Despite this advantage of a lesser number of equivalent GFMC, the drawbacks need to be weighed carefully. The consideration of the detailed network's topology in the EDAM is a crucial part of a valid STCA based EDAM. In Section 5.4, different STCA based EDAM are created and compared with each other. EDAM with an individual consideration of GFMC are compared with EDAM that comprise aggregated equivalent GFMC. The aggregation process of the latter is performed without any constraints, i.e., all GFMC of the detailed network are considered in the k-means clustering algorithm, and with the constraint of aggregating only neighboring GFMC of one branch. The model complexity of these EDAM is evaluated in Section 5.6.

4.3.4 Examples of STCA Based EDAM

A detailed MV network model is given comprising three GFMC in three separate branches as well as several GFLC and loads. The GFLC generation technology in the detailed network comprises PV with two different control strategies varying in the active power generation after a frequency drop below a particular threshold value. While the first set of GFLC control recovers to full active power generation, the second set reduces the active power generation to 0.5 pu of the pre-fault generation. The control parameters are the same within one set of control strategy.

Figure 4.3 shows the corresponding EDAM aggregated by STCA. Two equivalent GFLC represent the two control strategy clusters. The control parameters of these two GFLC are the same as the control parameters of the corresponding GFLC per cluster in the detailed network. Active, reactive, and apparent power of the equivalent GFLC result from the sum of the individual GFLC in the detailed network per cluster, i.e., the two control strategy clusters. The equivalent load's active, reactive, and apparent power result from the sum of the individual load's demand in the detailed network.

The detailed network contains three GFMC in three different branches. For an optimal GFMC consideration, the desired number of equivalent GFMC clusters equals the number of GFMC in the detailed network. This results in three equivalent GFMC connected in parallel in the EDAM. The parameters of the equivalent GFMC match those of the corresponding

GFMC in the detailed network. The individual GFMC are connected to the boundary bus via equivalent impedances to reproduce the voltage sensitivities at each PCC of the GFMC in the detailed network.
A slight change in the described detailed network model is done for the following example. Here, two GFMC are connected in one branch in the detailed network. Hence, these two GFMC are connected in series in the EDAM, whereas the third GFMC of a separate branch is connected in parallel in the EDAM (Figure 4.12). Otherwise, the EDAM is similar to the one in Figure 4.3.

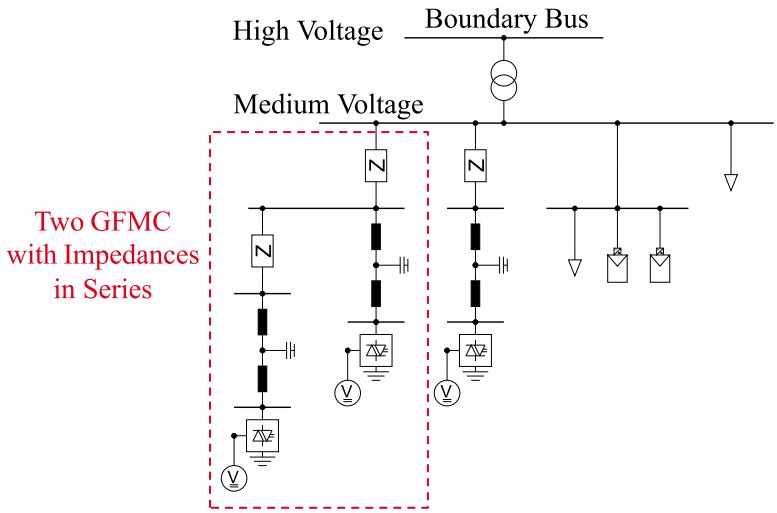

Figure 4.12: Schematic of an STCA based EDAM with two GFMC in one branch

4.4 Summary

This chapter introduced a method to create a gray-box EDAM that considers the dynamic behavior of GFMC by utilizing the voltage sensitivities $\vec{s}_i$ at the PCC of each GFMC i. Voltage sensitivities are good measures to represent the electrical grid's strength at the GFMC's PCC in the EDAM. The method builds up on the TCA (Section 2.3.3), so it is called Sensitivity-Technology-Control-Clustered Approach (STCA).
A most accurate representation of GFMC is achieved if the GFMC location within the detailed network can be considered in the EDAM. This is applicable if the number of equivalent GFMC clusters is equal to the number of GFMC in the detailed network or if only neighboring GFMC of one network branch are aggregated to one equivalent GFMC.

Chapter 5

STCA Evaluation

5.1 Simulation Scenario Overview

In this chapter, the performance of the proposed STCA is evaluated and validated by applying it to two test ADN models with varying numbers of GFMC. Three event scenarios are simulated, and results are compared between the detailed ADN and the EDAM aggregated by STCA. Furthermore, the TCA is also applied to the test network model, and results are compared for benchmarking purposes.

Two ADN network topologies are applied and adapted depending on the scenarios: an open ring (DINGO) and a closed ring (SimBench) topology (Section 5.3). This work focuses on equivalent ADN dominated by CBG, including GFMC. Hence, the CBG share of the models is almost 100 % of the ADN's total active power demand. 60 % of the CBG's active power generation is covered by GFMC, while the remaining 40 % is generated by GFLC. The location within the network and the total number of GFMC vary between the scenarios.

For this work, GFLC are represented by PV systems. GFLC representation in the resulting EDAM is similar to the TCA (Section 4.2). In [Böm16], the adequate consideration of different generation technologies in the TCA based EDAM has been extensively proven. To this end, no comprehensive investigation regarding the proper representation of different GFLC generation technologies in the EDAM was carried out. Instead, the focus was on the equivalent GFMC.

The GFLC are implemented with two different dynamic models according to [WEC14] (Section 3.2.2). The *generic model for distributed and small* as well as *for large-scale PV plants* differ in their threshold values for disconnection and post-fault power generation. GFMC are represented as PV systems with battery storage systems. All loads are modeled as con-

stant impedances. Overall, this results in a CBG dominated network model with a significant influence of GFMC.

Table 5.1 gives an overview of the scenarios that are simulated and described in detail in this chapter. The scenarios differ in network topology and the number of GFMC in the detailed network. Both TCA and STCA are applied to derive EDAM in all scenarios. Nevertheless, for the scenarios *DINGO8*, *DINGO20*, and *DINGO15*, this section describes the detailed results of only STCA based EDAM. Here, the focus is on evaluating STCA based EDAM with less equivalent GFMC compared to the number of GFMC in the detailed network. The detailed results of the TCA based EDAM can be found in Appendix B for these scenarios.

Table 5.1: Scenario Overview

Scenario Name	**Network Topology**	**Number of GFMC**	**Aggregation Method**	**Number of Equivalent GFMC (STCA)**
DINGO6	DINGO	6	TCA & STCA	6
SimBench10	SimBench	10	TCA & STCA	10
DINGO8	DINGO	8	STCA	8 & 4
DINGO20	DINGO	20	STCA	20 & 5
DINGO15	DINGO	15	STCA	15 & 4

Three events are considered to evaluate the proposed STCA. The first event is a phase angle jump from 0° to 10°. The second event is a frequency jump from 50 Hz to 50.25 Hz. An external voltage source induces both events. The third event is a three-phase short circuit fault at the PCC of the voltage source as marked in Figure 5.5. All events occur at 0 s, and the short circuit is cleared after 130 ms.

The frequency and voltage angle of the three events measured with a PLL at the boundary bus of the detailed network in the *DINGO6* scenario are shown in Figure 5.1. The parameters for the PLL component can be found in Section A.2.1. A positive phase angle jump is similar to a change of the grid impedance, e.g., a line disconnection, resulting in a sudden frequency rise. The frequency jump implicates a constant rate of change of the phase angle. As the most severe fault, the short circuit leads to a frequency and phase angle change and a severe voltage drop during the fault.

RMS simulation results of the EDAM aggregated by TCA or STCA are compared to the detailed ADN. The simulations are performed with an integration time step of 1 ms using the software *DIgSILENT PowerFactory*. As the link between the transmission and distribution system, the power flow at the boundary bus will be the focus of the evaluation.

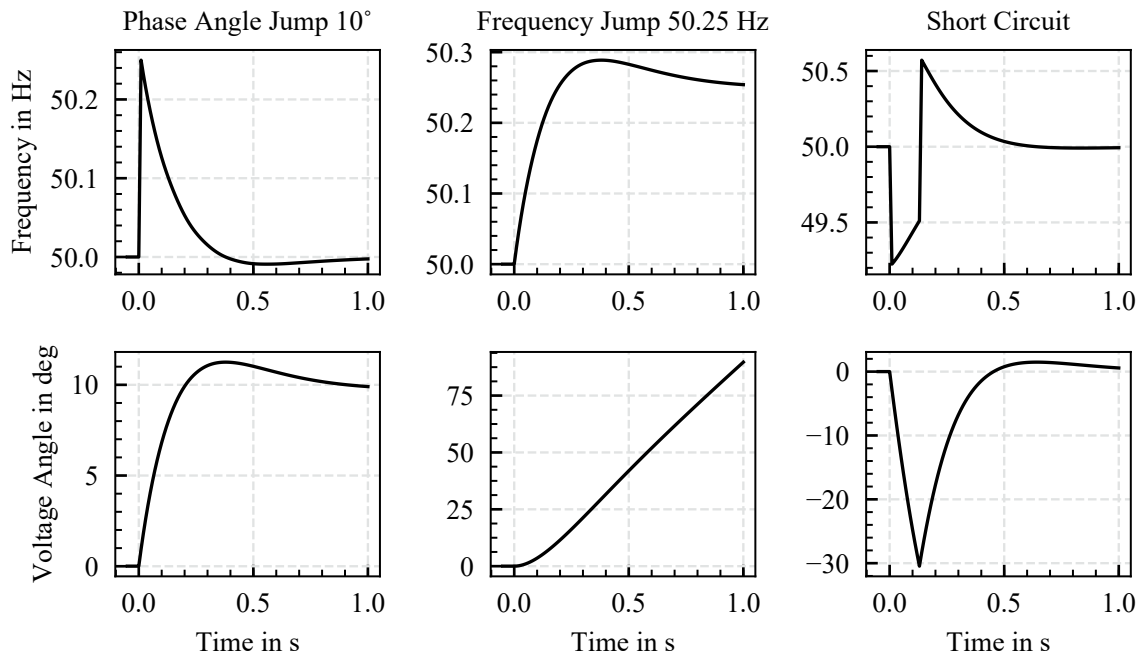

Figure 5.1: PLL measurements at boundary bus of detailed ADN in scenario *DINGO6* of frequency and voltage angle in different events

5.2 Validation Procedure

The validation procedure description of this section can be also found in [Ung+22b]. The performance of the two approaches, TCA and STCA, is validated by applying the method used in [FGW19] to the EDAM. Originally, the method evaluates CBG simulation models compared to their real components. To this end, simulations are conducted with the model, and simulation results are compared with measurements. In this work, simulation results of the detailed network represent the measurements of the real component and serve as a benchmark. The simulation results of the EDAM are then compared to those of the detailed network. The validation is based on the values for active and reactive power flows at the boundary bus normalized by the ADN's total active and reactive power demand.

The simulation results are divided into three periods: pre-fault (A), fault (B), and post-fault (C). A fault is defined as a period in which the boundary bus voltage is below 0.9 pu. The fault period ends as soon as the voltage rises above this threshold value. For each period, the following error metrics are evaluated:

- mean absolute error MAE:

$$\delta_{\mathrm{MAE}} = \frac{\sum_{n=1}^{N} |x_{\mathrm{E}}(n)|}{N} \tag{5.1}$$

- mean error ME:

$$\delta_{\mathrm{ME}} = \frac{\sum_{n=1}^{N} x_{\mathrm{E}}(n)}{N} \tag{5.2}$$

- maximum error MXE:

$$\delta_{\mathrm{MXE}} = max(|x_{\mathrm{E}}(1)|, |x_{\mathrm{E}}(2)|, ..., |x_{\mathrm{E}}(N)|) \tag{5.3}$$

in which $x_{\mathrm{E}}(n)$ is defined as the error between the simulation results of the detailed network model and the EDAM for each data point at time step n (taken every 10 ms) within the total number of N data points per period A, B, and C for active power as

$$x_{\mathrm{EP}}(n) = \frac{P_{\mathrm{ADN}}(n) - P_{\mathrm{EDAM}}(n)}{P_0}, \tag{5.4}$$

where P_0 is the total active power demand of the detailed ADN, and for reactive power as

$$x_{\mathrm{EQ}}(n) = \frac{Q_{\mathrm{ADN}}(n) - Q_{\mathrm{EDAM}}(n)}{Q_0}, \tag{5.5}$$

where Q_0 is the total reactive power demand of the detailed ADN. Threshold values for each error type per period are shown in Table 5.2.

Table 5.2: Threshold values for maximum allowed deviations [FGW19]

	$\hat{\delta}_{\mathrm{MAE}}$	$\hat{\delta}_{\mathrm{ME}}$	$\hat{\delta}_{\mathrm{MXE}}$
A Pre-fault	0.12	±0.10	0.15
B Fault	0.17	±0.15	0.17
C Post-fault	0.17	±0.15	0.17

In this work, only the short circuit event is considered as a fault since voltage dips for the other two events do not fall below 0.9 pu, as can be seen in Figure 5.9. Nevertheless, for the phase angle and frequency jump, simulation results are divided into pre-event A (before 0 s) and event C (after 0 s) periods to avoid a distorting weighting of the pre-event phase, where

deviations are less distinct. The total time range considered for the validation is from -1 s to 5 s.
The work of [BN+22] also provides a validation methodology for equivalent dynamic models. Nevertheless, threshold values for the validation are not provided and it is not distinguished between pre-event, event, and post-event time periods. Hence, this work utilizes the described methodology developed by [FGW19].

5.3 Detailed Base Network Models

An open ring, i.e., radial, and a closed ring MV ADN test model topology are utilized. In Germany 84.3 % of the MV networks are operated as open ring topologies [Büc+14]. To this end, greater focus is given to the radial topology in this evaluation. Both ADN topologies are connected to the boundary bus of a transmission system, which is not aggregated, via an EHV/MV transformer. The events as introduced in Section 5.1 are induced by the transmission system. Dependent on the scenario, GFMC are connected to different locations within the network. The scenario-specific modifications are described in the corresponding chapters (Section 5.4.1 to Section 5.4.5).

5.3.1 Transmission System

Both ADN are connected to a 230 kV voltage source with a 50 km transmission line (Figure 5.2). The transmission line parameters are based on the CIGRE benchmark subtransmission network line parameters in the European configuration [Str+14] and can be found in Table A.1. The voltage angle and frequency of the voltage source can be changed according to the desired event simulation. The short circuit fault is located at the PCC of the voltage source.

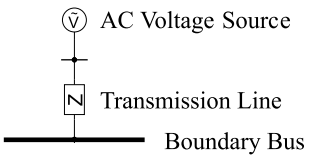

Figure 5.2: Transmission system comprising a 230 kV AC voltage source, a transmission line and the boundary bus [UL23]

The distribution networks considered in this work represent German networks. To this end, the 230 kV voltage of the transmission system is not in line with European standards. Never-

theless, this voltage was chosen for the transmission system since, in further investigations, the 230 kV voltage source can be replaced by the *IEEE 9 bus system* [Vit+19], which is a commonly used and validated 230 kV transmission system model.

5.3.2 Open Ring ADN Topology

The open ring ADN topology is based on a 10 kV distribution network of the open-source tool *Distribution Network Generator (DINGO)* that creates synthetic MV networks based on publicly available data of German power system networks [Amm+18]. This software project is part of the research project *open_eGo* and deals with interlinking grid extension planning and operation of transmission and distribution systems. The resulting synthetic MV networks are very close to real German networks regarding the number of transformers and line length (deviation less than 10 %). In this work, one of the MV topologies with a 10 kV voltage level is considered arbitrarily. The topology of the selected grid represents an urban network and is shown in Figure 5.3.

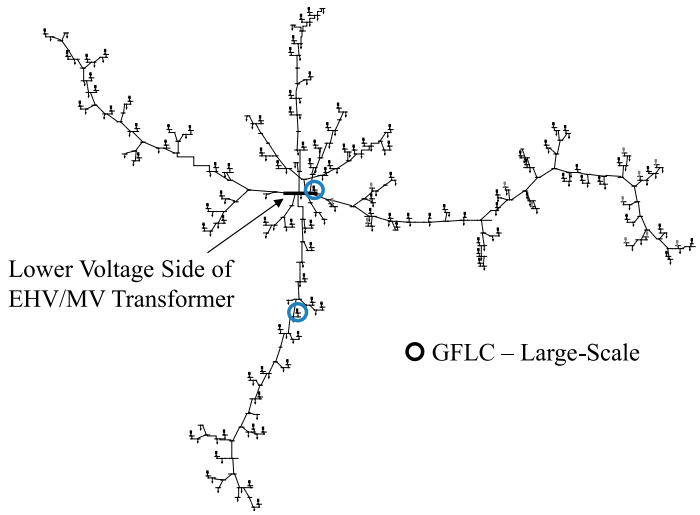

Figure 5.3: 10 kV ADN topology derived from the tool DINGO [UL23]

The tool DINGO differentiates between three load areas as listed in Table 5.3, whose data are obtained from [Hül+17].

Data for conventional and renewable generation are obtained from [Bun15; Deu14]. For this work, the spatial resolution of generators of the resulting synthetic MV network is kept. However, the generation technology is adapted to PV systems with different control strategies to obtain a CBG dominated urban area. Also, the aggregated load connected at the lower voltage side of the EHV/MV transformer was reduced compared to the MV network

Table 5.3: Load areas of DINGO

Aggregated	**Regular**	**Satellite**
• high peak demand • connection at lower voltage side of EHV/MV transformer • representation of an urban LV area	• peak demand > 100 kW • connection to a MV ring	• peak demand < 100 kW • connection directly to a MV ring or via a branch line

obtained from the DINGO tool by 50 % to guarantee a more even distribution of the load among the network. The resulting data for the generation and demand are given in Table 5.4. Line parameters of the selected grid are provided in Section A.1.

Table 5.4: Generation and demand data for adapted DINGO MV network [UL23]

Component	**Number of Units**	**Actual Active Power**	**Actual Reactive Power**
Aggregated Load	1	27.0 MW	6.8 Mvar
Regular Load	31	10.7 MW	2.7 Mvar
Satellite Load	90	2.3 MW	0.6 Mvar
Sum	**122**	**40.0 MW**	**10.1 Mvar**
GFLC – Large-Scale	2	9.6 MW	2.0 Mvar
GFLC – Small	94	6.6 MW	1.3 Mvar
Sum	**96**	**16.2 MW**	**3.3 Mvar**

5.3.3 Closed Ring ADN Topology

The closed ring ADN topology is based on a 20 kV distribution network obtained from the project *SimBench* [Mei+20]. This project has the objective of developing a benchmark data set for grid analysis, planning and operation. A publicly available data set comprising LV, MV, HV, and EHV exist for the German power network. MV networks are compiled synthetically and are categorized into rural, semi-urban, urban, and commercial classes. The semi-urban MV network is selected arbitrarily for this work. Usually, SimBench networks

have an open ring topology. However, three network rings are closed to consider such topology in the STCA evaluation. The resulting network covers a small geographical area with a total line length of 4.7 km and is shown in Figure 5.4.

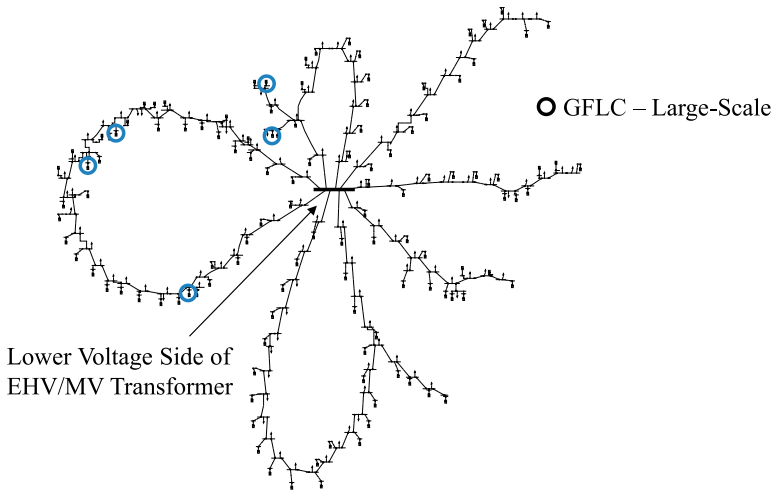

Figure 5.4: 20 kV ADN topology derived from the project SimBench [UL23]

Same as for the open ring topology derived from the tool DINGO, the location of generators of the SimBench network is kept. However, generation technology is changed to PV systems with different control strategies. The resulting data for the generation and demand are given in Table 5.5. Line parameters of the SimBench network are provided in Section A.1.

Table 5.5: Generation and demand data for adapted SimBench MV network [UL23]

Component	**Number of Units**	**Actual Active Power**	**Actual Reactive Power**
250 kW < Load < 441 kW	43	16.2 MW	6.4 Mvar
100 kW < Load < 250 kW	64	14.5 MW	5.7 Mvar
Load < 100 kW	7	0.6 MW	0.2 Mvar
Sum	**114**	**31.3 MW**	**12.3 Mvar**
GFLC – Large-Scale	5	5.0 MW	1.0 Mvar
GFLC – Small	114	7.3 MW	1.5 Mvar
Sum	**119**	**12.3 MW**	**2.5 Mvar**

5.3.4 Network Topology Limitations

The evaluation in this work focuses on two specific network topologies as representatives for German MV networks. While the open ring topology is more common in Germany [Büc+14], the closed ring network is applied to validate the STCA on a different topology. A closed ring topology allows one interconnection of two branches in the network, forming a closed ring. Also, branch lines connected to the ring are considered. However, this work does not consider more than one interconnection of two branches leading to a highly meshed network, e.g., meshed HV networks. These limitations are consistent with the generic topology introduced in Section 4.3.2.

Furthermore, MV networks with multiple EHV/MV transformers connected to different buses of the network are not investigated. Such an interconnected distribution network challenges the derivation of EDAM. Applying typical ADN models for stability analysis does not necessarily require the consideration of such interconnection and is therefore beyond the scope of this work.

Also, non-European topologies are not considered nor are LV networks. Nevertheless, as introduced in Section 4.2.1, the EDAM derivation process allows the implementation of LV networks in a bottom-up process, and a further investigation should be conducted in future work.

5.4 Simulation and Validation

5.4.1 Scenario: DINGO6

The content presented in this chapter has been published in [Ung+22b]. The detailed network comprising the transmission and distribution system (Figure 5.5) contains six GFMC, each in a different branch of the network. In this scenario, the number of equivalent GFMC clusters equals the number of GFMC in the detailed network. This results in six equivalent GFMC connected in parallel with six corresponding equivalent impedances in the STCA based EDAM (Figure 5.6). The GFMC are aggregated to one equivalent component in the TCA based EDAM. Due to the GFLC's two dynamic control models implemented in the detailed network model, the EDAM aggregated by both TCA and STCA are comprised of two equivalent GFLC representing these two control strategies. In addition to the equivalent load, a slack load as described in Section 4.2.1 is connected to the lower voltage side of the equivalent transformer of the STCA based EDAM.

The detailed network has an aggregated load connected at the lower voltage side of the EHV/MV transformer (Section 5.3.2). To cope with this significant demand, a GFMC is connected to this node with a higher generation than the other five GFMC. Nominal values for the six GFMC are listed in Table 5.6.

Table 5.6: Scenario *DINGO6*: nominal GFMC values

GFMC	**Rated Apparent Power**	**Active Power**	**Reactive Power**	**Maximum Current**
GFMC at lower voltage side of EHV/MV transformer	20 MVA	10.41 MW	2.61 Mvar	1.2 pu
Other 5 GFMC	4 MVA	2.68 MW	0.67 Mvar	1.2 pu
Sum	**40 MVA**	**23.81 MW**	**5.96 Mvar**	

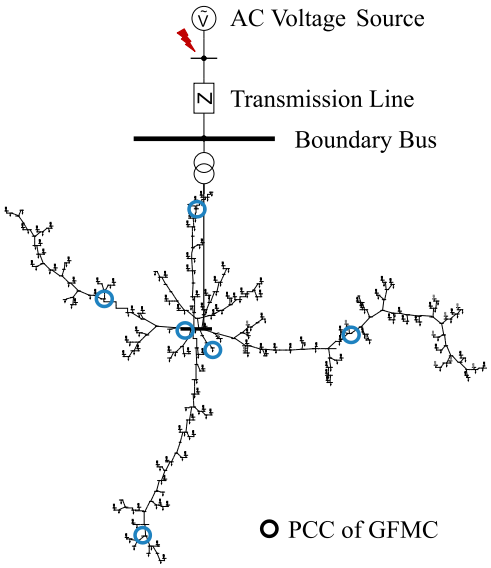

Figure 5.5: Schematic of detailed network of scenario *DINGO6* with GFMC's PCC

The three network models depicted in Figure 5.5 and Figure 5.6 are exposed to events induced by the voltage source in the transmission system (Section 5.1).
An essential feature of a GFMC is the capability of limiting the output current (Section 3.2.3). The dynamic control model of the GFMC calculates the set point for output current in a synchronous reference frame (dq-frame) based on the droop control output [PSS20]. If this calculated set point exceeds the maximum admissible current, the current set point is limited

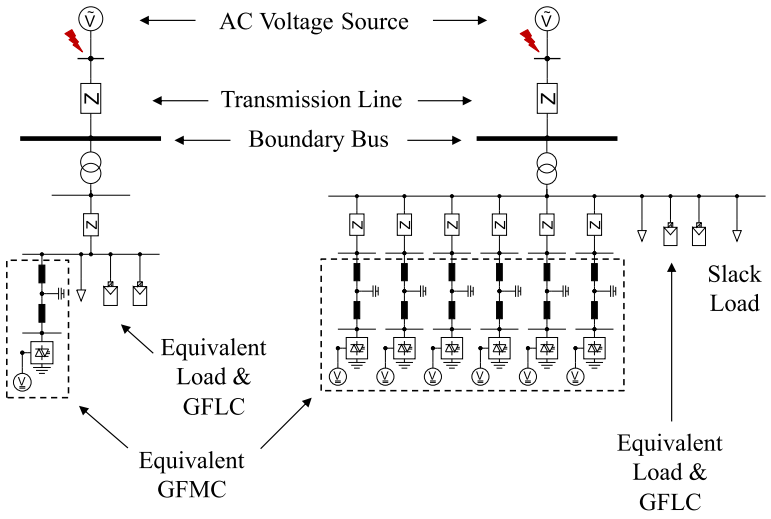

Figure 5.6: Schematic of EDAM aggregated by TCA (left) and STCA (right) of scenario *DINGO6*

accordingly. It is important to mention that the calculated set point during the current limitation mode does not comply with the actual output current, which is limited to the maximum current. Figure 5.7 shows the calculated current set points for all GFMC in the detailed network and the EDAM aggregated by TCA and STCA. The shown current set points $I_{\mathrm{GFMC\_Set}}$ are equal to the absolute values of the calculated currents $i^{*}_{\mathrm{c\,dq}}$ as the output of the voltage control model (Figure 3.6).

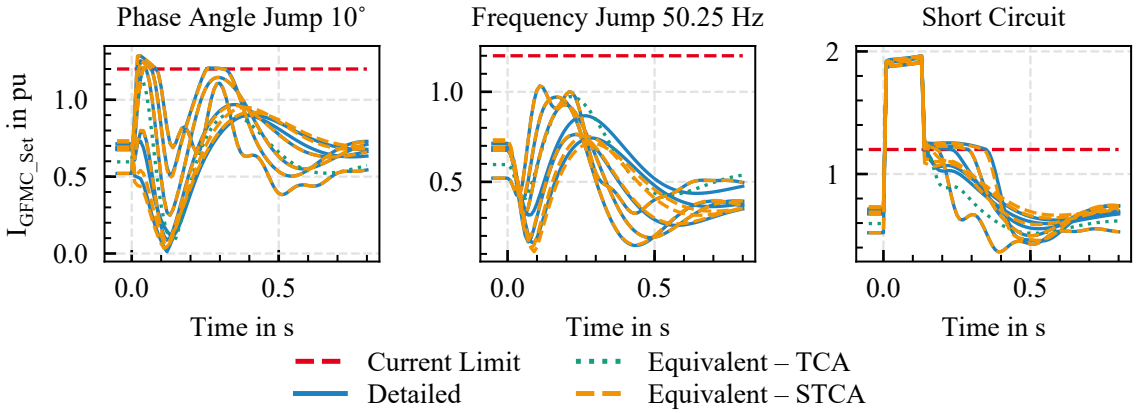

Figure 5.7: Scenario *DINGO6*: calculated set point for output current of GFMC $I_{\mathrm{GFMC\_Set}}$ in detailed and equivalent network models

For the phase angle jump, the equivalent GFMC of the TCA based EDAM does not reach the current limit as opposed to the GFMC of the detailed network and the EDAM aggregated

by STCA. For the short circuit fault, the current limit is reached by the equivalent GFMC of the EDAM aggregated by TCA for a shorter time compared to the GFMC of the detailed network. As opposed to this behavior, the GFMC of the STCA based EDAM that reaches the current limit behaves similarly to the detailed network's GFMC.

The first two rows of Figure 5.8 show the active and reactive power flow from the transmission to the distribution system at the boundary bus of the detailed network and EDAM aggregated by TCA and STCA for the three events. Before the events occur at 0 s, the active and reactive power of both EDAM match those of the detailed network well. This is ensured by the parameterization of the equivalent impedance in the TCA based EDAM and by the parameterization of the slack load in the STCA based EDAM.

The phase angle jump leads to active and reactive power swings in all models in transition to the pre-event values. It can be observed that the STCA based EDAM captures the dynamic behavior of the detailed ADN better than the TCA based EDAM. The differences in the dynamic behavior become more severe for the frequency jump event. After the event occurs, active and reactive power reach new values. However, the TCA based EDAM's post-fault reactive power is lower than the detailed network's. The TCA based EDAM's post-event active power is close to the detailed network's, but differences in the dynamic response can be seen. The STCA based EDAM reproduces the dynamic behavior of the detailed network well for both active and reactive power.

As the most severe event, the short circuit fault also leads to differences between the dynamic behavior of the TCA based EDAM and detailed network. During the short circuit, the active power flow of TCA based EDAM is close to the detailed network, while the reactive power flow slightly deviates. After the short circuit is cleared, TCA based EDAM behaves differently from the detailed network for both active and reactive power flows. The dynamic behavior of the STCA based EDAM is close to the detailed network during and after the fault.

For a better understanding of the behavior of the GFMC, the total active and reactive power provision by GFMC in each network model is shown in the last two rows of Figure 5.8. The observed responses of the GFMC of each model are similar to the power flows at the boundary bus. Active power generation of the equivalent GFMC of the TCA based EDAM deviates significantly from the generation of the GFMC in the detailed network. The deviations to the detailed network in the reactive power injection are more severe. For all three events, the pre-event and post-event values are not matching those of the GFMC in the detailed network. Opposed to that, the equivalent GFMC in the EDAM aggregated by STCA are close to the behavior of the GFMC in the detailed network model for all three events. Only a slight offset

can be observed in the reactive power injection of the equivalent GFMC for the frequency jump event and the short circuit fault.

Figure 5.9 shows the voltages at the low voltage side of the 230 kV/10 kV transformer of the three network models. Similar to the power flow at the boundary bus, the EDAM aggregated by STCA is remarkably close to the voltage measured in the detailed network for all three events. However, the TCA based EDAM voltages show different behaviors after the events occur. Especially the frequency jump results in severe deviations of the voltages compared to the detailed model.

Figure 5.10 shows the detailed validation results for all three events. Data points are colored according to the aggregation method, while their shape depends on the event. The results are subdivided into each period A, B, and C, as well as into the errors δ_{MAE}, δ_{ME}, and δ_{MXE} for each period (Section 5.2). The validation is failed when the calculated errors exceed the plotted threshold values listed in Table 5.2. Period B is only relevant for the short circuit fault since phase angle and frequency jump are only divided into pre-event and post-event periods.

Deviations in the pre-event period A are close to zero for all events in both TCA and STCA based EDAM due to the parameter identification process according to the steady-state power flow. In all three events, the active and reactive power threshold values for the error δ_{MXE} in the post-event period C are exceeded by the TCA based EDAM. The frequency jump also leads to reactive power threshold violations for all error parameters δ_{MAE}, δ_{ME}, and δ_{MXE} in the post-event period. The STCA based EDAM's active and reactive power deviations are within the threshold values in all events.

The results of the validation comply with the observations of the power plots. As opposed to the EDAM aggregated by TCA, the STCA based EDAM reproduces the dynamic behavior of the detailed network model independent of the event. The phase angle jump and the short circuit fault result in current limitation by the GFMC in the detailed network. Even such a highly nonlinear behavior is captured well by the EDAM aggregated by STCA.

In [Ung+22b], the STCA is applied on a similar scenario than the introduced *DINGO6*. Here, an STCA based EDAM is derived from a detailed network model with dynamic loads and other dynamic GFMC control models than the one implemented in this work. Also, one-phase and two-phase short circuits are simulated besides the three events investigated in this chapter.

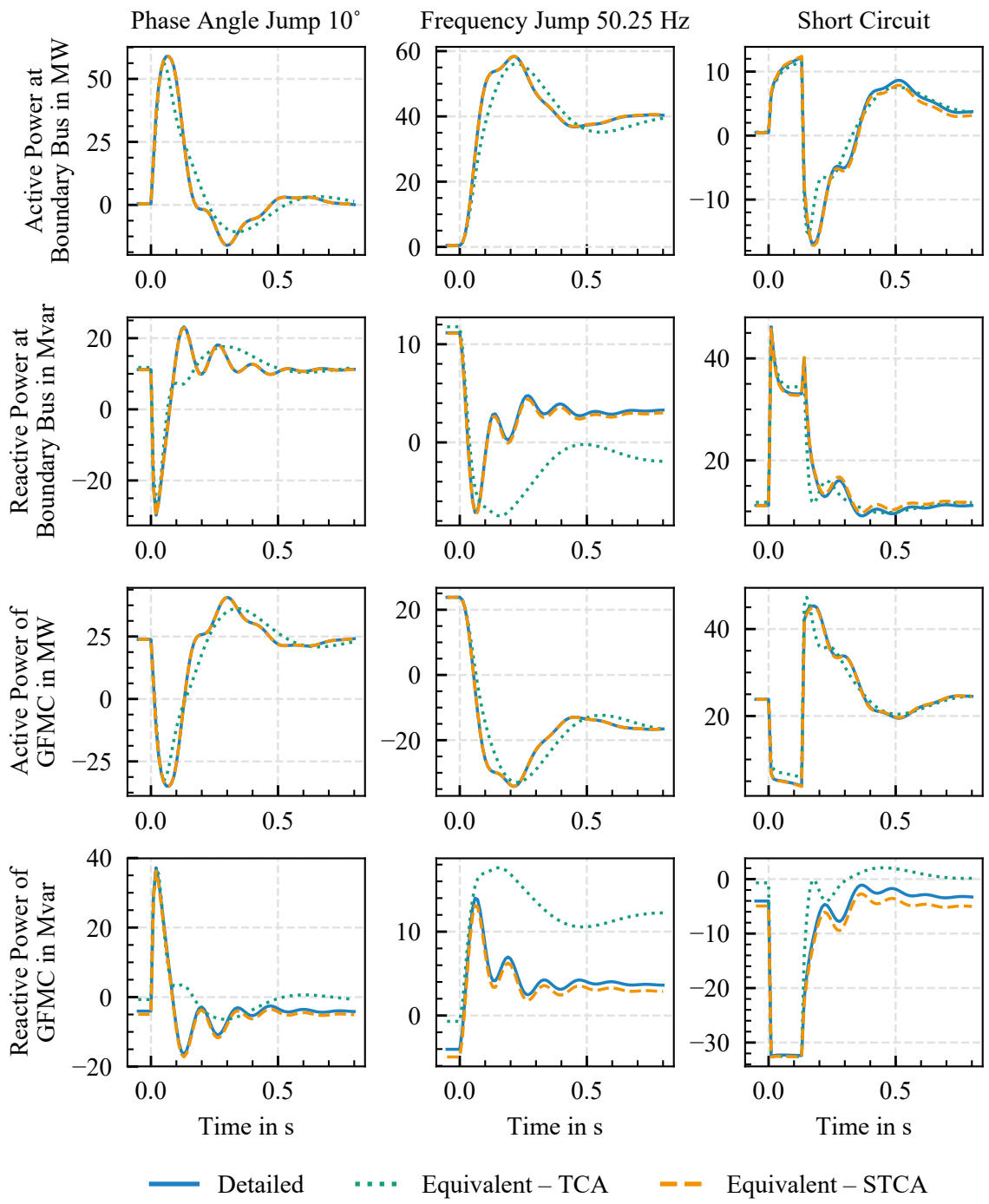

Figure 5.8: Scenario *DINGO6*: active and reactive power flow at boundary bus from transmission to distribution system of detailed and equivalent network models and sum of active and reactive power generation of all GFMC in detailed and equivalent network models; positive reactive power values: over-excited state; negative reactive power values: under-excited state

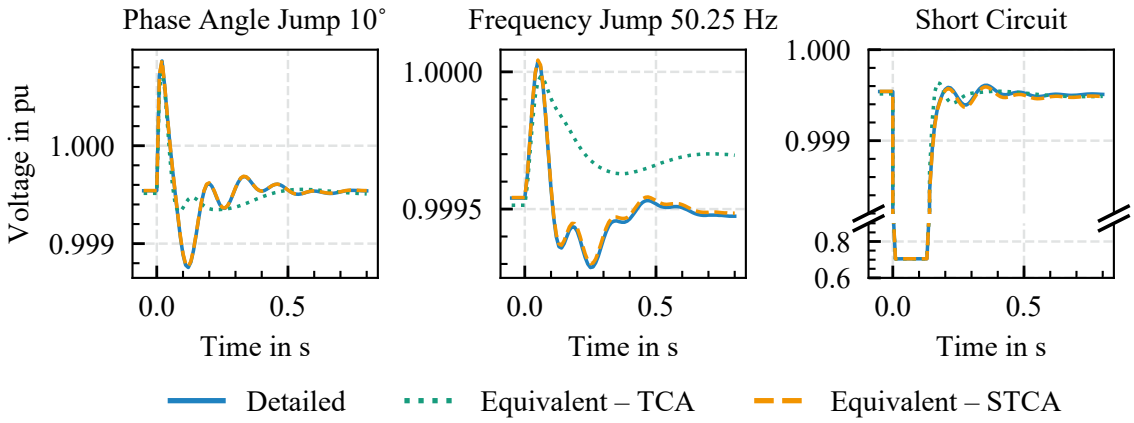

Figure 5.9: Scenario *DINGO6*: voltages at low voltage side of 230 kV/10 kV transformer in detailed and equivalent network models

5.4.2 Scenario: SimBench10

The content presented in this chapter has been published in [UL23]. The STCA based EDAM of an open ring topology with one GFMC per branch represented the dynamic behavior of the detailed network very well. In this chapter, the closed ring topology with 10 GFMC distributed among the network as shown in Figure 5.11 is analyzed. All GFMC are attributed with the same nominal values as listed in Table 5.7.

Table 5.7: Scenario *Simbench10*: nominal GFMC values [UL23]

GFMC	**Rated Apparent Power**	**Active Power**	**Reactive Power**	**Maximum Current**
10 GFMC	4 MVA	1.9 MW	1 Mvar	1 pu
Sum	**40 MVA**	**19.0 MW**	**10 Mvar**	

For the STCA based EDAM, the detailed network's topology with the three closed rings needs to be represented as introduced in Section 4.3 since multiple GFMC are connected to one ring. The resulting EDAM with the same number of equivalent GFMC as the GFMC in the detailed network is shown in Figure 5.12. Similar to the *DINGO6* scenario (Section 5.4.1), two GFLC dynamic control strategies are implemented leading to two equivalent GFLC in the EDAM. The topology of the TCA based EDAM is the same as in the scenario

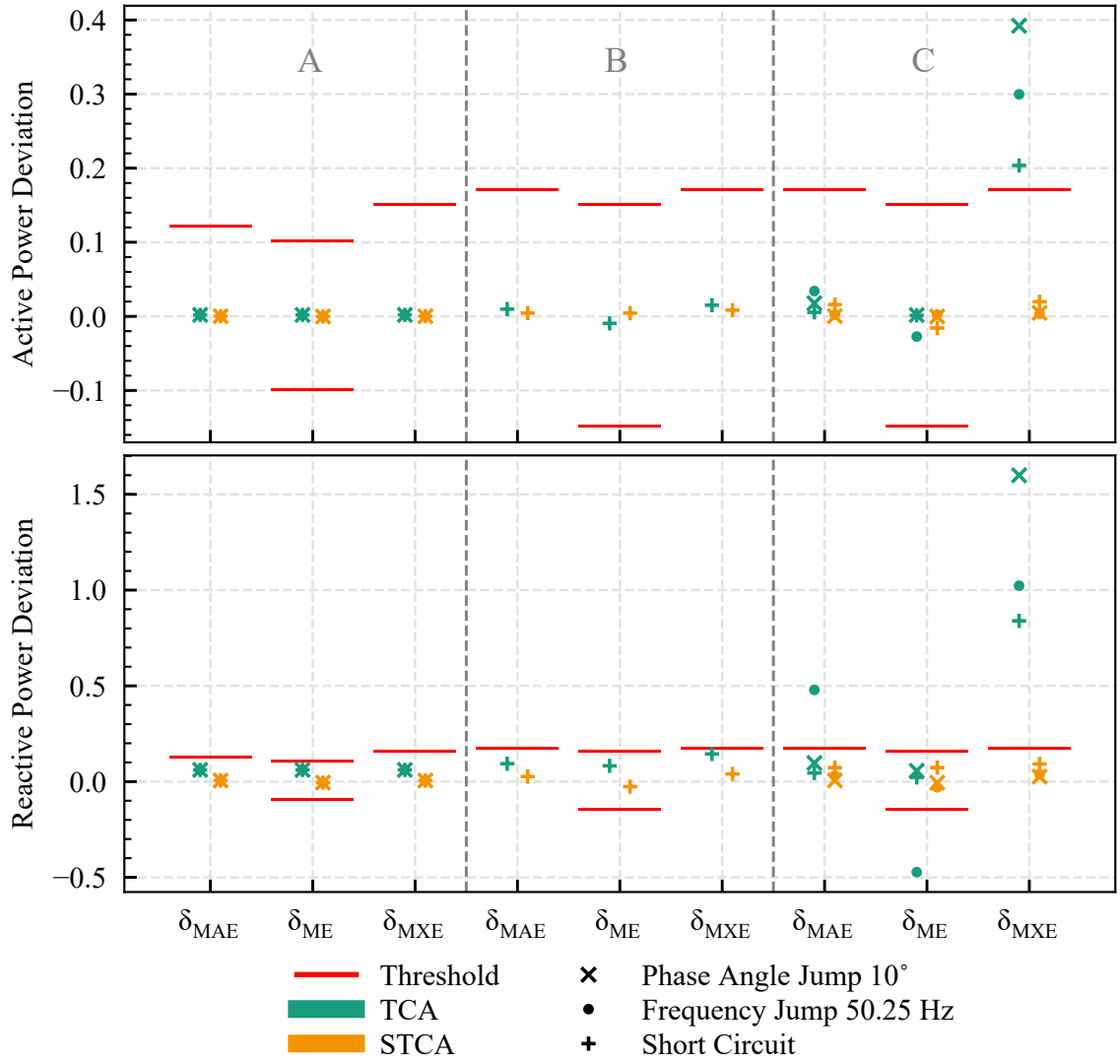

Figure 5.10: Scenario *DINGO6*: validation results for EDAM aggregated by TCA and STCA

DINGO6 (Figure 5.6), only the parameters of the components are adapted to this scenario as described in Section 2.3.3.

In this scenario, the GFMC in all three events reach their current limit (Figure 5.13). The calculated set points for the output current of the equivalent GFMC in the STCA based EDAM are close to those of the detailed network's GFMC except after the frequency jump. Here, the maximum current is exceeded for a shorter time in the STCA based EDAM. The equivalent GFMC of the TCA based EDAM calculates very different set points for its output current. The maximum current is not reached after the phase angle jump, while it is exceeded longer after the frequency jump event than the GFMC in the detailed network. For the short circuit, the calculated set point for the output current exceeds the current limit for a

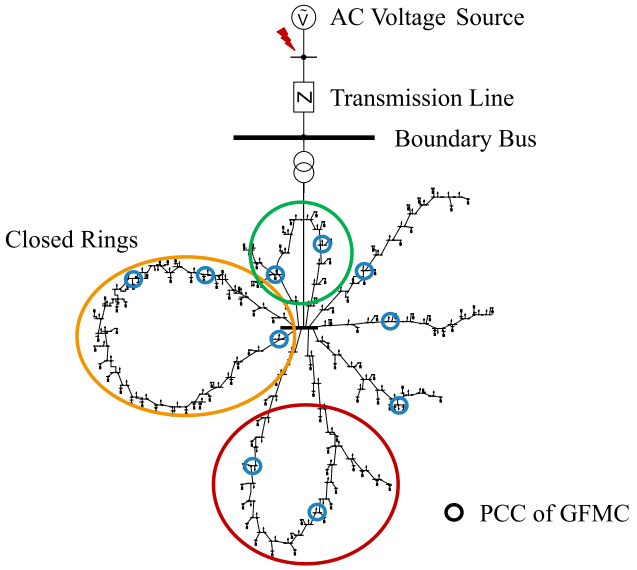

Figure 5.11: Schematic of detailed network of scenario *SimBench10* with GFMC's PCC [UL23]

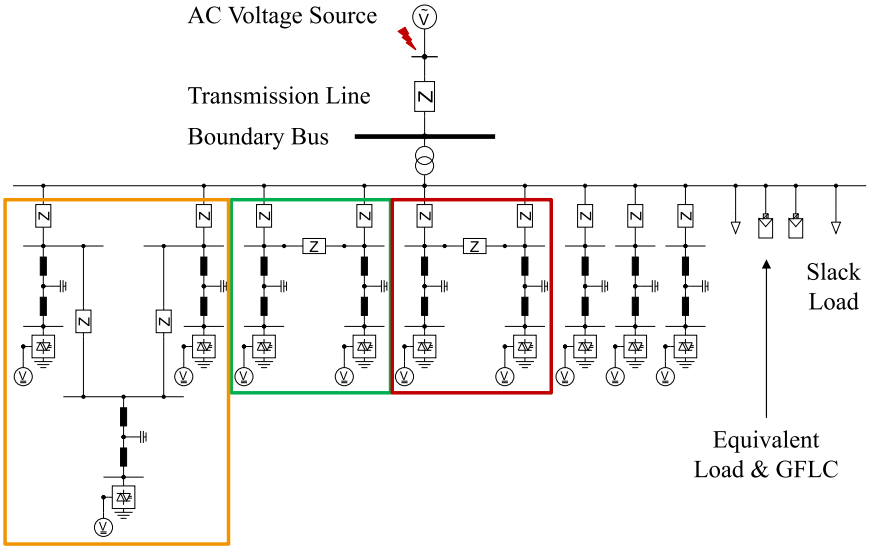

Figure 5.12: Schematic of EDAM aggregated by STCA of scenario *SimBench10* [UL23]

shorter time compared to the detailed network. Also, the post-fault current set points differ significantly from the GFMC's current set points in the detailed network.

The power flows at the boundary bus allow similar conclusions compared to the ones drawn from the observation of the calculated current set points (Figure 5.14). For the phase angle jump, the STCA based EDAM reproduces the detailed network's active and reactive power

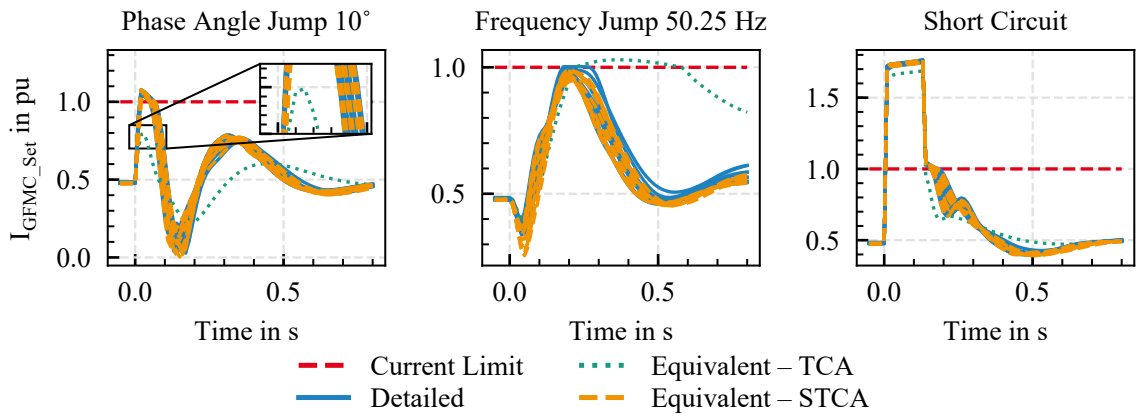

Figure 5.13: Scenario *SimBench10*: calculated set point for output current of GFMC I_{GFMC_Set} in detailed and equivalent network models

flows very well. The TCA based EDAM results in significantly different power curves since the equivalent GFMC is not reaching the maximum current.

Small offsets in the reactive power flow of the EDAM aggregated by STCA can be observed for the frequency jump event, while the active power flow matches the one of the detailed network. However, since the TCA based EDAM exceeds the current limit for a more extended time than the GFMC in the detailed network, the active and reactive power flows do not match the ones of the detailed network in the post-event period. Also, the new post-event stationary reactive power set point differs significantly from the stationary reactive power set point of the detailed network.

The reactive power flow at the boundary bus of the STCA based EDAM during and after the short circuit fault shows a small offset compared to the power flow of the detailed network. This is similar to the STCA based EDAM's reactive power offset after the frequency jump event. The active power flow of the EDAM aggregated by STCA captures the power flow of the detailed network very well. The TCA based EDAM shows offsets in the active and reactive power flow during the fault. Also, the post-fault behavior differs from the power curves observed in the detailed network.

The GFMC generation and the voltages at the lower voltage side of the EHV/MV transformer are shown in Figure B.9 and Figure B.10 of Appendix B for a more detailed investigation of the simulation results.

The numerical validation confirms the observations (Figure 5.15). In the pre-event phase, no threshold violations can be observed. During the short circuit fault, deviations are within limits except for the reactive power deviation δ_{MXE} of the TCA based EDAM. Also, the TCA based EDAM shows higher deviations than the STCA based EDAM. Validation failure can

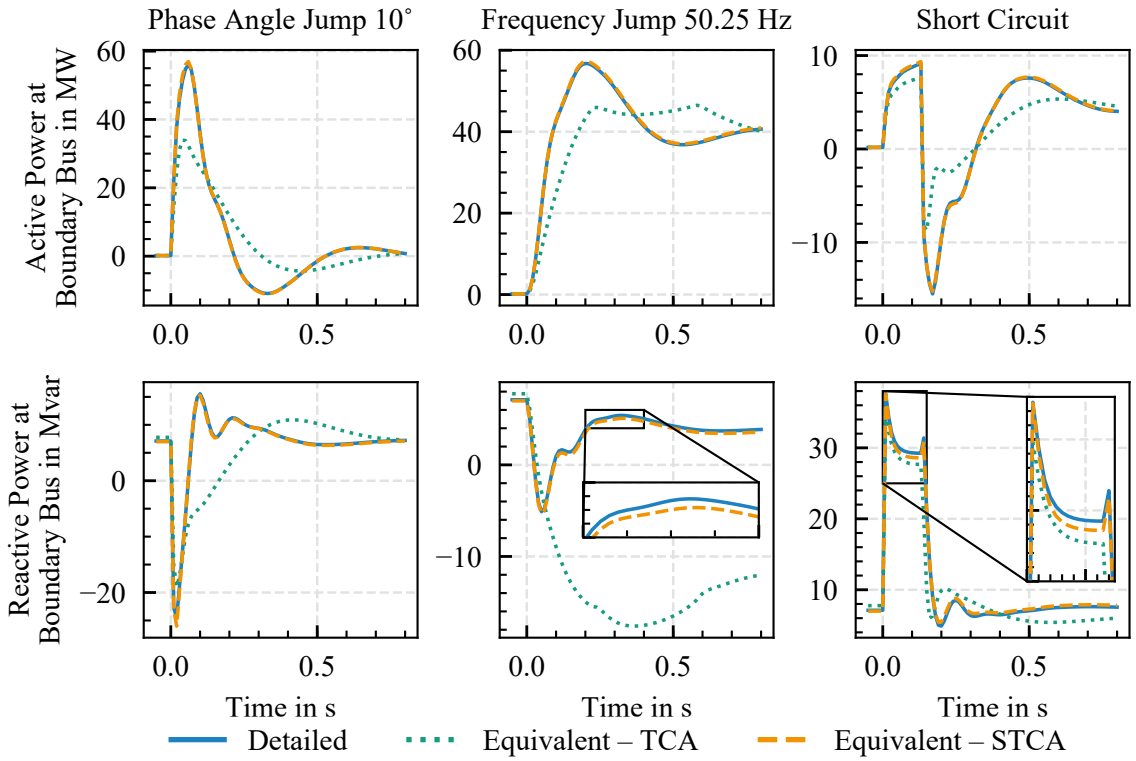

Figure 5.14: Scenario *SimBench10*: active and reactive power flow at boundary bus from transmission to distribution system of detailed and equivalent network models; positive reactive power values: over-excited state; negative reactive power values: under-excited state [UL23]

be observed for the TCA based EDAM in the post-event time period. The frequency jump leads to an active power threshold violation of the maximum error δ_{MXE} and to a failure of all validation parameters δ_{MAE}, δ_{ME}, and δ_{MXE} for the reactive power deviation. In the post-event period of the phase angle jump and the short circuit, active and reactive power exceed the allowed maximum deviation δ_{MXE}.

Opposed to that, the STCA based EDAM is not exceeding the thresholds of the three validation parameters δ_{MAE}, δ_{ME}, and δ_{MXE} for both active and reactive power.

In Section B.2, the accuracy of a different EDAM is shown. Here, no interconnections are considered in the EDAM, and all equivalent GFMC are connected in parallel. Such an EDAM neglecting the detailed network's topology shows worse validation values compared to the validation results presented in this chapter.

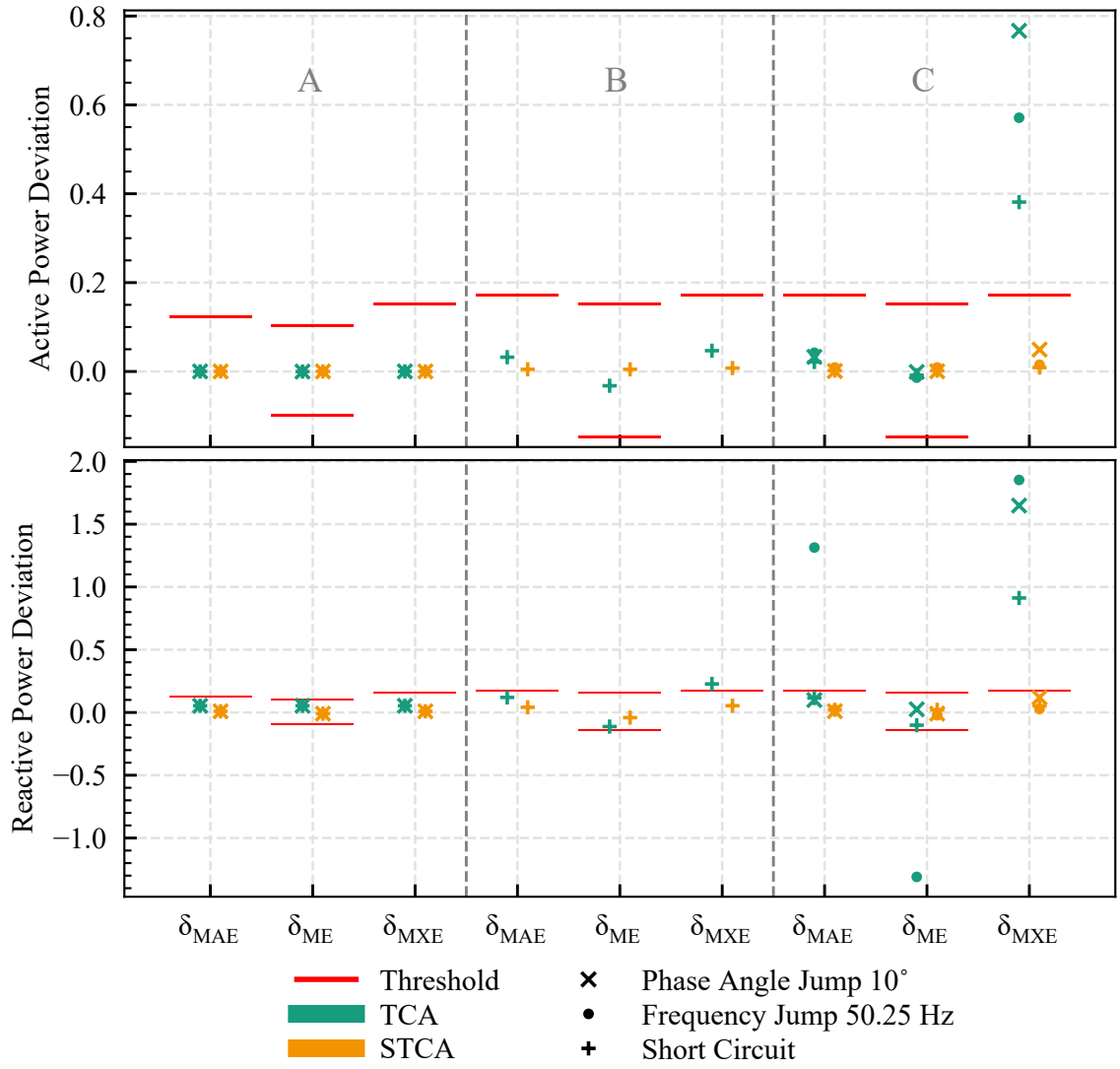

Figure 5.15: Scenario *SimBench10*: validation results for EDAM aggregated by TCA and STCA [UL23]

5.4.3 Scenario: DINGO8

The content presented in this chapter has been published in [UL23]. The following scenario builds upon the *DINGO6* scenario with two additional GFMC connected to each of the eight branches of the network (Figure 5.16). This scenario investigates the accuracy of the EDAM aggregated by STCA for a higher number of GFMC compared to the scenario *DINGO6*. Due to the increased number, two STCA based EDAM are compared:

1. *STCA 8 GFMC*: number of equivalent GFMC, i.e., eight, equals number of GFMC in the detailed network, i.e., eight.

2. *STCA 4 GFMC*: number of equivalent GFMC, i.e., four, is lower than number of GFMC in the detailed network, i.e., eight.

Since the eight GFMC are located at each of the eight branches of the network, the GFMC of the STCA based EDAM comprising eight GFMC are connected in parallel (Figure 5.17). Other components besides GFMC are modeled as described for the *DINGO6* scenario in Section 5.4.1. TCA is not applied on this network since the focus is on the differences between the STCA based EDAM of the two aggregation levels *STCA 8 GFMC* and *STCA 4 GFMC*.

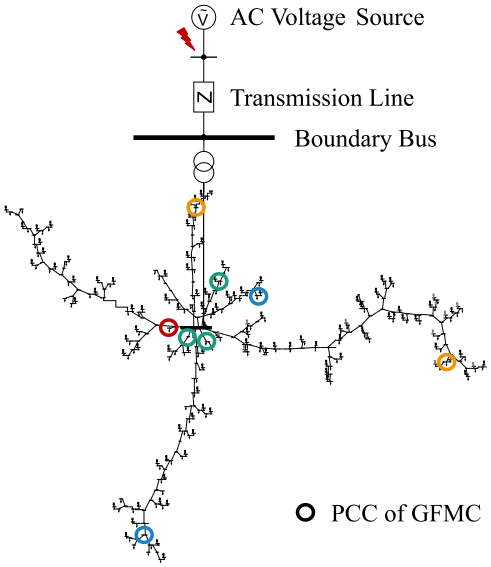

Figure 5.16: Schematic of detailed network of scenario *DINGO8* with GFMC's PCC colored according to the clusters of the aggregation level *STCA 4 GFMC* [UL23]

The GFMC of the detailed network are aggregated to equivalent GFMC in the aggregation level *STCA 4 GFMC* to avoid a high number of equivalent GFMC. Here, the GFMC in the detailed network are clustered to the desired number of equivalent GFMC, which is lower than the number of GFMC in the detailed network. However, aggregating multiple GFMC to one equivalent leads to accuracy drawbacks of the EDAM, which will be investigated in the following.

The k-means clustering algorithm [Mac67; Llo82] finds GFMC clusters with similar voltage sensitivities $\frac{\partial V_i}{\partial P_i}$, $\frac{\partial V_i}{\partial Q_i}$, $\frac{\partial \vartheta_i}{\partial P_i}$, and $\frac{\partial \vartheta_i}{\partial Q_i}$. However, the desired number of clusters needs to be known. To get an optimal number of clusters, the distance D_r is calculated for different number of clusters. Here, D_r is defined as the summed up distances from each data point x_i

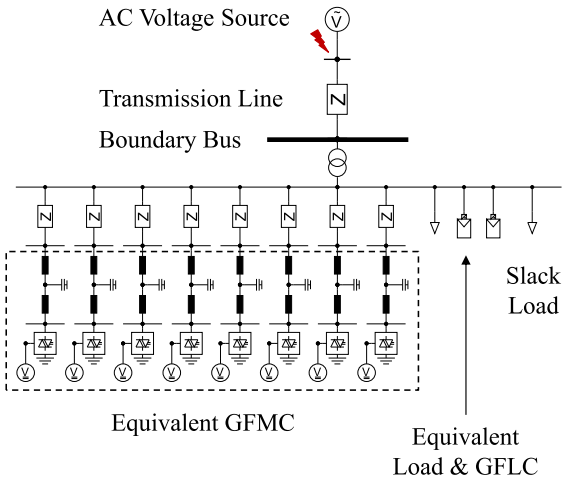

Figure 5.17: Schematic of EDAM aggregated by STCA of the aggregation level *DINGO8 STCA 8 GFMC* [UL23]

to its cluster center c_j, that is,

$$D_r = \sum_{j=1}^{r} \sum_{i=1}^{k_j} (x_i - c_j)^2, \tag{5.6}$$

with r as the number of clusters and k_j as the number of data points of one cluster j.

Cluster centers are found in four steps. First, random cluster centers are defined according to the predefined number of clusters. Data points around the cluster center are then added to the cluster. Now, a new cluster center is calculated depending on the data points of the corresponding cluster. The last step is the repetition of the second and third steps, i.e., the allocation of data points around a cluster center to the cluster and the calculation of a new cluster center depending on the cluster's data points. When the cluster center is not changing, the final center is found.

For the *DINGO8* scenario, the summed up distance from each data point to its cluster center D_r is shown for a different number of clusters in Figure 5.18. It can be seen how much D_r decreases if two clusters are applied instead of one GFMC cluster, which is equivalent to the GFMC consideration in the TCA based EDAM. In this scenario, four GFMC clusters are used since only a slight D_r decrease can be observed for a higher number of clusters.

The allocation of GFMC of a cluster in the detailed network can be seen in Figure 5.16. While the first cluster (marked green) includes three GFMC, the clusters two and three con-

Figure 5.18: Summed up distance from each data point to its cluster center D_r for different number of clusters. Input data for the k-means algorithm are the voltage sensitivities $\vec{s}_i$ at the PCC of each GFMC i in the detailed network of scenario *DINGO8*

tain two GFMC (marked orange and blue), and cluster four only consists of one GFMC (marked red).

It can be seen that the distribution of the GFMC corresponding to the same cluster is not necessarily a neighboring GFMC. The GFMC of cluster two (marked orange) for example are in different network branches. However, they both are located at the branch end, which in this case leads to similar voltage sensitivities. The consideration of the detailed network's topology is only applicable if the clustering algorithm allows the aggregation of neighboring GFMC. However, such a constraint results in less GFMC that can be aggregated in one cluster. For this scenario with all GFMC in different branches, such an aggregation of neighboring GFMC in one network branch is not possible.

The resulting EDAM of the aggregation level *STCA 4 GFMC* is shown in Figure 5.19. There are four equivalent GFMC corresponding to the four clusters. The other components are modeled identically to the STCA based EDAM. Since the detailed network's topology cannot be considered in this EDAM, all equivalent GFMC are connected in parallel.

Table 5.8 shows the nominal values of the GFMC for the STCA based EDAM of both aggregation levels *STCA 8 GFMC* and *STCA 4 GFMC*. Since multiple GFMC are aggregated to one GFMC, the nominal values of the equivalent GFMC in the STCA based EDAM of the aggregation level *STCA 4 GFMC* are the summation of the nominal values of the GFMC to be aggregated in the detailed network.

The calculated set points for the output current of each GFMC are plotted in Figure 5.20. For the phase angle jump, the calculated output current of the eight equivalent GFMC of the aggregation level *STCA 8 GFMC* are very close to the calculated output current of the corresponding GFMC in the detailed network. However, the aggregated GFMC of the aggre-

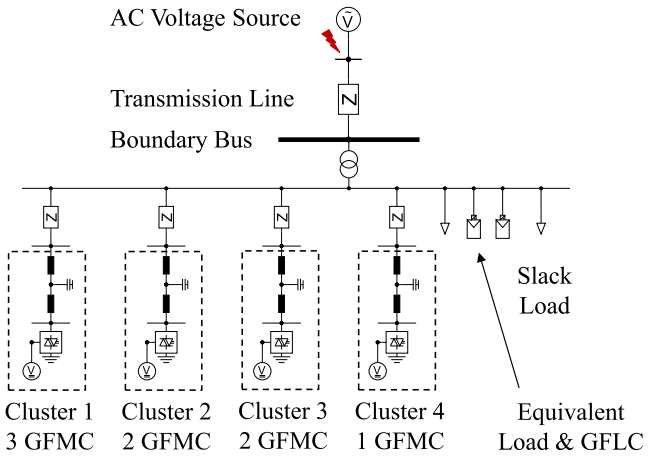

Figure 5.19: Schematic of EDAM aggregated by STCA with four GFMC clusters of the aggregation level *DINGO8 STCA 4 GFMC* [UL23]

Table 5.8: Scenario *DINGO8*: nominal GFMC values [UL23]

Aggregation Level	**GFMC**	**Rated Apparent Power**	**Active Power**	**Reactive Power**	**Maximum Current**
STCA 8 GFMC	8 GFMC	5 MVA	3 MW	0.75 Mvar	1 pu
	Sum	**40 MVA**	**24 MW**	**6.00 Mvar**	
STCA 4 GFMC	Cluster 1 (3 GFMC)	15 MVA	9 MW	2.25 Mvar	1 pu
	Cluster 2 and 3 (2 GFMC)	10 MVA	6 MW	1.50 Mvar	1 pu
	Cluster 4 (1 GFMC)	5 MVA	3 MW	0.75 Mvar	1 pu
	Sum	**40 MVA**	**24 MW**	**6.00 Mvar**	

gation level *STCA 4 GFMC* behave differently. Unlike the GFMC in the detailed network, three equivalent GFMC do not reach the maximum current. Only the equivalent GFMC of cluster 4 reaches the current limit for the same time as the corresponding GFMC in the detailed network. Since cluster 4 consists of only one GFMC, the equivalent impedance of cluster 4 could be parameterized to match the voltage sensitivities of the corresponding GFMC PCC in the detailed network very well.

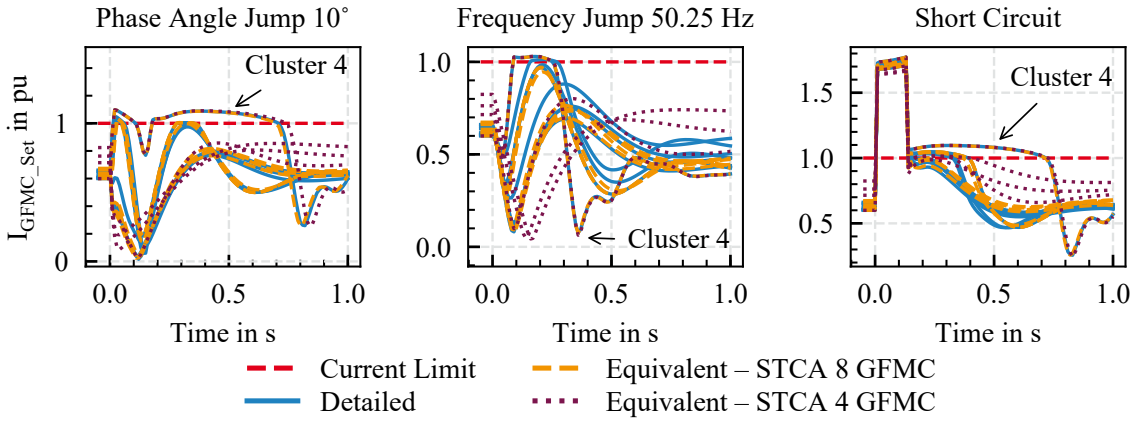

Figure 5.20: Scenario *DINGO8*: calculated set point for output current of GFMC I_{GFMC_Set} in detailed and equivalent network models

The frequency jump leads to more severe differences between the GFMC's calculated output current of the detailed network and the calculated output current of the equivalent GFMC of the aggregation level *STCA 8 GFMC*. Only one equivalent GFMC reaches the current limit, while two GFMC of the detailed network reach the current limit. Similar to the phase angle jump event, GFMC cluster 4 of the EDAM of the aggregation level *STCA 4 GFMC* is the only equivalent GFMC capable of reproducing the calculated output current of the corresponding GFMC in the detailed network. However, as in the aggregation level *STCA 8 GFMC*, only one equivalent GFMC reaches the current limit.

The calculated output currents of the equivalent GFMC of the aggregation level *STCA 8 GFMC* capture the calculated output currents of the detailed network's GFMC well during and after the short circuit fault. One equivalent GFMC exceeds the maximum current for a slightly longer time ($\approx 0.05\,\mathrm{s}$) compared to the corresponding GFMC in the detailed network. In the aggregation level *STCA 4 GFMC*, the equivalent GFMC of cluster 4 captures the calculated output current of the corresponding GFMC in the detailed network opposed to the GFMC of the other clusters.

The active and reactive power flows at the boundary bus from the transmission to the detailed ADN model and both EDAM of the aggregation levels *STCA 8 GFMC* and *STCA 4 GFMC* are shown in the first two rows of Figure 5.21. It can be observed that for the phase angle jump, the EDAM of the aggregation level *STCA 8 GFMC* captures the active as well as the reactive power flow of the detailed network very well. The power flows of the EDAM of the aggregation level *STCA 4 GFMC* show significant differences. The peak value of the active power flow of the detailed network ($\approx 45\,\mathrm{MW}$) after the event is not captured at all by the EDAM of the aggregation level *STCA 4 GFMC* ($\approx 25\,\mathrm{MW}$). Only the new steady-

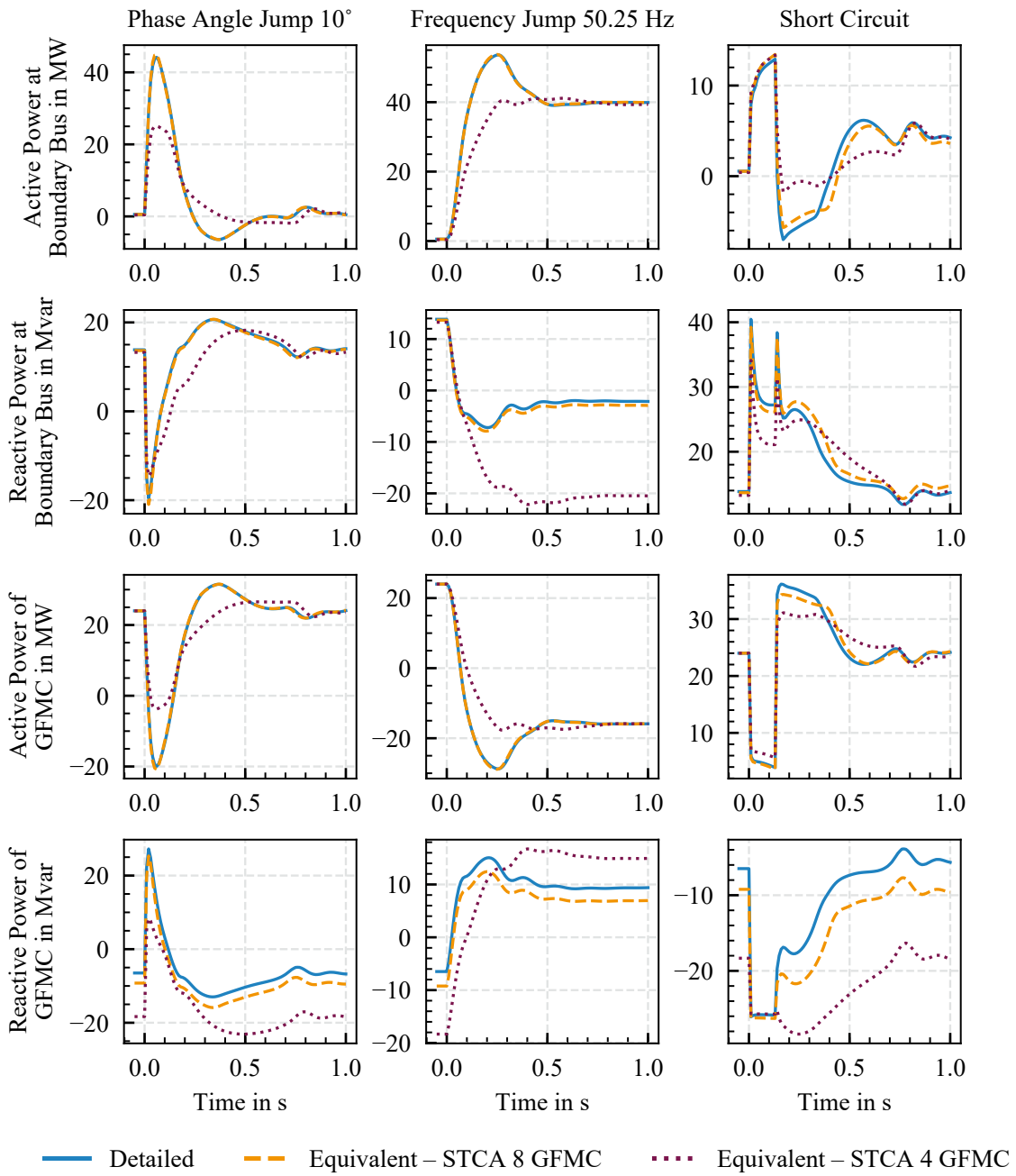

Figure 5.21: Scenario *DINGO8*: active and reactive power flow at boundary bus from transmission to distribution system of detailed and equivalent network models and sum of active and reactive power generation of all GFMC in detailed and equivalent network models; positive reactive power values: over-excited state; negative reactive power values: under-excited state

state value after the event is similar to the active power flow of the detailed network. The minimum value of the reactive power flow of the detailed network ($\approx -22\,\text{Mvar}$) is missed

by the EDAM by approximately 8 Mvar (≈ -14 Mvar). Only the steady-state reactive power flow after the event is close to the detailed network's power flow.

The EDAM of the aggregation level *STCA 8 GFMC* captures the active power flow of the detailed network after the frequency jump very well. Also, the reactive power flow is very close to the detailed network's reactive power flow, despite a small offset. However, the active power flow of the EDAM of the aggregation level *STCA 4 GFMC* is quite different. The active power peak after the event is not captured. Only the steady-state value after the event is close to the post-event steady-state value of the detailed network. The reactive power flow deviates significantly from the one of the detailed network. While the post-event steady-state reactive power flow of the detailed network is around -3 Mvar, the steady-state value of the EDAM levels at around -20 Mvar.

The short circuit as the most severe fault leads to the biggest deviations between the power flows of the detailed network and the EDAM of the aggregation level *STCA 8 GFMC*. As observed with the calculated output current set point of the EDAM, where one equivalent GFMC reached the maximum current for a longer time compared to the corresponding GFMC in the detailed network, the active and reactive power flows are similar to the one of the detailed network with a small offset (≈ 0.05 s later than the power flows of detailed network). Besides this offset, the shape is very similar to the shape of the detailed network's active and reactive power flows. The EDAM of the aggregation level *STCA 4 GFMC* captures the active power flow during the short circuit. However, the EDAM fails to reproduce the detailed network's active power flow in the post-fault period. The reactive power flows of the detailed network cannot be captured during and after the fault. Only the post-fault steady-state active and reactive power values of the EDAM of the aggregation level *STCA 4 GFMC* are close to the values of the detailed network.

The last two rows of Figure 5.21 show the total active and reactive power generation of the GFMC in the detailed network as well as the equivalent GFMC in both EDAM of the aggregation levels *STCA 8 GFMC* and *STCA 4 GFMC*. The observations made with the power flows at the boundary bus are in line with the GFMC generation after the phase angle jump. The active power generation of the equivalent GFMC of the aggregation level *STCA 8 GFMC* is very close to the GFMC generation in the detailed network. In contrast, an offset can be observed for reactive power generation. However, the equivalent GFMC of the aggregation level *STCA 4 GFMC* generate different active and reactive power compared to the GFMC in the detailed network. The generation peaks after the event are not captured for both active and reactive power. Also, the steady-state reactive power generation after the event is not close to the generation of the detailed network's GFMC.

Similar to the phase angle jump, the frequency jump leads to a very similar active and reactive power generation of the equivalent GFMC of the EDAM of the aggregation level *STCA 8 GFMC* compared to the GFMC in the detailed network. Only an offset of reactive power generation can be observed here. The aggregated equivalent GFMC of the aggregation level *STCA 4 GFMC* are not capable of capturing the detailed network's GFMC generation. Especially the reactive power generation shows considerable deviations, which is in line with the deviating reactive power flow at the boundary bus for this scenario.
The short circuit fault leads to slight deviations of active power GFMC generation of the EDAM of the aggregation level *STCA 8 GFMC* and quite different reactive power generation. However, the shape of reactive power generation is similar to the generation of the detailed network's GFMC. However, the deviations of the aggregated equivalent GFMC of the aggregation level *STCA 4 GFMC* are more severe. Especially, reactive power generation deviates significantly.

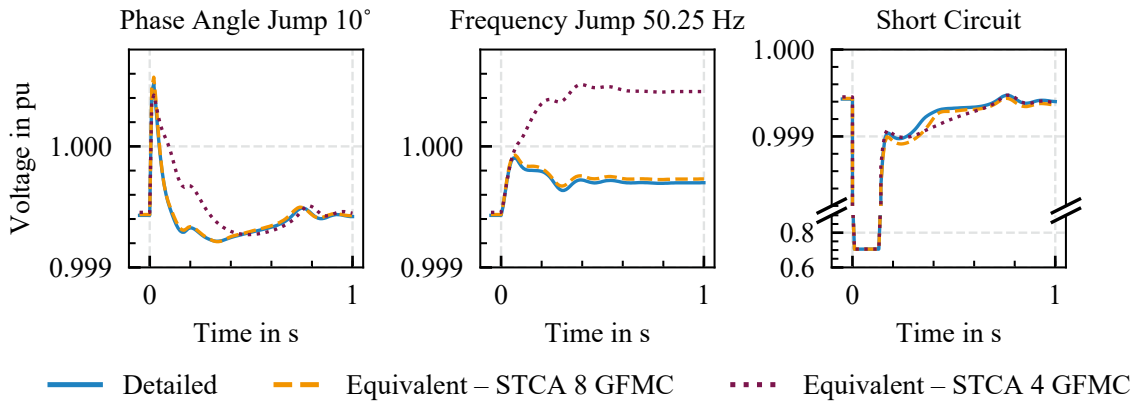

Figure 5.22: Scenario *DINGO8*: voltages at low voltage side of 230 kV/10 kV transformer in detailed and equivalent network models

Deviations between the two EDAM and the detailed model similar to the ones observed at the boundary bus power flow and GFMC generation can also be seen at the voltages at the lower voltage side of the EHV/MV transformer in Figure 5.22. The voltage of the EDAM of the aggregation level *STCA 8 GFMC* are very close to the voltage of the detailed network after the phase angle jump, while the EDAM of the aggregation level *STCA 4 GFMC* show differences. Only the steady-state post-event voltage is close to the detailed network.
A slight offset between the voltage of the EDAM of the aggregation level *STCA 8 GFMC* and the detailed network can be seen after the frequency jump. As opposed to that, the EDAM of the aggregation level *STCA 4 GFMC* reaches significantly higher voltages resulting in a very different reactive power flow at the boundary bus as observed in Figure 5.21.

Also, the short circuit results in different voltages in the post-fault time period between both EDAM and detailed network. Nevertheless, the deviations of the EDAM of the aggregation level *STCA 8 GFMC* are less significant than the differences between the voltage of the EDAM of the aggregation level *STCA 4 GFMC* and the detailed network.

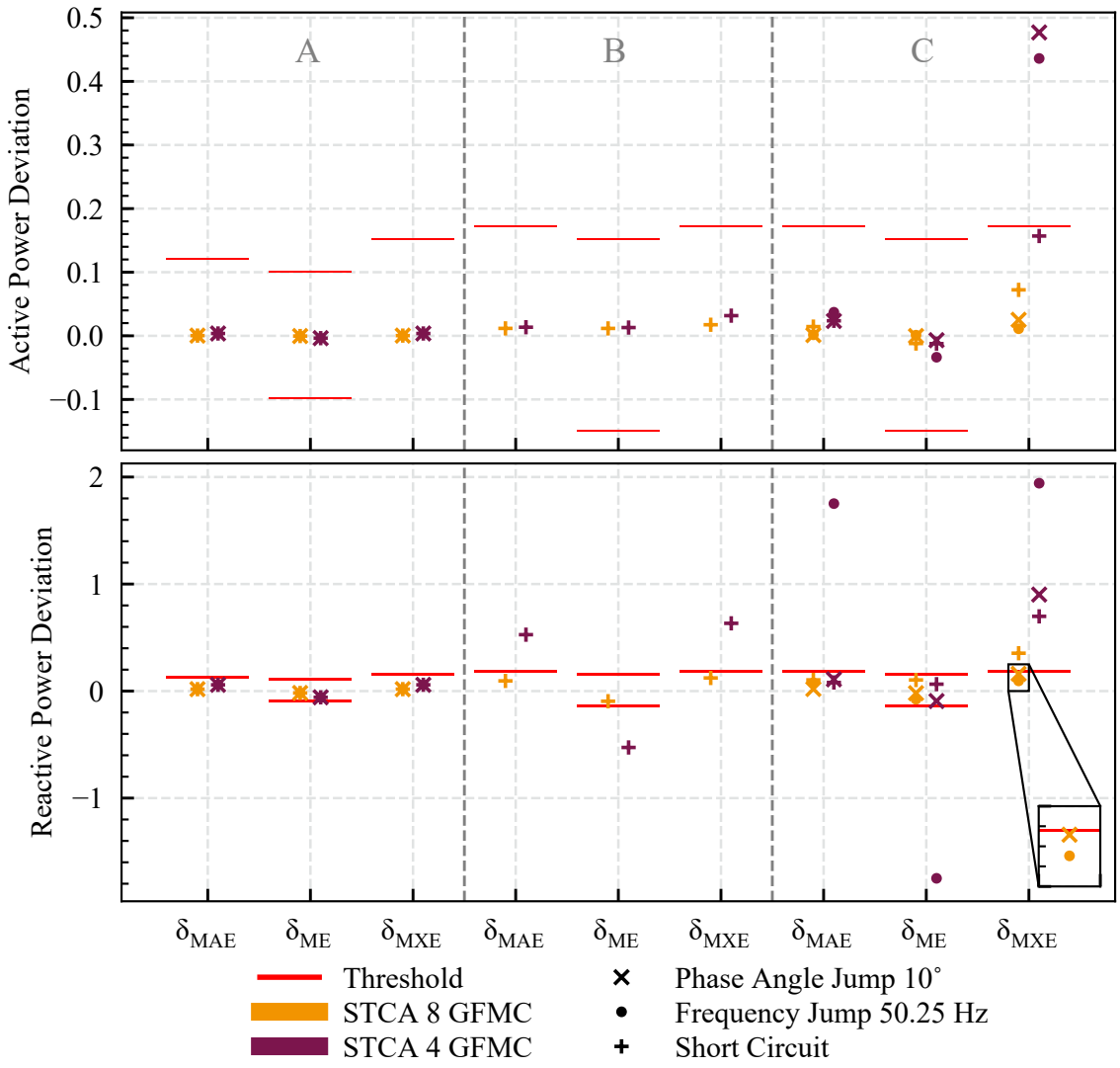

Figure 5.23: Scenario *DINGO8*: validation results for EDAM of both aggregation levels *STCA 8 GFMC* and *STCA 4 GFMC* [UL23]

These observations are in line with the results of the validation. Figure 5.23 shows in detail the validation results for all three events of both EDAM divided in the three error metrics δ_{MAE}, δ_{ME}, and δ_{MXE}. In the pre-event period A, all error metrics of both EDAM are close to zero and within the validation limits. This is due to the parameterization of the slack load.

During the short circuit fault, the active power deviations are close to zero for both EDAM and do not exceed the validation threshold. The reactive power deviations of the EDAM of the aggregation level *STCA 8 GFMC* are close to the validation limits but do not exceed the same. The EDAM of the aggregation level *STCA 4 GFMC* fails the validation for all error metrics during the short circuit.

Active power deviations in the post-event period C of the EDAM of the aggregation level *STCA 8 GFMC* are within the validation limits for all three events and error metrics. The EDAM of the aggregation level *STCA 4 GFMC* also passes the validation for the error metrics δ_{MAE} and δ_{ME} in all three events. As opposed to that, the active power deviation exceeds the threshold after the phase angle and frequency jump events for the maximum error δ_{MXE}. Reactive power deviations of the EDAM of the aggregation level *STCA 8 GFMC* exceeds the validation limit for the maximum error δ_{MXE} in the post-fault period of the short circuit. The other events do not lead to a validation threshold violation. Opposed to that, the frequency jump leads to reactive power validation failures of the EDAM of the aggregation level *STCA 4 GFMC* in the post-event period for all three error metrics. Also, the threshold value of δ_{MXE} is exceeded by the reactive power deviation in the post-event period of the phase angle jump and short circuit.

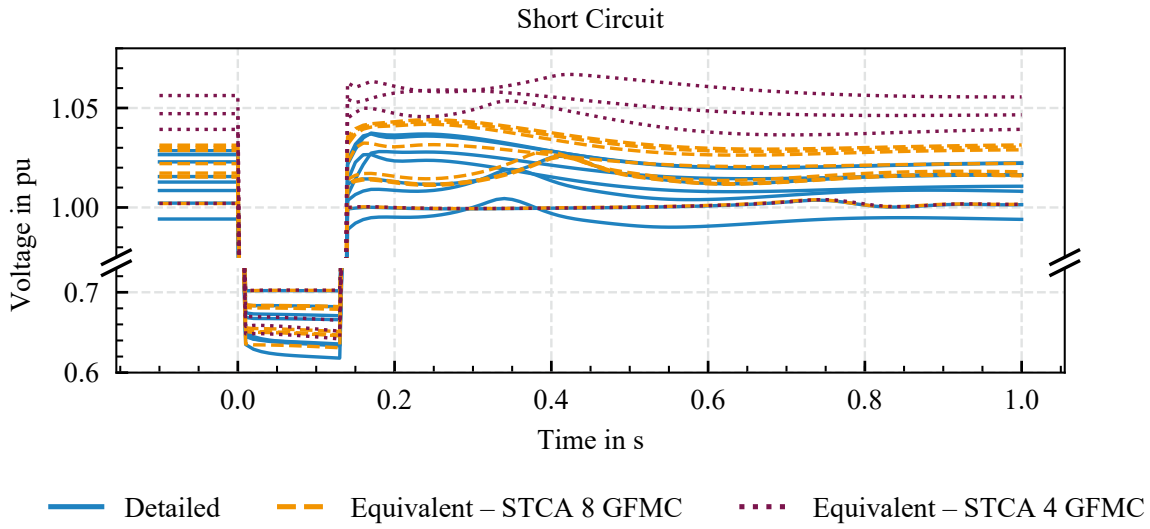

Figure 5.24: Scenario *DINGO8*: voltages at PCC of each GFMC in detailed and equivalent network models

The voltages at the PCC of each GFMC in the detailed network model and both EDAM are shown for the short circuit fault in Figure 5.24 to investigate the reasons for the validation violations, especially of the EDAM of the aggregation level *STCA 4 GFMC*. The voltages at

PCC of the equivalent GFMC of the aggregation level *STCA 8 GFMC* are pretty close to the voltages at the PCC of the GFMC in the detailed network model. However, a slight offset for some PCC voltages can be observed. Due to the complexity reduction of the EDAM, the behavior of the detailed network cannot be captured identically. Especially the components influencing the voltages at the respective PCC, like loads or GFLC, are not considered at the PCC of the equivalent GFMC. This leads to the offset in the PCC voltage and the validation failure of the maximum error δ_{MXE} of reactive power deviation in the post-fault period.

The equivalent GFMC of the aggregation level *STCA 4 GFMC* are connected to the EDAM, neglecting the detailed network's topology. Hence, this EDAM does not consider neighboring GFMC influencing the PCC voltages in the detailed network. As a result, the PCC voltages of the equivalent GFMC differ significantly from the corresponding voltages in the detailed network. This results in significant validation violations of the EDAM *STCA 4 GFMC* for all three events, but especially for the reactive power flows at the boundary bus. Hence, aggregating multiple GFMC to one equivalent GFMC leads to significant accuracy drawbacks.

Nevertheless, the STCA based EDAM with aggregated equivalent GFMC performs better than the TCA based EDAM. A comparison between these two approaches, STCA based EDAM of the aggregation level *STCA 4 GFMC* and TCA based EDAM, is provided in Section B.4.

5.4.4 Scenario: DINGO20

The scenario of this section investigates a detailed network with several GFMC, i.e., twenty GFMC. Suppose the number of equivalent GFMC should equal to the number of GFMC in the detailed network. In that case, the EDAM derivation process requires a higher computational effort for creating the STCA based EDAM compared to the scenarios with less GFMC, e.g., *DINGO6*. Not only the EDAM structure creation is more complex, but also more equivalent impedances need to be parameterized. Hence, in this chapter, a scenario is investigated in which an aggregation of multiple GFMC to equivalent GFMC reduces the EDAM complexity to a greater extent compared to scenario *DINGO8*. An EDAM containing twenty equivalent GFMC is compared with an EDAM containing aggregated five equivalent GFMC to investigate the importance of the individual consideration of GFMC:

1. *STCA 20 GFMC*: number of equivalent GFMC, i.e., twenty, equals number of GFMC in the detailed network, i.e., twenty.

2. *STCA 5 GFMC*: number of equivalent GFMC, i.e., five, is lower than number of GFMC in the detailed network, i.e., twenty.

Additionally, this section investigates the validity of an EDAM with a considerable amount of equivalent GFMC. To anticipate the result, the EDAM of the aggregation level *STCA 20 GFMC* shows slight validation violations after the short circuit.

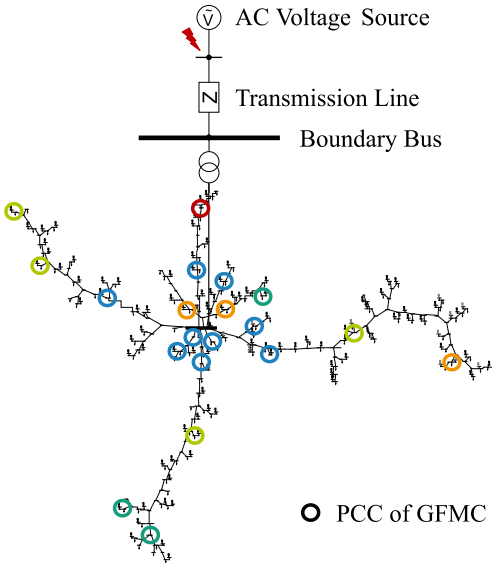

Figure 5.25: Schematic of detailed network of scenario *DINGO20* with GFMC's PCC colored according to the clusters of the aggregation level *STCA 5 GFMC*

The GFMC are distributed among the network as shown in Figure 5.25. For the aggregation level *STCA 20 GFMC*, the GFMC location in the detailed network needs to be considered as described in Section 4.3.2 resulting in the connection of the equivalent GFMC with equivalent impedances as shown in Figure 5.26. Since the detailed network model is identical to the one of scenario *DINGO6* despite the GFMC, the equivalent GFLC and equivalent load are modeled as described in Section 5.4.1. The slack load is parameterized to match the steady-state power flow at the boundary bus in the EDAM to the power flow at the boundary bus of the detailed network model.

For the aggregation level *STCA 5 GFMC*, the GFMC are clustered according to their voltage sensitivities $\vec{s}_i$ as described in Section 4.3.3 and Section 5.4.3. To identify the optimal number of clusters, the summed up distance from each data point to its cluster center D_r is calculated for different number of clusters (Figure 5.27). Since only marginal improvements can be observed for more than five clusters, five GFMC clusters are defined for this scenario.

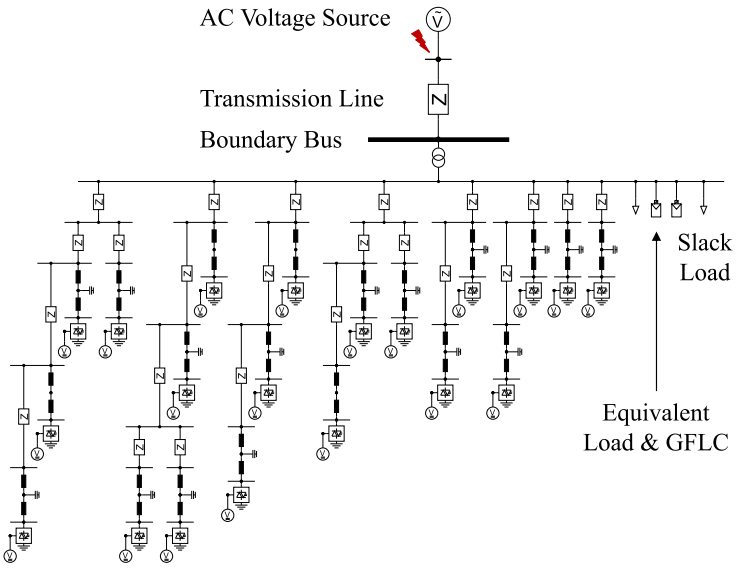

Figure 5.26: Schematic of EDAM aggregated by STCA of the aggregation level *DINGO20 STCA 20 GFMC*

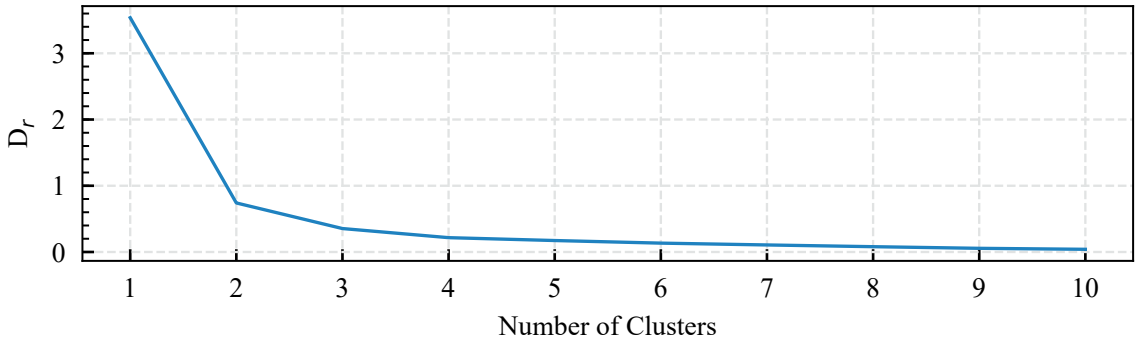

Figure 5.27: Summed up distance from each data point to its cluster center D_r for different number of clusters. Input data for the k-means algorithm are the voltage sensitivities $\vec{s}_i$ at the PCC of each GFMC i in the detailed network of scenario *DINGO20*

The PCC of GFMC of one cluster are colored accordingly in Figure 5.25 to observe the distribution of GFMC of the same cluster among the detailed network model. Considering the GFMC location by reproducing the detailed network's topology in the EDAM is not possible when multiple non-neighboring GFMC are aggregated according to their voltage sensitivities. Also, aggregating only neighboring GFMC of one branch to preserve the detailed network's topology will not significantly reduce complexity in this scenario since the constraint for the GFMC aggregation is too strict.

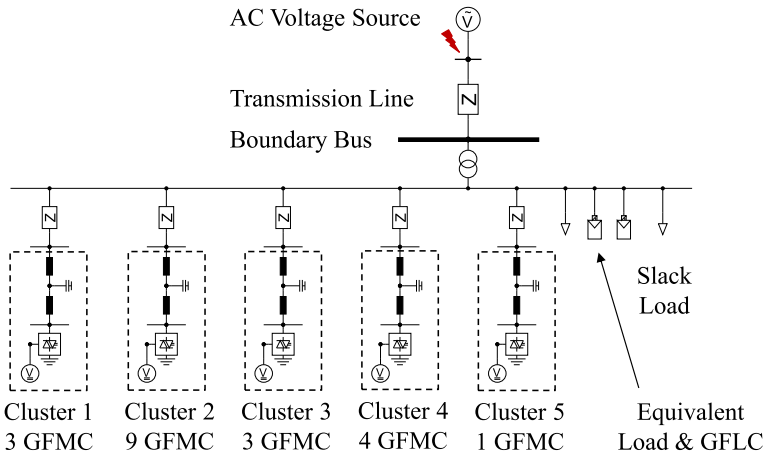

Figure 5.28: Schematic of EDAM aggregated by STCA with five GFMC clusters of the aggregation level *DINGO20 STCA 5 GFMC*

The resulting EDAM of the aggregation level *STCA 5 GFMC* is shown in Figure 5.28. Since the detailed network's topology cannot be considered with the aggregated GFMC in this scenario, the equivalent GFMC are connected in parallel. The number of aggregated GFMC in the detailed network is shown below the equivalent GFMC. The nominal values of the equivalent GFMC of each scenario are listed in Table 5.9.

Figure 5.29 shows the active and reactive power flows at the boundary bus of both the detailed ADN model and EDAM of the aggregation levels *STCA 20 GFMC* and *STCA 5 GFMC*. It can be observed that the active power flow after the phase angle jump of the EDAM of the aggregation level *STCA 20 GFMC* is very similar compared to the detailed network. However, the EDAM with the aggregated GFMC of the aggregation level *STCA 5 GFMC* shows significant differences in the active power flow resulting from the phase angle jump. After the event, the active power peak value is below the peak value of the detailed network's active power by approximately 18 MW. Also, the following dynamic behavior deviates from the one of the detailed network. Only the post-event steady-state values are similar to the detailed network.

The reactive power flow after the phase angle jump of the EDAM of the aggregation level *STCA 20 GFMC* shows a similar behavior compared to the power flow of the detailed network. However, the lowest reactive power value right after the phase angle jump of the EDAM of the aggregation level *STCA 5 GFMC* is approximately 7 Mvar higher compared to the one of the detailed network. Deviations from the reactive power flow of the detailed network can also be observed in the post-event dynamic behavior of this EDAM.

Table 5.9: Scenario *DINGO20*: nominal GFMC values

Aggregation Level	**GFMC**	**Rated Apparent Power**	**Active Power**	**Reactive Power**	**Maximum Current**
STCA 20 GFMC	20 GFMC	2 MVA	1.2 MW	0.3 Mvar	1 pu
	Sum	**40 MVA**	**24.0 MW**	**6.0 Mvar**	
STCA 5 GFMC	Cluster 1 and 3 (3 GFMC)	6 MVA	3.6 MW	0.9 Mvar	1 pu
	Cluster 2 (9 GFMC)	18 MVA	10.8 MW	2.7 Mvar	1 pu
	Cluster 4 (4 GFMC)	8 MVA	4.8 MW	1.2 Mvar	1 pu
	Cluster 5 (1 GFMC)	2 MVA	1.2 MW	0.3 Mvar	1 pu
	Sum	**40 MVA**	**24.0 MW**	**6.0 Mvar**	

The EDAM of the aggregation level *STCA 20 GFMC* exposed to the frequency jump leads to an active power flow at the boundary bus very similar to the power flow of the detailed network. However, the EDAM of the aggregation level *STCA 5 GFMC* has more significant differences in the dynamic behavior of the detailed network. The post-event steady-state active power is similar to the detailed network for both EDAM.

The reactive power flow of the EDAM of the aggregation level *STCA 20 GFMC* after the frequency jump deviates somewhat from the reactive power flow of the detailed network. Nevertheless, the deviations are less distinct compared to the deviations of the EDAM of the aggregation level *STCA 5 GFMC*. Here, the reactive power is significantly below the reactive power of the detailed network. The post-event steady-state value deviates by approximately 12 Mvar.

The short circuit leads to deviations of both EDAM compared to the detailed network. During the fault, the active power of both EDAM is close to the active power of the detailed network. After the short circuit is cleared, the EDAM of the aggregation level *STCA 20 GFMC* responses with an active power behavior that comes close to the detailed network's behavior but still shows deviations. As opposed to that, the active power response of the EDAM of the

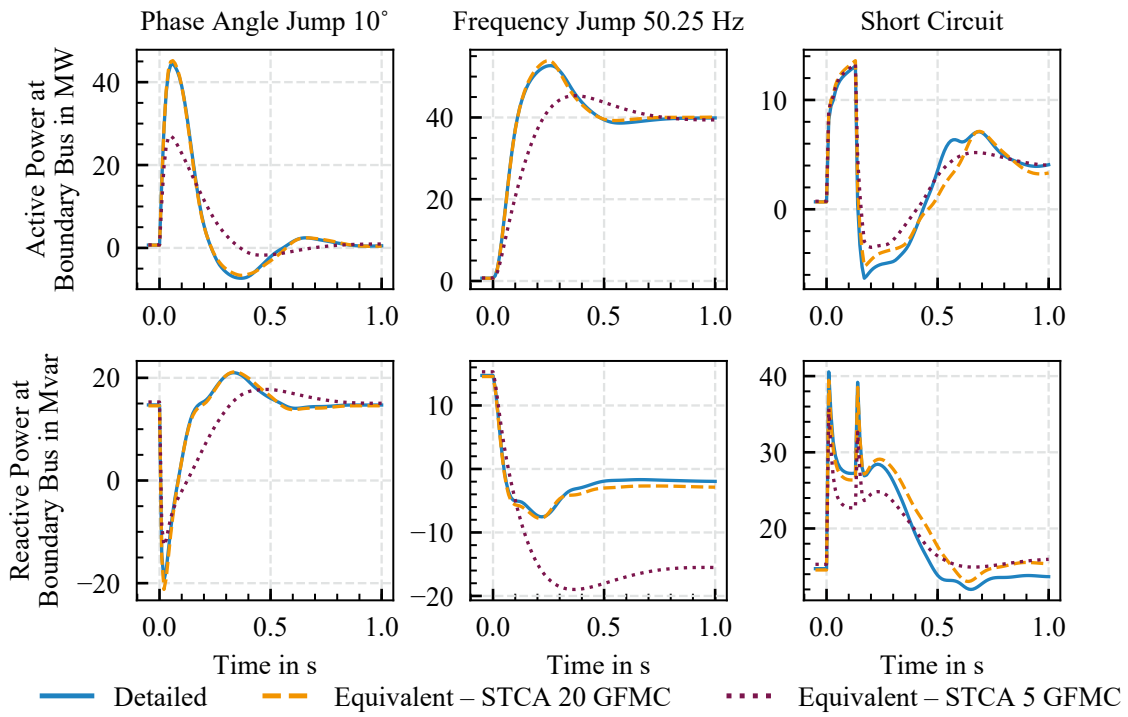

Figure 5.29: Scenario *DINGO20*: active and reactive power flow at boundary bus from transmission to distribution system of detailed and equivalent network models; positive reactive power values: over-excited state; negative reactive power values: under-excited state

aggregation level *STCA 5 GFMC* after the fault deviates significantly from the power flow of the detailed network.

While the reactive power of the EDAM of the aggregation level *STCA 20 GFMC* is close to the one of the detailed network during the short circuit, the EDAM of the aggregation level *STCA 5 GFMC* deviates significantly from the behavior of the detailed network. Severe reactive power deviations of the EDAM of both aggregation levels *STCA 20 GFMC* and *STCA 5 GFMC* compared to the detailed network can also be observed after the short circuit is cleared. The numerical validation is applied and described in the following paragraphs to quantify these deviations.

Figure 5.30 shows the validation results for active and reactive power deviations of the EDAM of both aggregation levels. The active power deviation of the EDAM of the aggregation level *STCA 20 GFMC* does not exceed any validation threshold for all three events. Likewise, the EDAM of the aggregation level *STCA 5 GFMC* also does not exceed active power thresholds except for the error δ_{MXE} in the post-event period of the phase angle and frequency jump.

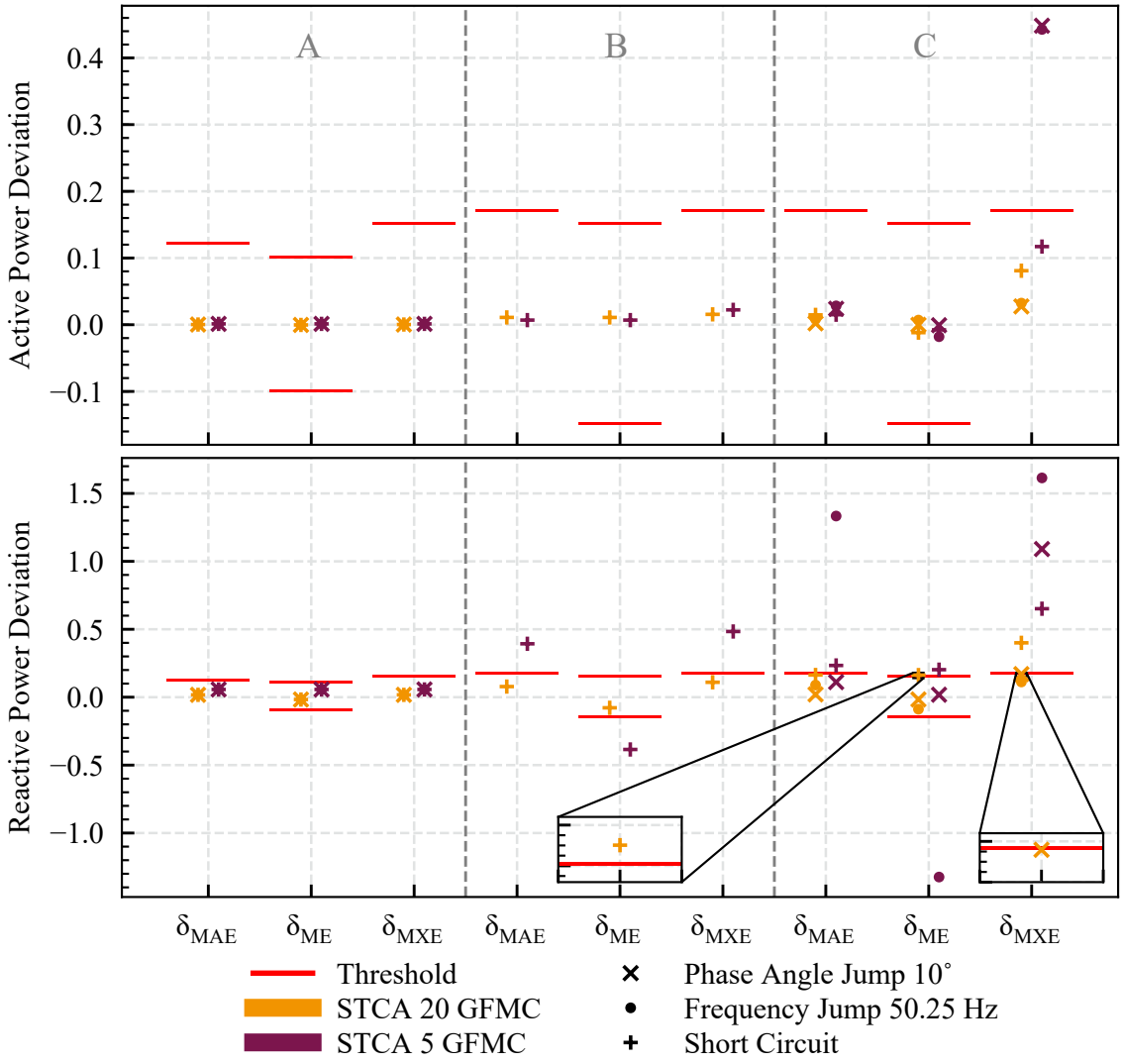

Figure 5.30: Scenario *DINGO20*: validation results for EDAM of both aggregation levels *STCA 20 GFMC* and *STCA 5 GFMC*

No validation violations of the reactive power can be observed in the pre-event phase for both EDAM. Also, during the short circuit fault, there are no violations of the EDAM of the aggregation level *STCA 20 GFMC*. Opposed to that, all error metrics δ_{MAE}, δ_{ME}, and δ_{MXE} exceed the allowed thresholds of the EDAM of the aggregation level *STCA 5 GFMC*. The short circuit leads to a minor violation of the error metric δ_{ME} and to a more significant violation of the error metric δ_{MXE} of the EDAM of the aggregation level *STCA 20 GFMC* in the post-fault period. The same EDAM does not exceed any threshold values in the post-event period of the phase angle and frequency jump. The EDAM of the aggregation level *STCA 5 GFMC* exceeds the threshold values of all error metrics in the post-event phase of all three events except for the error metrics δ_{MAE} and δ_{ME} after the phase angle jump.

Similar to scenario *DINGO8*, the aggregation of multiple GFMC to an equivalent GFMC results in significant accuracy drawbacks of the EDAM and validation violations. Nevertheless, the comparison between the EDAM of the aggregation level *STCA 5 GFMC* and the EDAM aggregated by TCA provided in Section B.6 shows the better reproduction of the dynamic behavior of the detailed network by the EDAM with the aggregated GFMC compared to the TCA based EDAM. The latter even shows unstable behavior as a response to the frequency jump event.

5.4.5 Scenario: DINGO15

The content presented in this chapter has been published in [UL23]. The results of scenarios *DINGO8* and *DINGO20* show that an aggregation of multiple GFMC to a fewer number of equivalent GFMC results in performance drawbacks of the STCA. The consideration of GFMC in an EDAM aggregated by STCA depends on the network topology of the detailed network (Section 4.1). However, by aggregating multiple non-neighboring GFMC the detailed network's topology cannot be taken into account in the EDAM.
Nevertheless, in the case of networks with a high number of GFMC in one branch or one closed ring, the aggregation of neighboring GFMC within this branch or closed ring can result in a significant complexity reduction and the detailed network's topology can still be considered in the EDAM. This case is investigated in the following scenario.
Here, a detailed network with 15 GFMC in one branch of the DINGO network topology (Section 5.3.2) as shown in Figure 5.31 is considered. Similar to the scenario *DINGO8*, an STCA based EDAM with 15 equivalent GFMC is compared to an STCA based EDAM with four GFMC:

1. *STCA 15 GFMC*: number of equivalent GFMC, i.e., 15, equals number of GFMC in the detailed network, i.e., 15.

2. *STCA 4 GFMC*: number of equivalent GFMC, i.e., four, is lower than number of GFMC in the detailed network, i.e., 15.

The resulting STCA based EDAM of the aggregation level *STCA 15 GFMC* is shown in Figure 5.32. Since all GFMC are located in one branch, this connection in series is kept in the connection of the equivalent GFMC. To derive the EDAM of the aggregation level *STCA 4 GFMC*, all GFMC are clustered according to their voltage sensitivities $\vec{s}_i$ as described in Section 5.4.3. By calculating the summed up distance from each data point to its cluster center D_r for different number of clusters, the optimal number of four GFMC clusters is

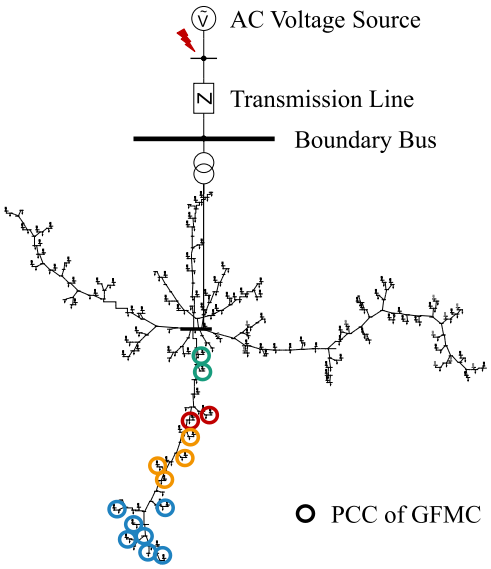

Figure 5.31: Schematic of detailed network of scenario *DINGO15* with GFMC's PCC colored according to the clusters of the aggregation level *STCA 4 GFMC* [UL23]

identified (Figure 5.33). The PCC of GFMC of one cluster are colored accordingly in Figure 5.31.

The resulting EDAM of the aggregation level *STCA 4 GFMC* is shown in Figure 5.34. The network topology of the detailed model could be kept since only neighboring GFMC of one branch are in one cluster. The number of aggregated GFMC in the detailed network and the nominal values of the equivalent GFMC of each aggregation level are listed in Table 5.10.

Figure 5.35 shows the active and reactive power flows at the boundary bus of the detailed ADN model and the EDAM aggregated by STCA of both aggregation levels *STCA 15 GFMC* and *STCA 4 GFMC*. It can be observed that the active power flow after the phase angle jump of the EDAM of the aggregation level *STCA 15 GFMC* is very similar compared to the detailed network, whereas the EDAM with the aggregated GFMC of the aggregation level *STCA 4 GFMC* differs slightly. Especially the active power peak following the phase angle jump cannot be captured by the EDAM of the aggregation level *STCA 4 GFMC*. Similarly, the reactive power flow after the phase angle jump of the EDAM of the aggregation levels *STCA 15 GFMC* and *STCA 4 GFMC* captures the dynamic behavior of the detailed network very well. Small deviations, however, can be observed for the latter.

The EDAM of the aggregation level *STCA 15 GFMC* exposed to the frequency jump leads to an active and reactive power flow at the boundary bus very similar to the corresponding power flow of the detailed network. However, the EDAM of the aggregation level *STCA 4 GFMC* slightly deviates from the detailed network's dynamic behavior.

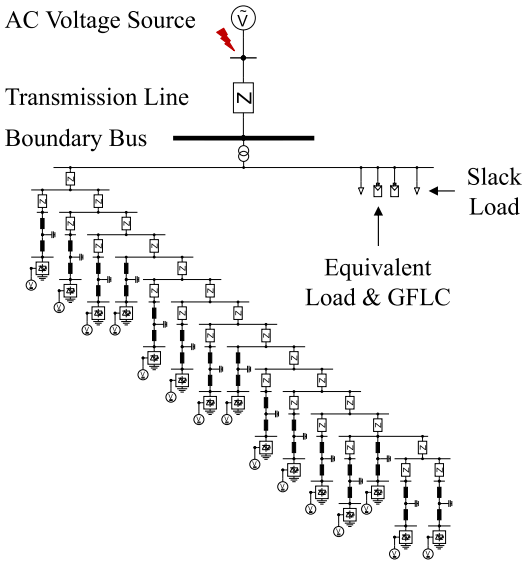

Figure 5.32: Schematic of EDAM aggregated by STCA of the aggregation level *DINGO15 STCA 15 GFMC* [UL23]

Figure 5.33: Summed up distance from each data point to its cluster center D_r for different number of clusters. Input data for the k-means algorithm are the voltage sensitivities $\vec{s}_i$ at the PCC of each GFMC i in the detailed network of scenario *DINGO15*

As observed with the other events, the dynamic behavior of the detailed network during and after the short circuit is captured by STCA based EDAM of both aggregation levels, whereas the EDAM of the aggregation level *STCA 15 GFMC* reproduces the detailed network's behavior more distinct.

The numerical validation is applied to quantify these deviations. Figure 5.36 shows the validation results for active and reactive power deviations of the EDAM aggregated by STCA of both aggregation levels. It can be seen that the STCA based EDAM of both aggregation

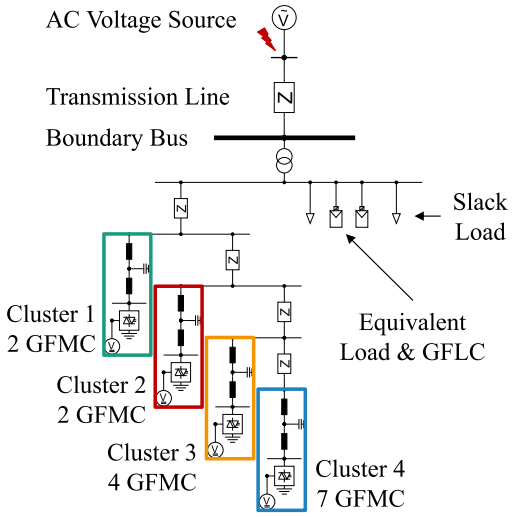

Figure 5.34: Schematic of EDAM aggregated by STCA with four GFMC clusters of the aggregation level *DINGO15 STCA 4 GFMC* [UL23]

Table 5.10: Scenario *DINGO15*: nominal GFMC values [UL23]

Aggregation Level	**GFMC**	**Rated Apparent Power**	**Active Power**	**Reactive Power**	**Maximum Current**
STCA 15 GFMC	15 GFMC	2.5 MVA	1.6 MW	0.4 Mvar	1 pu
	Sum	**37.5 MVA**	**24.0 MW**	**6.0 Mvar**	
STCA 4 GFMC	Cluster 1 and 2 (2 GFMC)	5.0 MVA	3.2 MW	0.8 Mvar	1 pu
	Cluster 3 (4 GFMC)	10.0 MVA	6.4 MW	1.6 Mvar	1 pu
	Cluster 4 (7 GFMC)	17.5 MVA	11.2 MW	2.8 Mvar	1 pu
	Sum	**37.5 MVA**	**24.0 MW**	**6.0 Mvar**	

levels do not exceed any validation threshold of active and reactive power deviation for all three events.

A comparison between the EDAM of the aggregation level *STCA 4 GFMC* and the EDAM aggregated by TCA is provided in Section B.8.

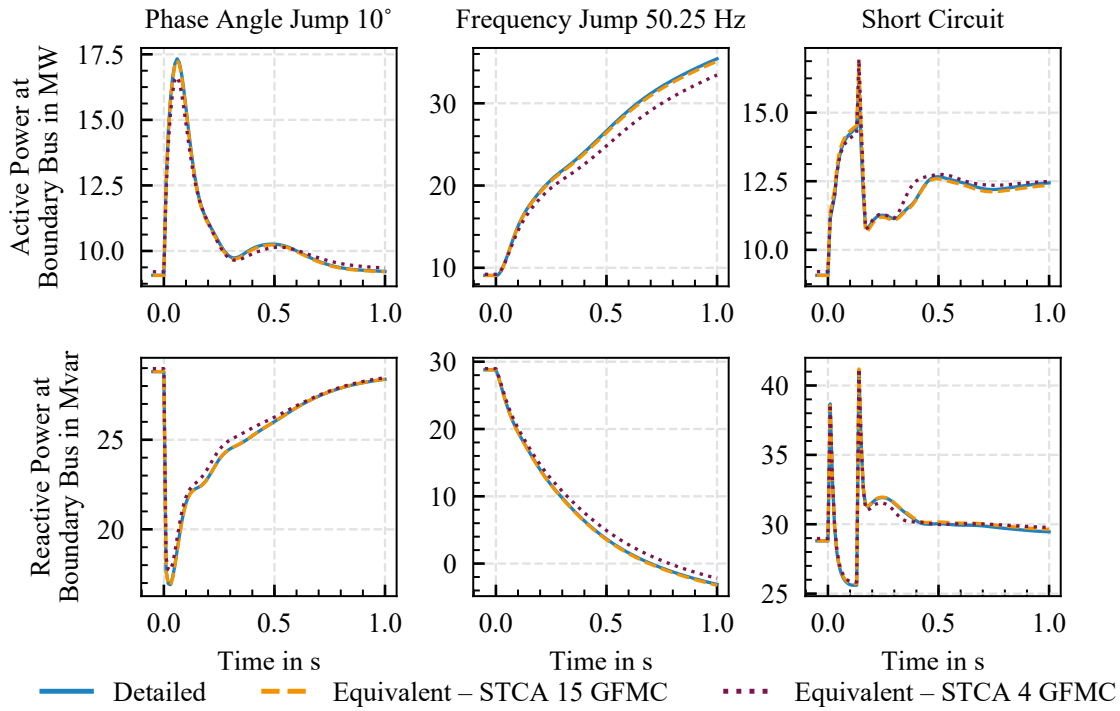

Figure 5.35: Scenario *DINGO15*: active and reactive power flow at boundary bus from transmission to distribution system of detailed and equivalent network models; positive reactive power values: over-excited state; negative reactive power values: under-excited state [UL23]

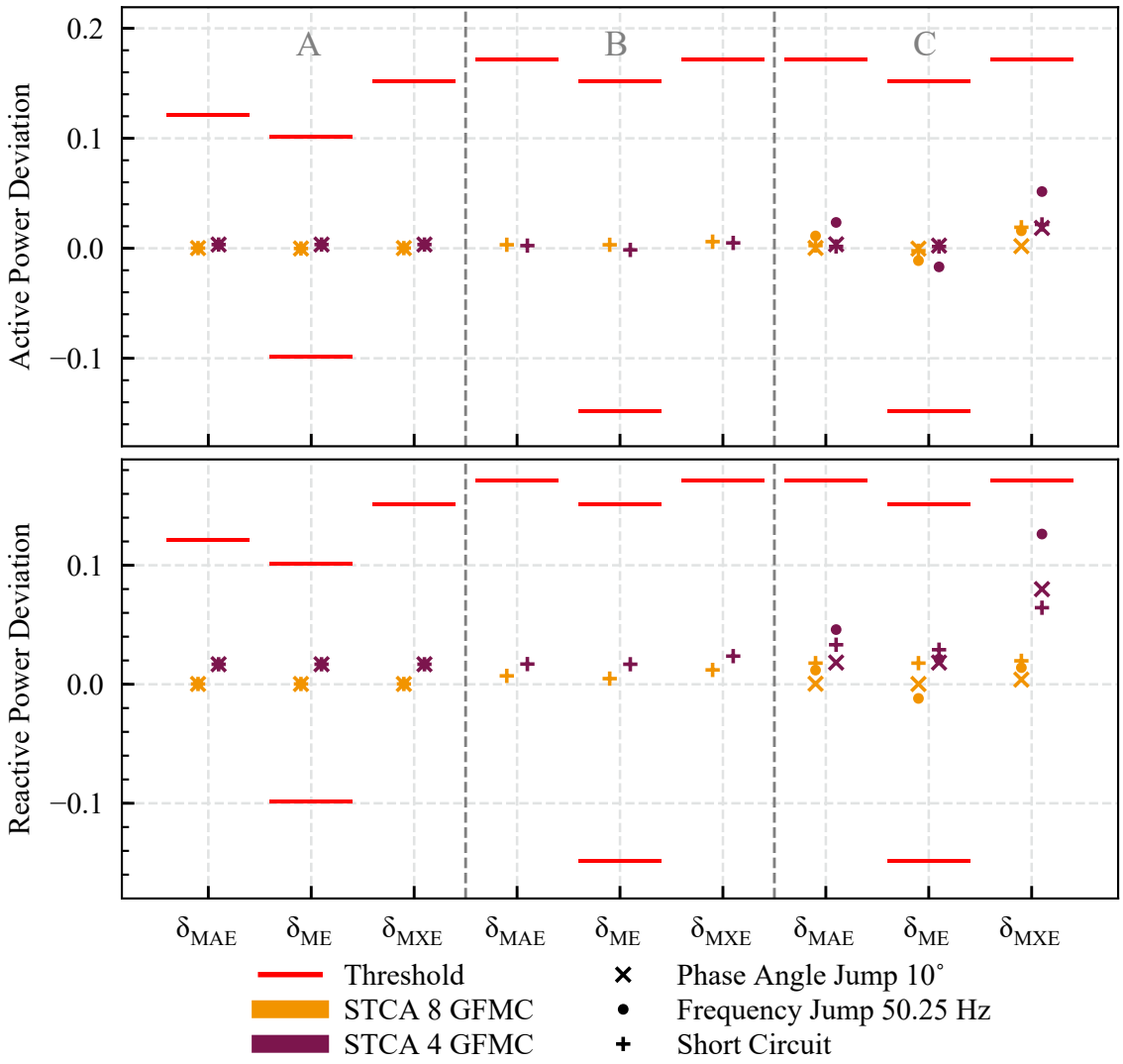

Figure 5.36: Scenario *DINGO15*: validation results for EDAM of both aggregation levels *STCA 15 GFMC* and *STCA 4 GFMC* [UL23]

5.5 Operating Point Dependency and Adaptation

The content presented in this chapter has partly been published [Ung+22a].

5.5.1 Methodology

The STCA based EDAM is parameterized according to one specific load and generation case of the corresponding detailed network. This section analyses the generalizability of EDAM with respect to changes in the corresponding detailed network's operating point. To this end, the EDAM derived from a base scenario is validated against the detailed network at different operating points. Additionally, relevant parameters of the EDAM are identified. A re-parameterization of these parameters will adapt the EDAM according to the new operating point of the detailed network. Identifying relevant parameters allows a simple update of the EDAM to different scenarios.

The base scenario is identical to the scenario *DINGO6* (Section 5.4.1). Hence, the STCA based EDAM considers each GFMC of the detailed network individually. Based on this base scenario, the total load and GFMC generation of the detailed network is changed by $\pm 5\%$, $\pm 10\%$, $\pm 15\%$, $\pm 20\%$, and $\pm 25\%$ by increasing and decreasing the nominal active and reactive power values of each load and GFMC, respectively. Additionally, the LCL output filter parameters of the GFMC are adapted according to the new GFMC nominal values as described in Section 3.2.3. A load change directly relates to an increase or decrease of the share of CBG generation in the detailed network. Nevertheless, the focus of the STCA is the adequate representation of GFMC in the EDAM. Hence, changes in the GFMC generation are essential to analyze separately.

To evaluate the operating point dependency of the EDAM to operating point changes in the detailed network, the EDAM parameterized to the base scenario is validated against the detailed network with changed operating points. The result of this analysis is a range of permissible deviations of the detailed network's operating point, in which the EDAM still passes the validation. Then, the ability of the EDAM to adapt to new operating points is evaluated by re-parameterizing relevant EDAM parameters and validating the resulting EDAM against the detailed network with the respective operating point.

The EDAM's performance is validated against the detailed network for each scenario by simulating a phase angle jump event, a frequency jump event, and a short circuit fault as introduced in Section 5.1. The validation procedure introduced in Section 5.2 is applied for this evaluation. It comprises the three periods pre-fault (A), fault (B), and post-fault (C). The fault period is only relevant for the short circuit fault. The different maximum allowed

threshold values for each validation error metric per period as listed in Table 5.2 makes a comparison of the validation results between the different scenarios difficult. Hence, the three error metrics are normalized as $\delta' = \frac{\delta}{\hat{\delta}}$, with $\hat{\delta}$ being the maximum allowed value, such that the value 1 (and ± 1 for δ_{ME}, respectively) corresponds to the threshold values as shown in Table 5.2. A value higher than 1 (or lower than -1, respectively) indicates a validation failure.

The reference values P_0 and Q_0 for the calculation of the error $x_{\mathrm{E}}(n)$ are $P_0 = 40\,\mathrm{MW}$ and $Q_0 = 10.1\,\mathrm{Mvar}$ (Table 5.4) as the total demand of the network model. These reference values will remain the same for all load and GFMC generation scenarios. Adapting these reference values according to the scenarios, i.e., the total demand of the model in the specific load scenario as reference values, will have a distorting effect on the validation results: higher reference values lead to fewer validation threshold violations for the same absolute deviations. Hence, the validation calculation is performed with the same reference values P_0 and Q_0 in all scenarios to ensure comparability.

The error metrics δ'_{MAE}, δ'_{ME}, and δ'_{MXE} are calculated both for active and reactive power deviations. The following plots will only show the worst values of both validation calculations. Hence, if the active power deviation δ'_{MAE} passes the validation with a value of 0.9, but the reactive power deviation δ'_{MAE} fails the validation with a value of 1.1, the reactive power deviation is shown in the following plots.

The active and reactive power deviations can be found in Section B.9. The same evaluation shown in the following for the STCA based EDAM is also conducted with the TCA based EDAM. The results can be found in Section B.9.

This section first analyses the EDAM dependency on changes in the detailed network's total load and GFMC generation. After that, relevant parameters of the EDAM are identified to adapt the EDAM to the new operating points of the detailed network without re-parameterizing the whole EDAM. Finally, to interpret the results, voltage sensitivities of the EDAM are compared to the detailed network's voltage sensitivities for the different operating points.

5.5.2 Operating Point Dependency

Figure 5.37 shows the results of the EDAM validity evaluation for changes in the detailed network's load, whereas the EDAM is parameterized according to the base scenario (0 % load change). For all three events, the error metrics of the pre-event period are the same.

Here, scenarios with load changes of 15 % or higher and −15 % or lower compared to the base scenario lead to a violation of the validation threshold values.

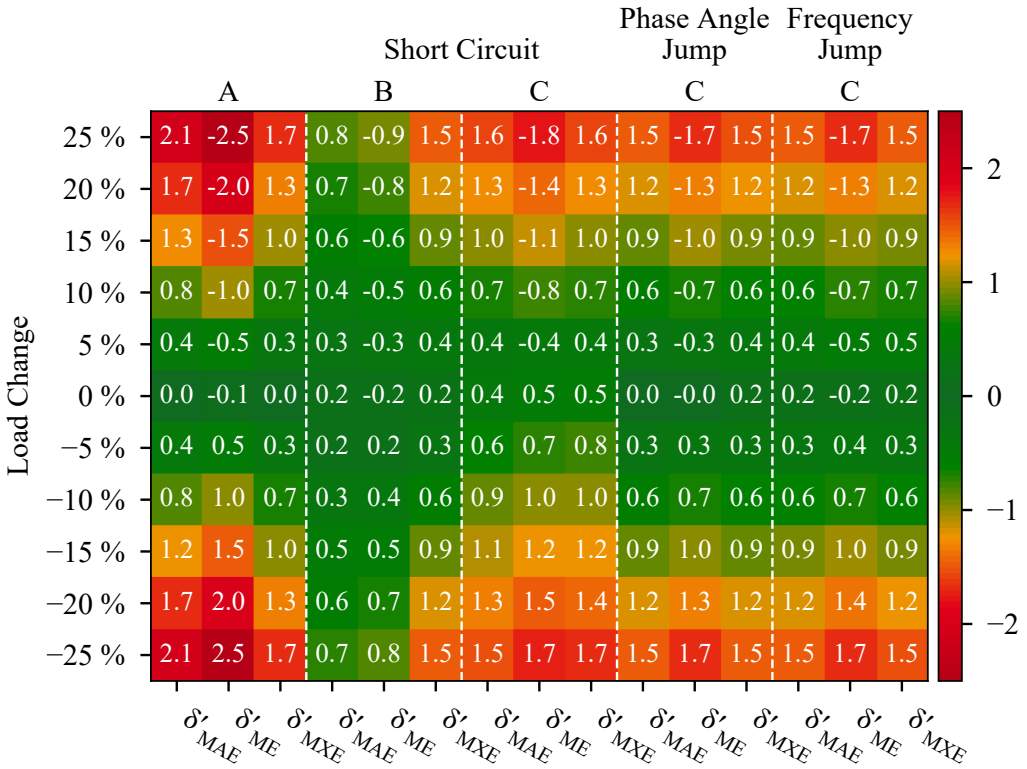

Figure 5.37: *Load scenarios*: validity evaluation of STCA based EDAM parameterized according to base scenario (0 %) for different load scenarios in the detailed network; values show worst validation results of both active and reactive power deviation

These violations are less distinct during the short circuit. Threshold violations, especially of the error metric δ_{MXE}, can be observed for scenarios with a load change of 20 % or higher and −20 % or lower. In the post-fault period of the short circuit, no validation failures occur within load changes of −10 % to 10 %. In the period after the phase angle jump, no validation failures can be observed for load changes from −15 % to 15 %. Similarly, load changes of −15 % to 15 % also do not affect the validity of the EDAM in the post-event period of the frequency jump. Considering all three events, the STCA based EDAM does not exceed any threshold violations for load changes of the detailed network from −10 % to 10 % compared to the base scenario the EDAM is parameterized to.

In Figure 5.38, the active and reactive power flow at the boundary bus from the transmission system to the ADN is shown. The power flows of both TCA and STCA based EDAM

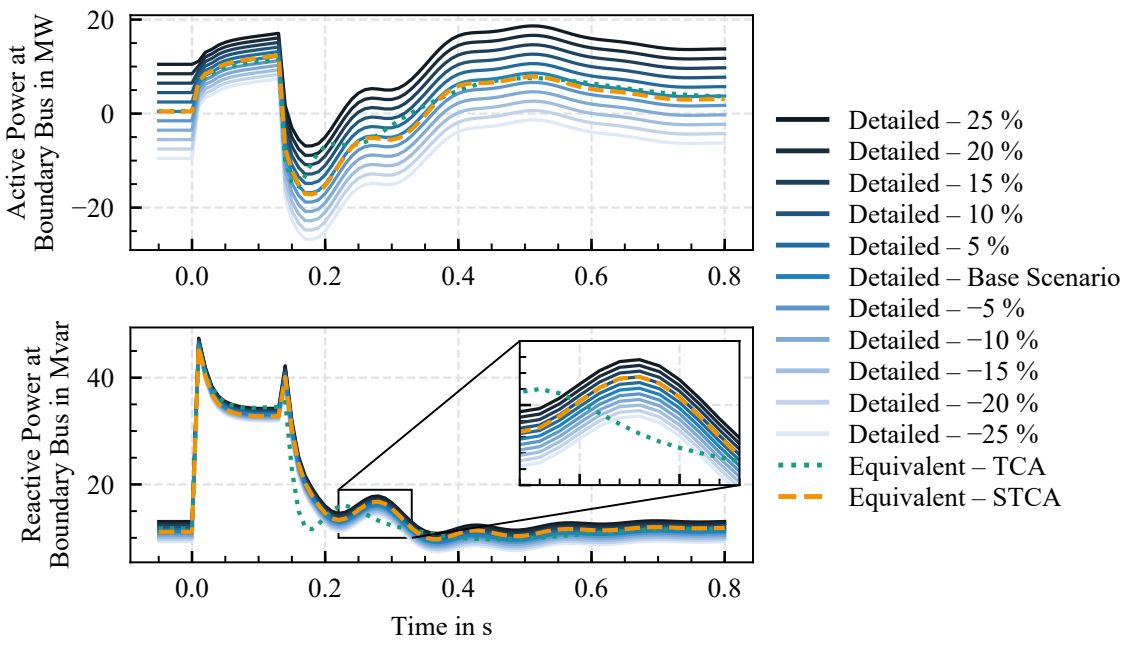

Figure 5.38: *Load scenarios*: active and reactive power flow at boundary bus from transmission to distribution system of detailed network model with different load scenarios as well as both equivalent network models of base scenario; positive reactive power values: over-excited state; negative reactive power values: under-excited state

parameterized to the base scenario, as well as the power flows of the detailed network for the different load scenarios are plotted.

It can be seen that the active and reactive power flow of the detailed network for the different load scenarios have a similar shape. An offset according to the respective scenario can be observed. The higher the total load, the higher the active and reactive power flow at the boundary bus and vice versa. The reactive power flow of the STCA based EDAM parameterized to the base scenario has a slight positive offset in the post-fault period compared to the reactive power flow of the detailed network parameterized to the base scenario. This can also be seen in Figure 5.8. These observations comply with the validation results of Figure 5.37. The higher or lower the total load of the detailed network compared to the base scenario, the higher the deviation to the EDAM.

In the second set of scenarios, the GFMC generation was increased and decreased by changing each GFMC's nominal generation values according to the respective scenario. The results of this evaluation are shown in Figure 5.39. Threshold violations of the error metrics can be observed in the pre-event period for GFMC generation changes of 15 % or higher and −15 % or lower than the GFMC generation of the base scenario.

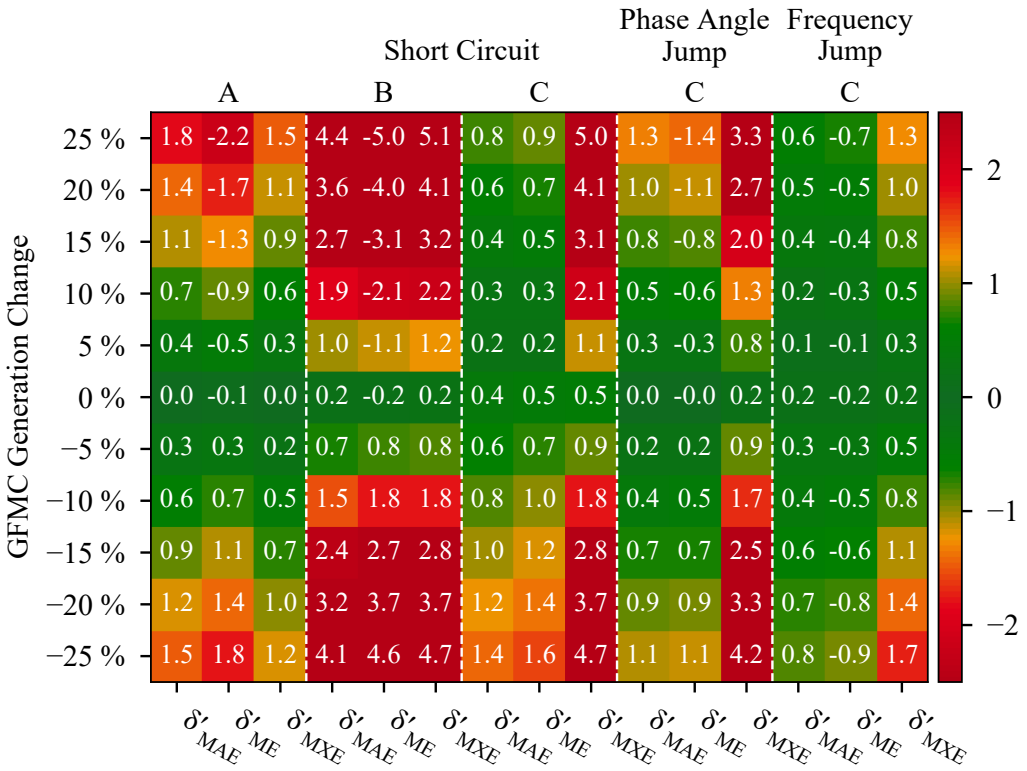

Figure 5.39: *GFMC generation scenarios*: validity evaluation of STCA based EDAM parameterized according to base scenario (0 %) for different GFMC generation scenarios in the detailed network; values show worst validation results of both active and reactive power deviation

During the short circuit, the allowed threshold values of the error metrics are exceeded as soon as the GFMC generation increases. In contrast, a decrease of the GFMC generation of −5 % is allowed. Similarly, threshold violations in the post-fault period of the short circuit can be observed for an increase in GFMC generation. In contrast, a GFMC generation decrease of −5 % does not affect the EDAM's validity. Therefore, the EDAM is valid in the post-event period of the phase angle jump for GFMC generation changes within ±5 %. The post-event period of the frequency jump has the minor validation failures of all three events. Here, the allowed GFMC generation changes range from −10 % to 20 %.

This leads to an overall validity of the EDAM for −5 % GFMC generation changes in the detailed network compared to the base scenario. All other scenarios result in a validation failure of at least one error metric. Especially the error metric δ_{MXE} exceeds the threshold values significantly in the post-event periods. Also, an increase in GFMC generation affects the EDAM validity more than a GFMC generation decrease.

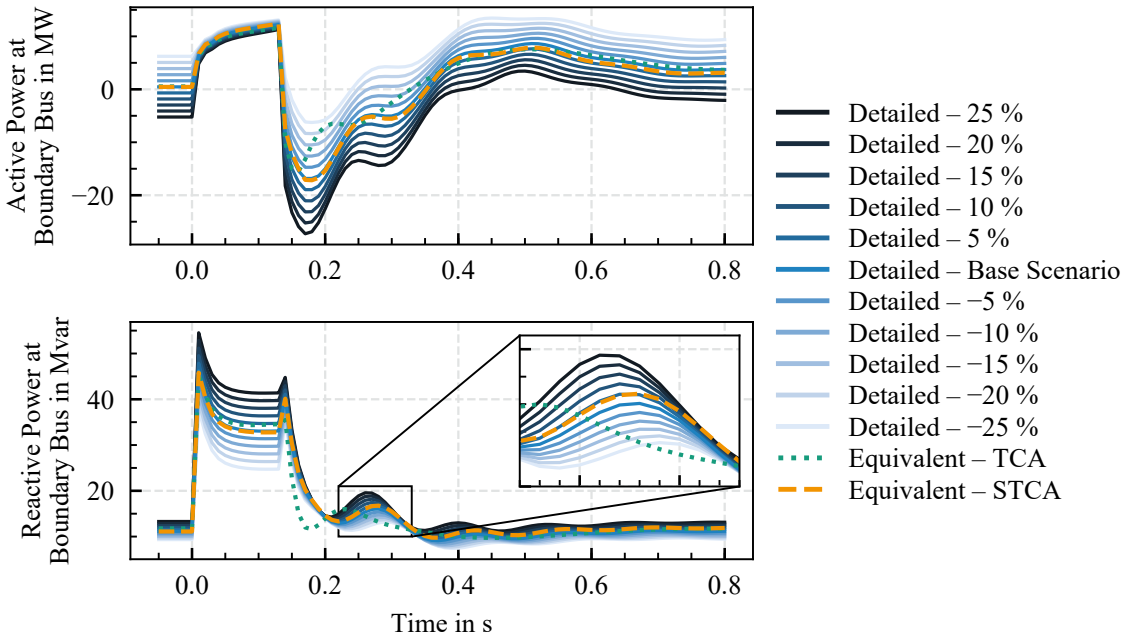

Figure 5.40: *GFMC generation scenarios*: active and reactive power flow at boundary bus from transmission to distribution system of detailed network model with different GFMC generation scenarios as well as both equivalent network models of base scenario; positive reactive power values: over-excited state; negative reactive power values: under-excited state

Similarly to Figure 5.38, Figure 5.40 shows the active and reactive power flow at the boundary bus of the detailed network model with different GFMC generation scenarios as well as both TCA and STCA based EDAM parameterized according to the base scenario. An increase in GFMC generation results in a decrease in active power flow and an increase in reactive power flow, respectively, compared to the base scenario. Especially the active power flow shapes are similar for the different GFMC generation scenarios.

The deviations between the reactive power flows of the different scenarios during the short circuit are very distinct. That complies with the validation results shown in Figure 5.39 and in Figure B.36. The latter shows the validation results of the reactive power deviation in detail.

5.5.3 Operating Point Adaptation

As shown in the previous paragraph, the dependency of the STCA based EDAM to the operating point, to which the EDAM was parameterized, is quite strong. However, it can be crucial for stability studies to calculate a considerable amount of different load and gen-

eration scenarios, and the effort to create an individual EDAM for each scenario may be disproportionate. Hence, a simplified update of the EDAM to operating point changes can reduce the computational effort significantly. To this end, this section identifies relevant parameters whose adaptation to the detailed network's operating point results in a valid EDAM. The operating point scenarios are identical to the ones investigated in Section 5.5.2.
Keeping in mind the EDAM derivation process (Section 4.2), the equivalent load corresponds to the total load of the detailed network. Similarly, each GFMC in the detailed network is represented in the EDAM by an equivalent GFMC with the same parameters compared to its counterpart. Additionally, an equivalent impedance matches the voltage sensitivities at the PCC of the equivalent GFMC to the voltage sensitivities at the PCC of the corresponding GFMC in the detailed network.

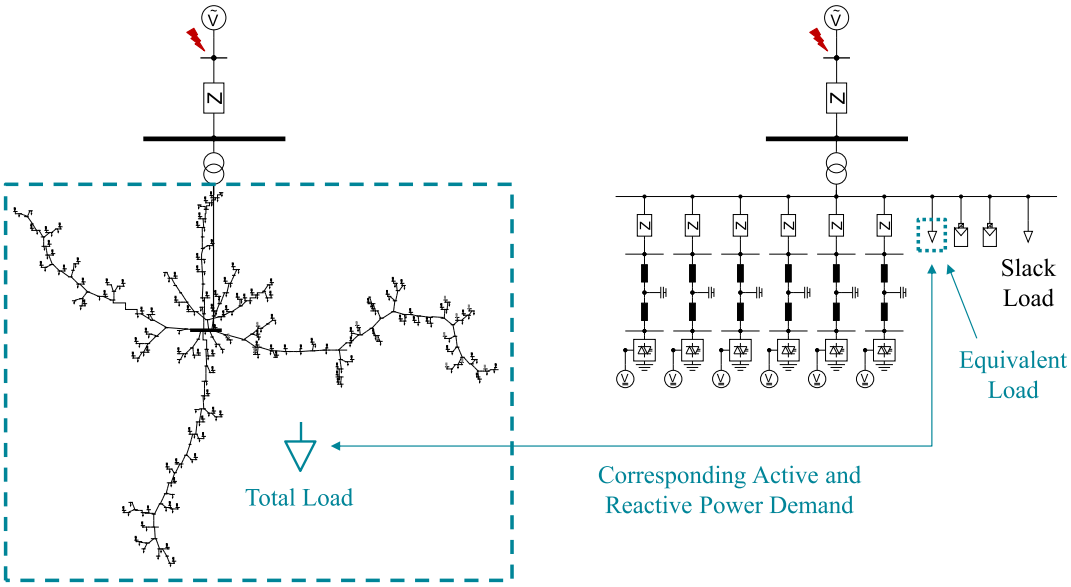

Figure 5.41: Schematic of corresponding active and reactive power demand of detailed network model and EDAM

Hence, changing the total load or GFMC generation in the detailed network should result in an analogous change of the corresponding equivalent components. The active and reactive power demand of the equivalent load in the EDAM will be changed according to the load scenario to adapt the EDAM to different load scenarios. Figure 5.41 illustrates this process in a simplified schematic. To adapt the EDAM to different GFMC generation scenarios, the generation of the respective equivalent GFMC will be changed according to the scenario. In contrast, the equivalent impedance is left unaltered as shown in Figure 5.42. Since the LCL output filter parameters of the GFMC are adapted according to the new GFMC nominal

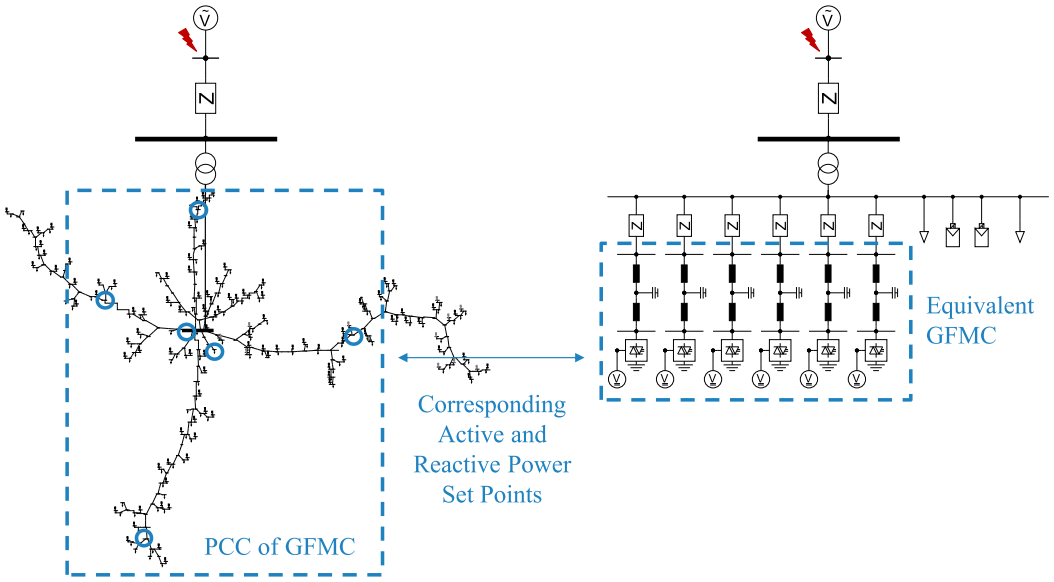

Figure 5.42: Schematic of the GFMC's corresponding nominal active and reactive power values of detailed network model and EDAM

values in the detailed network (Section 5.5.1), this filter parameter adaptation is also made for the equivalent GFMC.

The same scenarios as for the operating point dependency evaluation are calculated, i.e., load and GFMC generation changes of $-25\,\%$ to $25\,\%$ in steps of $5\,\%$ compared to the base scenario, and the EDAM is adapted to the respective scenario by changing the equivalent load and equivalent GFMC generation, respectively. The EDAM validity evaluation shows no validation failures for any error metric of these scenarios. Hence, further load and GFMC generation scenarios are investigated to reach the boundaries of the adaptation. The load and GFMC generation are changed to $\pm 50\,\%$, $\pm 75\,\%$, and $\pm 100\,\%$.

Figure 5.43 shows the worst values of the active and reactive power deviation in the load change scenarios. No validation threshold violations can be observed in the pre-event phase for load changes of $-25\,\%$ to $50\,\%$. During the short circuit, the validation threshold is not exceeded in load change scenarios from $-50\,\%$ to $75\,\%$. However, in the post-event phase of the short circuit fault no validation threshold violations can be observed for the load change scenarios from $-50\,\%$ to $25\,\%$. The error metrics in the post-event phase of both phase angle jump and frequency jump are quite similar. Here, the validation threshold is not exceed in load change scenarios from $-50\,\%$ to $75\,\%$.

The $100\,\%$ GFMC generation change scenario leads to validation failures in the post-fault period of the short circuit, as can be seen in Figure 5.44. The pre-event and the post-event

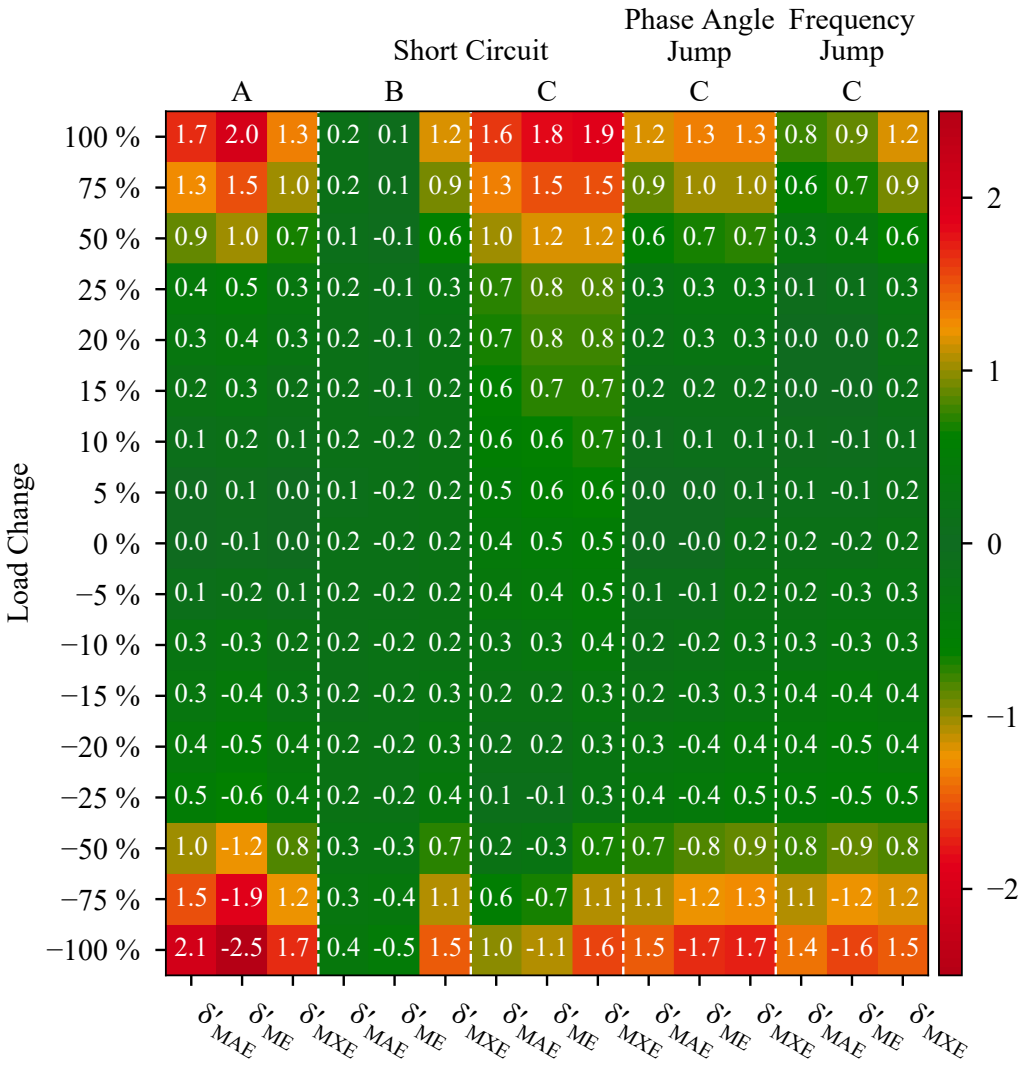

Figure 5.43: *Load scenarios*: validity evaluation of adapted STCA based EDAM for different load scenarios in the detailed network; values show worst validation results of both active and reactive power deviation

periods of the phase angle and frequency jump do not exceed threshold values even for the ±100 % scenarios. A decrease in GFMC generation of −100 % leads to validation failure in the pre-event period.

It can be seen that this simplified EDAM adaptation works well in a considerable range of operating point changes. However, especially in load change scenarios, the EDAM adaptation reaches its boundaries already at changes of around ±25 % compared to the base scenario. Additional plots of the active and reactive power validation, as well as the results of the adaptation of the TCA based EDAM, can be found in Section B.9.2.

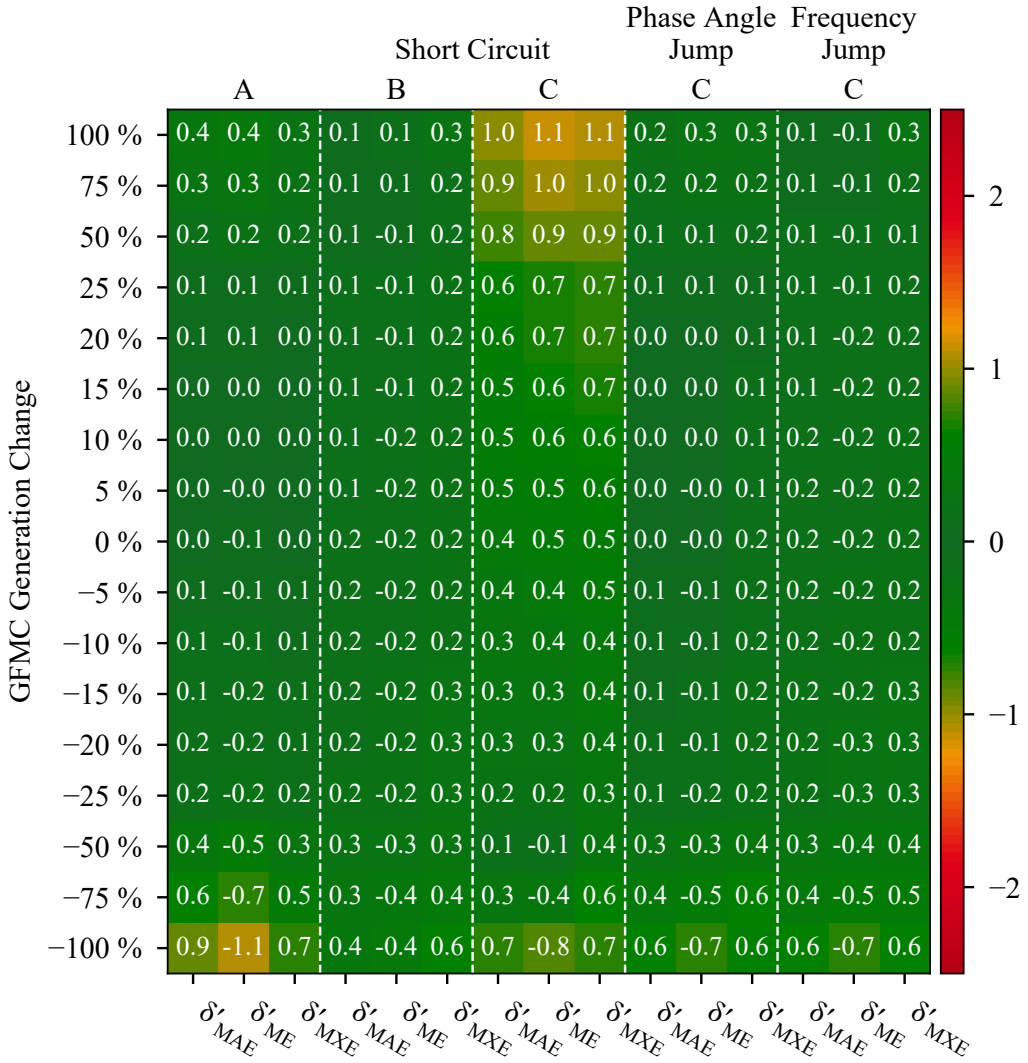

Figure 5.44: *GFMC generation scenarios*: validity evaluation of adapted STCA based EDAM for different GFMC generation scenarios in the detailed network; values show worst validation results of both active and reactive power deviation

5.5.4 Evaluation of Voltage Sensitivities

For a good STCA based EDAM performance, it is essential to achieve an optimal parameterization of the equivalent impedances. The goal is to match the voltage sensitivities at the PCC of the equivalent GFMC compared to the voltage sensitivities at the PCC of the GFMC in the detailed network. Nevertheless, the equivalent impedances were left unaltered for both load and GFMC generation change scenarios. Figure 5.45 and Figure 5.46 compare the voltage sensitivities at the PCC of all six equivalent GFMC with the voltage sensitivities at the PCC of all six GFMC in the detailed network for the different load and GFMC generation scenarios. In Figure 5.45, the voltage sensitivity deviations are shown for the operating point dependency evaluation, i.e., the EDAM is parameterized to the base scenario, whereas the detailed network is changed according to the scenario.

It can be seen that deviations for the load change scenarios are within $\pm 5\,\%$, an error margin that was found suitable for valid STCA based EDAM (Section 4.2.2). Nevertheless, validation was failed for most of the load scenarios (Figure 5.37), since the steady-state power flow at the boundary bus was not matching for the load scenarios anymore due to the power offset that was caused by the load operating point changes. This offset can be considered in the EDAM by changing the equivalent load according to the scenario. As opposed to that, a GFMC generation change directly influences the voltage sensitivities at the corresponding PCC. Therefore, the higher the deviation of GFMC generation compared to the base scenario, the higher the voltage sensitivity deviations between the EDAM and detailed network. This leads to deviations higher or lower than $\pm 5\,\%$.

Figure 5.46 shows the voltage sensitivity deviations between the adapted EDAM and the corresponding detailed network of the respective load and GFMC generation scenario. It can be seen that voltage sensitivity deviations for load change scenarios of $50\,\%$ and higher are outside the range of $\pm 5\,\%$. Also, the voltage sensitivity deviations of the $-100\,\%$ load change scenario is higher than $5\,\%$. Nevertheless, the validation threshold was not exceeded only in the load change scenarios of $\pm 25\,\%$. The adaption of the equivalent GFMC generation to the respective scenarios results in similar voltage sensitivities at the PCC of the equivalent GFMC compared to the GFMC's PCC in the detailed network for all considered scenarios. Nevertheless, GFMC generation change scenarios of $\pm 100\,\%$ lead to validation violations.

It can be concluded that the adaptation of equivalent GFMC generation to respective operating point changes results in an adaptation of the voltage sensitivities at their PCC. Also, voltage sensitivity deviations alone are not suitable as an indicator for evaluating the EDAM validity.

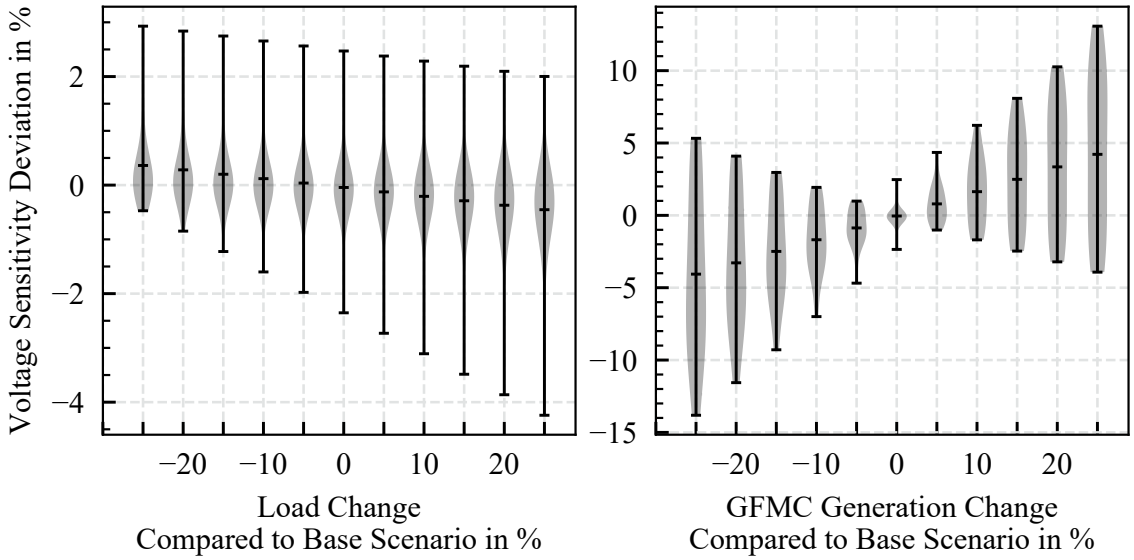

Figure 5.45: Operating Point Dependency: Deviation of voltage sensitivities at PCC of all equivalent GFMC in the EDAM (parameterized to base scenario) compared to the corresponding voltage sensitivities in the detailed network of different load and GFMC generation scenarios

5.6 Model Complexity Evaluation

In the following section, the model complexity of the different EDAM created for the scenarios in Section 5.4 is evaluated and put into relation to its validity. Here, the model complexity is defined as the simulation time and the number of nodes. For comparison purposes, the error metrics of Section 5.2 are redefined to new accuracy indicators. The total time range for analyzing the simulation time is from -5 s to 5 s.

It is important to mention that the number of nodes is not strongly related to the simulation time. It is rather a parameter to assess the size of the model. The simulation time is, amongst others, mainly related to the number of components with dynamic control models. This work considers loads as constant impedances (Section 3.1). Hence, the only components with dynamic control in the ADN are the generators, i.e., GFLC and GFMC. A comparison between different scenarios to assess the dependency of the simulation time can be found in the appendix in Section B.10.

In Table 5.11, the reduction of the EDAM complexity in terms of simulation time and number of nodes in relation to the corresponding detailed network model is investigated. This table is divided into the different scenarios introduced in Section 5.1. The scenarios *DINGO8*, *DINGO20*, and *DINGO15* comprise two different STCA based EDAM. An EDAM in which

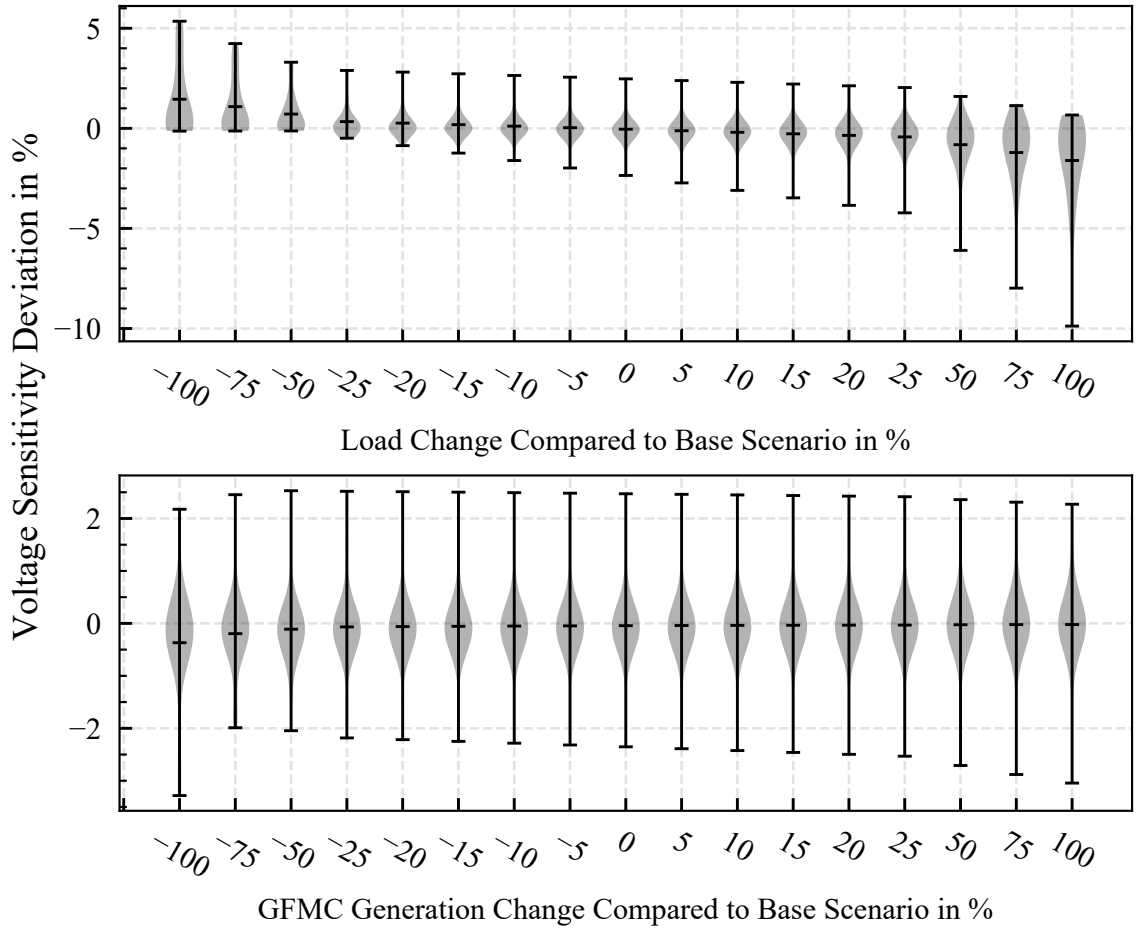

Figure 5.46: Operating Point Adaptation: Deviation of voltage sensitivities at PCC of all equivalent GFMC in the adapted EDAM compared to the corresponding voltage sensitivities in the detailed network of different load and GFMC generation scenarios

the number of GFMC in the detailed network is the same as the equivalent GFMC and an EDAM that comprises less equivalent GFMC than the GFMC in the detailed network. The short circuit as the most severe fault was utilized to evaluate the simulation time. It is important to mention that nodes considered to be part of a component are not taken into account for this evaluation, e.g., due to the LCL filter, the PWM component, and the DC voltage source, the GFMC component comprises multiple nodes which are not considered when counting the number of nodes in the network model.

The reduction in the number of nodes and simulation time is significant for all EDAM of all scenarios. In the TCA based EDAM, all GFMC of the detailed network are aggregated to one equivalent GFMC. This leads to few components in the EDAM and, therefore, to a speedy simulation up to 1 % of the detailed network's simulation time in the scenario *SimBench10* or

Table 5.11: Model complexity of EDAM exposed to a short circuit fault

Scenario	**Distribution Network Model**		**Simulation Time** relative
	Aggregation Method	Number of Nodes	to the Detailed Model
DINGO6	None (Detailed Model)	195	100 %
	TCA	2	2 %
	STCA	7	6 %
SimBench10	None (Detailed Model)	114	100 %
	TCA	2	1 %
	STCA	11	5 %
DINGO8	None (Detailed Model)	195	100 %
	TCA	2	2 %
	STCA *4 GFMC*	5	5 %
	STCA *8 GFMC*	9	8 %
DINGO20	None (Detailed Model)	195	100 %
	TCA	2	2 %
	STCA *5 GFMC*	6	3 %
	STCA *20 GFMC*	24	10 %
DINGO15	None (Detailed Model)	195	100 %
	TCA	2	1 %
	STCA *4 GFMC*	5	4 %
	STCA *15 GFMC*	26	5 %

DINGO15. Also, all equivalent components are connected to the same node. Together with the LV node of the equivalent transformer this leads to two nodes in the EDAM aggregated by TCA.

The STCA based EDAM with less equivalent GFMC than the GFMC in the detailed network reduces the complexity significantly. In the scenarios *DINGO8*, *DINGO20*, and *DINGO15* the GFMC were aggregated to four and five, respectively, equivalent GFMC clusters resulting in five and six, respectively, nodes in the EDAM. The low number of equivalent components also reduces the simulation time up to 3 % of the detailed network's simulation time.

When all GFMC of the detailed network are considered in the STCA based EDAM, the number of nodes is higher than the other EDAM. Considering the network's topology ne-

cessitates implementing branch nodes connecting three or more branches in the EDAM. To this end, the EDAM of scenario *DINGO20* comprising 20 GFMC consists of 24 nodes due to three branch nodes (Figure 5.26). The increased number of equivalent components compared to the other EDAM causes a slower simulation. However, the STCA based EDAM's complexity reduction is significant compared to the detailed network's number of nodes and simulation time.

In the following paragraphs the model complexity is put into relation to the model validity. In order to enable a comparison between number of nodes, simulation time, and the validation results, the error metrics of the validation procedure (Section 5.2) δ_{MAE}, δ_{ME}, and δ_{MXE} of each scenario are modified to new accuracy indicators $\nu_{\mathrm{P\_MAE}}$, $\nu_{\mathrm{P\_ME}}$, $\nu_{\mathrm{P\_MXE}}$, $\nu_{\mathrm{Q\_MAE}}$, $\nu_{\mathrm{Q\_ME}}$, and $\nu_{\mathrm{Q\_MXE}}$. These accuracy indicators indicate the average deviation in percentage of the respective error metric per scenario from the detailed network. Here, the value 100 % means that the EDAM matches the detailed network completely for the specific error metric. For example the accuracy indicator

$$\nu_{\mathrm{P\_MAE}} = 90\,\% \tag{5.7}$$

indicates the average active power error metric δ_{MAE} of one scenario is 10 %. Hence, the EDAM matches the detailed network by 90 % for this specific accuracy indicator.

The derivation of the new accuracy indicators is introduced in the following. As explained in Section 5.2, phase angle and frequency jump simulation results are divided into a pre-event and post-event phase, whereas the results for the short circuit fault are categorized in a pre-fault, fault, and post-fault period. For each period and for each event there is one corresponding active and reactive power error metric δ_{MAE}, δ_{ME}, and δ_{MXE}. Hence, each active or reactive power deviation error metric is calculated seven times per event ($N = 7$). For comparing the scenarios introduced in Section 5.1, these seven metrics can be put into a vector. As an example, the vector $\vec{\delta}_{\mathrm{P\_MAE}}$ is represented by the individual active power error

metric δ_{MAE} per event and period, that is,

$$\vec{\delta}_{\text{P\_MAE}} = \begin{pmatrix} |\delta_{\text{P\_MAE\_ph\_A}}| \\ |\delta_{\text{P\_MAE\_ph\_C}}| \\ |\delta_{\text{P\_MAE\_fr\_A}}| \\ |\delta_{\text{P\_MAE\_fr\_C}}| \\ |\delta_{\text{P\_MAE\_sc\_A}}| \\ |\delta_{\text{P\_MAE\_sc\_B}}| \\ |\delta_{\text{P\_MAE\_sc\_C}}| \end{pmatrix}, \tag{5.8}$$

where

$\delta_{\text{P\_MAE\_ph\_A}}$: pre-event (A) active power (P) δ_{MAE} of the phase angle jump (ph),
$\delta_{\text{P\_MAE\_ph\_C}}$: post-event (C) active power (P) δ_{MAE} of the phase angle jump (ph),
$\delta_{\text{P\_MAE\_fr\_A}}$: pre-event (A) active power (P) δ_{MAE} of the frequency jump (fr),
$\delta_{\text{P\_MAE\_fr\_C}}$: post-event (C) active power (P) δ_{MAE} of the frequency jump (fr),
$\delta_{\text{P\_MAE\_sc\_A}}$: pre-fault (A) active power (P) δ_{MAE} of the short circuit (sc),
$\delta_{\text{P\_MAE\_sc\_B}}$: fault (B) active power (P) δ_{MAE} of the short circuit (sc),
$\delta_{\text{P\_MAE\_sc\_C}}$: post-fault (C) active power (P) δ_{MAE} of the short circuit (sc).

Since δ_{ME} is the only metric that can have negative values, only the absolute values are relevant here. The error metrics of each vector are summed up, and the average deviation is calculated. This average is normalized such that the value 100 % means the EDAM matches the detailed network perfectly for the respective error metric in average. The resulting accuracy indicator $\nu_{\text{P\_MAE}}$ is defined as

$$\nu_{\text{P\_MAE}} = \begin{cases} \left(1 - \frac{\sum_{i=1}^{N} \vec{\delta}_{\text{P\_MAE}}(i)}{N}\right) \cdot 100\,\%, & \text{if } \frac{\sum_{i=1}^{N} \vec{\delta}_{\text{P\_MAE}}(i)}{N} \leq 1, \\ 0\,\%, & \text{otherwise,} \end{cases} \tag{5.9}$$

where $\vec{\delta}_{\text{P\_MAE}}(i)$ is the vector of (5.8) containing the respective error metric δ_{MAE} of the three faults phase angle jump, frequency jump, and short circuit, and N is the length of the vector, i.e., seven.

The other accuracy indicators $\nu_{\text{P\_ME}}$, $\nu_{\text{P\_MXE}}$, $\nu_{\text{Q\_MAE}}$, $\nu_{\text{Q\_ME}}$, and $\nu_{\text{Q\_MXE}}$ are calculated accordingly with the vectors $\vec{\delta}_{\text{P\_ME}}(i)$, $\vec{\delta}_{\text{P\_MXE}}(i)$, $\vec{\delta}_{\text{Q\_MAE}}(i)$, $\vec{\delta}_{\text{Q\_ME}}(i)$, and $\vec{\delta}_{\text{Q\_MXE}}(i)$, re-

spectively. The indices P and Q indicate an error metric corresponding to active and reactive power deviation, respectively.

The active and reactive power error metrics δ_{MAE}, δ_{ME}, and δ_{MXE} are set in relation to the active and reactive power demand of the detailed network P_0 and Q_0, respectively (Section 5.2). Hence,

$$\delta_{\mathrm{MAE}} = 1 \tag{5.10}$$

of the active power in the scenario *DINGO6* means that the mean absolute error equals 40 MW, i.e., the detailed network's total active power demand. Therefore, it is clear that for significant deviations the expression

$$\frac{\sum_{i=1}^{N} \vec{\delta}_{\mathrm{P\_MAE}}(i)}{N} \tag{5.11}$$

can reach values higher than one. Nevertheless, for this qualitative accuracy comparison of the EDAM within the scenarios it is sufficient to limit the maximum average deviation to one. Hence, (5.9) is a conditional expression limiting the minimum value to 0 %.

In Figure 5.47, the model complexity, i.e., simulation time and number of nodes, is compared to the six accuracy indicators as introduced in (5.9). The simulation time and the number of nodes are normalized such that 100 % is the simulation time and the number of nodes, respectively, of the detailed network. Each plot is related to one of the scenarios introduced in Section 5.1. Since this evaluation is qualitative, for quantitative results, it is recommended to check the validation results in the respective section in Section 5.4 and the model complexity listed in Table 5.11.

As the detailed network is the reference for the normalization, all parameters of Figure 5.47 in all scenarios equals 100 % and are plotted for benchmarking purposes. Two EDAM were considered in the *DINGO6* and *SimBench10* scenario: TCA based EDAM and the STCA based EDAM with the same amount of equivalent GFMC compared to the GFMC in the detailed network. The differences between these two EDAM in the model complexity, i.e., simulation time and the number of nodes, are hardly visible in the plot of scenario *DINGO6*. Nevertheless, the TCA based EDAM shows significantly worse validation results for the accuracy indicators $\nu_{\mathrm{P\_MXE}}$, $\nu_{\mathrm{Q\_MAE}}$, $\nu_{\mathrm{Q\_ME}}$, and $\nu_{\mathrm{Q\_MXE}}$. In contrast, the STCA based EDAM deviates hardly from the detailed network for any accuracy indicator.

The results of the scenario *SimBench10* can be interpreted similarly. Here, the simulation time and the number of nodes of the STCA based EDAM are slightly higher than the TCA based EDAM complexity. However, this model complexity reduction of the TCA based

EDAM results in a notable deviation from the detailed network for the accuracy indicators $v_{\text{P\_MXE}}$, $v_{\text{Q\_MAE}}$, $v_{\text{Q\_ME}}$, and $v_{\text{Q\_MXE}}$. The STCA based EDAM is very close to 100 % for all accuracy indicators except $v_{\text{Q\_MXE}}$, where a slight deviation can be observed.

The scenarios *DINGO8*, *DINGO20*, and *DINGO15* comprise three EDAM: TCA based EDAM and two STCA based EDAM. The first STCA based EDAM has the same number of equivalent GFMC compared to the number of GFMC in the detailed network. In the second STCA based EDAM the GFMC of the detailed network are aggregated to a fewer number of equivalent GFMC. Minor differences in the model complexity can be observed between the three EDAM for these three scenarios. STCA based EDAM with the same amount of equivalent GFMC compared to the GFMC in the detailed network has the highest model complexity, especially in the scenarios *DINGO20* and *DINGO15*. On the other hand, the STCA based EDAM with the aggregated GFMC, i.e., less equivalent GFMC than the GFMC in the detailed network, has a similar model complexity than the TCA based EDAM.

More severe differences between the three EDAM can be observed for the accuracy indicators. In the scenario *DINGO8*, the TCA based EDAM deviates significantly from the detailed network for the indicators $v_{\text{P\_MXE}}$ and $v_{\text{Q\_MAE}}$. The indicator $v_{\text{Q\_MXE}}$ even reaches 0 %. The STCA based EDAM with aggregated GFMC also deviates notably from the detailed network for the indicators $v_{\text{P\_MXE}}$, $v_{\text{Q\_MAE}}$, $v_{\text{Q\_ME}}$, and $v_{\text{Q\_MXE}}$. Nevertheless, the deviations are less distinct compared to the TCA based EDAM for the indicators $v_{\text{P\_MAE}}$, $v_{\text{P\_ME}}$, $v_{\text{P\_MXE}}$, and $v_{\text{Q\_MXE}}$. The STCA based EDAM with the same amount of equivalent GFMC compared to the GFMC in the detailed network deviates slightly from the detailed network for the reactive power indicators.

Also, the TCA based EDAM of scenario *DINGO20* deviates markedly from the detailed network for all accuracy indicators, especially for $v_{\text{P\_MXE}}$, $v_{\text{Q\_MAE}}$, $v_{\text{Q\_ME}}$, and $v_{\text{Q\_MXE}}$. The latter even reaches 0 %. The STCA based EDAM with less aggregated GFMC than GFMC in the detailed network deviates less from the detailed network than the TCA based EDAM. However, similar to scenario *DINGO8*, the parameters $v_{\text{P\_MXE}}$, $v_{\text{Q\_MAE}}$, $v_{\text{Q\_ME}}$, and $v_{\text{Q\_MXE}}$ indicate a notable deviation. As opposed to that, the EDAM aggregated by STCA considering an individual representation of all GFMC in the detailed network deviates only somewhat from the detailed network for all reactive power indicators, but especially for $v_{\text{Q\_MXE}}$.

The voltage sensitivity clustering of GFMC in the scenarios *DINGO8* and *DINGO20* without any constraints results in the aggregation of non-neighboring GFMC. Hence, the detailed network's topology cannot be considered in the connection of the aggregated equivalent GFMC. This is different for the EDAM of scenario *DINGO15*, in which only neighboring GFMC of

one network branch are aggregated and the detailed network's topology is considered. Here, only minor deviations between the two STCA based EDAM can be observed for the accuracy indicators, whereas the model complexity is higher for the EDAM in which no GFMC of the detailed network is aggregated. The TCA based EDAM also fails to reproduce the detailed network's dynamic behavior especially for the reactive power accuracy indicators $\nu_{\text{Q\_MAE}}$, $\nu_{\text{Q\_ME}}$, and $\nu_{\text{Q\_MXE}}$.

Assessing the qualitative deviations of the EDAM from the detailed network for each scenario, as shown in Figure 5.47, it becomes clear that all EDAM reduce the model complexity markedly. The higher the number of GFMC in the detailed network, the higher the STCA based EDAM's model complexity that considers each GFMC individually. Nevertheless, this higher EDAM complexity has to be put in relation to the reasonably accurate representation of the detailed network's dynamic behavior. Unless multiple GFMC are in one branch of the network allowing the aggregation of neighboring GFMC, the STCA based EDAM with aggregated equivalent GFMC deviates significantly from the detailed network. Also, the TCA based EDAM reduces the model complexity the most, but cannot capture the dynamic behavior of the detailed network for both considered network scenarios.

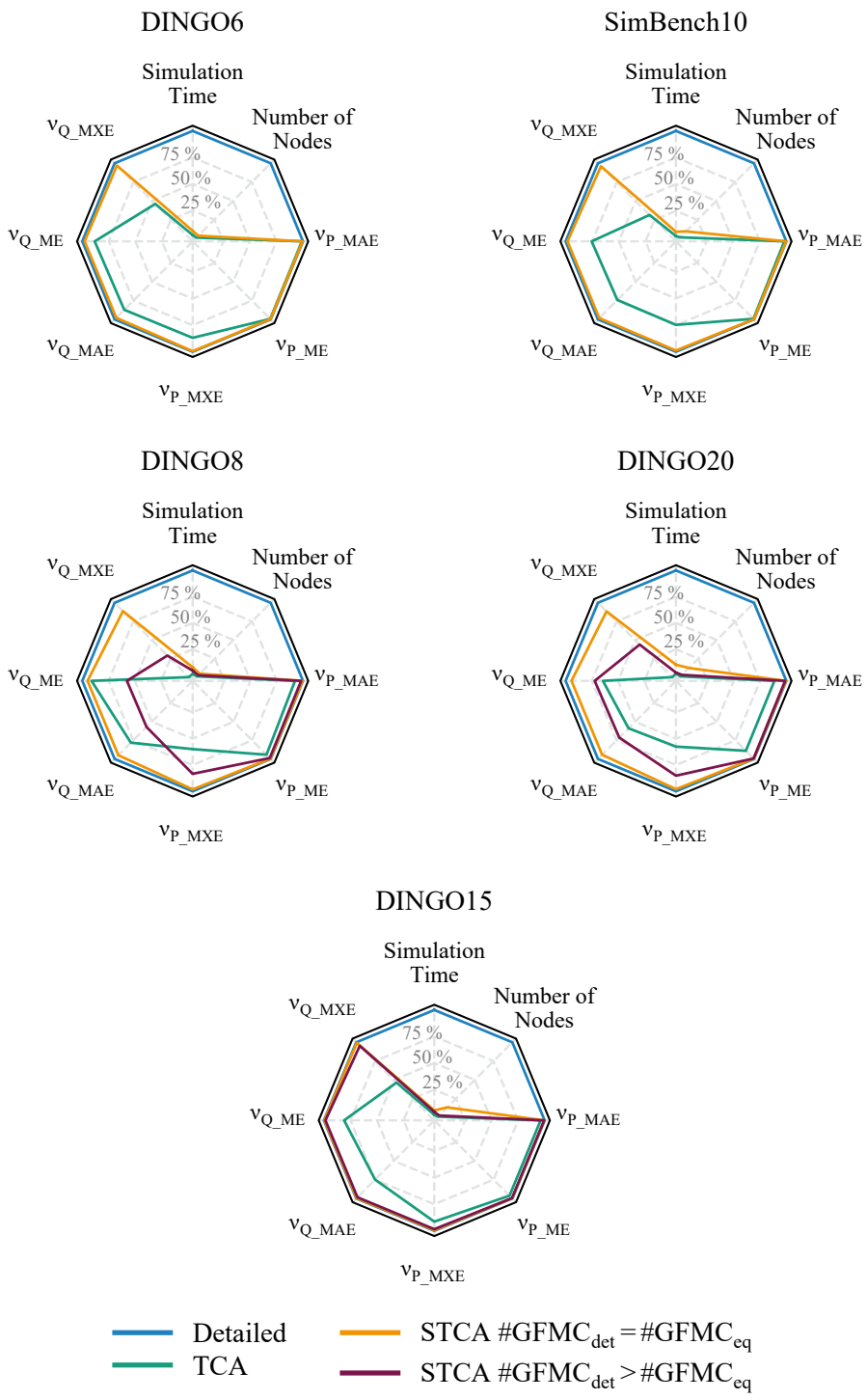

Figure 5.47: Comparison of model complexity, i.e., simulation time and number of nodes, and model validity of the scenarios described in Section 5.4 (*DINGO6, SimBench10, DINGO8, DINGO20, DINGO15*)

5.7 Summary

This section evaluates the performance of the proposed STCA in five different scenarios, varying the number of GFMC in the network to be aggregated and the topologies. Three different faults are simulated, and the results of the EDAM are compared with the results obtained from the detailed network. A validation procedure that is appropriate for the EDAM performance assessment is applied to check the validity of the EDAM.

Figure 5.48 shows a summary of all validation results evaluated in Section 5.4. To this end, for each aggregation method, all normalized error metric values as introduced in Section 5.5 of all periods (pre-event, event, and post-event), all the three events (phase angle jump, frequency jump, and short circuit), and all scenarios (*DINGO6, SimBench10, DINGO8, DINGO20*, and *DINGO15*) are presented in a violin plot. The aggregation methods are divided into TCA and STCA. The latter is subdivided in EDAM with the same number of equivalent GFMC compared to the number of GFMC in the detailed network, and in EDAM with less equivalent GFMC than the GFMC in the detailed network. This subdivision refers to the scenarios *DINGO8, DINGO20*, and *DINGO15*. However, only in the scenario *DINGO15*, the detailed network's topology is considered in the EDAM since only neighboring GFMC of one branch are aggregated.

The density of all active power deviations indicates significant validation violations of the EDAM aggregated by TCA. Also, the STCA based EDAM, in which fewer equivalent GFMC are considered compared to the number of GFMC in the detailed network, fails the validation in some cases. On the other hand, the active power deviations of the STCA based EDAM with the same amount of equivalent GFMC compared to the GFMC in the detailed network do not exceed any threshold values for all scenarios considered in Section 5.4.

The EDAM aggregated by TCA fails the reactive power validation to a greater extent than active power validation. Similarly, the STCA based EDAM with less GFMC in the EDAM than the GFMC in the detailed network fails the validation in multiple cases. If the same number of equivalent GFMC is considered in the EDAM compared to the number of GFMC in the detailed network, the STCA based EDAM performs significantly better. However, some validation violations can be observed for the post-fault period of the short circuit fault. The error metric δ'_{MXE} in the scenario *DINGO8* as well as the metrics δ'_{ME} and δ'_{MXE} in the scenario *DINGO20* exceed the allowed threshold.

It can be concluded that the active power deviations are less distinct in all EDAM compared to the respective reactive power deviations. Also, considering all the detailed network's GFMC in the EDAM improves the accuracy of the same significantly. However, the scenario

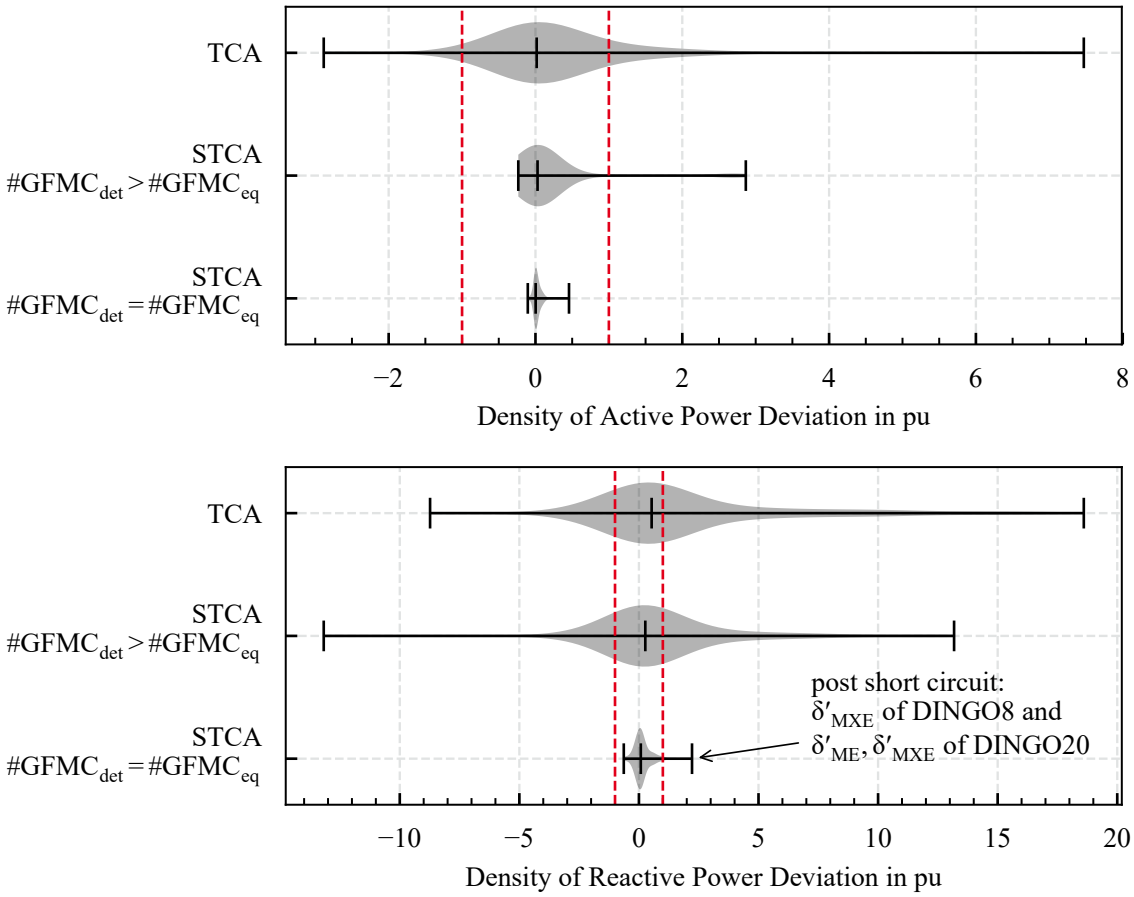

Figure 5.48: Violin plots of active and reactive power deviation per EDAM (aggregated by TCA and STCA with different number of equivalent GFMC); consideration of all normalized error metrics (δ'_{MAE}, δ'_{ME}, δ'_{MXE}), all time periods (pre-event, event, post-event) of the three events (phase angle jump, frequency jump, short circuit), and all scenarios described in Section 5.4 (*DINGO6, SimBench10, DINGO8, DINGO20, DINGO15*)

DINGO15 shows that an aggregation of only neighboring GFMC of one branch results in a valid STCA based EDAM.

Furthermore, the dependency of the STCA based EDAM of scenario *DINGO6* on the operating point as well as its adaptation is evaluated in this chapter. The results show that the EDAM is still valid if the total load of the detailed network changes by $-10\,\%$ to $10\,\%$ compared to the operating point the EDAM was parameterized to. Similarly, a total GFMC generation change in the detailed network of $-5\,\%$ does not influence the EDAM's validity.

The EDAM can be adapted to new load or GFMC generation operating points by changing the nominal values of the equivalent load or the equivalent GFMC, including a re-parameterization of the LCL output filter. Such a simplified update of the EDAM is valid for load changes ranging from $-25\,\%$ to $25\,\%$ and for GFMC generation changes ranging from $-75\,\%$ to $75\,\%$.

It is important to mention that the evaluation of the operating point dependency and adaptation considers one ADN model with a specific operating point for the base scenario, e.g., CBG penetration or GFMC share. In order to obtain generally valid statements, future work should conduct this evaluation in different ADN models with different base operating points. Also, this work considers load and GFMC generation changes in discrete steps. Scenarios with operating point changes in between these discrete steps should be simulated in future work.

Chapter 6

Conclusion

6.1 Summary and Main Contributions

The main objective of this thesis is to develop a methodology for creating EDAM of CBG dominated distribution networks, including GFMC, that can be applied in stability studies. A review of state-of-the-art methods for creating EDAM is conducted first, resulting in an overview of different categorizations of the methods found in the literature. Based on these, this work proposes a categorization focusing on EDAM for stability studies of future CBG dominated power systems. Mainly parameter identification based gray-box models created by utilizing clustering techniques are found to be the most suitable methods since it is assumed that the network model to be aggregated is known for stability studies of future power systems. It is found that the Technology-Control-Clustered Approach (TCA) is the most promising method for aggregating networks dominated by GFLC.

Then, the challenges of considering GFMC in EDAM are investigated. The dynamic active and reactive power injection of GFMC highly depends on the location of the GFMC within the network, i.e., the grid's strength and state at the PCC of the GFMC. However, these factors cannot be considered in the TCA. The voltage sensitivities $\vec{s}_i$ at the PCC of each GFMC i in the detailed network are found to be suitable parameters for considering these factors that influence the GFMC's dynamic behavior.

To better understand the components that should be considered in the EDAM, their modeling is described in a separate section. Loads are modeled as constant impedance loads and GFLC as PV systems with two different control strategies. GFMC are modeled with a cascaded inner and outer control loop. The inner control loop comprises a current and voltage control, including current limitation. The outer control loop is based on a droop concept.

Based on the findings, this work proposes the Sensitivity-Technology-Control-Clustered Approach (STCA) as a further TCA development. The main idea is the matching of voltage sensitivities at the PCC of each GFMC in the EDAM to the ones of the detailed network by parameterizing corresponding equivalent impedances accordingly. The consideration of the detailed network's topology in the EDAM creation process, specifically in the connection of the equivalent GFMC, is crucial for the accuracy of the EDAM. Hence, an individual consideration of the GFMC in the EDAM allows the connection of the equivalent GFMC according to the detailed network's topology. An aggregation of multiple GFMC to one equivalent GFMC should only be conducted if the detailed network's topology can be considered with the aggregated GFMC, i.e., only neighboring GFMC of one network branch should be aggregated to an equivalent GFMC. Otherwise, aggregating GFMC should be avoided if the increase in model complexity can be accepted.

An evaluation of five different scenarios shows the STCA based EDAM's accuracy by applying a suitable validation procedure. Scenarios differ in network topology, number of GFMC in the detailed network, and number of GFMC in the EDAM. Also, the TCA is applied on the respective test networks for benchmarking purposes, and results are compared with the EDAM aggregated by STCA. The most accurate reproduction of the detailed ADN's dynamic behavior is achieved with the STCA based EDAM that considers each GFMC of the detailed network individually in the EDAM. STCA based EDAM with less equivalent GFMC than the number of GFMC in the detailed network are less complex. Nevertheless, aggregating non-neighboring GFMC to one equivalent GFMC show significant validity drawbacks of the resulting EDAM. Similarly, EDAM aggregated by TCA are less complex, but the validity drawbacks are disproportionate.

The simulation of different scenarios is an essential part of stability studies. Therefore, the STCA based EDAM dependency on the operating point is investigated to avoid the need to derive a completely new EDAM for each scenario. To this end, based on a base scenario, the total load and GFMC generation in the detailed network are changed, while the EDAM parameters still correspond to the base scenario. Here, only a slight change in the total load and almost no GFMC generation change are allowed to keep the EDAM within validation limits. Hence, a simplified adaptation of the EDAM to new operating points is proposed. Here, the active and reactive power demand of the equivalent load and the nominal power values of the equivalent GFMC are adapted according to the operating point change.

The findings of this thesis provide a validated methodology for creating EDAM. The ADN to be aggregated can be CBG dominated and comprise GFMC. Hence, the proposed STCA is suitable for application in comprehensive stability studies of future power systems. This is

not only relevant for research studies, but also for transmission system operators investigating the stability of their future system. Here, the impact of GFMC on system stability as well as the optimal GFMC integration into a system can be investigated with the proposed EDAM.

6.2 Outlook

Based on this work, future research can evaluate and develop the proposed methodology further by focusing on the following topics:

Network model

- Consideration of multiple voltage levels for aggregation: Similarly to TCA, it is suggested that the STCA can be applied for multiple voltage levels in a bottom-up way, starting with the lowest voltage level. However, the test networks in this work only comprise one voltage level. Simulations with other networks of multiple voltage levels should be conducted in future work.
- Consideration of highly meshed networks: The STCA based EDAM was validated for network topologies in which two branches are interconnected by only one line. Also, only one boundary bus as the common link between ADN and transmission system was considered. The validity of an STCA based EDAM derived from a highly meshed network with multiple interconnections between two branches and multiple boundary buses needs to be further investigated.
- Significant amount of GFMC in a network: The network considered in this work comprises a maximum of twenty GFMC. Even an individual representation of GFMC in the EDAM reduces the complexity of the detailed network markedly. This may not be true for networks with a significantly higher amount of GFMC. Such a network should be evaluated with the goal of a maximum reduction of equivalent GFMC.
- Large-scale model: A network model comprising a transmission system and multiple ADN models, which are aggregated to EDAM, should be utilized, e.g., to investigate the influence of GFMC on the transmission system stability.

Different clustering criteria for ADN without GFMC

- Clustering according to voltage sensitivities of voltage-dependent GFLC control: The focus of this work was the consideration of GFMC in the EDAM. In a TCA based

EDAM, the dynamic behavior of GFLC is reproduced well. Nevertheless, with the neglect of local voltage differences at the PCC of GFLC, some drawbacks in the EDAM accuracy are accepted. Future work could analyze the advantages of a voltage sensitivity clustering of GFLC with voltage-dependent control.

- Clustering according to actual voltage values of voltage-dependent GFLC control: Besides a voltage sensitivity based clustering, clustering according to actual voltages at the PCC of GFLC with voltage-dependent control could be investigated.
- Clustering according to voltage reserve of voltage-dependent GFLC control: A clustering according to the voltage reserve, i.e., the difference from the actual voltage level at the PCC to the threshold value, should be considered. This is interesting, especially for capturing partial tripping of GFLC.
- Clustering according to voltage sensitivities of synchronous machines: GFMC emulate the inertia of synchronous machines. Hence, the dependencies of the dynamic behavior of synchronous machines are similar to the ones of GFMC. The performance of an STCA based EDAM with a voltage sensitivity based clustering of synchronous machines should be investigated. Such an EDAM can be helpful for aggregating networks with small distributed synchronous machines, e.g., hydropower plants or synchronous machine based loads.

Coherency based approaches for GFMC consideration in EDAM

Coherency based approaches utilize rotor angle swings of synchronous generators to find coherent generators that can be aggregated. Since GFMC emulate the dynamic behavior of synchronous machines, such an approach could be applied to find coherent GFMC. Similar internal angles of GFMC could be utilized to find coherent GFMC that can be aggregated.

EDAM update

Interpolation between discrete operating points: The operating point changes have discrete steps of $\pm 5\,\%$ or more. Operating point changes in between this range could be considered to find the actual limits of the simplified EDAM update.

Appendix A

Network and Component Parameters

A.1 Network Parameters

In the following section, detailed parameters for the networks introduced in Section 5.3 are provided.

Table A.1: Subtransmission line parameters of transmission line according to [Str+14]

Parameter	**Value**
Phases	3
Parallel Lines	2
Length	50 km
Rated Voltage	230 kV
Rated Current	5 kA
Positive Sequence Resistance	0.02 $\frac{\Omega}{\text{km}}$
Positive Sequence Reactance	0.09 $\frac{\Omega}{\text{km}}$
Positive Sequence Susceptance	0.00 $\frac{\Omega}{\text{km}}$
Zero Sequence Resistance	0.23 $\frac{\Omega}{\text{km}}$
Zero Sequence Reactance	1.46 $\frac{\Omega}{\text{km}}$
Zero Sequence Susceptance	1.50 $\frac{\Omega}{\text{km}}$

Table A.2: Line types of DINGO network [Amm+18]

Name	**Resistance in** Ω/km	**Inductance in** mH/km	**Capacitance in** $\mu\mathrm{F}/\mathrm{km}$	**Type**
NA2XS2Y 3x1x185	0.164	0.380	0.410	Cable
NA2XS2Y 3x1x240	0.125	0.360	0.470	Cable
NA2XS2Y 3x1x300	0.100	0.350	0.495	Cable
NA2XS2Y 3x1x400	0.078	0.340	0.570	Cable
NA2XS2Y 3x1x500	0.061	0.320	0.630	Cable
NA2XS2Y 3x1x150	0.206	0.401	0.240	Cable
NA2XS2Y 3x1x240	0.130	0.360	0.304	Cable
NA2XS(FL)2Y 3x1x300	0.100	0.370	0.250	Cable
NA2XS(FL)2Y 3x1x400	0.078	0.360	0.270	Cable
NA2XS(FL)2Y 3x1x500	0.060	0.340	0.300	Cable

Table A.3: Line types of SimBench network [Mei+20]

Name	**Resistance in** Ω/km	**Inductance in** mH/km	**Capacitance in** $\mu\mathrm{F}/\mathrm{km}$	**Type**
48-AL1/8-ST1A 20.0	0.594	1.184	0.009	OHL
NA2XS2Y 1x120 RM/25 12/20 kV	0.253	0.379	0.230	Cable
NA2XS2Y 1x70 RM/25 12/20 kV	0.443	0.420	0.190	Cable
NA2XS2Y 1x95 RM/25 12/20 kV	0.313	0.420	0.216	Cable

A.2 Component Parameters

A.2.1 Phase-Locked Loop

The PLL component used in this work refers to the model described in [DIg22a]. The model version three with a three-phase measurement is implemented. The PLL is parameterized as listed in Table A.4.

Table A.4: PLL parameters

Parameter	**Value**
Proportional Gain	10
Integration Gain	30
Upper Frequency Limit	1.2 pu
Lower Frequency Limit	0.8 pu

A.2.2 LCL filter parameterization

The LCL output filter of the GFMC as shown in Figure A.1 is parameterized according to [Rez+14] where

V_{DC} : DC side nominal voltage,

V_{AC} : AC side nominal phase to earth voltage,

f_{sw} : switching frequency, here 16 kHz,

f_{N} : nominal frequency, here 50 Hz,

S_{rated} : rated apparent power,

k_{a} : harmonic current relation $\frac{i_{\mathrm{g}}(h)}{i_{\mathrm{c}}(h)}$, here $\sqrt{\frac{1}{k_{\mathrm{a}}^2}} = 10$,

d : maximum power factory variation seen by the grid, here 5 %,

r : ripple of the rated current, here 10 %,

as

$$L_\mathrm{c} = \frac{V_\mathrm{DC} \cdot \sqrt{3} \cdot V_\mathrm{AC}}{6 \cdot f_\mathrm{sw} \cdot r \cdot \sqrt{2} \cdot S_\mathrm{rated}}, \tag{A.1}$$

$$C_\mathrm{f} = d \cdot \frac{S_\mathrm{rated}}{2\pi f_\mathrm{N} \cdot V_\mathrm{AC}^2}, \tag{A.2}$$

$$L_\mathrm{g} = \frac{\sqrt{\frac{1}{k_\mathrm{a}^2} + 1}}{C_\mathrm{f} \cdot (2\pi f_\mathrm{sw})^2}, \tag{A.3}$$

$$R_\mathrm{f} = \frac{1}{3 \cdot 2\pi f_\mathrm{c} \cdot C_\mathrm{f}}, \tag{A.4}$$

where the resonant frequency, that is,

$$f_\mathrm{c} = \frac{1}{2\pi} \cdot \sqrt{\frac{L_\mathrm{c} + L_\mathrm{g}}{L_\mathrm{c} \cdot L_\mathrm{g} \cdot C_\mathrm{f}}}, \tag{A.5}$$

should be in the range of

$$10 \cdot f_\mathrm{N} < f_\mathrm{c} < 0.5 \cdot f_\mathrm{sw}. \tag{A.6}$$

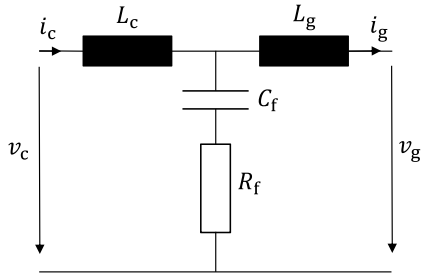

Figure A.1: One-phase equivalent circuit diagram of a LCL filter

A.2.3 GFLC: Generic Model for Large-Scale PV Plants

Table A.5: Parameters of REEC_B model (electrical controls of converter) according to [WEC14]

Parameter Name	Description	Value
PfFlag	Power Factor Flag (1: $\cos\varphi$ control; 0: Q control)	0
VFlag	Voltage Control Flag (1: Q control; 0: V control)	1
Tp	Filter Time Constant for Electrical Power Measurements in s	0.02
Kqp	Proportional Gain in pu	1
Kqi	Integral Gain in pu	0.7
QFlag	Reactive Power Control Flag (1: V control; 0: constant $\cos\varphi$ or Q control)	0
Kvp	Proportional Gain in pu	1
Kvi	Integral Gain in pu	0.7
Trv	Filter Time Constant for Voltage Measurements in s	0.02
db1	Voltage Deadband for Overvoltage i_q injection in pu	-0.05
db2	Voltage Deadband for Undervoltage i_q injection in pu	0.05
Kqv	Gain for Reactive Current Injection during Fault in pu	2
Vdip	Undervoltage Condition Trigger Voltage in pu	0.9
Vup	Overvoltage Condition Trigger Voltage in pu	1.1
Tiq	Time Constant on Lag Delay in s	0.02
Tpord	Time Constant in s	0.02
PqFlag	Priority on Current Limit Flag (1: P Priority; 0: Q Priority)	1
Imax	Maximum Allowable Total Converter Current Limit in pu	1.3
Qmin	Reactive Power Limit Minimum in pu	-0.43
Vmin	Voltage Control Minimum in pu	0.9
Iql1	Minimum Limit of Reactive Current Injection in pu	-1.1
Pmin	Minimum Power Reference in pu	0
dPmin	Ramp Rate on Power Reference in pu/s	-999
Qmax	Reactive Power Limit Maximum in pu	0.43
Vmax	Voltage Control Maximum in pu	1.1
Iqh1	Maximum Limit of Reactive Current Injection in pu	1.1
Pmax	Maximum Power Reference in pu	1
dPmax	Ramp Rate on Power Reference in pu/s	999

Table A.6: Parameters of REGC_A model (converter interface with grid) according to [WEC14]

Parameter Name	Description	Value
Tg	Converter Time Constant in s	0.02
Tfltr	Voltage Filter Time Constant in s	0.02
zerox	LVPL Zero Crossing in pu	0.4
brkpt	LVPL Breakpoint in pu	0.9
lvpl1	LVPL Gain Breakpoint in pu Current/pu Voltage	1.22
Volim	Voltage Limit for High Voltage Clamp Logic in pu	1.2
Iolim	Current Limit for High Voltage Clamp Logic in pu	-1.1
Khv	High Voltage Clamp Logic Accelerator Factor	0.7
lvpnt0	Min Low Voltage Active Current Breakpoint in pu	0.4
lvpnt1	Max Low Voltage Active Current Breakpoint in pu	0.8
Lvplsw	Low Voltage Power Logic Switch (1: Curve; 0: Zero)	1
Iqrmin	Min Reactive Current Rate Limit in pu/s	-999
Iqrmax	Max Reactive Current Rate Limit in pu/s	999
rrpwr	Active Current Rate Limit in pu/s	10

Table A.7: Parameters of protection model according to [WEC14]

Parameter Name	Description	Value
Umax1	Over Voltage Protection Threshold 1 in pu	1.1
t_Umax1	Disconnection Time for Over Voltage Range 1 in s	2
Umax2	Over Voltage Protection Threshold 2 in pu	1.2
t_Umax2	Disconnection Time for Over Voltage Range 2 in s	0.16
Umin1	Under Voltage Protection Threshold 1 in pu	0.7
t_Umin1	Disconnection Time for Under Voltage Range 1 in s	2
Umin2	Under Voltage Protection Threshold 2 in pu	0.45
t_Umin2	Disconnection Time for Under Voltage Range 2 in s	0.16
Fmax	Over Frequency Protection Threshold in Hz	51.66667
t_Fmax	Disconnection Time for Over Frequency in s	0.16
Fmin	Under Frequency Protection Threshold in Hz	47.08
t_Fmin	Disconnection Time for Under Frequency in s	0.16
Ulow	Minimum Voltage for Frequency Protection in pu	0.85
Tfblock	Frequency Protection Blocking Time after UVRT in s	0.15
Fnom	Nominal Frequency in Hz	50
TfMA	Time Interval of Moving Average Window in s	0.3
Tmax	Maximum Simulation Time Step in s	0.1

Table A.8: Voltage source reference according to [WEC14]

Parameter Name	Description	Value
Tpll	Angle Detection Time Constant in s	0.01
Xseries	Series reactance in %	10

A.2.4 GFLC: Generic Model for Distributed and Small PV Plants

Table A.9: Parameters of PVD1 model according to [WEC14]

Parameter Name	Description	Value
PqFlag	Priority on Current Limit Flag (1: P Priority; 0: Q Priority)	0
Imax	Maximum Allowable Total Converter Current in pu	1.1
Tg	Inverter Current Regulator Time Constant in s	0.02
Xc	Line Drop Compensation Reactance in pu	0
Qmx	Maximum Reactive Power in pu	0.328
Qmn	Minimum Reactive Power in pu	-0.328
v0	Low Voltage Threshold for Q(V) Control in pu	0.9
v1	High Voltage Threshold for Q(V) Control in pu	1.1
dqdv	Q(V) Droop Compensation in pu	0
vr_recov	Amount of Generation to Reconnect After Voltage Disconnection (0...1)	0.75
Vt0	Voltage Tripping Response Curve Point 0 in pu	0.7
Vt1	Voltage Tripping Response Curve Point 1 in pu	0.8
Vt2	Voltage Tripping Response Curve Point 2 in pu	1.1
Vt3	Voltage Tripping Response Curve Point 3 in pu	1.2
fr_recov	Amount of Generation to Reconnect After Frequency Disconnection (0...1)	0.5
Ft0	Frequency Tripping Response Curve Point 0 in pu	0.9416
Ft1	Frequency Tripping Response Curve Point 1 in pu	0.98
Ft2	Frequency Tripping Response Curve Point 2 in pu	1.02
Ft3	Frequency Tripping Response Curve Point 3 in pu	1.0333
fdbd	Frequency Deadband Over Frequency Rresponse in pu	0.001
Ddn	Down Regulation Droop in pu Power/pu Frequency	0

A.2.5 GFMC: Dynamic Control Model

Table A.10: Parameters of GFMC control model according to [PSS20]

Control Loop	Parameter Name	Description	Value
Droop	K_P	Active Power Droop Factor	0.005
	K_Q	Reactive Power Droop Factor	0.01
	ω_g	Frequency Set Point in pu	1
	v^*	Voltage Set Point in pu	1
	T_P	Time Constant of Active Power Droop Low-Pass Filter in s	0.1
	T_Q	Time Constant of Reactive Power Droop Low-Pass Filter in s	0.1
Voltage	K_pd	Proportional Gain d-component	1.2
	K_id	Integral Gain d-component	500
	K_pq	Proportional Gain on q-component	1.2
	K_iq	Integral Gain on q-component	500
	K_awd	Anti-Windup Gain on d-component	1
	K_awq	Anti-Windup Gain on q-component	1
Current	K_pd	Proportional Gain d-component	1
	K_id	Integral Gain d-component	200
	K_pq	Proportional Gain q-component	1
	K_iq	Integral Gain q-component	200
Virtual Impedance	R_v	Resistance in Ω	0.01
	L_v	Inductance in mH	1
PWM	v_DC	DC Voltage in kV	0.8
	v_AC	AC Voltage in kV	0.4

Appendix B

Additional Scenarios and Results

B.1 Multiple GFMC in One Network Branch

Figure B.1 refers to the simulation conducted in Section 4.3.1.

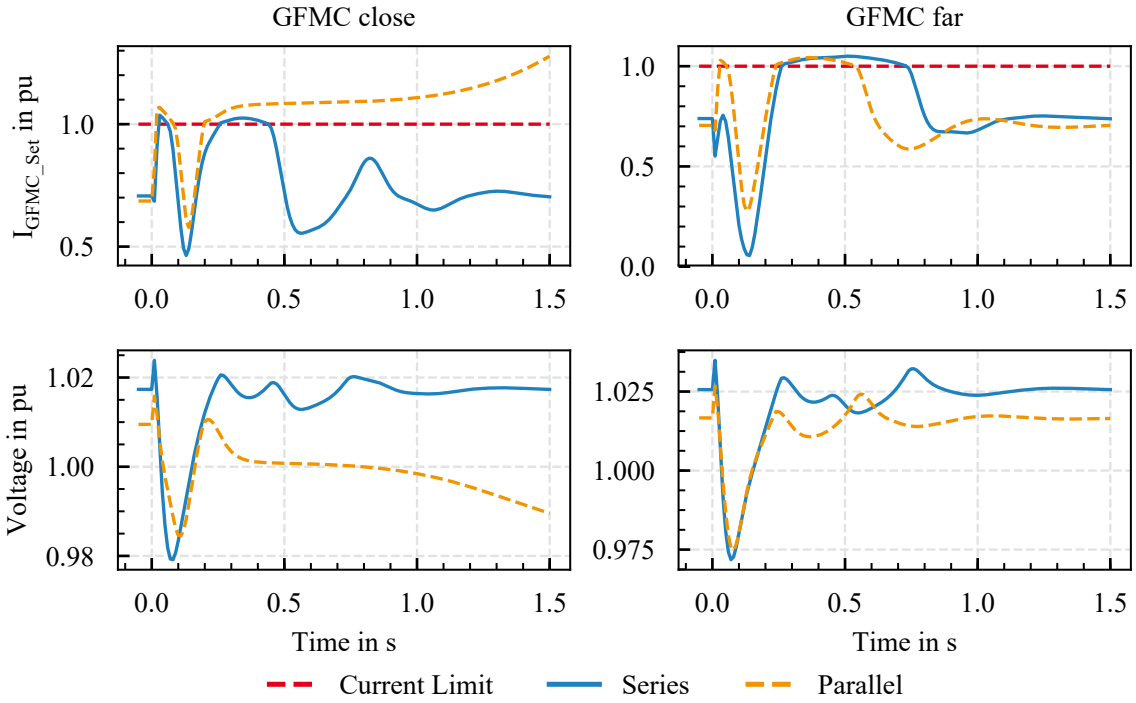

Figure B.1: Calculated set point for output current I_{GFMC_Set} of *GFMC close* and *GFMC far* and voltage at PCC of both GFMC

B.2 Scenario SimBench10: No Branch Interconnection Considered in EDAM

For this scenario, all rings of the SimBench network (Section 5.3.3) are closed. The resulting topology is shown in Figure B.2. GFMC generation data is given in Table B.1.

Table B.1: Scenario *Simbench10*: GFMC set points

GFMC	Rated Apparent Power	Active Power	Reactive Power	Maximum Current
10 GFMC	4 MVA	1.9 MW	1 Mvar	1 pu
Sum	**40 MVA**	**19.0 MW**	**10 Mvar**	

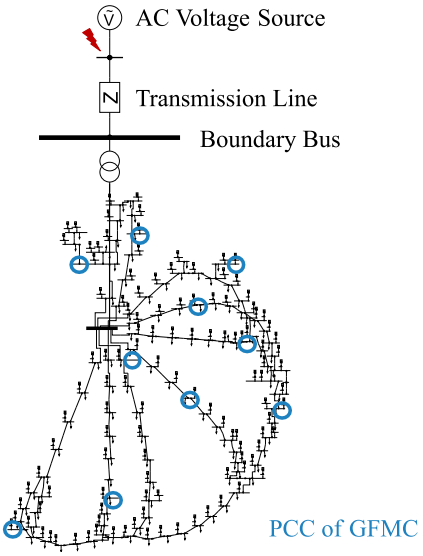

Figure B.2: Schematic of detailed network of scenario *SimBench10* with GFMC's PCC

According to Chapter 4, the closed ring topology would be reproduced in the EDAM by interconnecting branches. However, in this scenario the equivalent GFMC are connected in parallel without an interconnection, i.e., the detailed network is considered to be an open ring topology with one GFMC per branch (Figure B.3). This is opposed to the derivation process introduced. Nevertheless, this scenario wants to evaluate the simulation results, when the STCA is not properly applied.

Figure B.4 shows the calculated output current $I_{\text{GFMC\_Set}}$ of the GFMC in detailed and equivalent network model. The GFMC of all three events reach the maximum current.

In Figure B.5 it can be seen that the reactive power flow of the STCA based EDAM deviates from the reactive power flow of the detailed network model. This observation is emphasized by the validation failure of the STCA based EDAM in the time period after the phase angle jump for the error δ_{MXE} of the reactive power deviation. Nevertheless, the threshold value is only just exceeded, and all other error parameters are within the allowed limits.

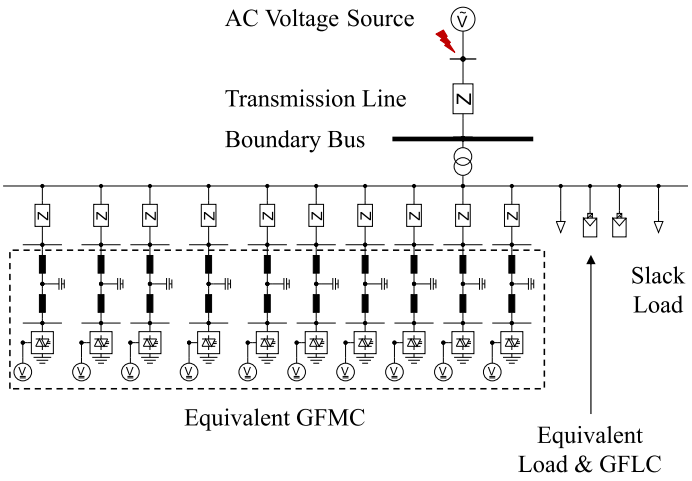

Figure B.3: Schematic of EDAM aggregated with STCA (right) of scenario *SimBench10* neglecting branch interconnections

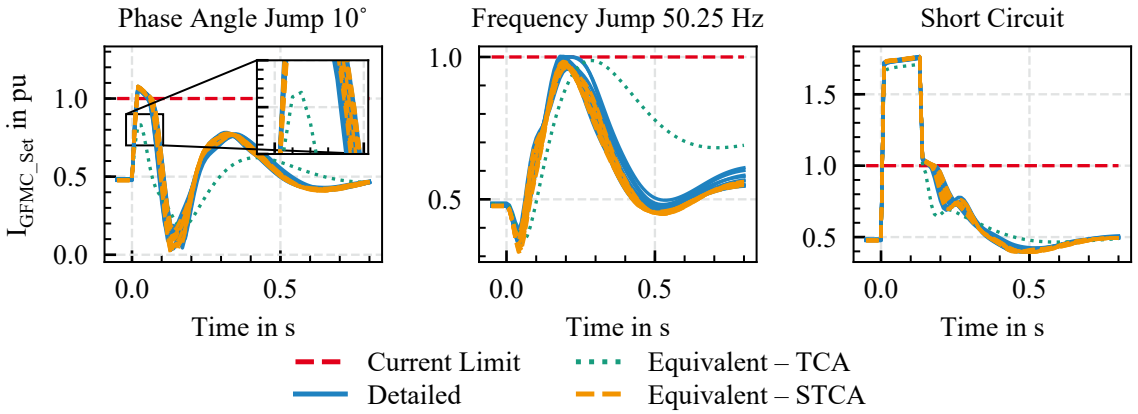

Figure B.4: Scenario *SimBench10*: calculated set point for output current of GFMC $I_{\mathrm{GFMC\_Set}}$ in detailed and equivalent network models

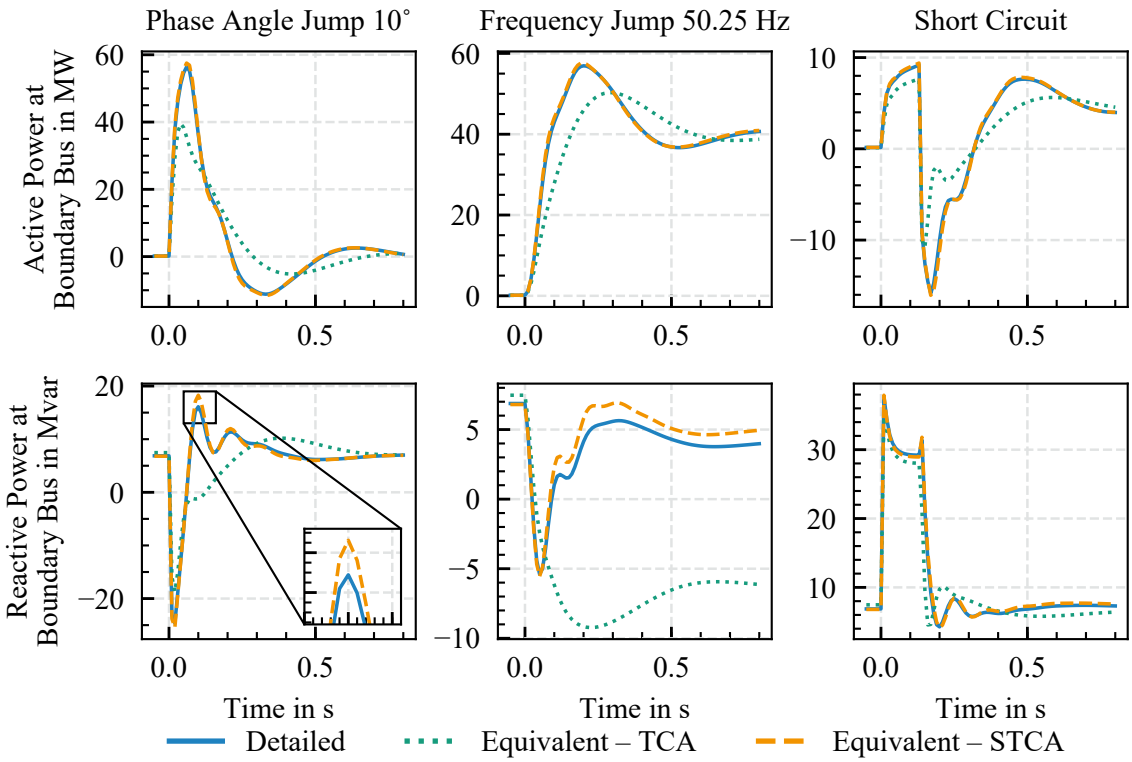

Figure B.5: Scenario *SimBench10*: active and reactive power flow at boundary bus from transmission to distribution system of detailed and equivalent network models; positive reactive power values: over-excited state; negative reactive power values: under-excited state

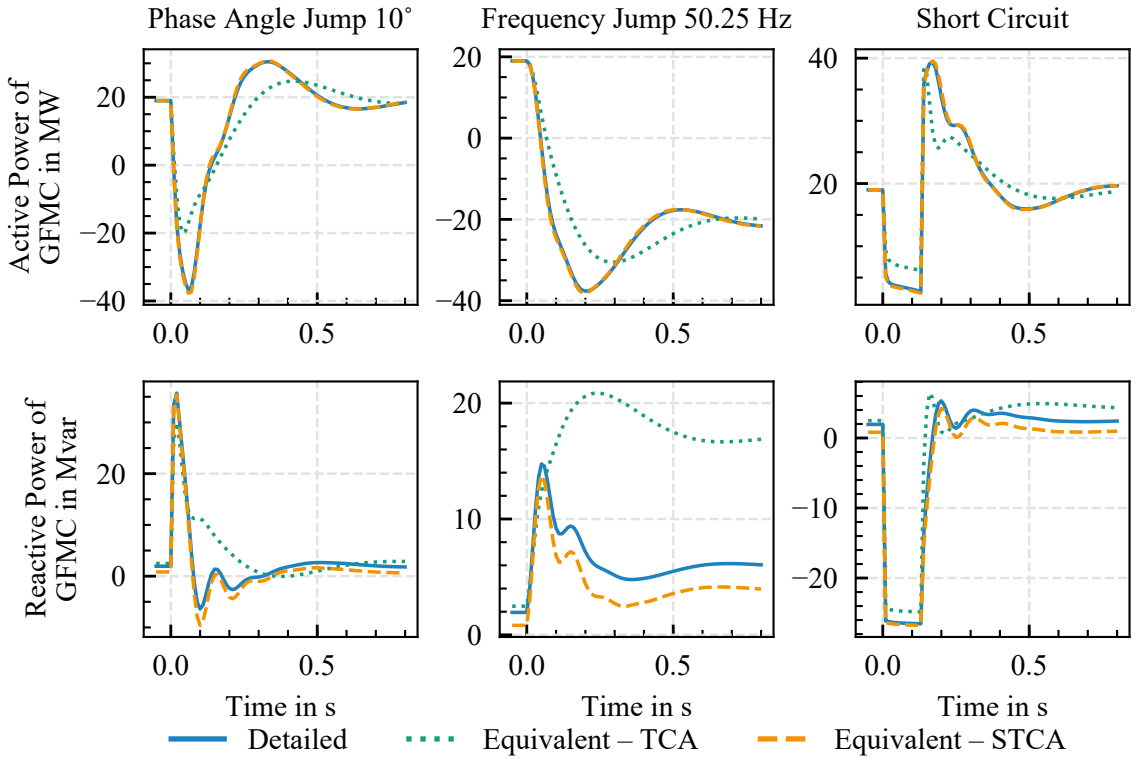

Figure B.6: Scenario *SimBench10*: sum of active and reactive power generation of all GFMC in detailed and equivalent network models; positive reactive power values: over-excited state; negative reactive power values: under-excited state

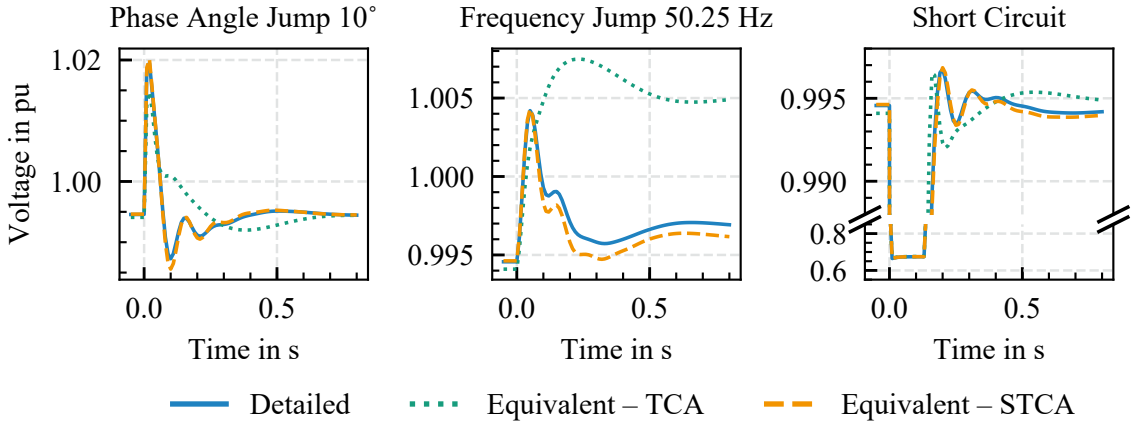

Figure B.7: Scenario *SimBench10*: voltages at low voltage side of 230 kV/10 kV transformer in detailed and equivalent network models

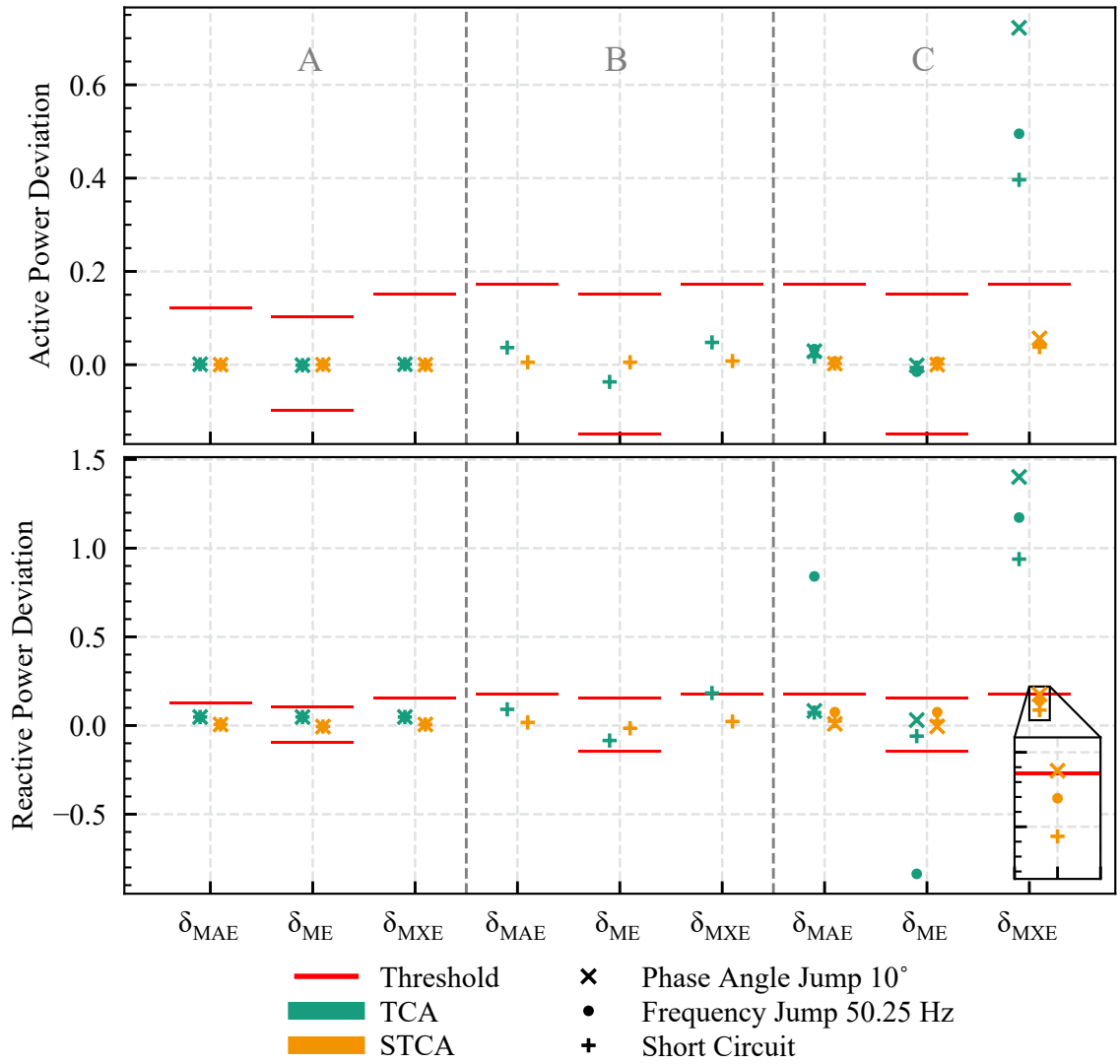

Figure B.8: Scenario *SimBench10*: validation results for EDAM aggregated with TCA and STCA

B.3 Scenario SimBench10: Additional Plots

In addition to the plots shown in Section 5.4.2, the sum of active and reactive power generation of all GFMC in the detailed network model and the EDAM as well as the voltages at the lower voltage side of the transformer in the detailed network model and the EDAM are shown in this chapter.

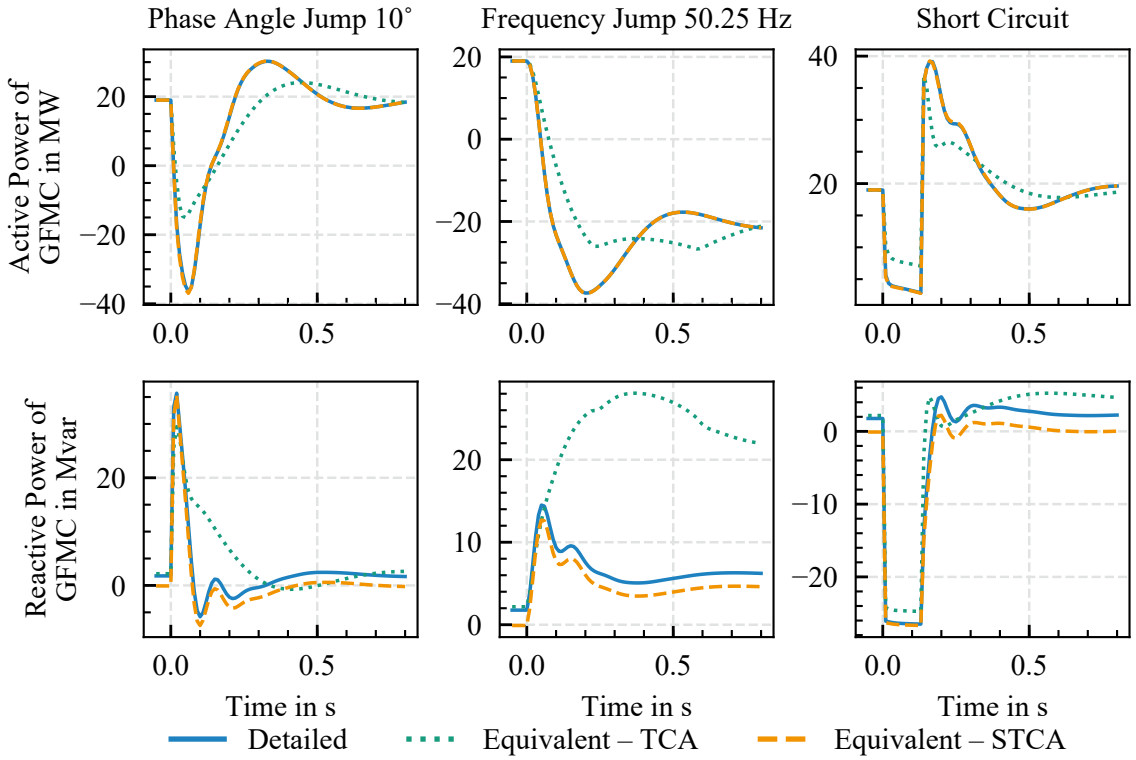

Figure B.9: Scenario *SimBench10*: sum of active and reactive power generation of all GFMC in detailed and equivalent network models; positive reactive power values: over-excited state; negative reactive power values: under-excited state

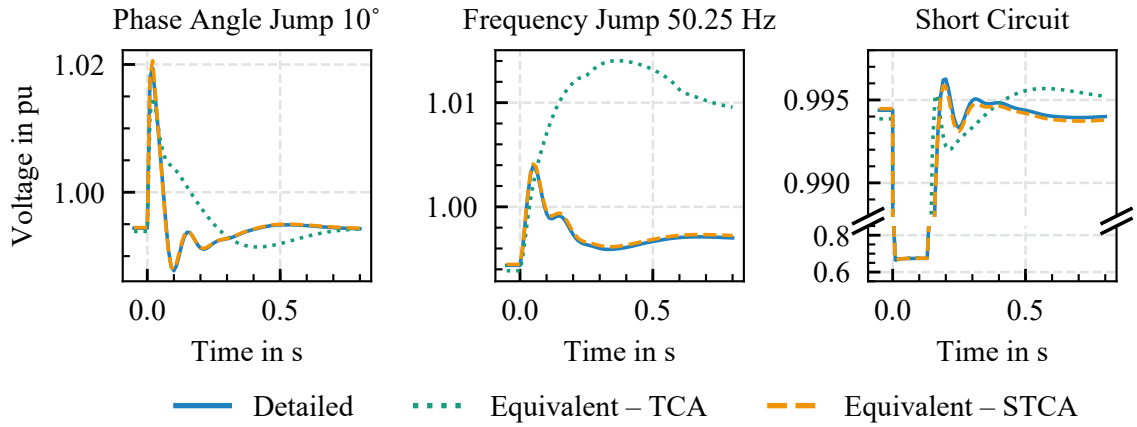

Figure B.10: Scenario *SimBench10*: voltages at low voltage side of 230 kV/10 kV transformer in detailed and equivalent network models

B.4 Scenario DINGO8: Comparison TCA based EDAM and STCA based EDAM of the Aggregation Level *STCA 4 GFMC*

In Section 5.4.3 the differences between the two STCA based EDAM with eight equivalent GFMC (aggregation level *STCA 8 GFMC*) and four aggregated equivalent GFMC (aggregation level *STCA 4 GFMC*) has been elaborated. The EDAM of the aggregation level *STCA 8 GFMC* captured the dynamic behavior of the detailed network model better than the EDAM of the aggregation level *STCA 4 GFMC*, which violated several validation metrics. Even though the EDAM with the four aggregated equivalent GFMC has major drawbacks, it still performs better than the EDAM aggregated with TCA.

The following simulation results and validation shows the differences between the TCA based EDAM and the STCA based EDAM of the aggregation level *STCA 4 GFMC*.

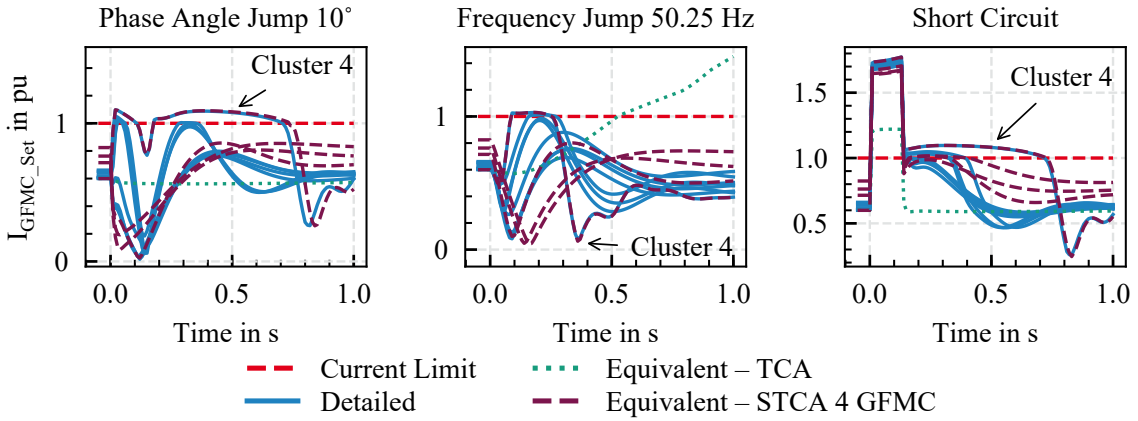

Figure B.11: Scenario *DINGO8*: calculated set point for output current of GFMC $I_{\text{GFMC\_Set}}$ in detailed and equivalent network models

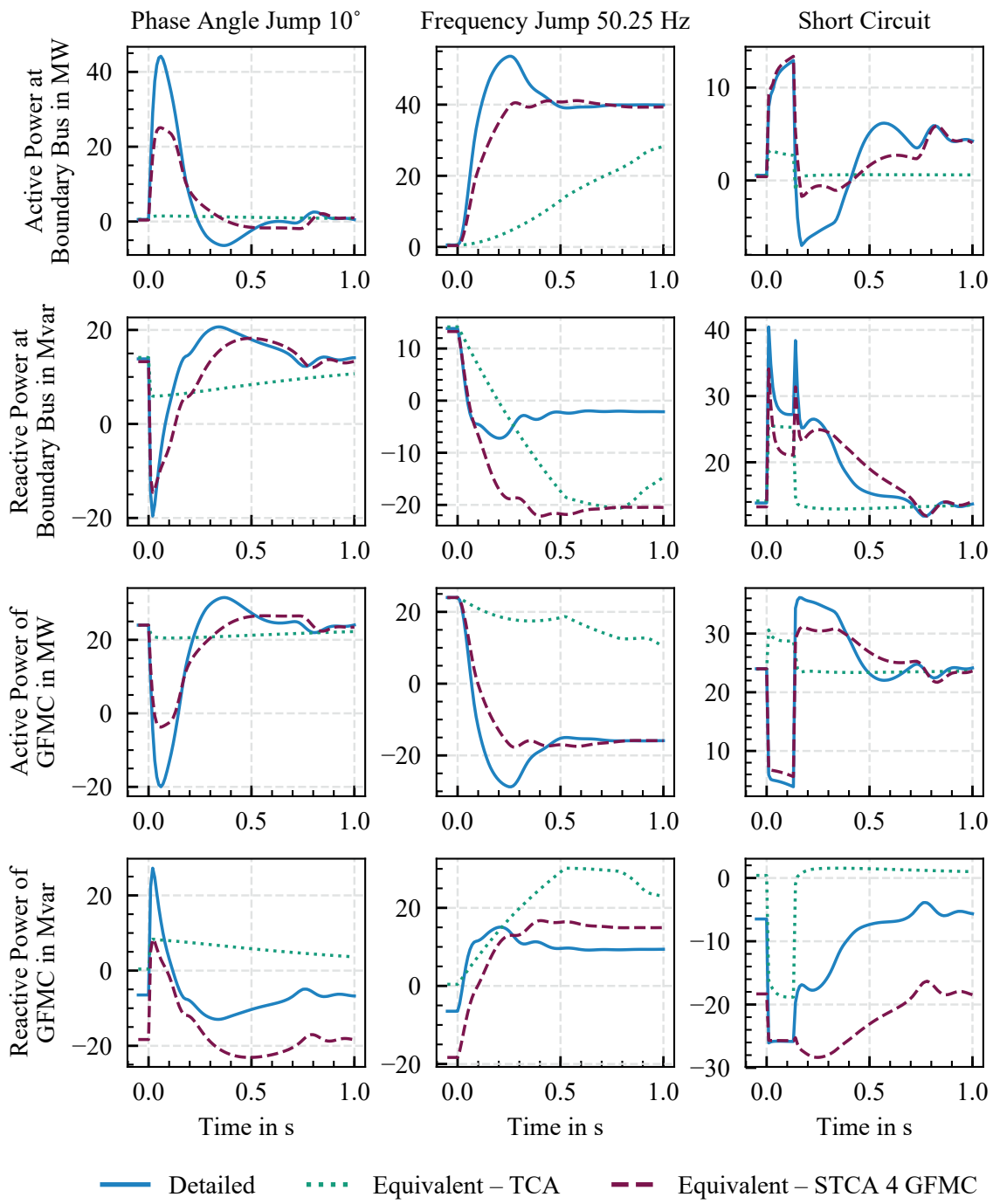

Figure B.12: Scenario *DINGO8*: active and reactive power flow at boundary bus from transmission to distribution system of detailed and equivalent network models and sum of active and reactive power generation of all GFMC in detailed and equivalent network models; positive reactive power values: over-excited state; negative reactive power values: under-excited state

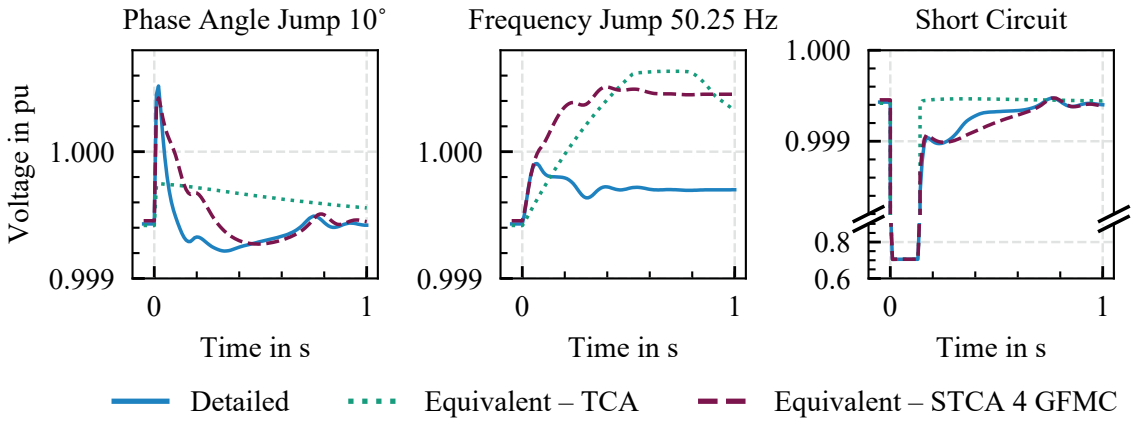

Figure B.13: Scenario *DINGO8*: voltages at low voltage side of 230 kV/10 kV transformer in detailed and equivalent network models

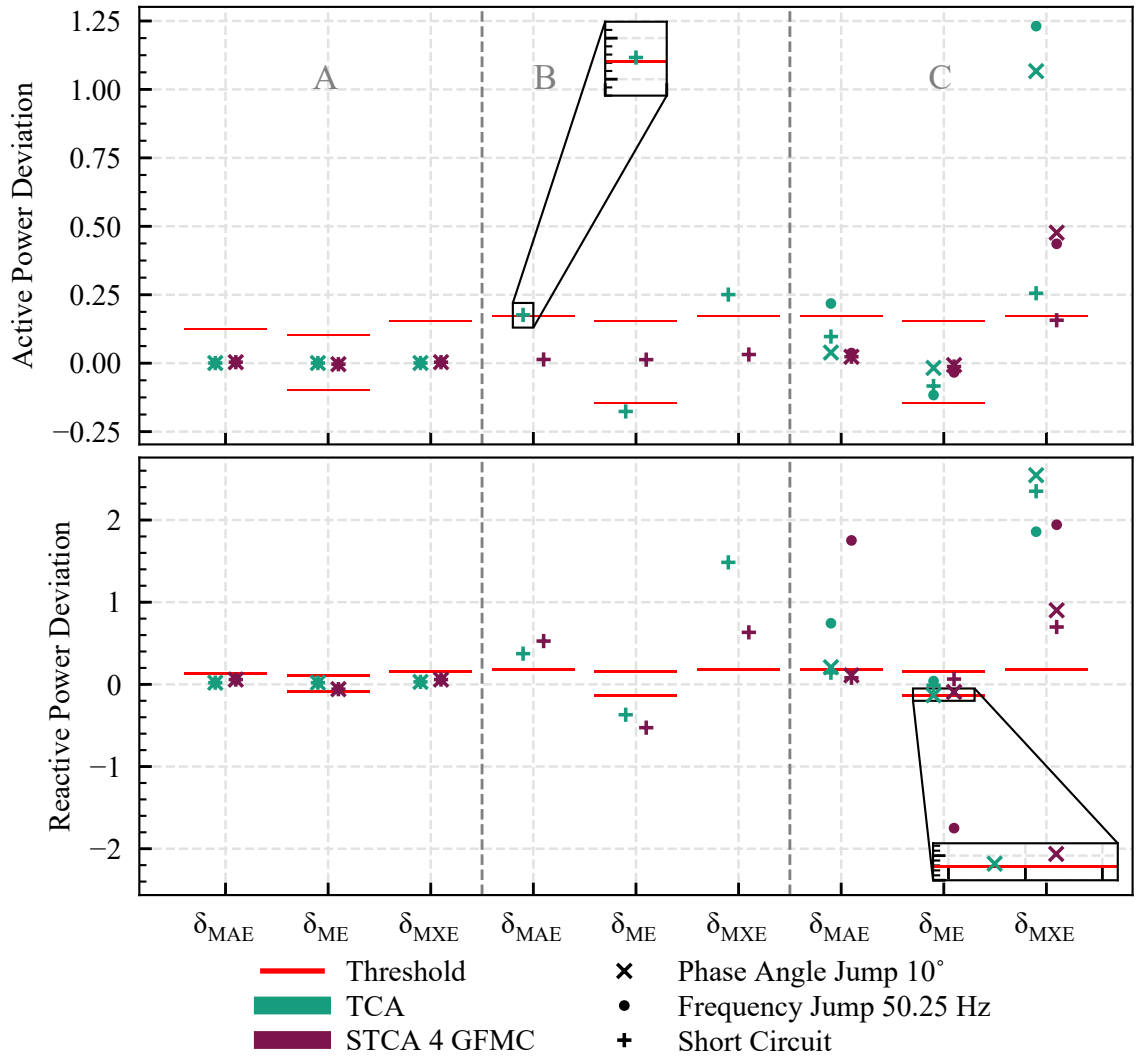

Figure B.14: Scenario *DINGO8*: validation results for EDAM aggregated with TCA and STCA with four equivalent GFMC cluster

B.5 Scenario DINGO20: Additional Plots

In addition to the plots shown in Section 5.4.4, the following section shows the calculated set points for the GFMC output current $I_{\text{GFMC\_Set}}$ in the detailed network model and the EDAM. Also, the sum of active and reactive power generation of all GFMC in the detailed network model and the EDAM is shown. For a better understanding of the deviations between the STCA based EDAM and the detailed network model, the voltages at the lower voltage side of the transformer in the detailed network model and the EDAM as well as the voltages at the PCC of each GFMC in the detailed network model and the EDAM are shown.

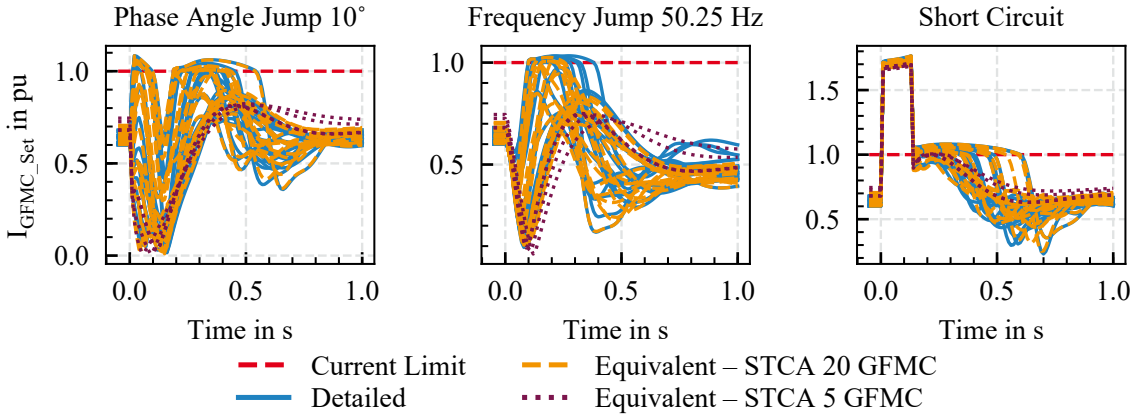

Figure B.15: Scenario *DINGO20*: calculated set point for output current of GFMC $I_{\text{GFMC\_Set}}$ in detailed and equivalent network models

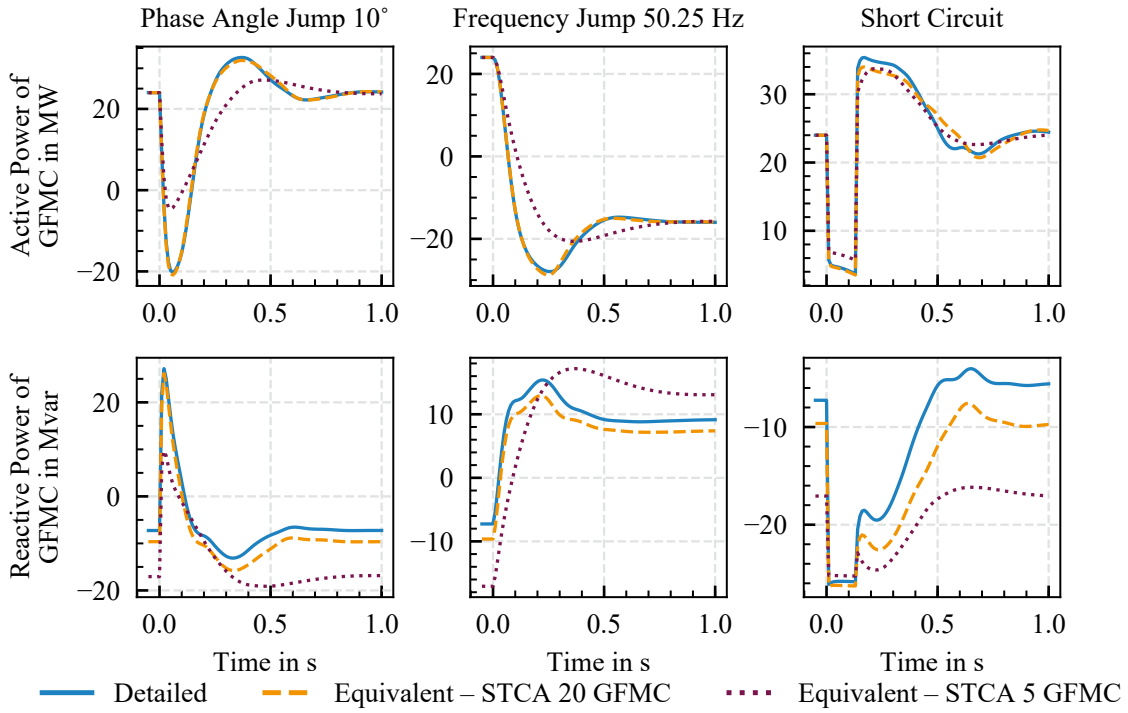

Figure B.16: Scenario *DINGO20*: sum of active and reactive power generation of all GFMC in detailed and equivalent network models; positive reactive power values: over-excited state; negative reactive power values: under-excited state

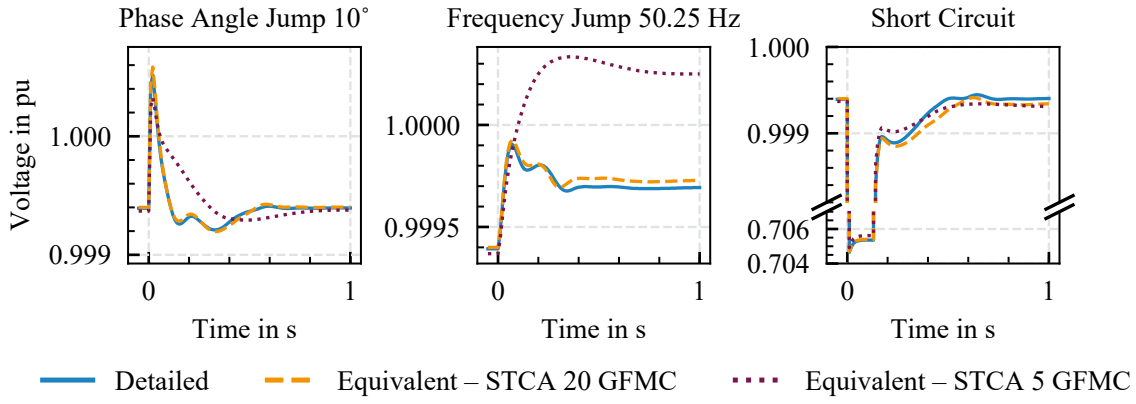

Figure B.17: Scenario *DINGO20*: voltages at low voltage side of 230 kV/10 kV transformer in detailed and equivalent network models

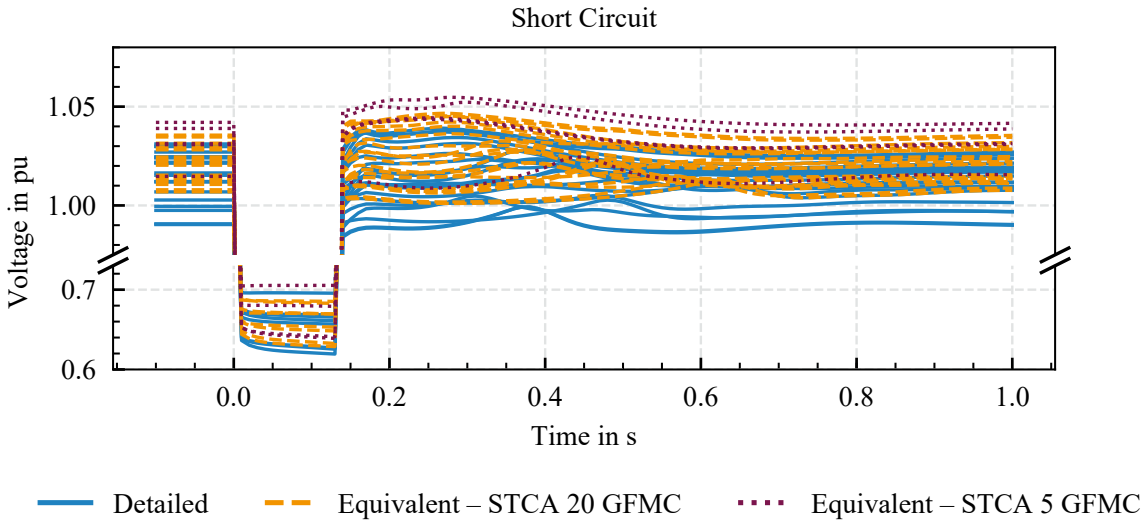

Figure B.18: Scenario *DINGO20*: voltages at PCC of each GFMC in detailed and equivalent network models

B.6 Scenario DINGO20: Comparison TCA based EDAM and STCA based EDAM of the Aggregation Level *STCA 5 GFMC*

In addition to the results shown in Section 5.4.4, this section shows the simulation and validation results of the TCA based EDAM of the scenario *DINGO20*. The TCA based EDAM is compared with the STCA based EDAM of the aggregation level *STCA 5 GFMC*. Even though the STCA based EDAM with the aggregated five GFMC shows a worse accuracy compared to the STCA based EDAM in which all GFMC are considered individually, it is clear that the TCA based EDAM is even less accurate. This can be seen in Figure B.20 showing the active and reactive power flows at the boundary bus as well as the sum of active and reactive power generation of all GFMC in the detailed network model and the EDAM. Also, the numerical validation shown in Figure B.22 complies with these observations.

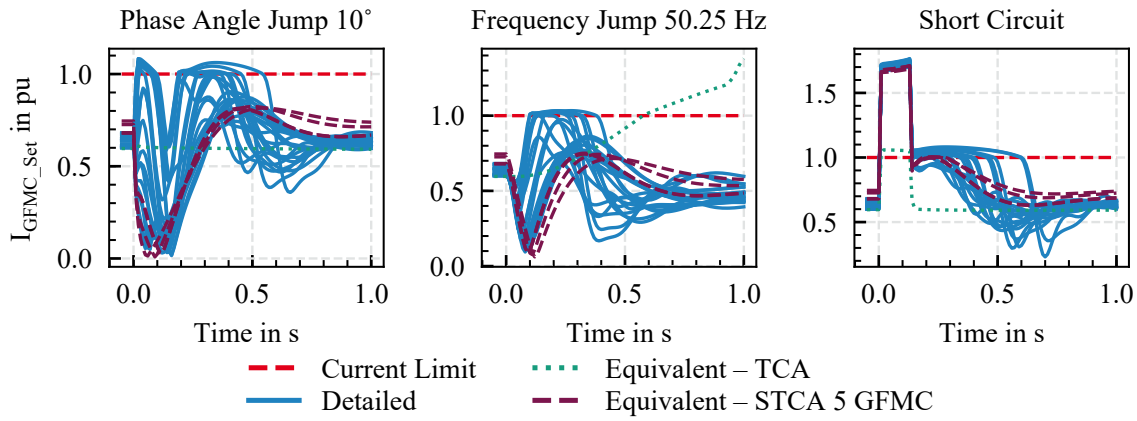

Figure B.19: Scenario *DINGO20*: calculated set point for output current of GFMC $I_{\mathrm{GFMC\_Set}}$ in detailed and equivalent network models

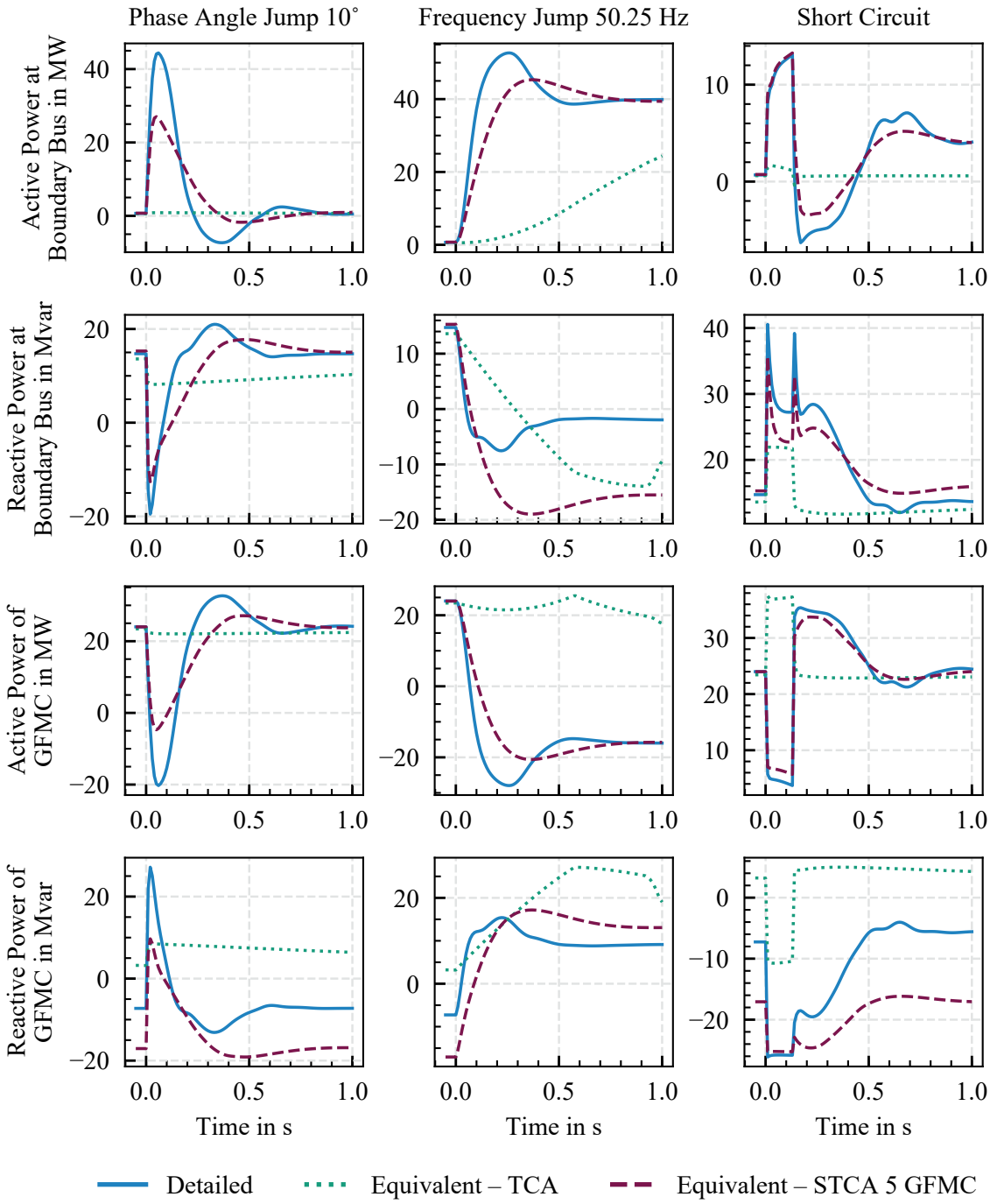

Figure B.20: Scenario *DINGO20*: active and reactive power flow at boundary bus from transmission to distribution system of detailed and equivalent network models and sum of active and reactive power generation of all GFMC in detailed and equivalent network models; positive reactive power values: over-excited state; negative reactive power values: under-excited state

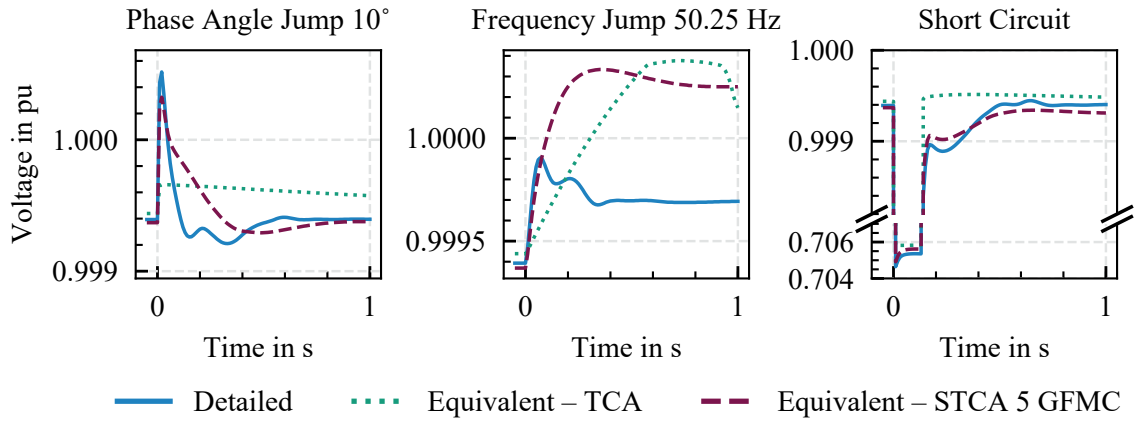

Figure B.21: Scenario *DINGO20*: voltages at low voltage side of 230 kV/10 kV transformer in detailed and equivalent network models

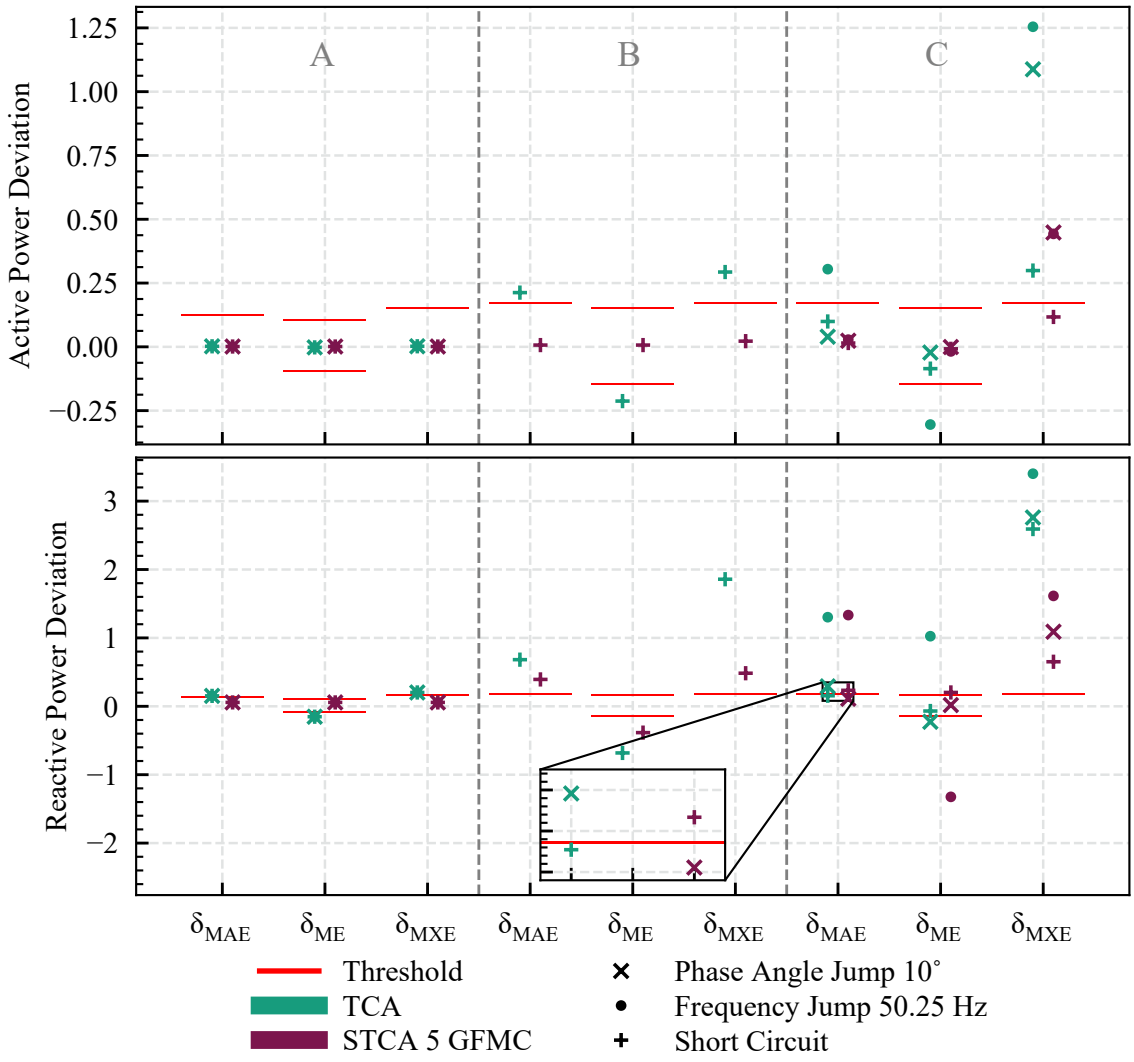

Figure B.22: Scenario *DINGO20*: validation results for EDAM aggregated with TCA and STCA with five equivalent GFMC cluster

B.7 Scenario DINGO15: Additional Plots

In addition to the plots shown in Section 5.4.5, the following section shows the calculated set points for the GFMC output current $I_{\mathrm{GFMC\_Set}}$ in the detailed network model and the EDAM and the sum of active and reactive power generation of all GFMC in the detailed network model and the EDAM. Also, the voltages at the lower voltage side of the transformer in the detailed network model and the EDAM as well as the voltages at the PCC of each GFMC in the detailed network model and the EDAM are shown.

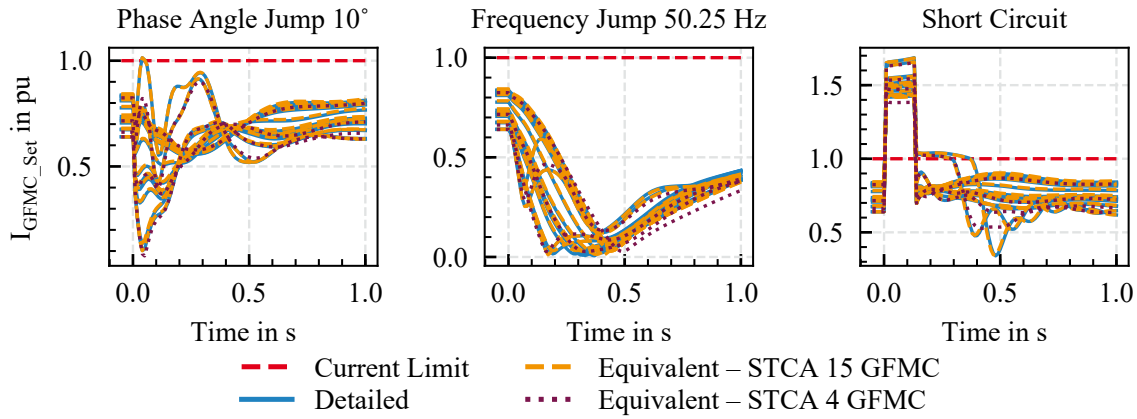

Figure B.23: Scenario *DINGO15*: calculated set point for output current of GFMC $I_{\mathrm{GFMC\_Set}}$ in detailed and equivalent network models

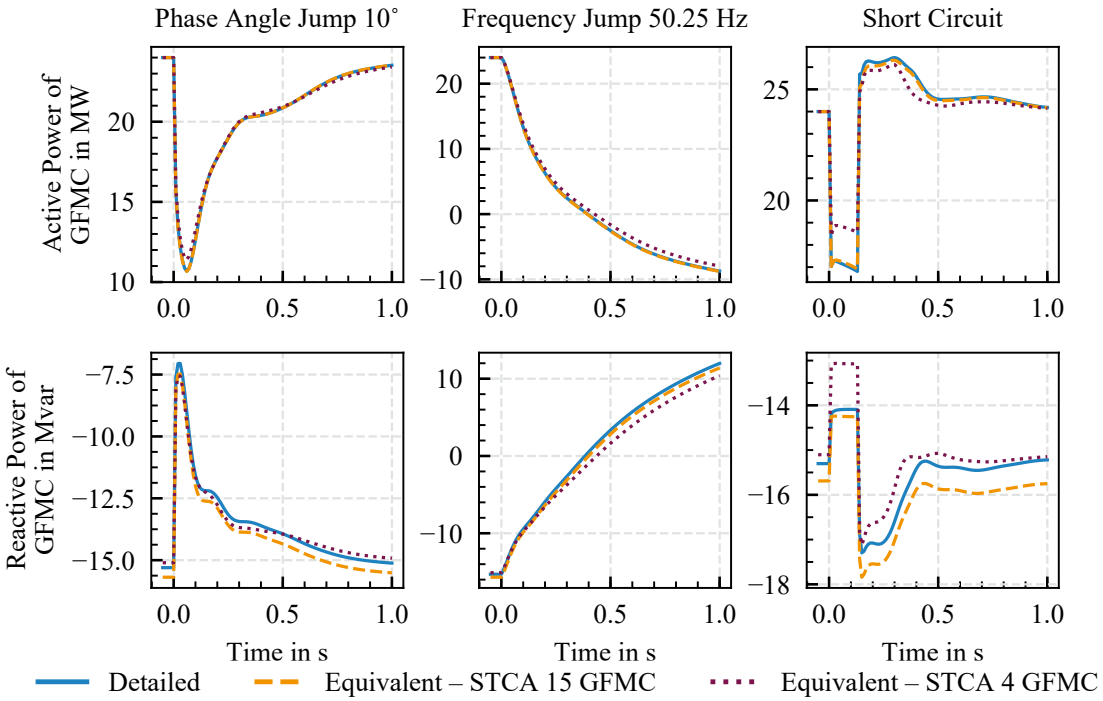

Figure B.24: Scenario *DINGO15*: sum of active and reactive power generation of all GFMC in detailed and equivalent network models; positive reactive power values: over-excited state; negative reactive power values: under-excited state

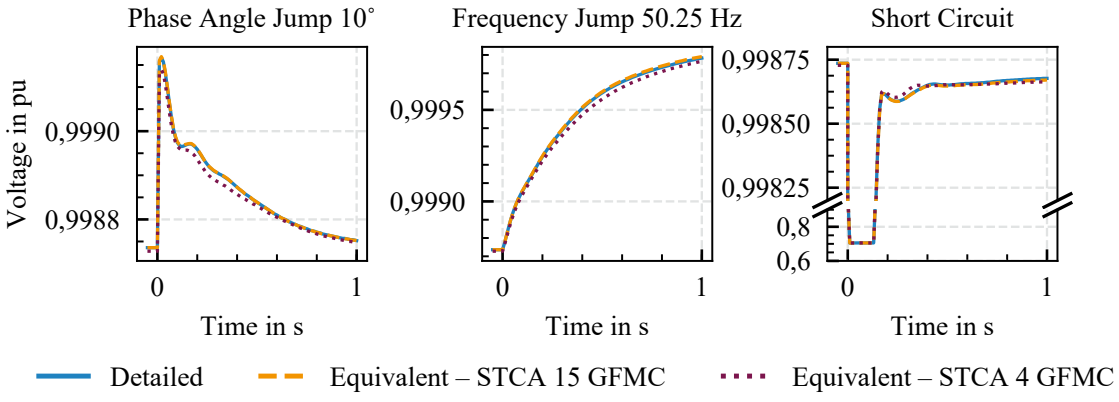

Figure B.25: Scenario *DINGO15*: voltages at low voltage side of 230 kV/10 kV transformer in detailed and equivalent network models

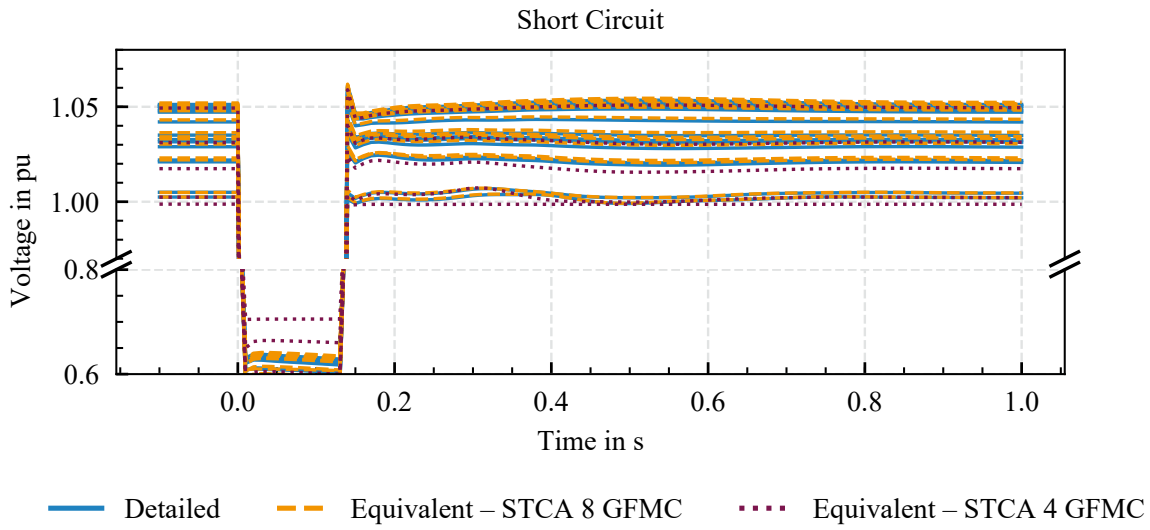

Figure B.26: Scenario *DINGO15*: voltages at PCC of each GFMC in detailed and equivalent network models

B.8 Scenario DINGO15: Comparison TCA based EDAM and STCA based EDAM of the Aggregation Level *STCA 4 GFMC*

In Section 5.4.5, the TCA is not applied on the detailed network. Therefore, this section shows the simulation and validation results of the TCA based EDAM of the scenario *DINGO15*. Also, the TCA based EDAM is compared with the STCA based EDAM of the aggregation level *STCA 4 GFMC*. The simulation results show the bad performance of the TCA applied to the detailed network of scenario *DINGO15*. This can be seen in Figure B.28 showing the active and reactive power flows at the boundary bus as well as the sum of active and reactive power generation of all GFMC in the detailed network model and the EDAM and in Figure B.30 showing the results of the numerical validation.

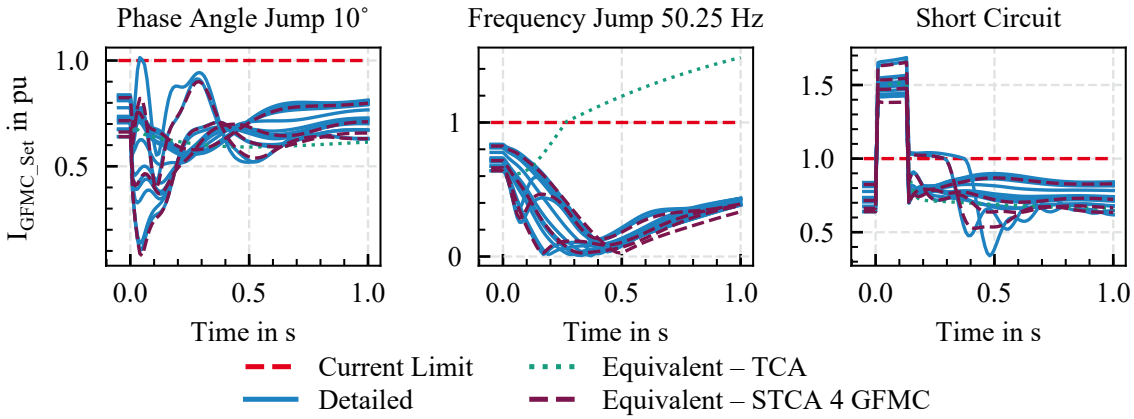

Figure B.27: Scenario *DINGO15*: calculated set point for output current of GFMC $I_{\text{GFMC\_Set}}$ in detailed and equivalent network models

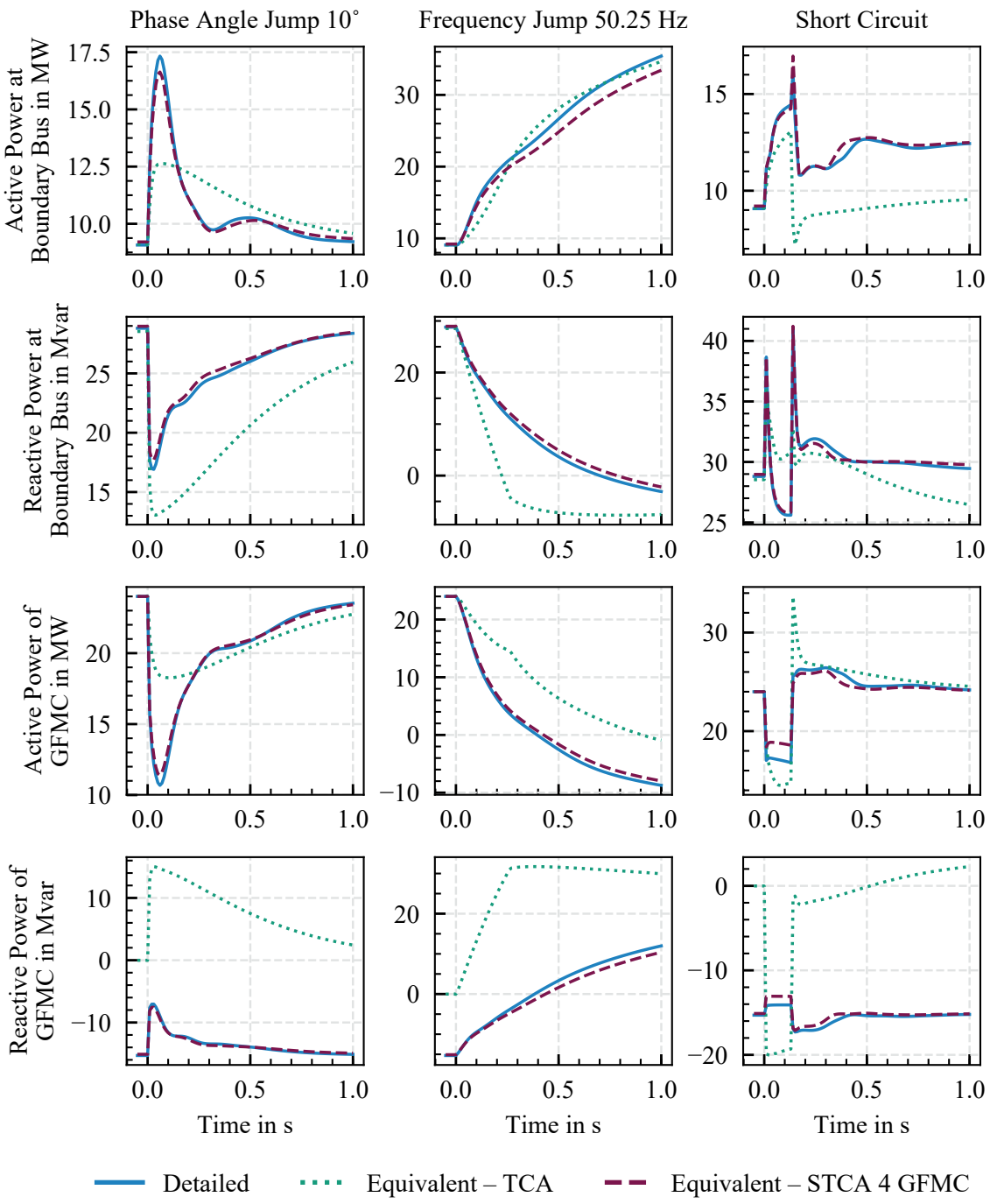

Figure B.28: Scenario *DINGO15*: active and reactive power flow at boundary bus from transmission to distribution system of detailed and equivalent network models and sum of active and reactive power generation of all GFMC in detailed and equivalent network models; positive reactive power values: over-excited state; negative reactive power values: under-excited state

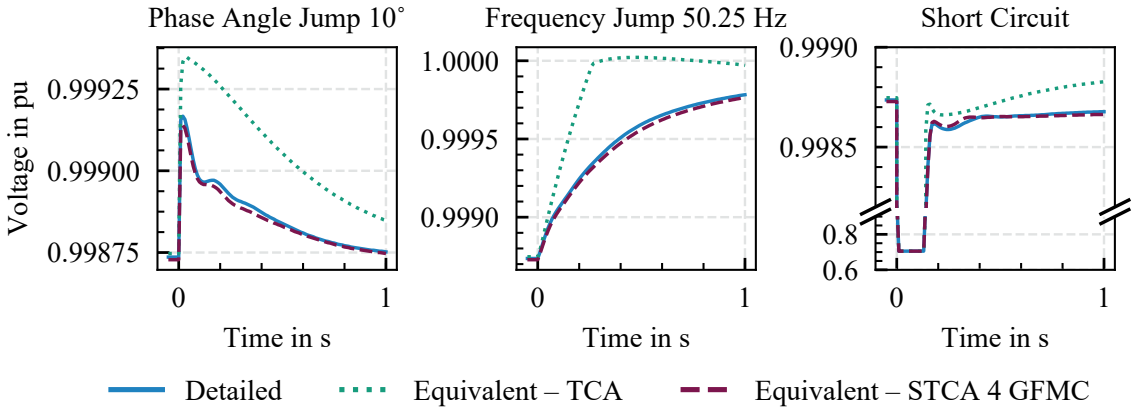

Figure B.29: Scenario *DINGO15*: voltages at low voltage side of 230 kV/10 kV transformer in detailed and equivalent network models

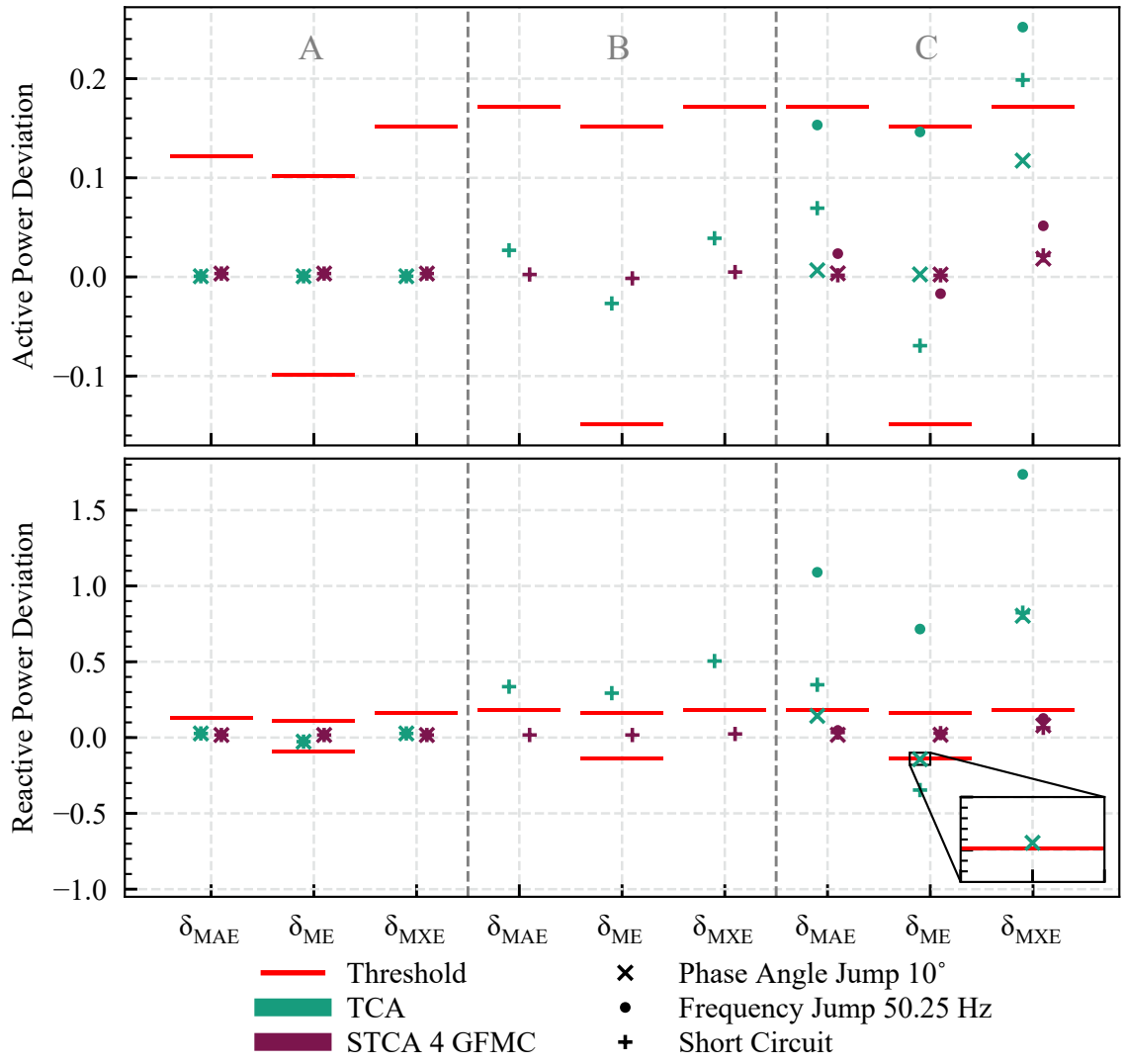

Figure B.30: Scenario *DINGO15*: validation results for EDAM aggregated with TCA and STCA with four equivalent GFMC cluster

B.9 Operating Point Dependency and Adaptation: Additional Plots

The plots in Section 5.5 only refer to the worst values of active and reactive power deviation of the STCA based EDAM. This section provides detailed results of both active and reactive power deviations. Additionally, the operating point dependency and adaptation was performed on a TCA based EDAM. The results of this evaluation is also provided in this chapter.

B.9.1 Operating Point Dependency

Load Scenarios

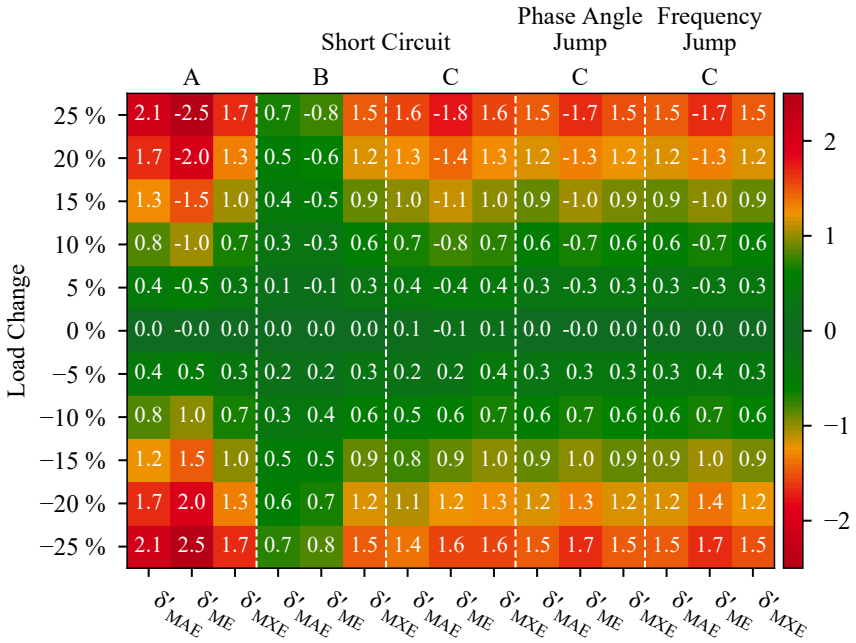

Figure B.31: *Load scenarios*: validity evaluation of STCA based EDAM parameterized according to base scenario (0 %) for different load scenarios in the detailed network; values show active power deviation

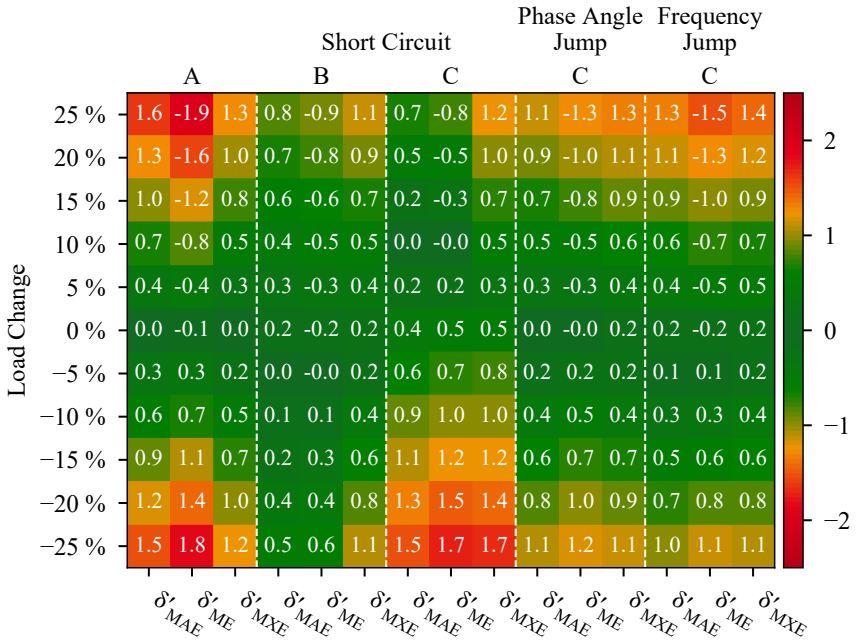

Figure B.32: *Load scenarios*: validity evaluation of STCA based EDAM parameterized according to base scenario (0 %) for different load scenarios in the detailed network; values show reactive power deviation

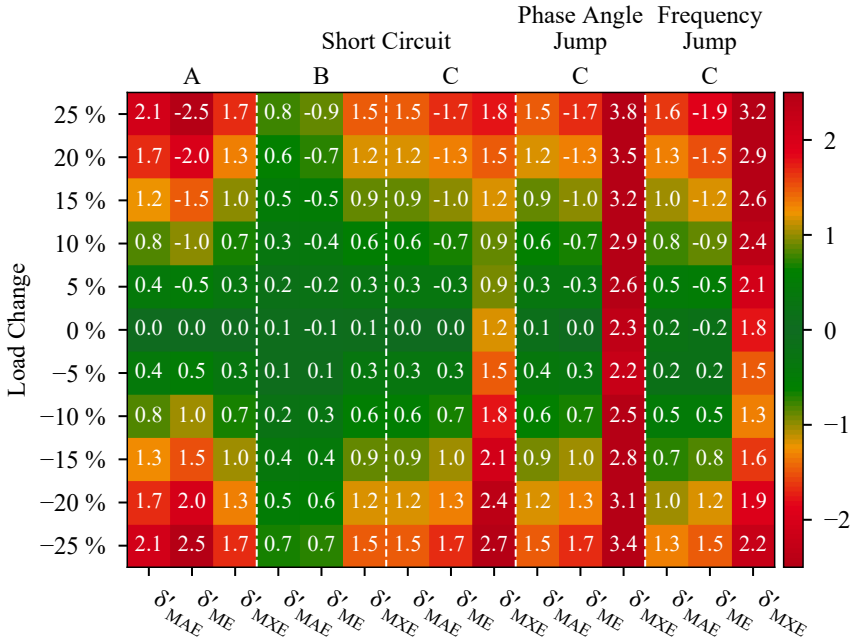

Figure B.33: *Load scenarios*: validity evaluation of TCA based EDAM parameterized according to base scenario (0 %) for different load scenarios in the detailed network; values show active power deviation

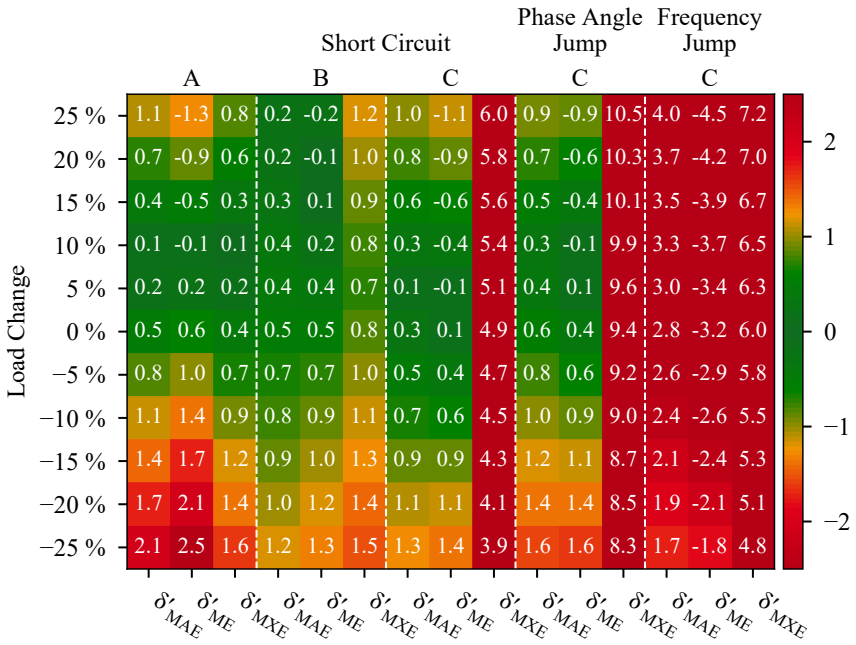

Figure B.34: *Load scenarios*: validity evaluation of TCA based EDAM parameterized according to base scenario (0 %) for different load scenarios in the detailed network; values show reactive power deviation

GFMC Generation Scenarios

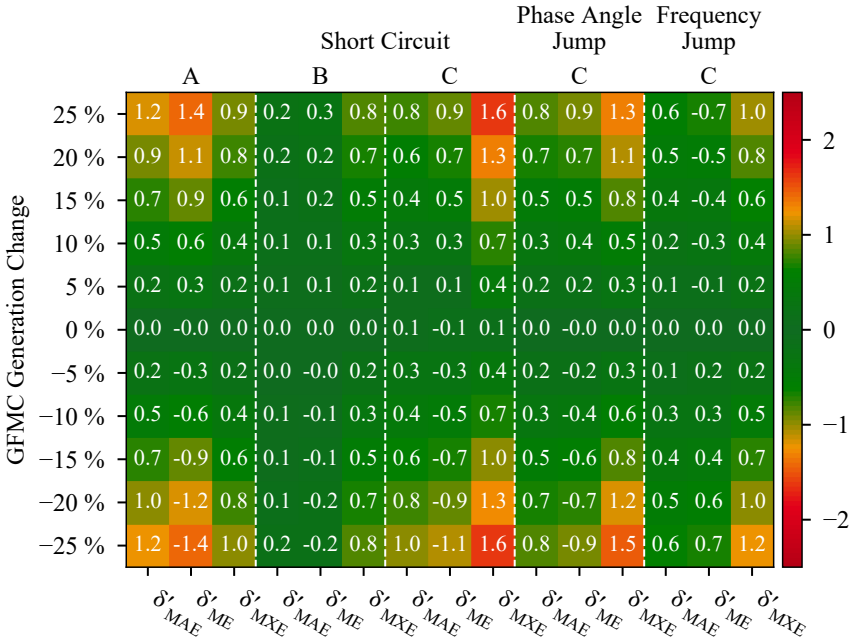

Figure B.35: *GFMC generation scenarios*: validity evaluation of STCA based EDAM parameterized according to base scenario (0 %) for different GFMC generation scenarios in the detailed network; values show active power deviation

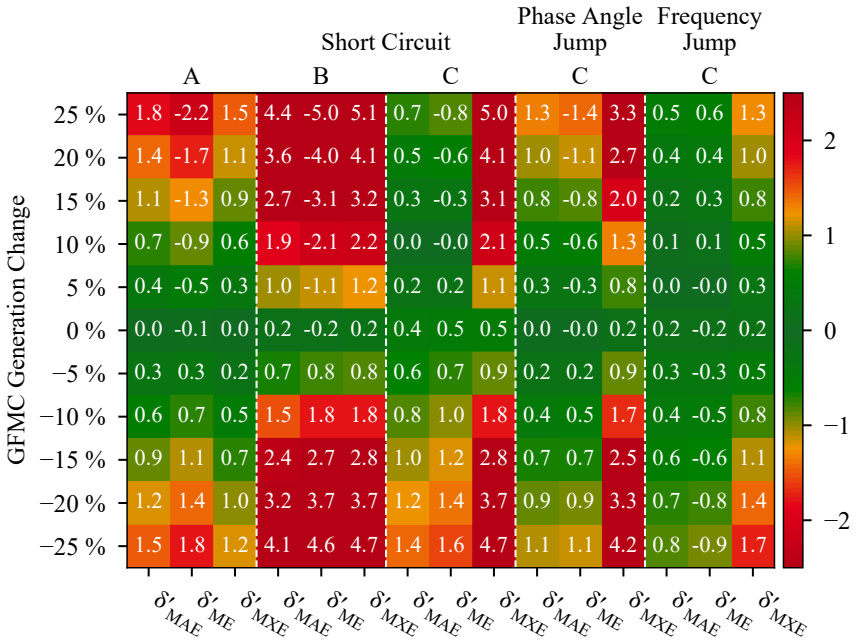

Figure B.36: *GFMC generation scenarios*: validity evaluation of STCA based EDAM parameterized according to base scenario (0 %) for different GFMC generation scenarios in the detailed network; values show reactive power deviation

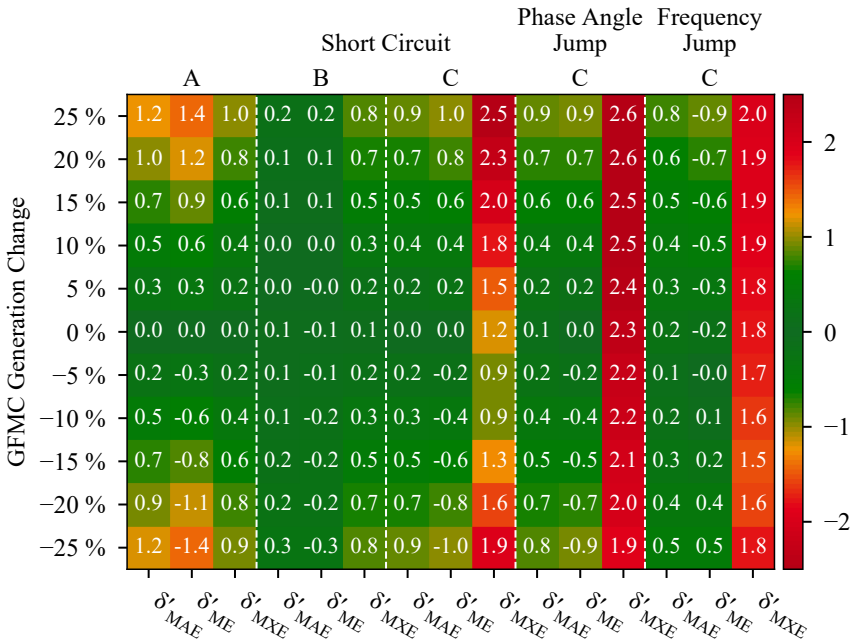

Figure B.37: *GFMC generation scenarios*: validity evaluation of TCA based EDAM parameterized according to base scenario (0 %) for different GFMC generation scenarios in the detailed network; values show active power deviation

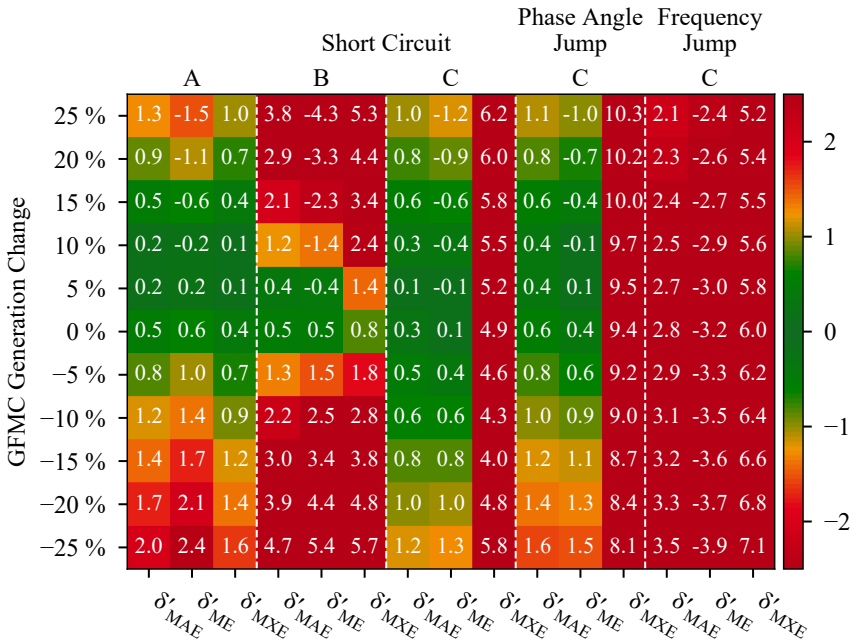

Figure B.38: *GFMC generation scenarios*: validity evaluation of TCA based EDAM parameterized according to base scenario (0 %) for different GFMC generation scenarios in the detailed network; values show reactive power deviation

B.9.2 Operating Point Adaptation

Load Scenarios

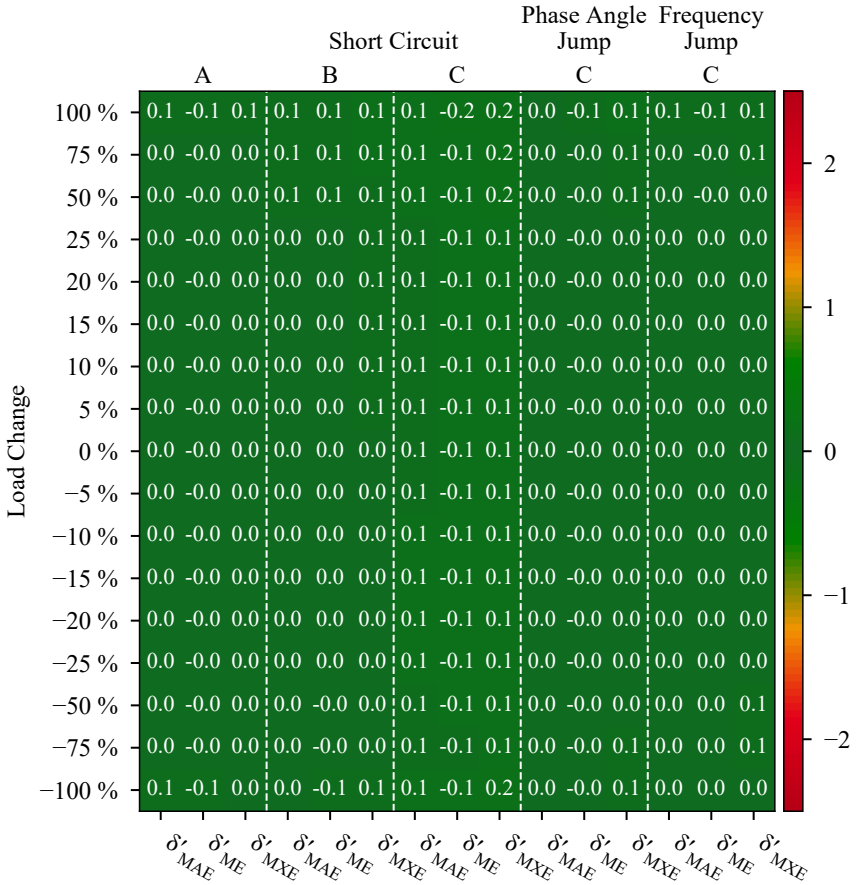

Figure B.39: *Load scenarios*: validity evaluation of adapted STCA based EDAM for different load scenarios in the detailed network; values show active power deviation

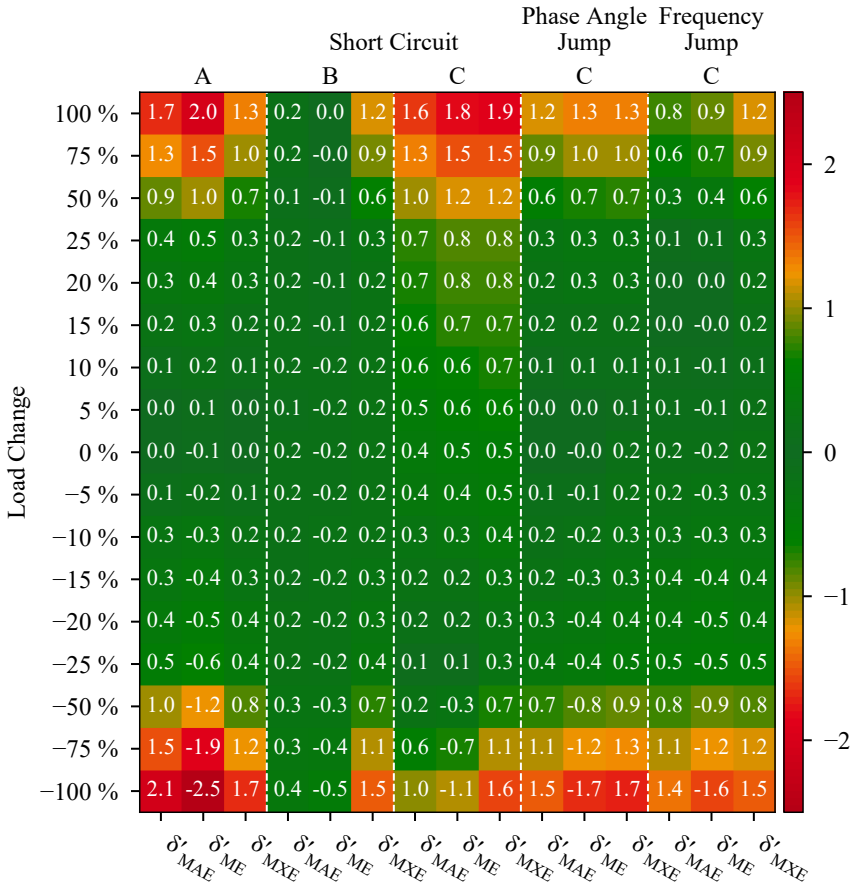

Figure B.40: *Load scenarios*: validity evaluation of adapted STCA based EDAM for different load scenarios in the detailed network; values show reactive power deviation

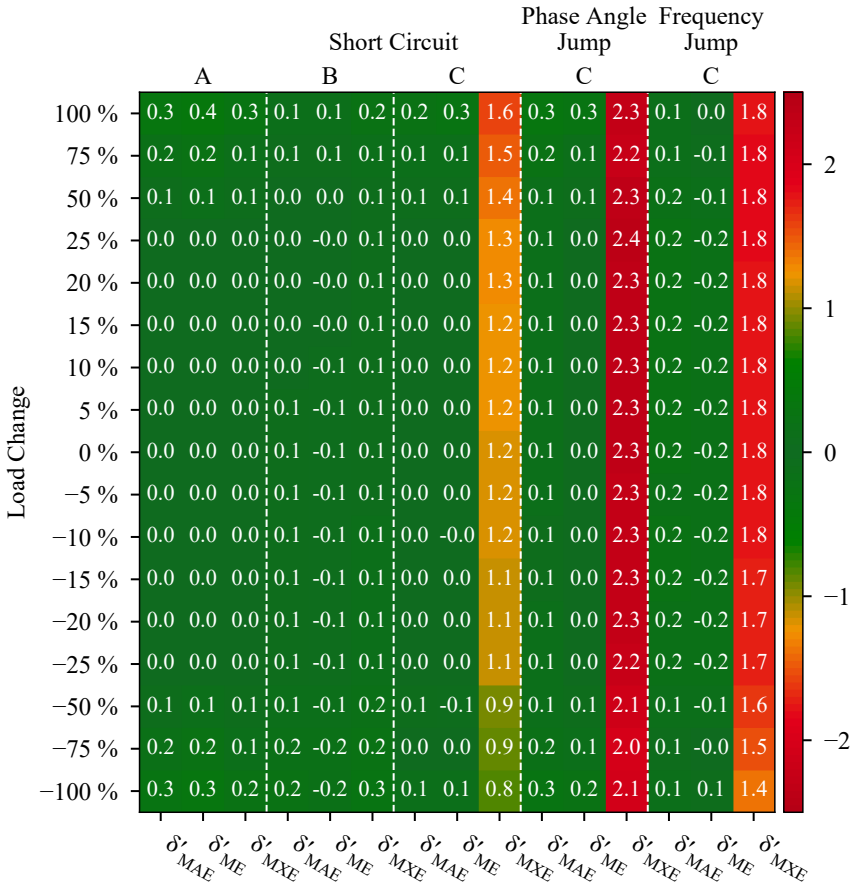

Figure B.41: *Load scenarios*: validity evaluation of adapted TCA based EDAM for different load scenarios in the detailed network; values show active power deviation

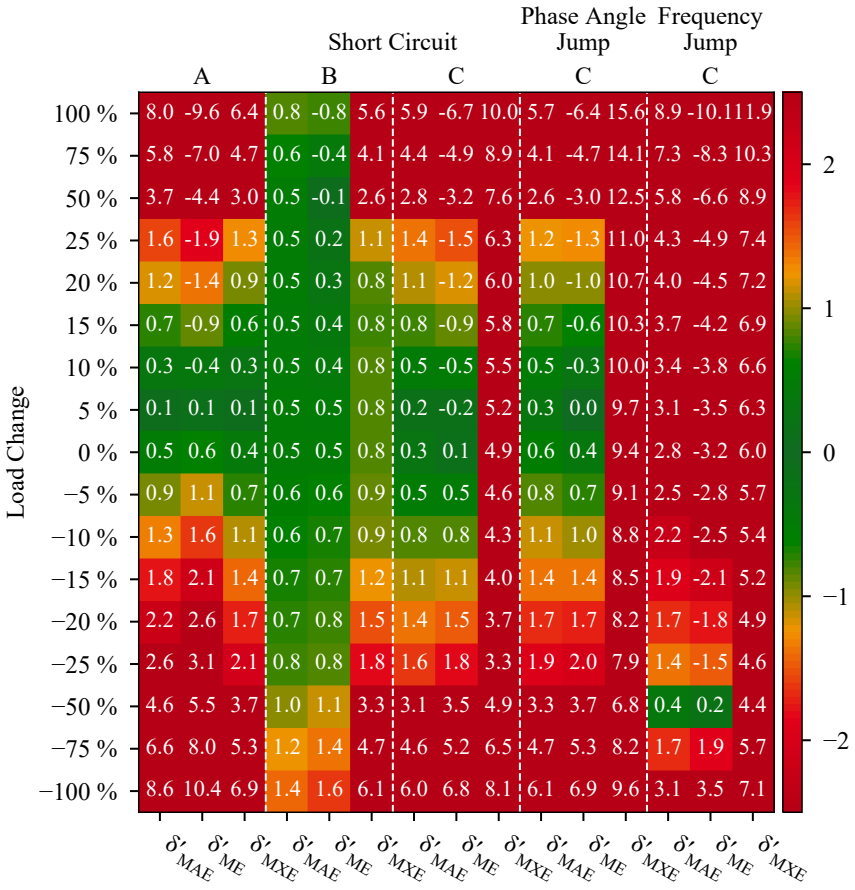

Figure B.42: *Load scenarios*: validity evaluation of adapted TCA based EDAM for different load scenarios in the detailed network; values show reactive power deviation

GFMC Generation Scenarios

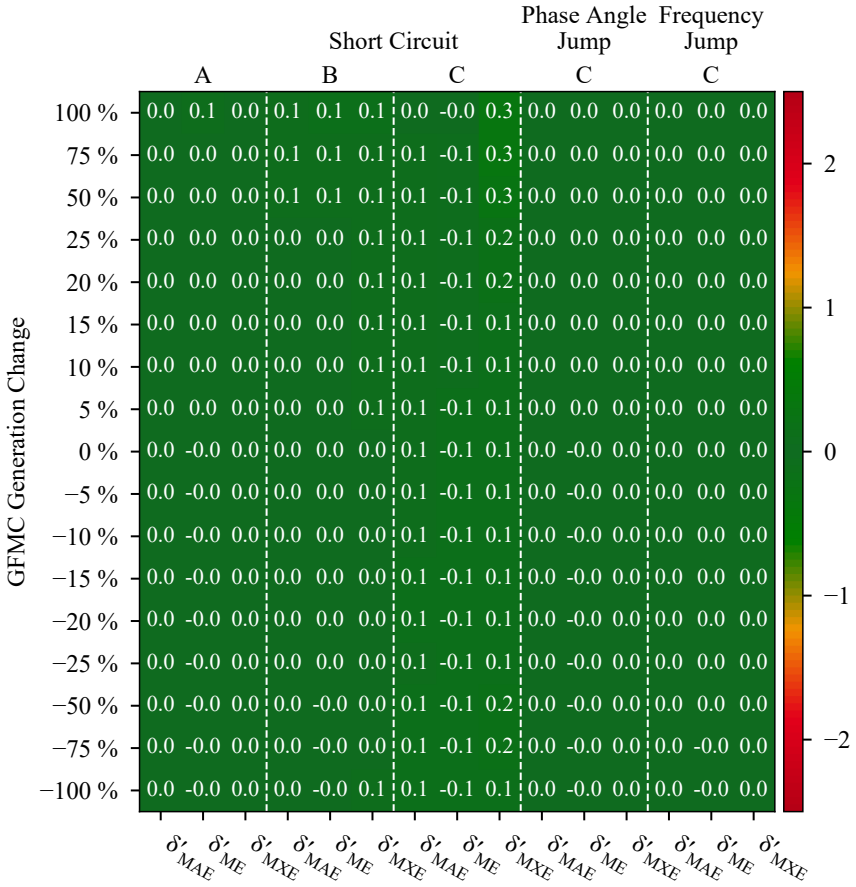

Figure B.43: *GFMC generation scenarios*: validity evaluation of adapted STCA based EDAM for different GFMC generation scenarios in the detailed network; values show active power deviation

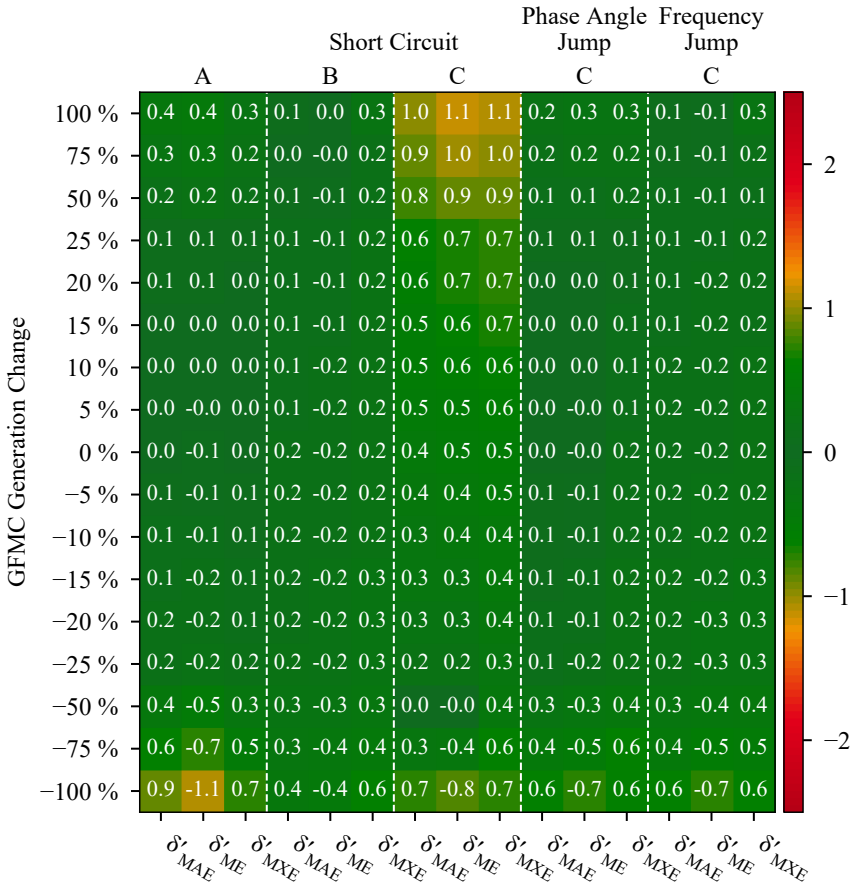

Figure B.44: *GFMC generation scenarios*: validity evaluation of adapted STCA based EDAM for different GFMC generation scenarios in the detailed network; values show reactive power deviation

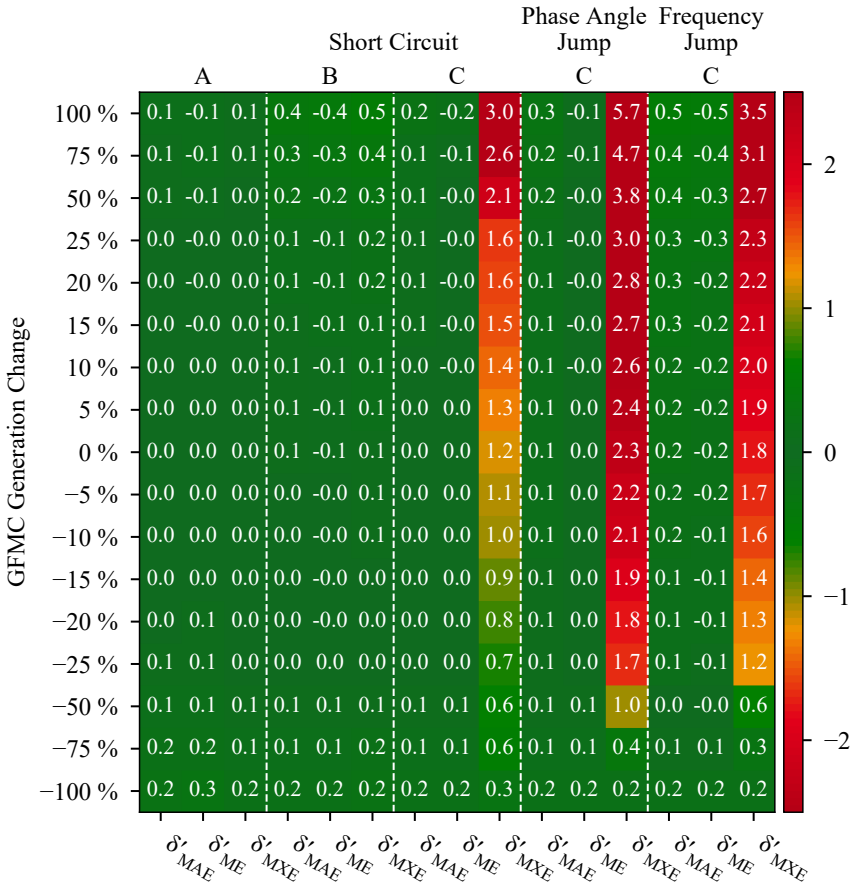

Figure B.45: *GFMC generation scenarios*: validity evaluation of adapted TCA based EDAM for different GFMC generation scenarios in the detailed network; values show active power deviation

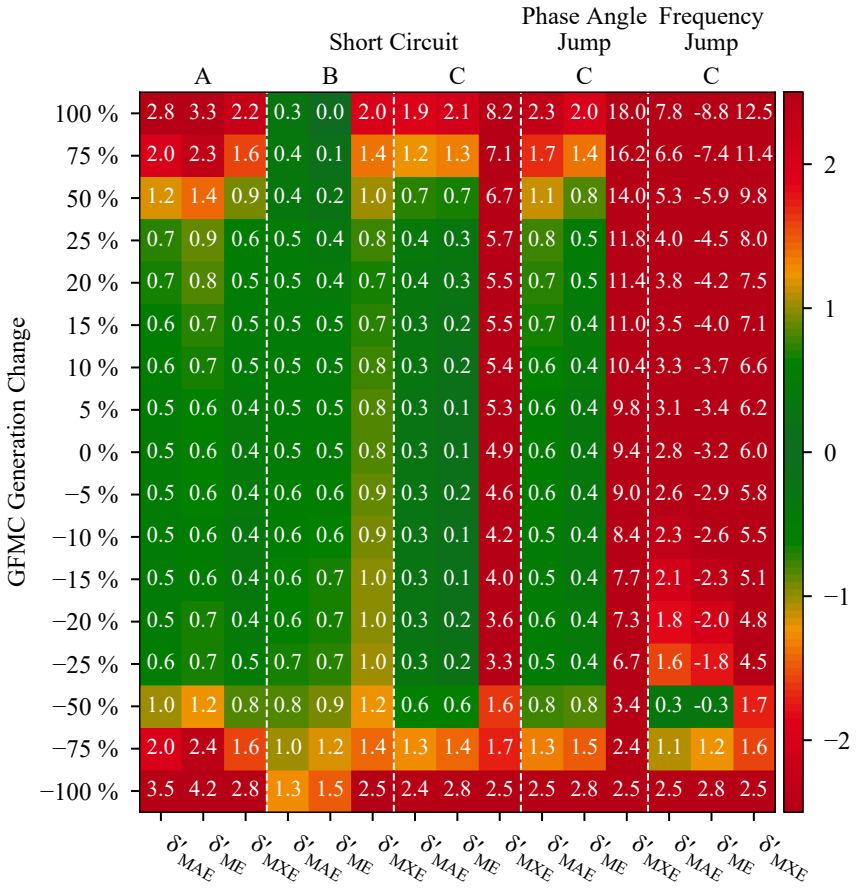

Figure B.46: *GFMC generation scenarios*: validity evaluation of adapted TCA based EDAM for different GFMC generation scenarios in the detailed network; values show reactive power deviation

B.10 Simulation Time Dependency

In order to investigate the dependency of a network on the simulation time, three scenarios are considered. The basis of all three scenarios is the DINGO topology described in Section 5.3.2. The first scenario is *DINGO20* introduced and evaluated in Section 5.4.4. The second scenario *DINGO20_99* adapts the network of *DINGO20* to a GFMC dominated system. Here, GFMC account for 99 % of the network's CBG, while GFLC provide 1 % of the total CBG. Neverthelesss, the total amount of GFLC components remain unaltered, only the nominal values of each GFLC was reduced accordingly. Opposed to that, in scenario *DINGO20_100* all GFLC components are disconnected and GFMC provide 100 % of the network's CBG (Table B.2).

Table B.2: Generation and demand data for adapted DINGO MV network of respective scenario

Scenario	**Component**	**Number of Units**	**Actual Active Power**	**Actual Reactive Power**
DINGO20	Load	122	40 MW	10.1 Mvar
	GFLC	96	16.2 MW	3.3 Mvar
	GFMC	20	24 MW	7.6 Mvar
DINGO20_99	Load	122	40.0 MW	10.1 Mvar
	GFLC	96	0.4 MW	0.1 Mvar
	GFMC	20	40.0 MW	15.7 Mvar
DINGO20_100	Load	122	40 MW	10.1 Mvar
	GFLC	0	0 MW	0.0 Mvar
	GFMC	20	40 MW	15.7 Mvar

The networks of the three scenarios are exposed to a short circuit fault as described in Section 5.1 and the simulation times are compared (Table B.3). The total time range considered for these simulations is from -5 s to 5 s.

The increase in GFMC generation does not lead to an increase in simulation time, but to a decrease. This is due to the fact that less components, i.e., twenty GFMC, cover almost the total CBG of the network. If all GFLC components are neglected in the network and the GFMC are the only CBG, the simulation time reduces significantly. Hence, the simulation time strongly depends on the number of components with dynamic control models.

Table B.3: Simulation time of detailed network of respective scenario

Scenario	**Simulation Time** relative to scenario *DINGO20*
DINGO20	100 %
DINGO20_99	86 %
DINGO20_100	10 %

Appendix C

Definitions

C.1 Power System Stability

[Kun+04] classifies power system stability as it can be seen in Figure C.1. If synchronous machines remain synchronized in power systems after a disturbance, the power system is stable according to the rotor angle. A differentiation is made into stability after a large or small disturbance. The former relates to faults leading to a nonlinear relation between the power and rotor angle, whereas the latter disturbance allows linearization of system equations. The frequency stability of a system is investigated for faults leading to a pronounced generation and demand imbalance. Here, the system remains stable if a steady frequency after the disturbance can be maintained. Voltage stability is established if a system sustains steady voltages at all buses after a disturbance influencing the bus voltages. Similar to rotor angle stability, voltage stability is subdivided according to the extent of the disturbance, i.e., large and small disturbances. [Kun+04]

Rotor angle responses to either large or small disturbances are usually within a time frame of interest of a few seconds. Hence, rotor angle stability is investigated in the short term. The time frame of interest for both frequency and voltage stability evaluations can be short, i.e., several seconds, or long, i.e., several minutes, dependent on the activation of devices and processes during and after the disturbance.

C.2 Grid Strength

The grid at a certain PCC is considered strong, if the short circuit ratio (SCR) is high and the relation of resistance to inductance R/X is low. The short circuit ratio at the PCC of a CBG

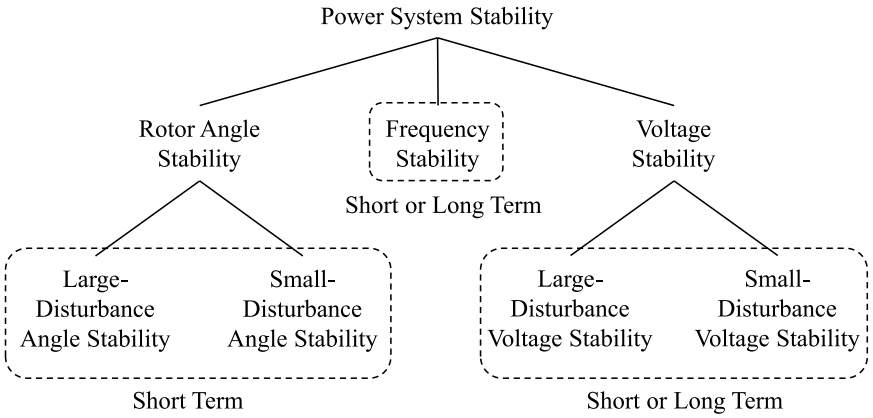

Figure C.1: Classification of power system stability according to [Kun+04]

is defined according to [Kun94, p. 528] as

$$\mathrm{SCR} = \frac{S_{\mathrm{sc}}}{P_{\mathrm{rat}}}, \tag{C.1}$$

where P_{rat} is the rated active power of the CBG and the short circuit apparent power of the AC system is defined as

$$S_{\mathrm{sc}} = \frac{V_{\mathrm{AC}}^2}{Z_{\mathrm{th}}}, \tag{C.2}$$

where V_{AC} is the bus voltage for an active power generation P_{rat} of the CBG and Z_{th} as the Thévenin equivalent impedance [Bri90] of the AC system.
In [Böm16] the SCR ranges as listed in Table C.1 define the grid's strength.

Table C.1: SCR ranges that define the grid's strength according to [Böm16, p. 152]

Strength	SCR
strong	> 10
modest	5...10
weak	< 5

References

[AES04] A. M. Azmy, I. Erlich & P. Sowa. “Artificial neural network-based dynamic equivalents for distribution systems containing active sources”. In: *IET Proceedings - Generation, Transmission and Distribution* 151.6 (2004), pp. 681–688.

[Amm+18] J. Amme, G. Pleßmann, J. Bühler, et al. “The eGo grid model: An open-source and open-data based synthetic medium-voltage grid model for distribution power supply systems”. In: *Journal of Physics: Conference Series*. Vol. 977. 2018.

[Ann+12] U. D. Annakkage, N.-K. C. Nair, Y. Liang, et al. “Dynamic System Equivalents: A Survey of Available Techniques”. In: *IEEE Transactions on Power Delivery* 27.1 (2012), pp. 411–420.

[BC55] W. T. Brown & W. J. Cloues. “Combination Load-Flow and Stability Equivalent for Power System Representation on A-C Network Analyzers”. In: *Transactions of the American Institute of Electrical Engineers. Part III: Power Apparatus and Systems* 74.3 (1955), pp. 782–787.

[BH07] H.-P. Beck & R. Hesse. “Virtual Synchronous Machine”. In: *9th International Conference on Electrical Power Quality and Utilisation*. IEEE, 2007.

[BN+22] G. Barzegkar-Ntovom, E. O. Kontis, T. A. Papadopoulos, et al. “Methodology for Evaluating Equivalent Models for the Dynamic Analysis of Power Systems”. In: *IEEE Transactions on Power Delivery* (2022).

[Böm16] J. C. Bömer. “On Stability of Sustainable Power Systems - Network Fault Response of Transmission Systems with Very High Penetration of Distributed Generation”. PhD thesis. Technische Universiteit Delft, 2016.

[Bra+21] J. Brandes, M. Haun, D. Wrede, et al. *Wege zu einem klimaneutralen Energiesystem - Die deutsche Energiewende im Kontext gesellschaftlicher Verhaltensweisen - Update November 2021: Klimaneutralität 2045*. Tech. rep. Freiburg: Fraunhofer Institute for Solar Energy Systems, 2021.

[Bri90] J. E. Brittain. "Thévenin's theorem". In: *IEEE Spectrum* 27.3 (1990), p. 42.

[Büc+14] J. Büchner, J. Katzfey, O. Flörcken, et al. *Moderne Verteilernetze für Deutschland (Verteilernetzstudie)*. Tech. rep. 44. 2014.

[Bun15] Bundesnetzagentur. *List of Power Plants*. 2015. URL: https://www.bundesnetzagentur.de/EN/Areas/Energy/Companies/SecurityOfSupply/GeneratingCapacity/PowerPlantList/start.html (visited on 06 Mar. 2022).

[Bur] B. Burger. *Energy-Charts*. URL: https://www.energy-charts.info/.

[CDA93] M. C. Chandorkar, D. M. Divan & R. Adapa. "Control of Parallel Connected Inverters in Standalone ac Supply Systems". In: *IEEE Transactions on Industry Applications* 29.1 (1993), pp. 136–143.

[CDS19] F. Conte, F. D'Agostino & F. Silvestro. "Operational Constrained Nonlinear Modeling and Identification of Active Distribution Networks". In: *Electric Power Systems Research* 168.March (2019), pp. 92–104.

[Cha+21] G. Chaspierre, G. Denis, P. Panciatici, et al. "A Dynamic Equivalent of Active Distribution Network: Derivation, Update, Validation and Use Cases". In: *IEEE Open Access Journal of Power and Energy* 8 (2021), pp. 497–509.

[Cho+06] B.-K. Choi, H.-D. Chiang, Y. Li, et al. "Measurement-Based Dynamic Load Models: Derivation, Comparison, and Validation". In: *IEEE Transactions on Power Systems* 21.3 (2006), pp. 1276–1283.

[Cou22] M. A. Coumont. "Dynamik und Modellierung aktiver Verteilnetze unter Berücksichtigung netzbildender Regelung". PhD thesis. Technische Universität Darmstadt, 2022.

[Dav66] E. J. Davison. "A Method for Simplifying Linear Dynamic Systems". In: *IEEE Transactions on Automatic Control* 11.1 (1966), pp. 93–101.

[Deu14] Deutsche Gesellschaft für Sonnenenergie e.V. *Die EEG-Anlagen der Region Bundesrepublik Deutschland (EnergyMap)*. 2014. URL: http://www.energymap.info/energieregionen/DE/105.html (visited on 06 Mar. 2022).

[DIg22a] DIgSILENT GmbH. *PowerFactory 2022 - Technical Reference - Phase Measurement Device*. Tech. rep. Gomaringen, Germany, 2022.

[DIg22b] DIgSILENT GmbH. *PowerFactory 2022 - Technical Reference - PWM Converter*. Tech. rep. Gomaringen, Germany, 2022.

[Dim75] P. Dimo. *Nodal Analysis of Power Systems*. Editura Academiei Republicii Socialisté România, 1975.

[DN06] A. S. Deese & C. O. Nwankpa. "Emulation of Power System Load Dynamic Behavior Through Reconfigurable Analog Circuits". In: *International Symposium on Circuits and Systems*. IEEE, 2006, pp. 1691–1694.

[DS14] S. D'Arco & J. A. Suul. "Equivalence of Virtual Synchronous Machines and Frequency-Droops for Converter-Based MicroGrids". In: *IEEE Transactions on Smart Grid* 5.1 (2014), pp. 394–395.

[Du+21] W. Du, F. K. Tuffner, K. P. Schneider, et al. "Modeling of Grid-Forming and Grid-Following Inverters for Dynamic Simulation of Large-Scale Distribution Systems". In: *IEEE Transactions on Power Delivery* 36.4 (2021), pp. 2035–2045.

[DV08] J. Driesen & K. Visscher. "Virtual Synchronous Generators". In: *IEEE Power and Energy Society General Meeting - Conversion and Delivery on Electrical Energy in the 21st Century*. 2008.

[EEa] ENTSO-E. *A short outage of French-Spain interconnection on 24 July 2021*. URL: https://www.entsoe.eu/news/2021/07/24/a-short-outage-of-french-spanish-interconnection-on-24-july-2021/ (visited on 17 May 2022).

[EEb] ENTSO-E. *Final Report on the local power grid incident in Rogowiec (Poland) substation on 17 May 2021*. URL: https://www.entsoe.eu/news/2022/03/18/final-report-on-the-local-power-grid-incident-in-rogowiec-poland-substation-on-17-may-2021/ (visited on 17 May 2022).

[EEc] ENTSO-E. *System split registered in the synchronous area of Continental Europe - Incident now resolved*. URL: https://www.entsoe.eu/news/2021/01/08/system-split-registered-in-the-synchronous-area-of-continental-europe-incident-now-resolved/ (visited on 17 May 2022).

[EE18] ENTSO-E. *Limited frequency sensitive mode - ENTSO-E guidance document for national implementation for network codes on grid connection*. Tech. rep. January. Available online: https://www.entsoe.eu/Documents/Network%20codes%20documents/NC%20RfG/IGD_LFSM-O-U_final.pdf: ENTSO-E, 2018.

[ENT20] ENTSO-E Technical Group on High Penetration of Power Electronic Interfaced Power Sources. *High Penetration of Power Electronic Interfaced Power Sources and the Potential Contribution of Grid Forming Converters*. Tech. rep. Available online: https://www.entsoe.eu/Documents/Publications/SOC/High_Penetration_of_Power_Electronic_Interfaced_Power_Sources_and_the_Potential_Contribution_of_Grid_Forming_Converters.pdf: ENTSO-E, 2020.

[Eur17] European Commission. *Commission Regulation (EU) 2017/2195 establishing a guideline on electricity balancing*. Available online: https://eur-lex.europa.eu/legal-content/EN/TXT/?uri=CELEX:02017R2195-20210315, 2017.

[Eur19] European Commission. *Communication from the Commission to the European Parliamant, the European Council, the Council, the European Economic and Social Committee and the Committee of the Regions - The European Green Deal*. Available online: https://eur-lex.europa.eu/legal-content/EN/TXT/?uri=CELEX:52019DC0640, 2019.

[FGW19] FGW. *Technische Richtlinien für Erzeugungseinheiten: Teil 4*. Tech. rep. Berlin: FGW e.V. Fördergesellschaft Windenergie und andere Dezentrale Energien, 2019.

[FLB07] X. Feng, Z. Lubośny & J. W. Bialek. "Identification based Dynamic Equivalencing". In: *IEEE Lausanne Power Tech*. 2007, pp. 267–272.

[Ful+20] N. Fulgêncio, C. Moreira, L. Carvalho, et al. "Aggregated Dynamic Model of Active Distribution Networks for Large Voltage Disturbances". In: *Electric Power Systems Research* 178 (2020).

[GDS15] A. Gkountaras, S. Dieckerhoff & T. Sezi. "Evaluation of Current Limiting Methods for Grid Forming Inverters in Medium Voltage Microgrids". In: *2015 IEEE Energy Conversion Congress and Exposition (ECCE)* (2015), pp. 1223–1230.

[Hül+17] L. Hülk, L. Wienholt, I. Cußmann, et al. “Allocation of Annual Electricity Consumption and Power Generation Capacities Across Multiple Voltage Levels in a High Spatial Resolution”. In: *International Journal of Sustainable Energy Planning and Management* 13 (2017), pp. 79–92.

[Iee] *IEEE 9-bus modified test system*. URL: https://www.kios.ucy.ac.cy/testsystems/index.php/dynamic-ieee-test-systems/ieee-9-bus-modified-test-system (visited on 10 Sept. 2019).

[IMK07] A. Ishchenko, J. M. Myrzik & W. L. Kling. “Dynamic equivalencing of distribution networks with dispersed generation using Hankel norm approximation”. In: *IET Generation, Transmission and Distribution* 1.5 (2007), pp. 818–825.

[Joh+14] B. B. Johnson, S. V. Dhople, A. O. Hamadeh, et al. “Synchronization of Parallel Single-Phase Inverters With Virtual Oscillator Control”. In: *IEEE Transactions on Power Electronics* 29.11 (2014), pp. 6124–6138.

[Joi18] Joint Working Group C4/C6.35/CIRED. *Modelling of inverter-based generation for power system dynamic studies*. Tech. rep. CIGRE, 2018.

[KE95] J. Kennedy & R. Eberhart. “Particle Swarm Optimization”. In: *Proceedings of ICNN’95 - International Conference on Neural Networks*. IEEE, 1995, pp. 1942–1948.

[KH94] D. Karlsson & D. J. Hill. “Modelling and identification of nonlinear dynamic loads in power systems”. In: *IEEE Transactions on Power Systems* 9.1 (1994), pp. 157–166.

[Kon+19] E. O. Kontis, T. A. Papadopoulos, M. H. Syed, et al. “Artificial-Intelligence Method for the Derivation of Generic Aggregated Dynamic Equivalent Models”. In: *IEEE Transactions on Power Systems* 34.4 (2019), pp. 2947–2956.

[Ksg] *Bundes-Klimaschutzgesetz (KSG)*. 2021. URL: https://www.gesetze-im-internet.de/ksg/.

[Kun+04] P. Kundur, J. Paserba, V. Ajjarapu, et al. “Definition and Classification of Power System Stability”. In: *IEEE Transactions on Power Systems* 19.2 (2004), pp. 1387–1401.

[Kun94] P. Kundur. *Power System Stability And Control*. New York: McGraw-Hill, 1994.

[Lam+17] G. Lammert, K. Yamashita, L. D. P. Ospina, et al. “International industry practice on modelling and dynamic performance of inverter based generation in power system studies”. In: *CIGRE Science and Engineering Journal* 8 (2017), pp. 25–37.

[LBH05] M. Liserre, F. Blaabjerg & S. Hansen. “Design and Control of an LCL-Filter-Based Three-Phase Active Rectifier”. In: *IEEE Transactions on Industry Applications* 41.5 (2005), pp. 1281–1291.

[Lin+93] C.-J. Lin, Y.-T. Chen, C.-Y. Chiou, et al. “Dynamic Load Models in Power Systems Using the Measurement Approach”. In: *IEEE Transactions on Power Systems* 8.1 (1993), pp. 309–315.

[Liu+20] Z. Liu, N. Bornhorst, S. Wende-von Berg, et al. “A Grid Equivalent Based on Artificial Neural Networks in Power Systems with High Penetration of Distributed Generation with Reactive Power Control”. In: *IEEE Conference on Sustainable Energy Supply and Energy Storage Systems (NEIS)*. 2020.

[Llo82] S. P. Lloyd. “Least Squares Quantization in PCM”. In: *IEEE Transactions on Information Theory* 28.2 (1982), pp. 129–137.

[Mac67] J. MacQueen. “Some Methods for Classification and Analysis of Multivariate Observations”. In: *5th Berkeley Symposium on Mathematical Statistics and Probability*. Ed. by L. M. Le Cam and J. Neyman. Vol. 1. University of California Press, 1967, pp. 281–297.

[Mat+19] J. Matevosyan, B. Badrzadeh, T. Prevost, et al. “Grid-Forming Inverters: Are They the Key for High Renewable Penetration?” In: *IEEE Power and Energy Magazine* 17.6 (2019), pp. 89–98.

[MBB11] J. Machowski, J. W. Bialek & J. R. Bumby. *Power System Dynamics: Stability and Control*. 2nd. John Wiley and Sons, Ltd, 2011.

[Mei+20] S. Meinecke, D. Sarajlić, S. R. Drauz, et al. “SimBench - A Benchmark Dataset of Electric Power Systems to Compare Innovative Solutions Based on Power Flow Analysis”. In: *Energies* 13.12 (2020).

[MF02] V. Miranda & N. Fonseca. “EPSO - Evolutionary Particle Swarm Optimization, a New Algorithm with Applications in Power Systems”. In: *IEEE/PES Transmission and Distribution Conference and Exhibition*. IEEE, 2002, pp. 745–750.

[Mig] *The Massive Integration of Power Electronic Devices - MIGRATE*. URL: https://www.h2020-migrate.eu/.

[Mil+18] F. Milano, F. Dörfler, G. Hug, et al. "Foundations and Challenges of Low-Inertia Systems". In: *20th Power Systems Computation Conference (PSCC)*. July. IEEE, 2018.

[ML21a] G. Mitrentsis & H. Lens. "A Dynamic Active Distribution Network Equivalent for Enhancing the Generalization Capability of the Exponential Recovery Model in Stability Studies". In: *IEEE Transactions on Power Systems* 36.3 (2021), pp. 2709–2712.

[ML21b] G. Mitrentsis & H. Lens. "Data-Driven Dynamic Models of Active Distribution Networks Using Unsupervised Learning Techniques on Field Measurements". In: *IEEE Transactions on Smart Grid* 12.4 (2021), pp. 2952–2965.

[MV12] F. Ma & V. Vittal. "A Hybrid Dynamic Equivalent Using ANN-Based Boundary Matching Technique". In: *IEEE Transactions on Power Systems* 27.3 (2012), pp. 1494–1502.

[Nav05] I. R. Navarro. "Dynamic Power System Load - Estimation of Parameters from Operational Data". PhD thesis. Lund Institute of Technology, 2005.

[OO11] D. Oeding & B. R. Oswald. *Elektrische Kraftwerke und Netze*. 7th. Springer Berlin Heidelberg, 2011.

[Øru+15] E. Ørum, M. Kuivaniemi, M. Laasonen, et al. *Future System Inertia*. Tech. rep. ENTSO-E, 2015.

[PAVS82] I. J. Pérez-Arriaga, G. C. Verghese & F. C. Schweppe. "Selective Modal Analysis with Applications to Electric Power Systems, Part I: Heuristic Introduction". In: *IEEE Transactions on Power Apparatus and Systems* PAS-101.9 (1982), pp. 3117–3125.

[PPG07] N. Pogaku, M. Prodanović & T. C. Green. "Modeling, Analysis and Testing of Autonomous Operation of an Inverter-Based Microgrid". In: *IEEE Transactions on Power Electronics* 22.2 (2007), pp. 613–625.

[PR81] W. W. Price & B. A. Roth. "Large-Scale Implementation of Modal Dynamic Equivalents". In: *IEEE Transactions on Power Apparatus and Systems* PAS-100.8 (1981), pp. 3811–3817.

[Pri+78] W. W. Price, E. M. Gulachenski, P. Kundur, et al. “Testing of the Modal Dynamic Equivalents Technique”. In: *IEEE Transactions on Power Apparatus and Systems* PAS-97.4 (1978), pp. 1366–1372.

[PSS20] P. N. Pham, A. Salman & R. Singer. “Improving, Modelling and Simulation of Droop Controller for Grid-forming Inverters in DIgSILENT PowerFactory”. In: *Solar Integration Workshop*. 2020.

[Ram+96] G. N. Ramaswamy, L. Rouco, O. Filiatre, et al. “Synchronic Modal Equivalencing (SME) for Structure-Preserving Dynamic Equivalents”. In: *IEEE Transactions on Power Systems* 11.1 (1996), pp. 19–29.

[Ram99] J. M. Ramirez Arredondo. “Obtaining dynamic equivalents through the minimization of a line flows function”. In: *International Journal of Electrical Power and Energy Systems* 21.5 (1999), pp. 365–373.

[RCRPP20] A. Rodriguez-Cabero, J. Roldán-Pérez & M. Prodanovic. “Virtual Impedance Design Considerations for Virtual Synchronous Machines in Weak Grids”. In: *IEEE Journal of Emerging and Selected Topics in Power Electronics* 8.2 (2020), pp. 1477–1489.

[Rez+14] A. Reznik, M. G. Simoes, A. Al-Durra, et al. “LCL Filter Design and Performance Analysis for Grid-Interconnected Systems”. In: *IEEE Transactions on Industry Applications* 50.2 (2014), pp. 1225–1232.

[RJH06] H. Renmu, M. Jin & D. J. Hill. “Composite Load Modeling via Measurement Approach”. In: *IEEE Transactions on Power Systems* 21.2 (2006), pp. 663–672.

[RMM13] F. O. Resende, J. Matevosyan & J. V. Milanovic. “Application of Dynamic Equivalence Techniques to Derive Aggregated Models of Active Distribution Network Cells and MicroGrids”. In: *IEEE Grenoble Conference PowerTech*. 2013.

[Roc+12] J. Rocabert, A. Luna, F. Blaabjerg, et al. “Control of Power Converters in AC Microgrid”. In: *IEEE Transactions on Power Electronics* 27.11 (2012), pp. 4734–4749.

[Rog+21] S. Rogalla, A. Greulich, J. Lehner, et al. “Grid Forming Converters in Interconnected Systems - Final Results from the Joint Research Project VerbundnetzStabil”. In: *20th Wind Integration Workshop*. September. 2021.

[ĐS12] S. D. Đukić & A. T. Sarić. “Dynamic Model Reduction: An Overview of Available Techniques with Application to Power Systems”. In: *Serbian Journal of Electrical Engineering* 9.2 (2012), pp. 131–169.

[Sam+15] A. Samadi, L. Söder, E. Shayesteh, et al. “Static Equivalent of Distribution Grids With High Penetration of PV Systems”. In: *IEEE Transactions on Smart Grid* 6.4 (2015), pp. 1763–1774.

[Sch12] A. J. Schwab. *Elektroenergiesysteme: Erzeugung, Transport, Übertragung und Verteilung elektrischer Energie*. 3. Berlin: Springer, 2012.

[Sha+19] X. Shang, Z. Li, J. Zhang, et al. “Equivalent Model of Active Distribution Network Considering the Spatial Uncertainty of Renewable Energy Resources”. In: *International Journal of Electrical Power and Energy Systems* 112.1 (2019), pp. 83–91.

[SL21] C. Schöll & H. Lens. “Design- and Simulation-based Comparison of Grid-Forming Converter Control Concepts”. In: *20th Wind Integration Workshop*. 2021.

[Str+14] K. Strunz, E. Abbasi, C. Abbey, et al. *Benchmark Systems for Network Integration of Renewable and Distributed Energy Resources*. Tech. rep. April. CIGRE, 2014.

[SZ22] P. Sowa & D. Zychma. “Dynamic Equivalents in Power System Studies: A Review”. In: *Energies* 15.4 (2022).

[Tam+17] U. Tamrakar, D. Shrestha, M. Maharjan, et al. “Virtual Inertia: Current Trends and Future Directions”. In: *Applied Sciences* 7.7 (2017).

[UL23] J. Ungerland & H. Lens. “Evaluation of Equivalent Dynamic Active Distribution Network Models with Individual and Aggregated Consideration of Grid Forming Converters”. In: *Energy Technology* 2300336 (2023).

[Und+71] J. M. Undrill, J. A. Casazza, E. M. Gulachenski, et al. “Electromechanical Equivalent for Use in Power System Stability Studies”. In: *IEEE Transactions on Power Apparatus and Systems* PAS-90.5 (1971), pp. 2060–2071.

[Ung22] J. Ungerland. *Forschungsprojekt VerbundnetzStabil - Fachbericht 3A: Äquivalente Verteilungsnetzmodelle*. 2022.

[Ung+22a] J. Ungerland, R. Bhadani, W. Biener, et al. “Operating Point Dependency and Adaptation of Dynamic Active Distribution Network Equivalents”. In: *13th IEEE International Symposium on Power Electronics for Distributed Generation Systems (PEDG)*. 2022.

[Ung+22b] J. Ungerland, N. Poshiya, W. Biener, et al. “A Voltage Sensitivity Based Equivalent for Active Distribution Networks Containing Grid Forming Converters”. In: *IEEE Transactions on Smart Grid* 14.4 (2022), pp. 2825 –2836.

[UP20] J. Ungerland & P. Pant. “Challenges of Modelling Equivalent Active Distribution Grids under Consideration of Grid Forming Inverters”. In: *Virtual 19th Wind Integration Workshop*. 2020.

[UT71] J. M. Undrill & A. E. Turner. “Construction of Power System Electromechanical Equivalents by Modal Analysis”. In: *IEEE Transactions on Power Apparatus and Systems* PAS-90.5 (1971), pp. 2049–2059.

[Vit+19] V. Vittal, J. D. McCalley, P. M. Anderson, et al. *Power System Control and Stability*. 3rd. Wiley-IEEE Press, 2019.

[VPAS82] G. C. Verghese, I. J. Pérez-Arriaga & F. C. Schweppe. “Selective Modal Analysis With Applications to Electric Power Systems, Part II: The Dynamic Stability Problem”. In: *IEEE Transactions on Power Apparatus and Systems* PAS-101.9 (1982), pp. 3126–3134.

[VRU20] M. F. Valois-Rodriguez & J. Ungerland. “Evaluation of Grid Reduction Techniques for Distribution Networks with a High Penetration of Inverter-based Generation”. In: *IEEE PES Innovative Smart Grid Technologies Europe (ISGT-Europe)*. 2020, pp. 824–828.

[War49] J. B. Ward. “Equivalent Circuits for Power-Flow Studies”. In: *Transactions of the American Institute of Electrical Engineers* 68 (1949).

[WEC10] WECC. *WECC Guide for Representation of Photovoltaic Systems In Large-Scale Load Flow Simulations*. Tech. rep. August. Available online: https://www.wecc.org/_layouts/15/WopiFrame.aspx?sourcedoc=/Reliability/WECCPVPlantPowerFlowModelingGuide.pdf&action=default: Western Electricity Coordinating Council, 2010.

[WEC14] WECC Renewable Energy Modeling Task Force. *WECC PV Power Plant Dynamic Modeling Guide*. Tech. rep. Available online: https://www.wecc.org/Reliability/WECC%20Solar%20Plant%20Dynamic%20Modeling%20Guidelines.pdf: WECC, 2014.

[Wes+09] M. P. N. van Wesenbeeck, S. W. H. de Haan, P. Varela, et al. "Grid Tied Converter with Virtual Kinetic Storage". In: *IEEE Bucharest PowerTech Conference*. 2009.

[Wu16] X. Wu. "New Approaches to Dynamic Equivalent of Active Distribution Network for Transient Analysis". PhD thesis. RWTH Aachen University, 2016.

[Wu+18] X. Wu, X. Lei, Y. Lan, et al. "A New Dynamic Equivalent of Active Distribution Network for Transient Analysis". In: *IEEE International Conference on Power System Technology, POWERCON*. 2018, pp. 529–536.

[Zal12] S. M. Zali. "Equivalent Dynamic Model of Distribution Network with Distributed Generation". PhD thesis. University of Manchester, 2012.

[Zhu09] J. Zhu. *Optimization of Power System Operation*. New Jersey: John Wiley and Sons, 2009.

[Zhu64] L. A. Zhukov. "Simplified transformation of circuit diagrams of complex electric power systems". In: *Izvestia Akademii Nauk SSSR, Energetika i Transport* 2 (1964).

[ZM13] S. M. Zali & J. V. Milanović. "Generic Model of Active Distribution Network for Large Power System Stability Studies". In: *IEEE Transactions on Power Systems* 28.3 (2013), pp. 3126–3133.

[ZW11] Q.-C. Zhong & G. Weiss. "Synchronverters: Inverters That Mimic Synchronous Generators". In: *IEEE Transactions on Industrial Electronics* 58 (2011), pp. 1259–1267.

Danksagung

Ein besonderer Dank geht an Prof. Dr. Hendrik Lens, der ganz elementar zum Gelingen der Arbeit beigetragen hat. Angefangen beim Schärfen der thematischen Ausrichtung bis zur finalen Schriftfassung wurde ich durch scharfsinnige Fragen, Kommentare und Vorschläge unterstützt. Neben den regelmäßigen Betreuungsgesprächen haben die wertvollen Beiträge als Ko-Autor einiger Publikationen die Arbeit qualitativ deutlich verbessert. Darüber hinaus möchte ich mich bei Prof. Dr. Christof Wittwer bedanken für die Übernahme des Zweitgutachters und für zahlreiche spannende Diskussionen. Weiterhin war er ein entscheidender Treiber für die Bewerbung bei der Stiftung Nagelschneider.

Ohne die finanzielle Unterstützung der Arbeit durch die Stiftung Nagelschneider wäre diese Arbeit nicht zustande gekommen. Ein großes Dankeschön für den unbürokratischen Ablauf des Stipendiums sowie die interessanten Diskussionen in den jährlichen Sitzungen.

Ein herzlicher Dank geht an die Kolleginnen und Kollegen des Fraunhofer-Institut für Solare Energiesysteme ISE. Von vielen Seiten habe ich dort große Unterstützung erhalten, ohne die die Arbeit nicht möglich gewesen wäre. Wolfgang Biener hat entscheidend in der Themenfindung mitgewirkt und war in jedem Schritt der Arbeit mit seinen Gedanken und Ideen zur Stelle. Dr. Ammar Salman hat mich in die Möglichkeiten von PowerFactory eingeweiht, wovon ich bis heute profitiere. Philipp Ernst und Rebekka Denninger waren mit ihrer Kompetenz immer zur Seite, wenn ich Fragen zu netzbildenden Wechselrichtern hatte. Unserer Mathematikerin Jasmin Montalbano und unserem Mathematiker Dr. Benedikt Köpfer sowie unserem Optimierungsexperten Arne Groß bin ich sehr dankbar, dass sie ein Auge auf meine Formeln geworfen haben und sowohl die Komplexität als auch den Stil deutlich verbessern konnten. Neben der fachlichen Unterstützung bin ich meinen Kolleginnen und Kollegen sehr dankbar, dass sie für eine Erdung durch regelmäßige Sportaktivitäten, Motivationssprüche, Feierabend-Aufrufe oder Gänge zur Kaffeemaschine gesorgt haben. Stellvertretend ein Dankeschön an Janis Kähler, Arne Surmann, Sebastian Kaiser, Dr. Matthias Kühnbach und Dr. Bernhard Wille-Haussmann.

Ein großes Dankeschön geht an die motivierten und kompetenten Studenten Manuel Fernando Valois-Rodriguez, Prashant Pant, Nikhilkumar Poshiya und Rachit Bhadani, deren Masterarbeit ich im Laufe der Doktorarbeit betreuen durfte.
In meinem privaten Umfeld möchte ich mich für die stete Unterstützung und das Verständnis bei Uta Ungerland und Johann Ziegler, Carl-Georg Ungerland, meinen Geschwistern Sophia und Lukas, meiner Großmutter Hannelore Schlichting, meinen Mitbewohnern Dr. Niels Schwaderlapp und Max Fuchs bedanken. Ein besonderes Dankeschön an meine Verlobte Catherina Klop, auf deren offenes Ohr ich mich immer verlassen kann.

Jakob Ungerland
Freiburg i. Br., im Dezember 2022